Numerical modeling of multiphase flow and phase separation phenomena in the system $H_2O-NaCl$ with applications to magmatic hydrothermal systems at fast-spreading mid-ocean ridges

Dissertation

zur Erlangung des Doktorgrades der Naturwissenschaft
der Mathematisch-Nuturwissenschaftlichen Fakultät
der Christian-Albrechts-Universität zu Kiel

vorgelegt von
Falko Vehling

Kiel, 2021

Erstgutachter: Prof. Dr. Lars Rüpke

Zweitgutachter: Prof. Dr. Colin Devey

Tag der mündlichen Prüfung: 15.02.2022

Zum Druck genehmigt: 15.02.2022

____

Der Dekan

Zusammenfassung

Der weitaus größte Teil der vulkanischen Aktivität der Erde findet entlang der 61.000 km langen mittelozeanischen Rücken statt, wo Magma aus dem Erdmantel aufsteigt und neue ozeanische Kruste bildet. Die Kruste wird durch eine hydrothermale Fluidzirkulation abgekühlt, die Metalle aus den Krustengesteinen löst und sie zum Meeresboden trägt, wo vulkanogene Massivsulfide an bis zu 400 °C heißen Austrittsstellen gebildet werden. Ausströmende Spurenelemente beeinflussen die biogeochemischen Ozeankreisläufe im globalen Maßstab und düngen im Falle von Eisen den Ozean. An mittelozeanischen Rücken sind die inneren Prozesse hydrothermaler Systeme schwer zugänglich. Sie müssen indirekt durch geophysikalische Messungen, durch petrologische Analysen ozeanischer Kruste oder aus geochemischen Analysen von ausströmenden hydrothermalen Fluiden erforscht werden. Numerische Modelle haben sich nützlich erwiesen, um die hydrothermale Fluiddynamik zu untersuchen, und ermöglichen es, Forschern die Beobachtungen und Interpretationen anderer Disziplinen besser zu verstehen. An sich schnell spreizenden Rücken werden Fluide durch flachen Magmatismus erhitzt, wobei die Fluide in hochsalzhaltige Sole und in salzarmen Wasserdampf getrennt werden. Hydrothermale Quellen spiegeln diese Prozesse mit zeitlichen Schwankungen in der Temperatur und des Salzgehalts wider.

In dieser Arbeit präsentiere ich meinen selbst entwickelten numerischen zweidimensionalen Simulator für poröses Fließen im System $H_2O-NaCl$, der zur Untersuchung von Phasentrennungsprozessen an der axialen Magmakammer und magmatischen Gangintrusionen verwendet wird. Der numerische Simulator für Strömungen im porösen Medium basiert auf der Control-Finite-Volume-Methode, wobei die Basisgleichungen simultan mit dem Newton-Raphson-Ansatz gelöst werden. Diese Methode ist lokal massen- und energieerhaltend und geeignet für große Gradienten der Temperatur und des Salzgehaltes. Zuerst konzentriere ich mich auf den Fall der Zweiphasenströmung für H_2O und evaluiere verschiedene numerische Methoden wie das Zeitschrittverfahren und die Stromaufwärtsgewichtung von Fluideigenschaften. Der numerische Ansatz zeigt eine gute Stabilität, die auch für nichtlineare Fluideigenschaften bei Druck- und Temperaturbedingungen um den kritischen Punkt von H_2O gilt. Vergleichstests mit dem Simulator HYDROTHERM zeigen eine hohe Genauigkeit und Effizienz. In der ersten Anwendung im System $H_2O-NaCl$ untersuche ich die Bildung und Mobilisierung der Sole oberhalb der axialen Magmakammer, die die hydrothermale Zirkulation antreibt und die im Modell durch eine schwankende basale Temperatur-Randbedingung realisiert wird. Diese Simulationen zeigen, dass die Erhitzung zu einer schnellen Phasentrennung und zur Bildung einer stabilen Schichtung der Sole führt. Diese Schichtung führt zu einer thermischen Isolation der Wärmequelle. Während die Soleschicht unter stationären Bedingungen stabil ist, werden durch die Reduzierung des Wärmeeintrags Solen mobilisiert. Dies führt zu deren Mitnahme in die Aufstromzone und zur Erhöhung des Salzgehaltes der Quellen. In der Praxis beobachtete hohe Wärmeflüsse an den hydrothermalen Quellenfeldern stehen im Gegensatz zu der von numerischen Modellen vorhergesagten isolierenden Soleschicht. Die zweite Anwendung untersucht Gangintrusionen unter Bedingungen, wie sie am East Pacific Rise (EPR) gefunden werden. Für den Bereich 9°50,3'N am EPR wurde der Salzgehalt und die Temperatur heißer Quellen über einen Zeitraum von >25 Jahren wiederholt gemessen. Nach einer Gangintrusion 1991/92 wurde beobachtet, dass auf niedrige Salinitäten nach einigen Jahren höhere Salinitäten folgen. Die Gangintrusionen wurden in einem 2D-Modellaufbau simuliert, das hydrothermale Konvektion auf der axialen Magmakammer nachbildet. Die Simulationsanalyse umfasst Phasenseparation und Salzakkumulation und Halitaus-fällungen in der Nähe der Gangintrusion sowie die verzögerte Mobilisierung der Sole. In einer Reihe von Modellläufen habe ich die entscheidenden Parameter identifiziert, die die Entwicklung des Salzgehalts der Quellen steuern. Diese Parameter sind die Durchlässigkeit und die Porosität des Gesteins sowie die Temperatur und der Salzgehalt der zentralen aufwärtsgerichteten Strömungszone, wo die Gangintrusion eindringt. Die Simulationen können durch Anpassung der Modellparameter die beobachteten Daten für den Bereich 9°50,3'N am EPR im Wesentlichen reproduzieren.

Abstract

By far the largest part of the earth's volcanic activity occurs along the 61,000 km long mid-ocean ridges, where magma rises from the earth's mantle and forms new oceanic crust. The crust is cooled by hydrothermal fluid circulation, which leaches metals from the crustal rocks and carries them to the ocean floor to form volcanogenic massive sulfide deposits around up to 400 °C hot venting sites. Venting trace elements affect the global scale biogeochemical ocean cycles and especially iron fertilizes the ocean. Hydrothermal venting sites host highly specialized and endemic ecosystems. At mid-ocean ridges, the inner workings of hydrothermal systems are difficult to access directly and have to be investigated indirectly through geophysical measurements, petrological studies of disclosed oceanic crust brought to the surface, or geochemical analysis of venting hydrothermal fluids. Numerical models have become a beneficial tool to study hydrothermal fluid dynamics and allow researchers to better synthesize and understand observations and interpretations obtained by other scientific disciplines. At fast-spreading ridges, hydrothermal fluids are heated by shallow magmatism separating the fluids into a high-salinity liquid and a low-salinity vapor phase. At the seafloor, these processes are reflected by temporal variations in temperature and salinity of hydrothermal vents.

In this thesis I present my self-developed two-dimensional numerical simulator for porous flow in the system $H_2O-NaCl$, which is applied to study phase separation processes at the axial magma lens and dike intrusions. The numerical simulator is based upon the control-finite-volume method in combination with the coupled approach, where the governing transport equations are solved simultaneously using the Newton-Raphson-approach. This method is locally mass-conserving and energy-conserving and can deal with high gradients of temperature and composition. First, I focus on the case of pure water two-phase flow problems and evaluate different numerical methods such as upwind-weighting of fluid properties and time-stepping schemes. Overall the numerical approach shows a good stability also for non-linear fluid properties at pressure-temperature conditions around the critical point of the pure water. A sufficient number of benchmark test cases against the geothermal system simulator HYDROTHERM attests high accuracy and good efficiency.

In the first application, I investigate the brine formation and mobilization in hydrothermal systems driven by a transient basal temperature boundary condition, which represents the axial magma lens. It was found that basal heating results in rapid phase segregation and the formation of a stable brine layer that thermally insulates the driving heat source of flow circulation. While this brine layer is stable under steady-state conditions, a reduction of the heat input mobilizes the brines. This leads to their entrainment in the upflow zone and fluid venting with elevated salinity. The observation of high heat fluxes of hydrothermal vent fields is contrary to the existence of the insulating brine layer, which is predicted by the numerical model. The second application studies dike intrusions for conditions found at the East Pacific Rise (EPR). At EPR 9°50.3’N, vent fluid salinity and temperature at individual vents in the axial summit trough have been repeatedly measured over a 25+ year-long period. After the 1991/92 diking event it was observed that low salinities are followed by higher salinities after a few years. The short-term salinity variations are likely to be super-imposed on a long-term background salinity signal, which is modulated by the changing rate of phase separation on top of the axial magma lens. The dike intrusion was simulated in a two-dimensional setup, which reproduces hydrothermal convection on top of the axial magma lens. The simulation analysis includes brine accumulation and halite precipitation close to the dike as well as two-phase flow and the delayed brine upflow when the dike has cooled. In a comprehensive suite of model runs, I have identified key parameters, which control the vent salinity evolution. These parameters are rock permeability and porosity plus the background fluid temperature and salinity of the hydrothermal upflow zone, where the dike is emplaced. By adjusting the model parameter, the simulations can approximately reproduce the observed data at EPR 9°50.3’N.

Contents

Pages

List of Figures

1 Introduction

1.1 Magmatic hydrothermal systems

Rock melts as well as aqueous fluids have an enormous impact on the geochemical evolution of the earth's crust. As fluids are by definition a mobile phase, they can move through fractures, faults and fissures and bypass different geologic reservoirs up to the earth's surface. Both fluids, rock melts and aqueous fluids, have a high heat capacity and control heat transfer through the earth's lithosphere. Often both fluids are interconnected. For example, metamorphic aqueous fluids derived from devolatilization of subducted rock minerals can migrate upwards and lower the melting temperature. The fluids are incorporated in these melts, which migrate through the lithosphere. Within the upper crust, these fluids and other gases will leave the magmatic intrusion and are added to the vital hydrothermal flow system, which is powered by heat release from crystalizing magma. As hot hydrothermal fluids are highly reactive, alter rocks and leach minerals, they produce local geochemical anomalies when minerals precipitate from the fluid. These processes include the formation of ore deposits, which are the basis of modern onshore mines.

Hydrothermal systems are defined as subsurface geological settings containing aqueous fluids related to hot temperature anomalies within the earth. These systems are characterized by fluid convection due to their density differences and by the thermodynamic equilibrium between rocks and fluid. The term geothermal system also includes hydrothermal systems, but dry and hot geological settings are included. Especially in the geothermal energy industry, the term “geothermal system” is often used instead of hydrothermal system. The term geothermal system is also often used for deep aquifers in sedimentary basins, which are heated due to the geothermal gradient between 25 and 30 °C/km. Hydrothermal systems with the supplement “magmatic” are heated by magmatic intrusions and could, in addition, contain fluids of volatile elements released from the magma.

Magma intrusions, which have an initial temperature between 900 °C and 1200 °C depending on depth and composition, can directly heat the pore fluids when they intrude into permeable rocks or sediments, but often magmatic heat is transferred by temperature conduction through an impermeable boundary layer into an overlaying hydrothermal convection cell. Therefore rock permeability is an important parameter, which controls the configuration and lifetime of a magmatic hydrothermal system. The rock permeability decreases substantially with depth and increasing temperatures, which favor ductile over brittle deformation of the rock, and consequently also reduces porosity and fractures of the rock. This behavior changes gradually over a range of temperatures and is called brittle-ductile transition. From lab experiments it has been derived that granites, the most abundant rock in the continental crust, deform brittle for temperatures below 400 ± 100 °C (Violay et al., 2017) and basalts of the oceanic crust deform brittle below temperatures up to 550 ± 100 °C (Violay et al., 2012). Petrological studies of basalts infer alteration temperatures of up to 750 °C suggesting that permeability is not negligibly low at nominally ductile temperatures, which was also found in lab experiments for granites (Watanabe et al., 2017). For permeabilities below 10^{-16} m² the system’s heat transport changes from advective to a conductive.

In magmatic hydrothermal system, magmatic intrusions usually lead to, boiling fluids intersecting the liquid-vapor coexisting phase region or entering the so-called “super-hot” state, defined by fluid temperatures above the temperature at the critical point of pure water (374.15 °C and 22.06 MPa). Fluids around the critical point of pure water can efficiently mine heat from the magmatic intrusion because of high heat capacity and low viscosity. The hydrothermal convection pattern is a self-organizing system, where heat transport is maximized in order to reduce temperature anomalies.

Magmatic hydrothermal systems are found in regions with high volcanic activity (Fig 1.1), which is primarily related to magmatic creation of new oceanic crust for divergent plate motions at mid-ocean ridges. Here the total heat loss of the inner earth sums up to $20 - 25\%$ (Stein and Stein, 1994), driving hydrothermal venting at the seafloor. Second, magmatic activity is related to subducting oceanic lithosphere for convergent plate motions, where the released fluid of the oceanic plate reduces the melting point of the mantle and crustal rocks. Then, these melts migrate into the overlying crust, forming intrusive magmatic bodies, or they erupt on the submarine or subaerial surface. This primarily occurs in the Pacific region, where old dense oceanic crust is subducted beneath continental or oceanic crust leading to either volcanic chains in South and North America or to several submarine and subaerial arc volcano chains in the whole western Pacific. Here, also back-arc spreading centers evolve due to slab rollback, having spreading rates comparable to mid-ocean ridges. Intraplate volcanism related to hot mantle plumes or continental rift zones represents the smallest part of the world's magmatic budget.

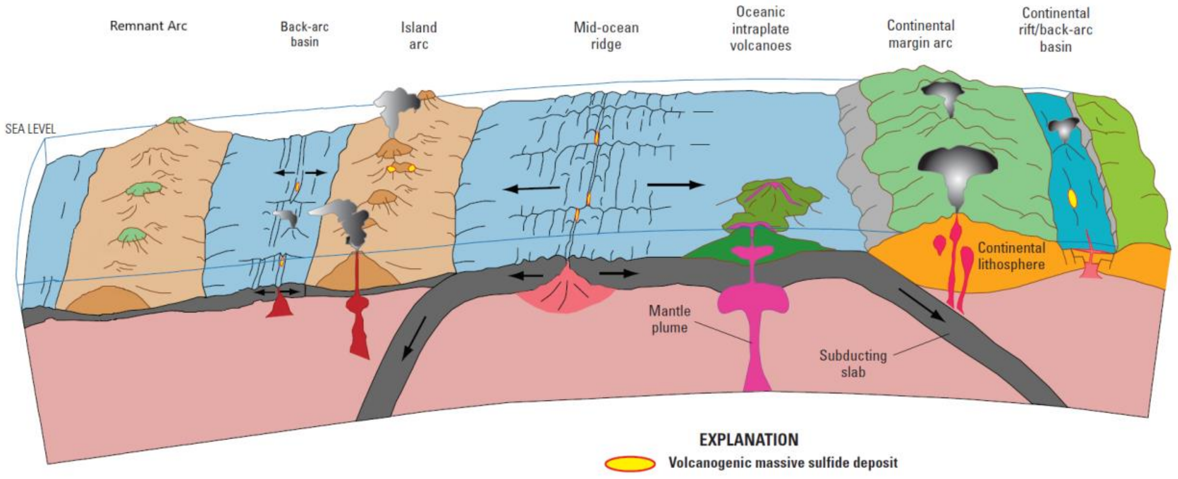

Figure 1.1: Volcanism related to different geological settings, modified after (Shanks III, 2012)

Submarine and subaerial systems differ substantially in their appearance at the seafloor and land surface respectively. At deep submarine systems like mid ocean ridges, where pressure conditions are below the critical point of pure water, hot liquids with up to 400 °C are vented. When these hot fluids are immediately cooled by ocean water, the dissolved minerals precipitate as dark particles venting mainly into the ocean but also building several meters high chimneys called "black smoker". These precipitated minerals are predominant metal sulfides. Also, so-called "white smokers" with lower temperatures and emit grey to white minerals like barite, anhydrite and calcite. If the main tectonic settings are unchanged over ten thousand years, hydrothermal mounds of pyrite-anhydrite breccias of tens of meters thickness grow in several cycles of active venting. (Hannington et al., 1998).

For the subaerial case, the upwelling hot fluids are mixed with meteoric waters and flow such as groundwater to topographic lows. When these hot fluids are not mixed and cooled with meteoric waters, the pressure drop leads to boiling and the water steam escapes from holes adjacent to the volcano crater as so-called fumaroles. The steam is often enriched in volcanic gasses like CO_2, SO_2 and H_2S. Consequently, around fumaroles often elemental sulfur or sulfur containing minerals were deposited. In the subsurface, these systems could build various ore deposits of economic interest. They arises when crystallizing magma releases fluids with high metal content or acidic hot fluids leach metals from the rocks close to the magmatic intrusion in the reaction zone. Metal precipitation within the magmatic hydrothermal systems is caused by changes of the physical and chemical state of the fluid, which often occur by cooling, mixing, boiling and chemical reactions with the host rock. Each metal precipitates under different conditions leading to a wide variety of ore deposits. Deposits related to magmatic hydrothermal systems are the most important source of Cu, Mo, W and Sn and a major source of Au, Ag, Zn and Pb (Kesler and Simon, 2015). As fluids with temperatures higher than 150 °C are favorable for electrical power generation, these fluids are mined for reliable power production, which is of increasing interest as more unreliable wind and solar power stations are built worldwide.

The research on the deeper parts of active magmatic hydrothermal systems is hampered by weak data availability. Borehole drillings become very expensive towards these depths and have to deal with extreme conditions of high temperatures, corrosive fluids and hard rocks. Additionally, targets are located in distant or unexplored areas leading to expensive costs for equipment like drilling ships. Geochemical analysis of altered rocks of hydrothermal flow are essential for understanding these systems, just like investigation of mineralized veins of ore deposits, which have been exhumed by erosion and have become accessible for open pit mining. The disadvantage is that this investigation does not deliver information over the entire evolution of the past flow systems. Therefore numerical modelling of magmatic hydrothermal systems has become a preferred tool to explore the thermal evolution and complex fluid dynamics (Ingebritsen et al., 2010). They are particularly useful when solutes like NaCl are present and phase separation of heated fluids occur, because these non-linear two-phase flow systems are difficult to predict and additionally, they behave substantially differently from pure water systems (Coumou et al., 2009b; Driesner and Geiger, 2007; Scott et al., 2017). NaCl is enriched in submarine hydrothermal systems due to crustal seawater circulation, in continental magmatic systems, where chloride is added from magmatic fluids into the system, or in sedimentary basins, which formation water can be NaCl saturated with up to approx. 30 wt% NaCl. After phase separation processes have taken place, the NaCl content can locally exceed 70 wt% NaCl. As NaCl is often the most abundant solute, the equations of state and the phase diagram of H_2O−NaCl, which displays the phase boundaries between single-phase and coexisting two-phase or three-phase regions in the pressure-temperature-composition space, are an essential part of numerical simulators and the analysis of fluid behavior in hydrothermal systems (Driesner and Heinrich, 2007). Phase boundaries are only moderately shifted by the presence of other major solutes such as KCl (Anderko and Pitzer, 1993b; Hovey et al., 1990; Sterner et al., 1992). Magmatic fluids add contents of CO_2 into the hydrothermal system, which is the most abundant volatile species after H_2O in submarine systems. Therefore the usage of the ternary system (H_2O−NaCl−CO_2) is more accurate, but the thermodynamic models and equations of state are still incomplete (Ingebritsen et al., 2010). Neglecting CO_2 in numerical models for submarine systems is often acceptable, as they are H_2O−NaCl dominated and small portions of CO_2 only slightly change phase boundaries in the pressure-temperature space.

1.2 Concept of numerical modeling of hydrothermal systems

The basis of any numerical simulator for a hydrothermal system is a mathematical-physical model. The Navier-Stokes equations describe the motion of a viscous fluid and express the conservation of momentum and the conservation of mass. They are used for many phenomena in earth science or engineering applications like atmospheric convection, ocean currents or convection of the earth mantle and the liquid core or magma reservoirs. For the fluid flow within a porous media the Darcy equation is used, which is derived from the Navier-Stokes law for laminar flow:

$$\vec{\mathbf{v}}_\mathrm{f} = -k\frac{k_\mathrm{rf}}{\eta_\mathrm{f}}\left(\nabla p - \rho_\mathrm{f}\vec{\mathbf{g}}\right) \tag{1.1}$$

where subscript f stands for either liquid (l) or vapor (v) phase and $\vec{\mathbf{v}}$ is the Darcy velocity, k is the rock permeability, k_r is the relative phase permeability, η is the viscosity, ρ is the density, p is the pressure and $\vec{\mathbf{g}}$ is the earth's gravity acceleration. The Darcy equation and its expansion for multiphase flow have many hydrogeological applications. In the near subsurface, it is used in the context of thermal energy storage and for describing groundwater flow for withdrawal and protecting drinking water. In the petroleum industry, it is used for oil and gas reservoir engineering and CO_2 underground storage in sedimentary basins. Finally, the Darcy law is part of the two governing equations for mass and heat transport for modeling and investigating hydrothermal systems. The following equations are simplified but sufficient for many applications for hydrothermal simulators:

$$\frac{\partial\left(\Phi\rho_\mathrm{m}\right)}{\partial t} = -\nabla\cdot\left(\sum_{\mathrm{f}\in\{\mathrm{l,v}\}}\rho_\mathrm{f}\vec{\mathbf{v}}_\mathrm{f}\right) \tag{1.2}$$

$$\frac{\partial E}{\partial t} = \frac{\partial}{\partial t}(\Phi\rho_\mathrm{m}h_\mathrm{m}) + \rho_\mathrm{r}c_\mathrm{r}\frac{\partial(T(1-\Phi))}{\partial t} = \nabla\cdot K\nabla T - \nabla\cdot\left(\sum_{\mathrm{f}\in\{\mathrm{l,v}\}}h_\mathrm{f}\rho_\mathrm{f}\vec{\mathbf{v}}_\mathrm{f}\right) \tag{1.3}$$

Here ρ_m is the mean density and h_m the mean specific enthalpy of the composition of both phases. E is total energy stored in rock and fluid, T is the temperature, Φ is rock porosity, K is conductivity of rock, ρ_r is rock density, c_r is the specific heat capacity and t is the time. These governing equations are also called conservation equations and are partial differential equations, where evolution in time is stated by a first-order derivative in time and the diffusive and adjective transport terms inhibit spatial derivatives of second order. This set could be supplemented by the transport equation of fluid components with additional chemical reactions between fluid and rock. In hot magmatic hydrothermal systems, the governing equations are strongly coupled by fluid properties, which depend on temperature, pressure and composition. For example, the heat transport changes fluid density by temperature increase, which changes mass transport, which in turn changes heat transport. This coupling of the governing equation has to be treated with the numerical solution method. The equation of state (EOS) of the fluid, which defines phase relation and fluid properties, can also be more complex when multiple components are present. The governing equations could also be added by variable rock properties. In general, the complexity of the mathematical-physical model is not restricted by the complexity of nature but by the researcher, who has to find a reasonable reduced mathematical-physical model, which is actionable in a numerical simulator and also suitable for the research problem.

After finding the mathematical-physical model, the size of the modeling domain and its spatial discretization together with a numerical method for solving the governing equations has to be selected. Here too both choices depend on the hydrogeological setting and should support each other. In the last 40 years, several numerical methods have been applied. First, the finite difference method (FDM) and finite element method (FEM) have been applied, and now the integrated finite difference method (IFDM) and finite volume method (FVM) are often used in current simulators. All numerical methods have in common that they calculate for each time step a set of physical fluid properties for every grid point, which describe the state of the fluid, for example, fluid pressure, temperature and composition. A linear set of equations has to be solved for these calculations, which linearly grows with the number of grid points. Therefore a higher number of grid points needs higher computational resources and sometimes parallel computing algorithms. As the spatial discretization in three dimensions needs one order of magnitude more grid points, when the spatial resolution should be equal, simulations in two dimensions were preferred in the past. Moreover simulators capable of three dimension are often restricted to simplified physical assumptions like pure water approaches, but studies have shown that fluid flow is mostly organized in three-dimensional configurations. Hence in the future, more three-dimensional hydrothermal simulation studies will be obtained including two-phase flow, when computational power is easier available for high resolution grids.

The last important part of setting up a hydrothermal simulation is to implement the boundary conditions. The researcher has to decide at which boundaries fluid flow is allowed to cross the modeling domain or if no flow is allowed. The heat source that drives hydrothermal convection given by magmatic intrusions or magma chambers is realized by a heat flow or temperature boundary condition, which can be fixed or variable in time. Alternatively, magmatic intrusions are often implemented as an initial hot impermeable rock within the modeling domain, which cools during the simulation and becomes permeable. Especially magmatic intrusions into cold surrounding rocks lead to high temperature gradients followed by rapid vapor expansion and high flow velocities due to high pressure increase. Here numerical methods have to be stable, which means that the iterative solver has to converge and does not produce numerical oscillations in the temperature field or in fluid compositions. Numerical methods like IFDM or FVM, which are mass-conserving and heat-conserving for the predefined area around each grid point, have advantages as they are better suited to reduce numerical oscillations. In conclusion, it should be noted that no numerical method is the best choice in terms of efficiency, stability and accuracy for all applications for modeling hydrothermal systems.

1.3 The system $H_2O-NaCl$ and the geometric topology of its phase diagram

The work on accurate correlation formulae for the phase relations in the space of pressure (P), temperature (T) and NaCl composition (X) have been motivated particularly by the need for numerical modeling. Here, the need for complete formulations was realized when the research interest shifted from shallow sub-critical systems (lower pressures than at the critical point of pure water ($p_{\mathrm{crit}} = 22.06$ MPa, $T_{\mathrm{crit}} = 374.15$ °C)) to the deep hot roots of magmatic hydrothermal systems. Especially in the 80s and 90s, a lot of experimental data on $H_2O-NaCl$ fluid properties have been acquired (Bischoff and Rosenbauer, 1988; Bodnar et al., 1985; Knight and Bodnar, 1989; Olander and Liander, 1950; Sourirajan and Kennedy, 1962; Sterner et al., 1992). These were transformed into equations of states, but unfortunately their validity had limited intervals and not all fluid properties have been accurately treated (Anderko and Pitzer, 1993a; Archer, 1992; Bischoff and Rosenbauer, 1985; Pitzer and Tanger, 1988). Two complete sets of correlations of phase relations and fluid properties have been published (Driesner, 2007; Driesner and Heinrich, 2007; Palliser and McKibbin, 1998a; Palliser and McKibbin, 1998b; Palliser and McKibbin, 1998c). The numerical simulator presented in this thesis uses an implementation of the correlations formulae of Driesner and Heinrich (2007) and Driesner (2007) because they cover a sufficient range of pressures from 0 to 500 MPa, of temperatures from 0 to 1000 °C and NaCl mass fractions from 0 to 1.

In total, seven states of phase are found in the phase diagram of the system $H_2O-NaCl$, which is shown in Figure 1.2. The black surface separates the single-phase region from the liquid + vapor (L+V) coexisting region. The critical curve (dashed red line) follows the crest of this surface and indicates whether a single-phase fluid enters the two-phase region as vapor-like or liquid-like fluid. It starts from the critical point of pure water, which is the high-pressure ending point of the boiling curve of pure water. A single-phase fluid below the pure water boiling temperature is always in a liquid state and will boil when it is heated to the two-phase boundary. At higher pressures, the critical curve moves to higher salt compositions, which implies that when a single-phase fluid with a salt content lower than the critical curve is heated until it hits the two-phase boundary, it is a vapor-like fluid from which brine droplets condense.

Throughout this thesis, the critical curve is used to distinguish between vapor- and liquid-like in the single-phase region at pressures higher than p_{crit} with vapor always having a lower density than a fluid on the critical curve for a given pressure. Therefore, a "vapor" is a fluid, which has a density below the density at the critical point of pure water (321.9 kg/m^3), or a fluid having a higher temperature and a lower salt content than the critical curve at a given pressure. In Figure 1.3 and Figure 1.4 the boundary between liquid and vapor is marked by the red dashed line. The vapor phase can carry several wt% NaCl within the lower temperature range of the L+V region at higher pressures (Fig. 1.3d).

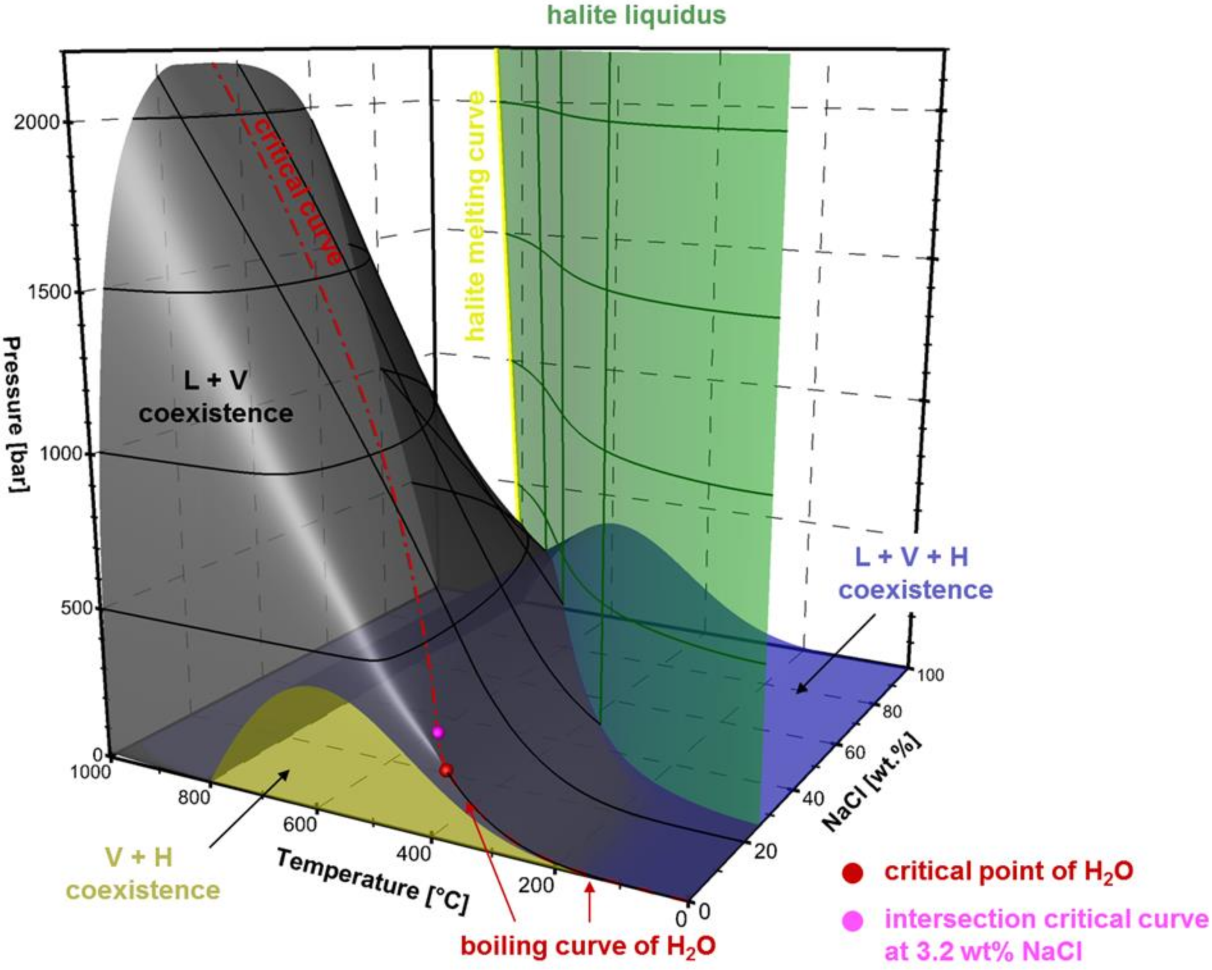

Figure 1.2: Phase Diagram of the system H_2O−NaCl in temperature-pressure-composition coordinates with isolines for pressure and composition on surfaces. L (liquid), V (vapor), H (halite)

The green surface marks the halite liquidus and the halite melting curve linearly increases starting from the triple point (800.7 °C and 50 Pa) to 825 °C at 100 MPa. In the liquid + halite (L+H) coexisting region, halite saturation increases linearly with increasing salt content when the temperature stays constant. The liquid, vapor and halite (L+V+H) coexisting surface (blue) forms the lower pressure boundary of the L+V region and the (L+H) region. The V+H coexisting region is bounded by the dark yellow surface, which, at low salinities, separates it from the vapor (single-phase) region. The L+V+H surface forms the upper pressure boundary of the V+H coexisting region.

Using coordinates in the PTX space has the drawback that the respective phase saturations cannot be calculated for all PTX-coordinates. This is the case for pure water boiling below the critical pressure, for the L+V+H coexisting region and for the halite melting curve. Depending on the numerical method used in a simulator, the primary searching variables, which are normally pressure, temperature and composition, have to be changed and supplemented by a phase saturation (Kissling, 2005b). Alternatively the phase saturations are calculated within extra iterative steps to match the thermal energy (Weis et al., 2014). An alternative solution is to use the specific enthalpy (H) as one of the searching variables instead of temperature, because then for the above-mentioned regions, the phase saturations could be calculated. For translating the EOS from PTX-space to PHX-space, I have implemented an iterative bisection method. This Method for calculating fluid properties is accurate but slow, especially at phase boundaries. Therefore, for calculating fluid properties via fast linear interpolations, I have computed a three-dimensional look-up table, which has tetrahedral elements fitting the phase boundaries.

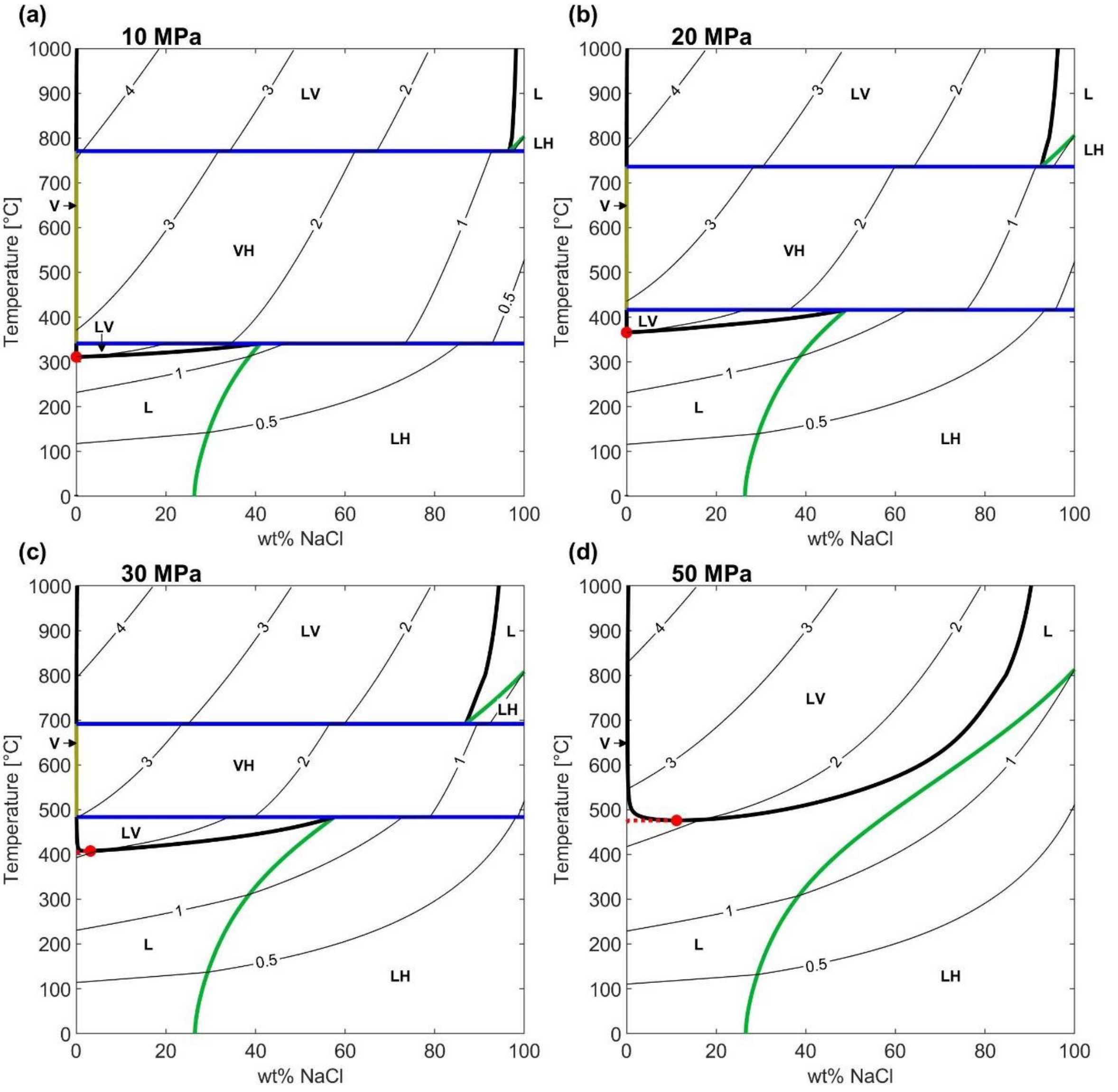

Figure 1.3: Isobaric cross sections of temperature versus fluid NaCl content within the PTX phase diagram. Colored bold lines show same phase region boundaries as shown in Fig. 1.3. Thin black lines are isenthalps, labels are in MJ/kg. **a**, **b** Red dots at the left border show the temperature for boiling of pure water; boiling temperature is in **a** 311 °C and in **b** 366 °C. Figure design has been adapted from Driesner (2013).

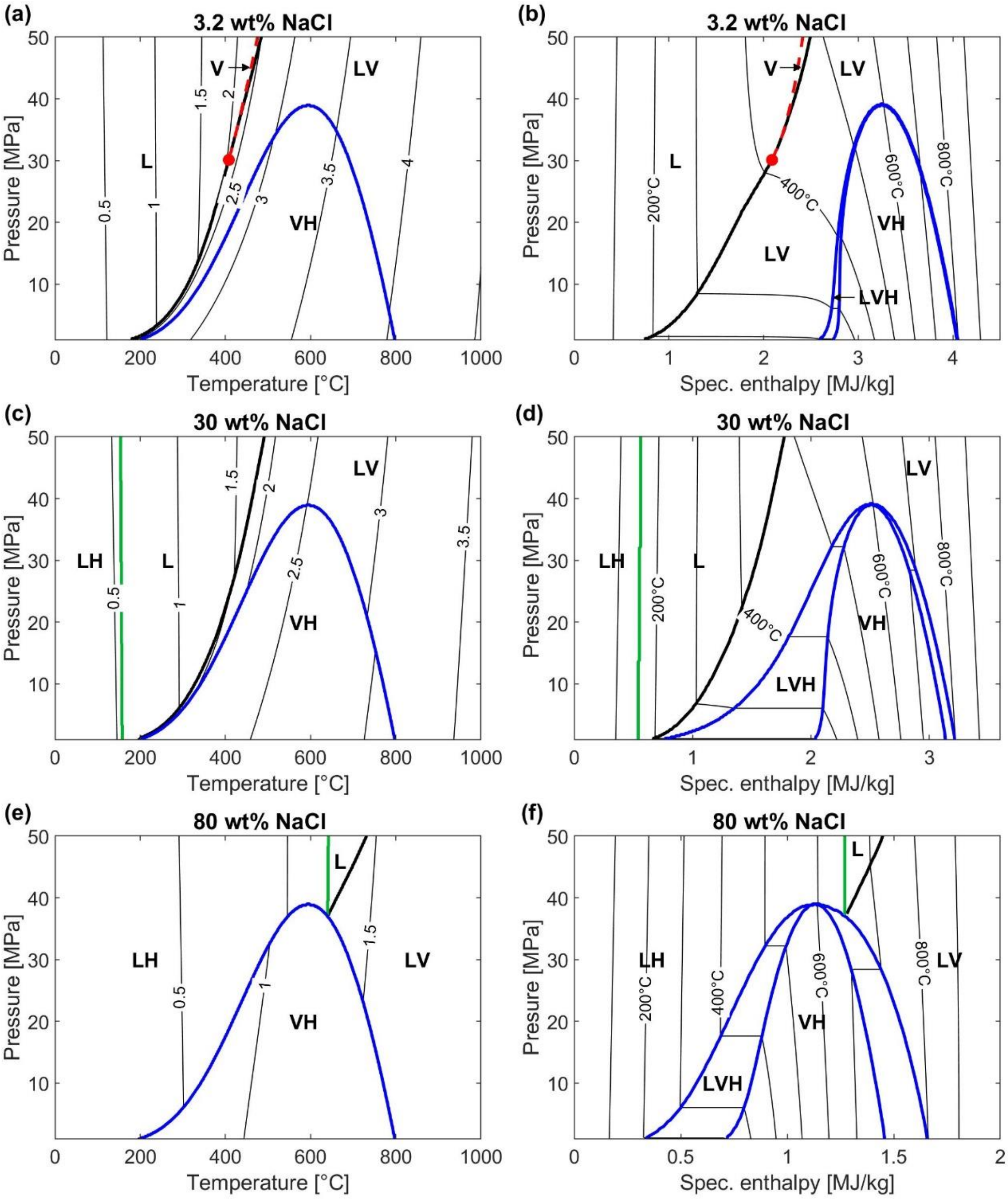

Figure 1.4: Isohaline cross sections for different salinity within the PHX phase diagram. Colored bold lines show same phase region boundaries as shown in Fig. 1.2. **a**, **c**, **e** Pressure versus temperature, contour lines show isenthalps with label unit in MJ/kg. **b**, **d**, **f** Pressure versus bulk spec. enthalpy. Thin black lines are isotherms. **a**, **b** Red dots show the intersections of the critical curve and dashed red line mark transition between liquid and vapor as defined in the text.

In Figure 1.4. PT- and PH-projections are shown for direct comparison and in Figure 1.5 isobaric HX-projections resolve regions of constant temperatures. At $X = 0$, below the critical pressure and between the specific enthalpies of vapor and liquid, isothermal boiling of pure water is resolved (Fig 1.5a, b). When salt is added, the salt content of the liquid phase increases with increasing temperature within the L+V coexisting region. For a given temperature, salt contents and the spec. enthalpies of both phases can be read off at the intersection of the respective isotherms with the phase region boundaries (bold lines). Around the critical point of pure water and for seawater salinities around the critical curve at 30 MPa even small temperature changes lead to reasonable changes in the bulk spec. enthalpy (Fig 1.4a, b) and density. Therefore the choice of specific enthalpy is here beneficial as a primary searching variable.

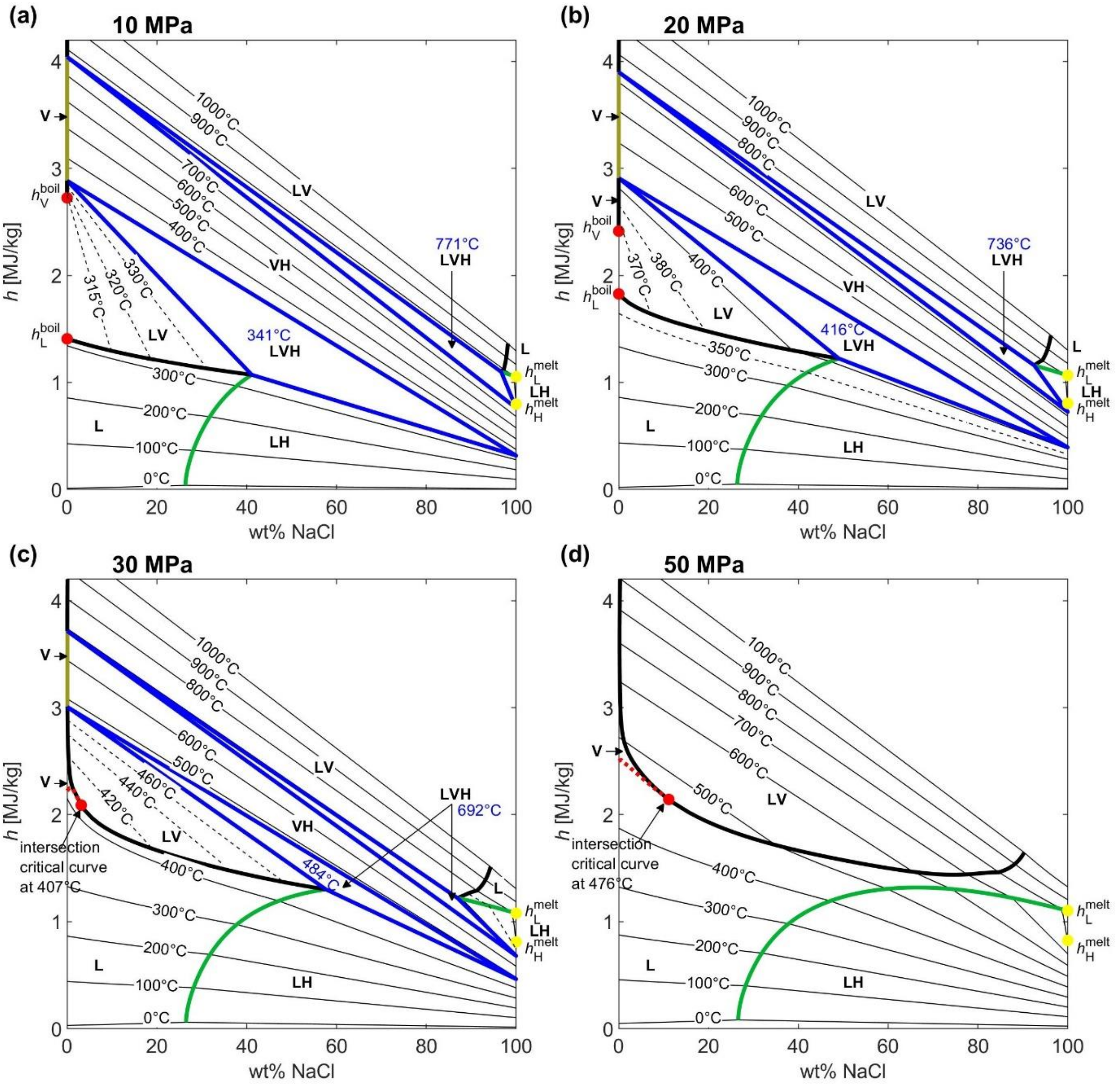

Figure 1.5: Isobaric cross sections of bulk spec. enthalpy (*h*) versus fluid NaCl content within the PHX phase diagram. Colored bold lines show same phase region boundaries as shown in Fig. 1.1. Thin black lines are isotherms, crossing phase region boundaries. Dashed thin black lines are isotherms restricted to phase regions. **a**, **b** Red dots at the left border show spec enthalpies for boiling of pure water; boiling temperature is in **a** 311 °C and in **b** 366 °C. Temperatures of L+V+H regions are marked blue. Yellow dots show the spec. enthalpy of melting halite h_H and the corresponding melt h_L. Molten halite is part of phase region L. Figure design has been adapted from Driesner (2013)

At pressures lower than 39.015 MPa, the isothermal L+V+H coexisting region appears twice and the spec. enthalpies of each phase can be read off at the triangle corners (Fig. 1.5a, b, c). Within each (isothermal) lower temperature L+V+H region, an increase of the bulk specific enthalpy results in the separation of liquid into vapor and halite, i.e., the liquid saturation decreases with halite and vapor saturation increasing. In the higher temperature L+V+H regions, vapor and halite are progressively mixed to a hyper-saline liquid (>85 wt% NaCl) with increasing bulk enthalpy. Halite melting is isothermal and saturations of solid and molten halite change between the yellow dots at X = 100 wt% NaCl (Fig. 1.5).

While the transport of NaCl within hydrothermal systems can be simulated by numerical models, which have incorporated the EOS for NaCl, fluid properties and two-phase flow, the transport of metals is much more challenging to calculate because solubility and vapor-liquid (brine) partitioning of each metal depends on a complex interconnection of pressure, temperature and composition of major fluid components.

The liquid and the vapor phase have fundamentally different properties. The liquid phase is dense, incompressible and a good solvent for electrolytes and on the contrary, the vapor phase is compressible and a good solvent of nonpolar gases. Fluid inclusion analysis of rocks from extinct magmatic hydrothermal systems has shown how metals are distributed between coexisting vapor and brine phases. Elements such as Na, K, Fe, Pb, Ag and Zn accumulate in the dense brine phase, as they build chloride complexes (Pester et al., 2015). The vapor phase is often enriched in sulfur by the degassing of SO_2 and H_2S from the magmatic intrusion. Cu and Au also build hydrogen sulfide complexes and are not as highly enriched in the brine phase as above mentioned metals. Fluid inclusions often show for Au a higher partitioning in the vapor phase (Pokrovski et al., 2008). Metalloids such as As, Sb and B tend to build hydroxide complexes and distribute approx. equal into both phases (Pokrovski et al., 2005). The partitioning of many metals is also affected by fluid acidity, whose pH values can become as low as 2.

In order to model the transport of metals and the formation of ore deposits, geochemical reactions have to be calculated, which is very difficult for super-hot conditions and two-phase conditions. Therefore, only a few crustal scale fluid convection simulations of ore deposit formation by metal transport and precipitation have been published in the last decade. Making the reasonable assumption that metal solubility is controlled by temperature, Weis et al. (2012) and Korges et al. (2020) have simulated the formation of a porphyry-copper ore shell deposit with saline multiphase flow and Rodríguez et al. (2021) have simulated a Zn ore deposit formation in a sedimentary basin by saline single phase.

1.4 Applications for multi-phase thermohaline numerical simulators

Hydrothermal systems are distributed within many geological settings with different magmatic supplies (Fig. 1.6). Most hydrothermal systems are not surveyed well enough to apply investigations trough numerical simulations to get meaningful results that allow reasonable explanations of observed phenomena. Especially the crustal permeability is unknown if it is not measured by borehole measurements. Often, different subsurface conditions could match observed data and a complete analysis of parameter studies have to be applied to make statements about specific systems and generalize them for other types of hydrothermal systems.

Therefore applications for multi-phase hydrothermal numerical simulators could be roughly subdivided into two groups. In the first group, the numerical simulator is used to explore the fundamental physical fluid dynamics and elaborate conceptual models of hydrothermal flow. In the second group, the simulator is used to investigate two-phase flow phenomena for specific geological settings. Numerical simulations could be adapted to and calibrated based on observations if sufficient data have been collected for a site, for example a set of some of the following data: crustal structure (faults and rocks properties), thermal structure of the crust, heat source properties, heat flux measurements, venting fluid temperature and salinities.

The capability of new numerical codes, which correctly treat two-phase flow for non-linear phase properties around the critical curve has given new insights. The qualitative understanding of thermohaline two-phase convection in two-dimension has been investigated by several authors (Geiger, 2005; Geiger et al., 2006a; Geiger et al., 2006b; Kissling, 2005a; Kissling, 2005b). The hydrothermal two-dimensional convection has also been studied for simplified settings of submarine systems (Choi and Lowell, 2015; Coumou et al., 2009a; Han et al., 2013; Kawada et al., 2004; Lewis and Lowell, 2009; Singh et al., 2013; Weis et al., 2014). The goal was to understand temporal variations in venting salinities as well as the salinity distribution within the system. Until today, no results of three-dimensional saline multiphase simulations have been published for higher pressure and temperature conditions above the critical point of pure water. However, new insights into fluid dynamics could be expected from these simulations because three-dimensional single-phase simulations gave important new insights into the organization of hydrothermal cells for fast-spreading mid-ocean centers (Coumou et al., 2009a; Coumou et al., 2008; Hasenclever et al., 2014).

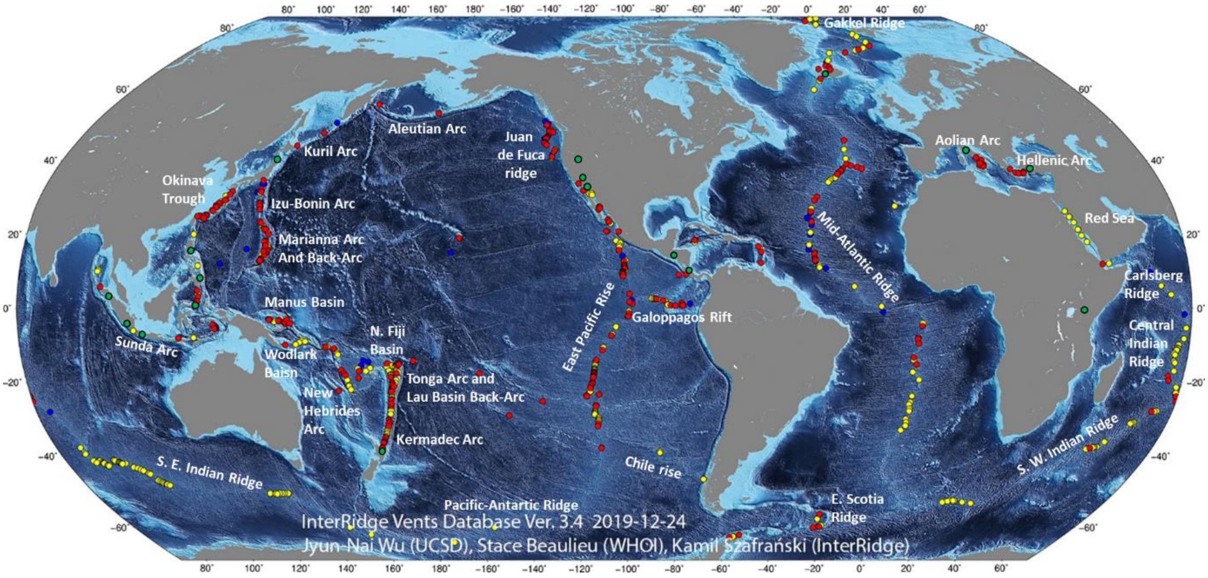

Figure 1.6: Map of submarine hydrothermal vents. Yellow dots mark inferred vents, red dots mark confirmed vents, blue dots mark inactive vents, green dots mark local regions of geothermal power plants with more than 100 MW accumulated power, modified after Beaulieu and Szafranski (2020)

Submarine hydrothermal vents often show salinities that differ from seawater salinity, indicating phase separation processes. Furthermore, they are distributed within many geological settings (Fig. 1.6), making them a good target for hydrothermal simulations for elaborating their differences. The most abundant places are found for divergent plate motions at mid-ocean spreading centers and for convergent plate motion when subducting oceanic plates lead to volcanic arcs and back-arc spreading centers. The remaining vents are related to intraplate submarine volcanoes. Additionally, the thickness of seafloor sediments, having a lower permeability than upper near-surface basalts, changes the characteristics of hydrothermal circulation and vent chemistry.

1.4.1 Mid-ocean ridges

Mid-ocean ridges, which have a total length of ~61,000 km upon definition on ridge segments (Gale et al., 2013), are subdivided according to spreading velocities into fast (~80 −180 mm/yr), intermediate (~55 – 70 mm/yr), slow (less than ~55 mm/yr) and ultra-slow ones (less than ~20 mm/yr) (Beaulieu et al., 2015; Dick et al., 2003). This classification is based on different magma production rates and their consequences for the ridge geomorphology, the main visible difference. Below the separating plates, decompression melting of the underlying mantle leads to the formation of a basaltic and gabbroic oceanic crust of around 6 km thickness for spreading velocities higher than 20 mm/yr. In total, 75% of earth volcanism is produced at mid-ocean ridges (Crisp, 1984). Here, cooling through hydrothermal convection dominates conductive cooling and therefore it is involved in the creation process of the oceanic crust and its alteration.

Fast-spreading centers like the East Pacific Rise and parts of the Pacific-Antarctic Ridge are characterized by an axial melt lens (AML), which is elongated along the ridge and is located between 1 and 2 km depth below seafloor (Detrick et al., 1987; Xu et al., 2014). Here periodic magmatic events create a two-layer upper crust with a top layer of pillow basalts (layer 2A) and below, a layer of basaltic dikes (layer 2B). The lower part of the 6 km thick oceanic crust is made of gabbros crystalized at the AML and in sills below the AML. At periods of high activity, eruptive events happen every 10 to 20 years. Therefore, the morphology is related to high magmatic activity close to the axis, where a topographic high evolves (~ 400 m) often with a thin summit trough of around 10 m width. In this small area, hydrothermal activity is concentrated as it follows the ascending dikes here (Fornari et al., 2012). Numerical models and alteration of the lower oceanic crust predict hydrothermal cooling of the lower crust (Nehlig, 1993; Theissen-Krah et al., 2016).

Intermediate-spreading ridges show morphologies of fast or slow ridges and have no unique specific morphology. Slow-spreading ridges like the Mid-Atlantic Ridge have an axial rift valley of variable depth between ~400 m to 2500 m and a rough rift mountain topography (Dick et al., 2003; Macdonald, 1998; Small, 1998). The morphology is often asymmetric and magmatic crustal accretion is controlled by short-lived crustal spherical magma chambers with a depth of > 3 km (Purdy et al., 1992; Singh et al., 2006; Sinha et al., 1997). Here hydrothermal vents are more difficult to find as the new volcanic zone is not well-defined and the deep crustal faults enable enhanced discharge of hydrothermal circulation spreading the distribution over a much larger area (Baker and German, 2004; Beaulieu et al., 2015). The ultra-slow ridges, which comprise ~20,000 km of the global ridge system, have partially not magmatic sections, where mantle rocks have been brought to the seafloor without experiencing partial melting. Surprisingly, despite the low magmatic activity, several high-temperature hydrothermal vents have recently been found at the Gakkel Ridge and the Southwest Indian Ridge having different salinity compared to seawater (Kinsey and German, 2013; Pedersen et al., 2010; Tao et al., 2012).

In this thesis, the developed simulator is used for modeling processes such as brine layer formation on top of the axial magma lens and magmatic diking events at mid-ocean fast-spreading ridges. The fast-spreading ridges have been chosen because geophysical and geochemical investigations show that hydrothermal venting at the ridge axis is mainly controlled by fluid convection on top of the axial magma lens. Additionally, at some locations the recurrently measured data of vent salinities and temperatures, which cover cyclical changes, make it beneficial for numerical simulations of this specific geological setting. Slow-spreading ridges are less appropriate for numerical simulations for the following reasons. The key components that control hydrothermal circulation at slow-spreading ridges are deep permeable normal fault systems and deep transient magmatic intrusions, whose sizes are difficult to determine with geophysical measurements. Measurements of the trans-Atlantic Geotraverse (TAG) hydrothermal field show that venting was inactive over thousands of years (Lalou et al., 1995; Lalou et al., 1998). The cyclical evolution of hydrothermal convection is not well understood as faults could be pathways for cold downflow or hot upflow, which could in principle change over time. The permeability of faults is difficult to estimate and therefore it is not clear how hot upwelling fluids follow faults (Andersen et al., 2015). Here measurements at hydrothermal fields could only show a small snapshot of cyclical changes. Overall, it is not clear if faulting and magmatic intrusions follow regular cycles, which are then reflected in hydrothermal venting. In the future numerical models that are improved and validated at the simpler fast-spreading ridges can help to transmit insights of multi-phase fluid dynamics to slow-spreading ridges and quantifying processes there.

1.4.2 Volcanic arcs and back-arc spreading centers

The tectonic setting, where the oceanic lithosphere (slab) is subducting, subdivides submarine volcanic arcs and back-arc spreading centers in different classes. At intra-oceanic settings, the volcanic arc has built on oceanic crust. Spreading on the backside of the volcanic arc is caused by the rollback of the slab, i.e. the diving point of the slab migrates away from the volcanic arc leading to extensional forces and crustal rifting. With ongoing rifting passive upwelling of mantle rocks occurs comparable to mid-ocean crustal accretion. Examples of intra-oceanic settings are the Mariana arc and its back-arc spreading center, the Izu-Bonin arc, the Tonga-Kermadec arc and the attached Lau basin in the western Pacific, and the onset of the Lau basin rifting has split the former volcanic arc (cf. remnant arc in Fig 1.1). At the volcanic arc high-temperature hydrothermal vents are often found at the caldera walls because during caldera collapse, permeable pathways were generated leading to focused flow (Hannington et al., 2005). Additionally, many submarine volcanoes often show diffuse venting. At magmatic active back-arc spreading centers, hydrothermal vent fields are placed within first few hundred meters from the spreading axis and are similar to mid-ocean ridges (Anderson et al., 2017; Taylor, 1995).

When a slab is subducted below the basement of a continental margin, the rifting at the back-arc is similar to continental breakup-rifting, characterized by volcanic eruptions with higher silica content differentiated in deep-seated magma chambers within the continental crust of more than 10 km thickness like the Ryūkyū arc at the Okinawa Trough (Arai et al., 2017). The extension of the back-arc rifting region is distributed over a larger area than for oceanic crust because of the thicker continental crust (Hannington et al., 2005). Here hydrothermal activity is distributed within depths between a few hundred meters and 2500 m at the slope of the Okinawa Trough towards the Ryukyu arc primarily located at volcanic knolls (Sakai et al., 1990).

Island arcs and related back-arc rifts are called “transitional” when they occur in a basement of young continental crust or preexisting arc crust, and are commonly found in complex collisional zones including microplates. This variety of involved tectonic elements is reflected in the complex and versatile chemistry of both the arc and back-arc magmas, with arc-like magmas erupted in the back-arc region (Hannington et al., 2005). Examples are the Aeolian and Hellenic Arc and the southern end of the Kermadec Arc, where rifting extends to the continental shelf of New Zealand. The volcanic arcs which surround the Manus Basins and the Woodlark Basins cover some of the youngest and richest porphyry Cu-Mo-Au deposits on earth (Brandl et al., 2020; Holm et al., 2019). The massive sulfide deposits at the Manus Basins are also of economic interest to the new emerging marine mining industry.

The formation of porphyry ore deposits is controlled by the transport of brines, where the metals are enriched into. Numerical simulations using saline two-phase flow can reproduce some characteristics of the formations of porphyry copper deposits in volcanic arc systems. Here investigations have been done for synthetic subaerial systems (Weis, 2015; Weis et al., 2012) as well as for a specific site of the submarine Brothers Volcano at the Kermadec Arc (Gruen et al., 2014).

1.4.3 Saline magmatic hydrothermal systems used for geothermal power generation

Geothermal power production has been growing over the last years. Most of the high-enthalpy hydrothermal systems used for electric power generation are dominated by meteoric water, but moreover considerable examples of saline multiphase systems occurs hosted in the USA, Mexico and Iceland. At the Salton Sea Geothermal System (SSGS) in California, sedimentary rocks have been deposited in a pull-apart basin at the San-Andreas transform fault intruded by shallow Quaternary basalt and rhyolite bodies. The intrusions increase the fluid temperatures to 350 °C at a depth of 1400 m and cause contact metamorphism and multi-phase flow within the fluvial and lacustrine sediments, including hyper-saline brines in the deeper sediments (Elders and Sass, 1988; Helgeson, 1968; Mazzini et al., 2011). The Cerro Prieto Geothermal system is one of the oldest and most reliable systems for electrical power production in the world. It is located at the northern Baja California and is, like the SSGS, a pull-apart basin including the Cerro Prieto Volcano. It is characterized by a boiling upflow plume (Elders et al., 1984). Here too, the existence of hyper-saline brines have been inferred from drillings at the lower sediment layers on top of the crustal basement (Lippmann et al., 1991).

At the Reykjanes peninsula, the Mid-Atlantic spreading center reaches the surface due to excess magmatism by the ascending Icelandic mantle plume leading to abnormal high crustal thicknesses (Sæmundsson et al., 2020). Because of the deep rifting faults, the hydrothermal system is recharged by seawater. A scientific exploration well of the Icelandic Deep Drilling Project 2 (IDDP2) has reached a vertical depth of ~4500 m and the bottom hole temperature is estimated to be 535 °C at 34 MPa, which would be the world’s hottest geothermal well (Friðleifsson et al., 2020; Friðleifsson et al., 2017). These hot temperatures are known to be found close to the magmatic heat source. This region is called reaction zone defined by the high intensity of fluid-rock reactions (rock alteration). At these temperatures, heated seawater would be separated into two phases. The superhot vapor phase is very suitable for electric power generation because of its huge expansion when it depressurizes. Compared to fluids in the boiling zones with temperatures between 200 °C to 300 °C, where geothermal fluids are mined conventionally, the power production from these vapors have the potential to be 10 times higher per well. This information has been inferred from fluid extraction tests at the IDDP1 well (Friðleifsson et al., 2017). For both wells, technical difficulties have to be solved before these vapors could be extracted.

The shallow subsurface of geothermal systems is usually intensively investigated with geophysical borehole measurements. It is difficult to extrapolate from the measured temperature field and permeability structure to the deeper parts, leaving the depth of the magmatic heat source and its heat budget uncertain. In addition to the exploration drillings in supercritical pressures conditions towards the magmatic heat source, numerical simulations capable of handling magmatic temperatures are helpful to find the best places and depth for production wells and to figure out if the system is not at the end of its life (Scott et al., 2015). In the case of saline hydrothermal systems such as Reykjanes, investigations with numerical simulations show how phase separation could lead to accumulation of low-mobility hyper-saline brines and halite precipitation that reduces the efficiency of heat and mass transfer on top of the magmatic intrusion (Scott et al., 2017). It could also be an option to use deep drillings to inject water close to the magmatic heat source to increase fluid extraction rate of shallower production wells, which could be investigated with numerical simulations.

1.5 Scope of the thesis

In this thesis, I present my self-developed numerical approach for modeling multiphase flow in the system H_2O–NaCl as well as applications to magmatic hydrothermal systems at fast-spreading mid-ocean ridges. The thesis has a cumulative structure and consists of three papers. The research work has been conducted applying of my self-developed numerical approach. Results were preprocessed and edited by myself. I have submitted all three papers as first-author to scientific journals. My co-authors have contributed to the paper structure and to the written text. The first paper (Chapter 2) focuses on numerical methods and implementation strategies for two-phase flow in porous media. Here a detailed description of the control-finite-volume method in combination with the coupled approach is made, where the governing equations are solved simultaneously with searching variables of pressure and spec. enthalpy. This numerical simulator is restricted to two dimensions and pure water, but it is able to deal with temperature and pressure conditions at the critical point of pure water and beyond. The efficiency and accuracy are shown by a sufficient number of benchmark test cases against the geothermal system simulator HYDROTHERM.

The second paper (Chapter 3) introduces the extension of the numerical approach to the binary system of H_2O−NaCl. For this purpose, the equation of state of Driesner and Heinrich (2007) was implemented in pressure-temperature-composition-space and then translated with a bisection method in pressure-spec. enthalpy-composition-space. The solid phase halite is treated as immobile and reduces the rock permeability. The new simulator is applied to investigate brine formation and mobilization in hydrothermal systems driven by a transient basal temperature boundary condition. This model setup corresponds to seawater circulation systems found at mid-ocean ridges, and its simulation allows to quantitatively evaluate the thermal insulation of a stable brine layer on top of an axial melt lens.

In the third paper (Chapter 4), the developed simulator is applied to link magmatic diking events at fast-spreading ridges to observed vent fluid salinity evolution at the seafloor. This study includes phase separation phenomena like brine accumulation and halite precipitation at the dike as well as brine mobilization and two-phase flow. In addition, key parameter are analyzed, which control vent salinity evolution like rock permeability and porosity as well as the background fluid temperature and salinity of the hydrothermal upflow zone, wherein the dike is emplaced. Then the simulated salinity and temperature curves are compared with P-vent and Bio9-vent evolution at EPR 9°50.3’N after the dike intrusion in 1991/1992.

1.6 Bibliography

Anderko, A., Pitzer, K.S., 1993a. Equation-of-State Representation of Phase-Equilibria and Volumetric Properties of the System Nacl-H2o above 573-K. Geochimica Et Cosmochimica Acta, 57(8): 1657-1680.

Anderko, A., Pitzer, K.S., 1993b. Phase equilibria and volumetric properties of the systems KCl-H2O and NaCl-KCl-H2O above 573 K: Equation of state representation. Geochimica et Cosmochimica Acta, 57(20): 4885-4897, https://doi.org/10.1016/0016-7037(93)90127-I.

Andersen, C., Rüpke, L., Hasenclever, J., Grevemeyer, I., Petersen, S., 2015. Fault geometry and permeability contrast control vent temperatures at the Logatchev 1 hydrothermal field, Mid-Atlantic Ridge. Geology, DOI:10.1130/G36113.1.

Anderson, M.O. et al., 2017. Geological interpretation of volcanism and segmentation of the Mariana back-arc spreading center between 12.7 degrees N and 18.3 degrees N. Geochemistry Geophysics Geosystems, 18(6): 2240-2274, DOI:10.1002/2017gc006813.

Arai, R. et al., 2017. Crustal structure of the southern Okinawa Trough: Symmetrical rifting, submarine volcano, and potential mantle accretion in the continental back-arc basin. Journal of Geophysical Research: Solid Earth, 122(1): 622-641, https://doi.org/10.1002/2016JB013448.

Archer, D.G., 1992. Thermodynamic Properties of the NaCl+H2O System l. Thermodynamic Properties of NaCl(cr). Journal of Physical and Chemical Reference Data, 21(1): 1-21, DOI:10.1063/1.555913.

Baker, E.T., German, C.R., 2004. On the Global Distribution of Hydrothermal Vent Fields, Mid-Ocean Ridges, pp. 245-266.

Beaulieu, S.E., Baker, E.T., German, C.R., 2015. Where are the undiscovered hydrothermal vents on oceanic spreading ridges? Deep-Sea Research Part Ii-Topical Studies in Oceanography, 121: 202-212, DOI:10.1016/j.dsr2.2015.05.001.

Beaulieu, S.E., Szafranski, K., 2020. InterRideg Global Database of Active Submarine hydrothermal Vent Fileds, version 3.4. World Wide Web electronoc publication available from http://vents-data-interridge.org

Bischoff, J.L., Rosenbauer, R.J., 1985. An Empirical-Equation of State for Hydrothermal Seawater (3.2-Percent Nacl). American Journal of Science, 285(8): 725-763, DOI:10.2475/ajs.285.8.725.

Bischoff, J.L., Rosenbauer, R.J., 1988. Liquid-Vapor Relations in the Critical Region of the System Nacl-H2o from 380-Degrees-C to 415-Degrees-C - a Refined Determination of the Critical-Point and 2-Phase Boundary of Seawater. Geochimica Et Cosmochimica Acta, 52(8): 2121-2126, DOI:10.1016/0016-7037(88)90192-5.

Bodnar, R.J., Burnham, C.W., Sterner, S.M., 1985. Synthetic Fluid Inclusions in Natural Quartz .3. Determination of Phase-Equilibrium Properties in the System H2o-Nacl to 1000-Degrees-C and 1500 Bars. Geochimica Et Cosmochimica Acta, 49(9): 1861-1873, DOI:10.1016/0016-7037(85)90081-X.

Brandl, P.A., Hannington, M.D., Geersen, J., Petersen, S., Gennerich, H.-H., 2020. The submarine tectono-magmatic framework of Cu-Au endowment in the Tabar-to-Feni island chain, PNG. Ore Geology Reviews, 121: 103491, https://doi.org/10.1016/j.oregeorev.2020.103491.

Choi, J., Lowell, R.P., 2015. The response of two-phase hydrothermal systems to changing magmatic heat input at mid-ocean ridges. Deep-Sea Research Part Ii-Topical Studies in Oceanography, 121: 17-30, DOI:10.1016/j.dsr2.2015.05.005.

Coumou, D., Driesner, T., Geiger, S., Paluszny, A., Heinrich, C.A., 2009a. High-resolution three-dimensional simulations of mid-ocean ridge hydrothermal systems. Journal of Geophysical Research-Solid Earth, 114: 15, DOI:10.1029/2008jb006121.

Coumou, D., Driesner, T., Heinrich, C.A., 2008. The structure and dynamics of mid-ocean ridge hydrothermal systems. Science, 321(5897): 1825-1828, DOI:10.1126/science.1159582.

Coumou, D., Driesner, T., Weis, P., Heinrich, C.A., 2009b. Phase separation, brine formation, and salinity variation at Black Smoker hydrothermal systems. Journal of Geophysical Research, 114, DOI:10.1029/2008jb005764.

Crisp, J.A., 1984. Rates of Magma Emplacement and Volcanic Output. Journal of Volcanology and Geothermal Research, 20(3-4): 177-211, DOI:10.1016/0377-0273(84)90039-8.

Detrick, R.S. et al., 1987. Multichannel Seismic Imaging of a Crustal Magma Chamber Along the East Pacific Rise. Nature, 326(6108): 35-41, DOI:10.1038/326035a0.

Dick, H.J.B., Lin, J., Schouten, H., 2003. An ultraslow-spreading class of ocean ridge. Nature, 426(6965): 405-412, DOI:10.1038/nature02128.

Driesner, T., 2007. The system H2O-NaCl. Part II: Correlations for molar volume, enthalpy, and isobaric heat capacity from 0 to 1000 degrees C, 1 to 5000 bar, and 0 to 1 X-NaCl. Geochimica Et Cosmochimica Acta, 71(20): 4902-4919, DOI:10.1016/j.gca.2007.05.026.

Driesner, T., 2013. Enthalpy and phase relations in saline geothermal fluids to "supercritical" conditions, American Geophysical Union, 2013 Fall Meeting, San Francisco, California, 9-13 December, V33C-2761.

Driesner, T., Geiger, S., 2007. Numerical simulation of multiphase fluid flow in hydrothermal systems. Fluid-Fluid Interactions, 65: 187-212, DOI:10.2138/rmg.2007.65.6.

Driesner, T., Heinrich, C.A., 2007. The system H2O-NaCl. Part I: Correlation formulae for phase relations in temperature-pressure-composition space from 0 to 1000 degrees C, 0 to 5000 bar, and 0 to 1 X-NaCl. Geochimica Et Cosmochimica Acta, 71(20): 4880-4901, DOI:10.1016/i.gca.2006.01.033.

Elders, W.A., Bird, D.K., Williams, A.E., Schiffman, P., 1984. Hydrothermal flow regime and magmatic heat source of the Cerro Prieto geothermal system, Baja California, Mexico. Geothermics, 13(1): 27-47, https://doi.org/10.1016/0375-6505(84)90005-1.

Elders, W.A., Sass, J.H., 1988. THE SALTON SEA SCIENTIFIC DRILLING PROJECT. Journal of Geophysical Research: Solid Earth, 93(B11): 12953-12968, https://doi.org/10.1029/JB093iB11p12953.

Fornari, D.J. et al., 2012. The East Pacific Rise Between 9°N and 10°N: Twenty-Five Years of Integrated, Multidisciplinary Oceanic Spreading Center Studies. Oceanography, 25(1): 18-43.

Friðleifsson, G.Ó. et al., 2020. The Iceland Deep Drilling Project at Reykjanes: Drilling into the root zone of a black smoker analog. Journal of Volcanology and Geothermal Research, 391: 106435, https://doi.org/10.1016/j.jvolgeores.2018.08.013.

Friðleifsson, G.Ó. et al., 2017. The Iceland Deep Drilling Project 4.5 km deep well, IDDP-2, in the seawater-recharged Reykjanes geothermal field in SW Iceland has successfully reached its supercritical target. Sci. Dril., 23: 1-12, DOI:10.5194/sd-23-1-2017.

Gale, A., Dalton, C.A., Langmuir, C.H., Su, Y., Schilling, J.-G., 2013. The mean composition of ocean ridge basalts. Geochemistry, Geophysics, Geosystems, 14(3): 489-518, https://doi.org/10.1029/2012GC004334.

Geiger, S., 2005. On the dynamics of NaCl-H2O fluid convection in the Earth's crust. Journal of Geophysical Research, 110(B7), DOI:10.1029/2004jb003362.

Geiger, S., Driesner, T., Heinrich, C., Matthäi, S., 2006a. Multiphase Thermohaline Convection in the Earth’s Crust: I. A New Finite Element – Finite Volume Solution Technique Combined With a

New Equation of State for NaCl–H<sub>2</sub>O. Transport in Porous Media, 63(3): 399-434, DOI:10.1007/s11242-005-0108-z.

Geiger, S., Driesner, T., Heinrich, C.A., Matthai, S.L., 2006b. Multiphase thermohaline convection in the earth's crust: II. Benchmarking and application of a finite element - Finite volume solution technique with a NaCl-H2O equation of state. Transport in Porous Media, 63(3): 435-461, DOI:10.1007/s11242-005-0109-y.

Gruen, G., Weis, P., Driesner, T., Heinrich, C.A., de Ronde, C.E.J., 2014. Hydrodynamic modeling of magmatic-hydrothermal activity at submarine arc volcanoes, with implications for ore formation. Earth and Planetary Science Letters, 404: 307-318, DOI:10.1016/j.epsl.2014.07.041.

Han, L., Lowell, R.P., Lewis, K.C., 2013. The dynamics of two-phase hydrothermal systems at a seafloor pressure of 25 MPa. Journal of Geophysical Research-Solid Earth, 118(6): 2635-2647, DOI:10.1002/jgrb.50158.

Hannington, M., Galley, A., Herzig, P., Petersen, S., 1998. Comparison of the TAG mound and stockwork complex with Cyprus-type massive sulfide deposits. Oceanographic Literature Review, 158: 1557-1558.

Hannington, M.D. et al., 2005. Sea-Floor Tectonics and Submarine Hydrothermal Systems, One Hundredth Anniversary Volume. Society of Economic Geologists, pp. 0.

Hasenclever, J. et al., 2014. Hybrid shallow on-axis and deep off-axis hydrothermal circulation at fast-spreading ridges. Nature, 508(7497): 508-512, DOI:10.1038/nature13174.

Helgeson, H.C., 1968. Geologic and thermodynamic characteristics of the Salton Sea geothermal system. American Journal of Science, 266(3): 129-166, DOI:10.2475/ajs.266.3.129.

Holm, R.J., Tapster, S., Jelsma, H.A., Rosenbaum, G., Mark, D.F., 2019. Tectonic evolution and copper-gold metallogenesis of the Papua New Guinea and Solomon Islands region. Ore Geology Reviews, 104: 208-226, https://doi.org/10.1016/j.oregeorev.2018.11.007.

Hovey, J.K., Pitzer, K.S., Tanger, J.C., Bischoff, J.L., Rosenbauer, R.J., 1990. Vapor-liquid phase equilibria of potassium chloride-water mixtures: equation-of-state representation for potassium chloride-water and sodium chloride-water. The Journal of Physical Chemistry, 94(3): 1175-1179, DOI:10.1021/j100366a032.

Ingebritsen, S.E., Geiger, S., Hurwitz, S., Driesner, T., 2010. Numerical simulation of magmatic hydrothermal systems. Reviews of Geophysics, 47: 33, DOI:10.1029/2009rg000287.

Kawada, Y., Yoshida, S., Watanabe, S.-i., 2004. Numerical simulations of mid-ocean ridge hydrothermal circulation including the phase separation of seawater. Earth, Planets and Space, 56(2): 193-215, DOI:10.1186/BF03353403.

Kesler, S.E., Simon, A.C., 2015. Mineral Resources, Economics and the Environment. Cambridge University Press, Cambridge.

Kinsey, J.C., German, C.R., 2013. Sustained volcanically-hosted venting at ultraslow ridges: Piccard Hydrothermal Field, Mid-Cayman Rise. Earth and Planetary Science Letters, 380: 162-168, https://doi.org/10.1016/j.epsl.2013.08.001.

Kissling, W.M., 2005a. Transport of three-phase hyper-saline brines in porous media: Examples. Transport in Porous Media, 60(2): 141-157, DOI:10.1007/s11242-004-4795-7.

Kissling, W.M., 2005b. Transport of three-phase hyper-saline brines in porous media: Theory and code implementation. Transport in Porous Media, 61(1): 25-44, DOI:10.1007/s11242-004-3306-1.

Knight, C.L., Bodnar, R.J., 1989. Synthetic Fluid Inclusions .9. Critical Pvtx Properties of Nacl-H2o Solutions. Geochimica Et Cosmochimica Acta, 53(1): 3-8, DOI:10.1016/0016-7037(89)90267-6.

Korges, M., Weis, P., Andersen, C., 2020. The role of incremental magma chamber growth on ore formation in porphyry copper systems. Earth and Planetary Science Letters, 552: 116584, https://doi.org/10.1016/j.epsl.2020.116584.

Lalou, C., Reyss, J.-L., Brichet, E., Rona, P.A., Thompson, G., 1995. Hydrothermal activity on a 105-year scale at a slow-spreading ridge, TAG hydrothermal field, Mid-Atlantic Ridge 26°N. Journal of Geophysical Research: Solid Earth, 100(B9): 17855-17862, https://doi.org/10.1029/95JB01858.

Lalou, C., Reyss, J.L., Brichet, E., 1998. Age of sub-bottom sulfide samples at the TAG active mound, PROCEEDINGS-OCEAN DRILLING PROGRAM SCIENTIFIC RESULTS. NATIONAL SCIENCE FOUNDATION, pp. 111-118.

Lewis, K.C., Lowell, R.P., 2009. Numerical modeling of two-phase flow in the NaCl-H2O system: Introduction of a numerical method and benchmarking. Journal of Geophysical Research, 114, DOI:10.1029/2008jb006029.

Lippmann, M.J., Truesdell, A.H., Halfman-Dooley, S.E., A, M., 1991. A review of the hydrogeologic-geochemical model for Cerro Prieto. Geothermics, 20(1): 39-52, https://doi.org/10.1016/0375-6505(91)90004-F.

Macdonald, K.C., 1998. Linkages Between Faulting, Volcanism, Hydrothermal Activity and Segmentation on Fast Spreading Centers, Faulting and Magmatism at Mid-Ocean Ridges, pp. 27-58.

Mazzini, A., Svensen, H., Etiope, G., Onderdonk, N., Banks, D., 2011. Fluid origin, gas fluxes and plumbing system in the sediment-hosted Salton Sea Geothermal System (California, USA). Journal of Volcanology and Geothermal Research, 205(3): 67-83, https://doi.org/10.1016/j.jvolgeores.2011.05.008.

Nehlig, P., 1993. Interactions between magma chambers and hydrothermal systems: Oceanic and ophiolitic constraints. Journal of Geophysical Research: Solid Earth, 98(B11): 19621-19633, https://doi.org/10.1029/93JB01822.

Olander, A., Liander, H., 1950. The Phase Diagram of Sodium Chloride and Steam above the Critical Point. Acta Chemica Scandinavica, 4(9): 1437-1445, DOI:10.3891/acta.chem.scand.04-1437.

Palliser, C., McKibbin, R., 1998a. A model for deep geothermal brines, I: T-p-X state-space description. Transport in Porous Media, 33(1-2): 65-80, DOI:10.1023/A:1006537425101.

Palliser, C., McKibbin, R., 1998b. A model for deep geothermal brines, II: Thermodynamic properties - Density. Transport in Porous Media, 33(1-2): 129-154, DOI:10.1023/A:1006597626918.

Palliser, C., McKibbin, R., 1998c. A model for deep geothermal brines, III: Thermodynamic properties - Enthalpy and viscosity. Transport in Porous Media, 33(1-2): 155-171, DOI:10.1023/A:1006549810989.

Pedersen, R.B. et al., 2010. Discovery of a black smoker vent field and vent fauna at the Arctic Mid-Ocean Ridge. Nature Communications, 1(1): 126, DOI:10.1038/ncomms1124.

Pester, N., Ding, K., Seyfried, W., 2015. Vapor-liquid partitioning of alkaline earth and transition metals in NaCl-dominated hydrothermal fluids: An experimental study from 360 to 465 °C, near-critical to halite saturated conditions. Geochimica et Cosmochimica Acta, 168, DOI:10.1016/j.gca.2015.07.028.

Pitzer, K.S., Tanger, J.C., 1988. Near-Critical Nacl-H2o - an Equation of State and Discussion of Anomalous Properties. International Journal of Thermophysics, 9(5): 635-648, DOI:10.1007/Bf00503232.

Pokrovski, G.S., Borisova, A.Y., Harrichoury, J.-C., 2008. The effect of sulfur on vapor–liquid fractionation of metals in hydrothermal systems. Earth and Planetary Science Letters, 266(3-4): 345-362.

Pokrovski, G.S., Roux, J., Harrichoury, J.-C., 2005. Fluid density control on vapor-liquid partitioning of metals in hydrothermal systems. Geology, 33(8): 657-660, DOI:10.1130/g21475ar.1.

Purdy, G.M., Kong, L.S.L., Christeson, G.L., Solomon, S.C., 1992. Relationship between spreading rate and the seismic structure of mid-ocean ridges. Nature, 355(6363): 815-817, DOI:10.1038/355815a0.

Rodríguez, A., Weis, P., Magnall, J.M., Gleeson, S.A., 2021. Hydrodynamic Constraints on Ore Formation by Basin-Scale Fluid Flow at Continental Margins: Modelling Zn Metallogenesis in the Devonian Selwyn Basin. Geochemistry, Geophysics, Geosystems, 22(6): e2020GC009453, https://doi.org/10.1029/2020GC009453.

Sæmundsson, K., Sigurgeirsson, M.Á., Friðleifsson, G.Ó., 2020. Geology and structure of the Reykjanes volcanic system, Iceland. Journal of Volcanology and Geothermal Research, 391: 106501, https://doi.org/10.1016/j.jvolgeores.2018.11.022.

Sakai, H. et al., 1990. Venting of carbon dioxide-rich fluid and hydrate formation in mid-okinawa trough backarc basin. Science, 248(4959): 1093-6, DOI:10.1126/science.248.4959.1093.

Scott, S., Driesner, T., Weis, P., 2015. Geologic controls on supercritical geothermal resources above magmatic intrusions. Nature Communications, 6: 6, DOI:10.1038/ncomms8837.

Scott, S., Driesner, T., Weis, P., 2017. Boiling and condensation of saline geothermal fluids above magmatic intrusions. Geophysical Research Letters, 44(4): 1696-1705, DOI:10.1002/2016gl071891.

Shanks III, W.C.P., 2012. Hydrothermal alteration in volcanogenic massive sulfide occurrence model. U.S. Geological Survey Scientific Investigations Report 2010-5070-C, chap.11, 12 p.

Singh, S., Lowell, R.P., Lewis, K.C., 2013. Numerical modeling of phase separation at Main Endeavour Field, Juan de Fuca Ridge. Geochemistry Geophysics Geosystems, 14(10): 4021-4034.

Singh, S.C. et al., 2006. Discovery of a magma chamber and faults beneath a Mid-Atlantic Ridge hydrothermal field. Nature, 442(7106): 1029-1032, DOI:10.1038/nature05105.

Sinha, M.C. et al., 1997. Evidence for accumulated melt beneath the slow-spreading Mid-Atlantic ridge. Philosophical Transactions of the Royal Society a-Mathematical Physical and Engineering Sciences, 355(1723): 233-253, DOI:10.1098/rsta.1997.0008.

Small, C., 1998. Global Systematics of Mid-Ocean Ridge Morphology, Faulting and Magmatism at Mid-Ocean Ridges, pp. 1-25.

Sourirajan, S., Kennedy, G.C., 1962. System H2o-Nacl at Elevated Temperatures and Pressures. American Journal of Science, 260(2): 115-&, DOI:10.2475/ajs.260.2.115.

Stein, C.A., Stein, S., 1994. Constraints on Hydrothermal Heat-Flux through the Oceanic Lithosphere from Global Heat-Flow. Journal of Geophysical Research-Solid Earth, 99(B2): 3081-3095, DOI:10.1029/93jb02222.

Sterner, S.M., Chou, I.M., Downs, R.T., Pitzer, K.S., 1992. Phase relations in the system NaCl-KCl-H2O: V. Thermodynamic-PTX analysis of solid-liquid equilibria at high temperatures and pressures. Geochimica et Cosmochimica Acta, 56(6): 2295-2309.

Tao, C. et al., 2012. First active hydrothermal vents on an ultraslow-spreading center: Southwest Indian Ridge. Geology, 40(1): 47-50, DOI:10.1130/g32389.1.

Taylor, B.E., 1995. Backarc Basins. Tectonics and Magmatism,. Geological Magazine.

Theissen-Krah, S., Rüpke, L.H., Hasenclever, J., 2016. Modes of crustal accretion and their implications for hydrothermal circulation. Geophysical Research Letters, 43(3): 1124-1131, DOI:10.1002/2015GL067335.

Violay, M. et al., 2012. An experimental study of the brittle-ductile transition of basalt at oceanic crust pressure and temperature conditions. Journal of Geophysical Research: Solid Earth, 117(B3), https://doi.org/10.1029/2011JB008884.

Violay, M., Heap, M.J., Acosta, M., Madonna, C., 2017. Porosity evolution at the brittle-ductile transition in the continental crust: Implications for deep hydro-geothermal circulation. Scientific Reports, 7(1): 7705, DOI:10.1038/s41598-017-08108-5.

Watanabe, N. et al., 2017. Potentially exploitable supercritical geothermal resources in the ductile crust. Nature Geoscience, 10(2): 140-144, DOI:10.1038/ngeo2879.

Weis, P., 2015. The dynamic interplay between saline fluid flow and rock permeability in magmatic-hydrothermal systems. Geofluids, 15(1-2): 350-371, https://doi.org/10.1111/gfl.12100.

Weis, P., Driesner, T., Coumou, D., Geiger, S., 2014. Hydrothermal, multiphase convection of H2O-NaCl fluids from ambient to magmatic temperatures: a new numerical scheme and benchmarks for code comparison. Geofluids, 14(3): 347-371, DOI:10.1111/gfl.12080.

Weis, P., Driesner, T., Heinrich, C.A., 2012. Porphyry-Copper Ore Shells Form at Stable Pressure-Temperature Fronts Within Dynamic Fluid Plumes. Science, 338(6114): 1613-1616.

Xu, M. et al., 2014. Variations in axial magma lens properties along the East Pacific Rise (9 degrees 30'N-10 degrees 00'N) from swath 3-D seismic imaging and 1-D waveform inversion. Journal of Geophysical Research-Solid Earth, 119(4): 2721-2744, DOI:10.1002/2013jb010730.

2 Implementation strategies for accurate and efficient control volume-based two-phase hydrothermal flow solutions

2.1 Abstract

Numerical models of magmatic hydrothermal systems have become powerful tools for linking surface and seafloor observations to chemical and fluid-dynamical processes at depth. This task requires resolving multi-phase flow over large distances of several kilometers, a wide range of pressure (p) and temperature (T) conditions, and over time scales of several thousands of years. The key numerical challenge is that realistic simulations have to consider the high non-linearity and strong coupling of the governing conservation equations for mass and energy, while also being numerically efficient so that the required spatial and temporal scales can be resolved.

Here we outline possible solutions to this problem by evaluating different implementation strategies and presenting a numerical scheme for fully coupled accurate and efficient flow solutions. The general scheme, based on the Newton-Raphson (NR) method, is presented for the simplified case of 2-D pure water convection and uses a control volume (CV) discretization on unstructured meshes. We find that the presented techniques significantly reduce the computational effort with respect to sequential/decoupled schemes. Key to this are a theta-time-differencing method for better accuracy, stability and convergence behavior of the NR-iterations, as well as improvements regarding upwinding. These features make the presented methods useful for coupled simulations of magmatic hydrothermal systems and a potential basis for future 3-D multi-phase codes.

2.2 Introduction

Numerical modeling has become an indispensable tool for investigating magmatic hydrothermal systems. In the context of submarine hydrothermal systems, integration of seafloor observations with numerical model predictions can put bounds on the hydrothermal mass and energy fluxes between oceanic crust and seafloor (Andersen et al., 2015; Cathles, 2011; Fontaine et al., 2007; Gruen et al., 2014; Hasenclever et al., 2014; Theissen-Krah et al., 2016). Such studies help quantifying the hydrothermal influence on ocean and crustal chemistry, the thermal evolution of young oceanic plates, and the formation of metal-rich massive sulfide deposits. Likewise, studies that integrate numerical models with data in continental areas are essential for assessing geothermal resources and ore deposits related to geothermal processes (Ingebritsen et al., 2010; Scott et al., 2015; Weis et al., 2012).

A significant progress has been made in hydrothermal system modeling over the past decades (Ingebritsen et al., 2010; Lowell, 1991). In particular, the use of realistic equations-of-states (EOS) and fewer fluid-dynamic simplifications have led to fundamental progress in understanding the inner workings of magmatic hydrothermal systems (Coumou et al., 2008; Hasenclever et al., 2014; Jupp and Schultz, 2000; Lewis and Lowell, 2009; Weis et al., 2014). Yet, robust simulations of multi-phase phenomena remain challenging due to the high non-linearity and strong coupling of the governing conservation equations for mass and energy (Faust and Mercer, 1979; Ingebritsen et al., 2010). This is particularly difficult to handle when boiling and condensation phenomena occur, which can go along with large volume changes. Further complications arise if the flow of salt water instead of pure water is simulated due to the increased complexity of the EOS, the occurrence of phase separation phenomena above the critical point of pure water, and the precipitation of halite (Driesner and Heinrich, 2007).

A recent review on modeling magmatic hydrothermal systems by Ingebritsen et al. (2010) provides an overview on currently used multiphase codes. Codes like HYDROTHERM (Kipp Jr et al., 2008), FEHM (Zyvoloski et al., 1997), and TOUGH2 (Pruess et al., 2012) are primarily tailored for simulating geothermal systems. For submarine applications, codes must be able to handle the flow of saline hydrothermal fluids over wider pressure and temperature ranges and to resolve two- and three-phase behavior. These requirements are currently only fulfilled by the academic codes CSMP++ (e.g. Weis et al., 2014) and FISHES (Lewis and Lowell, 2009) as well as, with some restrictions concerning fluid properties at pressures above the critical point of water, the NaCl-TOUGH2 extension of TOUGH2 (Kissling, 2005).

Interestingly, none of the existing codes is capable of simulating three-dimensional multi-phase flow of saline fluids over a sufficiently large p-T range to investigate realistic flow patterns in submarine settings. The few 3-D simulations of submarine hydrothermal systems that do exist have all been done assuming single-phase supercritical pure water convection (Coumou et al., 2008; Fontaine et al., 2014; Hasenclever et al., 2014; Travis et al., 1991). One of the reasons why this crucial development step has not yet been done is that it remains unclear, which numerical method and which implementation strategy is most suitable and efficient for robust 3-D multi-phase simulations over a wide p-T range.

Current modeling approaches can be divided into two different concepts: (i) coupled schemes that solve for mass and energy transport simultaneously and (ii) sequential schemes that decouple the governing equations. The widely used geothermal modeling codes TOUGH2, HYDROTHERM and FEHM use coupled schemes and resolve the non-linearity of fluid properties by iterations. This has the advantages that a physically consistent solution is obtained in every time step and that the error only depends on the imposed tolerances. The time step size can be much larger than in sequential schemes and is mainly bounded by desired accuracy and the convergence behavior of the iteration scheme.

The FISHES and CSMP++ codes use a sequential approach that decouples the conservation equations of mass and energy (Coumou et al., 2008; Lewis and Lowell, 2009; Weis et al., 2014). Note that an upcoming revision of the FISHES code will include a coupled scheme (personal communication with K. Lewis). The sequential CSMP++ code does this by reformulating the mass conservation equation as an elliptic pressure equation that is solved using the finite element (FE) method (Coumou et al., 2009) or the control volume-finite element (CVFE) method (Weis et al., 2014). From this solution, the velocity field of each fluid phase is calculated. The energy conservation equation is split into an explicit energy advection part and an implicit thermal diffusion part, which are solved independently. This approach results in conservation of mass and energy but requires a thermal equilibration step between rock and fluid to compute the non-conservative properties like pressure, temperature, and saturation. The sequential approach has the advantages that the numerical method that seems best suited for a certain type of equation can be used for each subproblem (Ingebritsen et al., 2010). The downside is that the decoupling between mass and energy transport and the operator splitting in the energy equation result in an error in the flow solution. This error scales with time step size and has to be corrected for in the subsequent time step via a source term in the pressure equation. The time step size is further restricted by the explicit advection step that has to meet the Courant-Friedrichs-Lewy (CFL) criterion. As a consequence, the size of the time step must be chosen much smaller than in coupled schemes in order to keep numerical errors within reasonable bounds and to ensure stability of the entire scheme.

Whether a coupled or sequential approach provides a preferable combination of stability, efficiency, and accuracy depends on the application. For example, time step restrictions are less problematic in 2-D than they are in 3-D, where solving matrix equations with a large number of unknowns is computationally more expensive. In the case of hydrothermal circulation patterns at mid-ocean ridges, the existing 3-D single-phase simulations (Coumou et al., 2008; Fontaine et al., 2014; Hasenclever et al., 2014) have shown that future more realistic multi-phase 3-D models will need to resolve seawater convection over several kilometers along and across the ridge-axis and also vertically down to the crust-mantle boundary. In addition, several thousand to tens of thousands of years need to be simulated for capturing the temporal evolution of hydrothermal convection at fast- and slow-spreading ridges. While no model is currently able to perform such a calculation, it appears likely that coupled schemes are better suited for this task as the larger time steps make the run-time of 3-D models more tractable. The challenge is, however, to derive coupled schemes that ensure stability without sacrificing accuracy.

This paper investigates implementation strategies for a control volume scheme able to provide two-phase hydrothermal flow solutions that are both stable and accurate at large time step sizes beyond the CFL criterion. This scheme, currently made for resolving 2-D pure water convection, allows for large computational time steps as well as the use of unstructured meshes to resolve complex geological features and employs strictly mass- and energy-conserving advection methods within the framework of a coupled solution that fully accounts for the non-linearity of fluid properties. It thereby integrates methods and ideas that proved to work well in sequential models into a fully coupled approach. The main focus during the development was on deriving a stable numerical scheme that shows a good convergence of the employed Newton-Raphson(NR)-iterations and allows for large time steps without loss in accuracy. For this purpose, different upwinding and time-stepping algorithms were explored.

Table 2.1: Variables

Variable	**Meaning**	**Unit**
ce	center point of Ω_{il}	
cf	subscript for facet midpoint	
c_{pr}	specific rock heat	J/(kg·K)
dt_{CFL}	Courant-Friedrichs-Lewy time step	s
dt_{OUT}	outflow time step criterion	s
dx	distance between nodes	m
E	total energy in fluid and matrix	J
F_{ik}	facet k of control volume i	m
f_{f}	scalar product of hydrostatic pressure gradient and unit normal vector of facet	Pa/m
f_w	upwind weighting threshold	Pa/m
$\vec{\mathbf{g}}$	gravitational acceleration	m/s²
h_{f}	fluid specific enthalpy	J/kg
h_{m}	mean specific enthalpy	J/kg
$h_{\mathrm{m,source}}$	mean specific enthalpy of source fluid	J/kg
K	mean conductivity of rock matrix and fluid	W/(m·K)
k	isotropic permeability of porous medium	m²
$k_{r\mathrm{f}}$	relative permeability	-
n	number of grid nodes	-

$\vec{\mathbf{n}}_i$	outerward pointing unit normal vector field of the control volume *i*	-
$\vec{\mathbf{n}}_{ik}$	outerward pointing unit normal vector of the control volume *i* of facet *k*	-
N	number of facets of a control volume	-
N_i	finite element shape functions	-
p	pore pressure	Pa
Q_m	mass source	Kg/s
Q_E	energy source	J/s
q_m	mass flux	Kg/(m^2·s)
S_l	liquid saturation	-
S_v	vapor saturation	-
t	time	s
T	rock and fluid temperature	°C
up	subscript for upstream node	
$\vec{\mathbf{v}}_\mathrm{f}$	Darcy velocity	m/s
w_f	upstream weighting factor	-
x	arbitrary point in domain Ω	
x_F	arbitrary point on a facet	
η_f	fluid viscosity	Pa·s
ρ_f	fluid density	kg/m^3
ρ_m	mean density of fluids	kg/m^3
ρ_r	rock density	kg/m^3
Ω	modeling domain	m^2
Ω_i	control volume	m^2
Ω_{il}	part *l* of control volume *i*	m^2
$\partial\Omega_i$	boundary of control volume *i*	m
θ	time differencing weighting	-
Φ	porosity	-

2.3 Governing equations

The laminar flow of a fluid trough a porous medium can be described by Darcy’s law. Considering multiphase flow and an isotropic permeability *k*, the Darcy velocity of each fluid phase is defined as:

$$\vec{\mathbf{v}}_\mathrm{f} = -k\frac{k_\mathrm{rf}}{\eta_\mathrm{f}}\left(\nabla p - \rho_\mathrm{f}\vec{\mathbf{g}}\right) \tag{2.1}$$

All variables are defined in Table 2.1 and subscript f is either l (liquid), v (vapor) or s (high-pressure fluid).

In this study we consider pure water so that only the dense liquid phase and light vapor phase can coexist. Above the critical pressure of pure water ($p = 22.06$ MPa) the fluid is always in a single-phase state but its properties change continuously. The phase region above the critical temperature and pressure is often called supercritical, where the fluid state changes gradually from liquid-like to vapor-like across the critical density of water (Fig. 2.1). For pragmatic and numerical reasons we handle fluid above the critical pressure as a separate artificial phase in order to circumvent known stability issues in previously proposed coupled schemes around the critical point of water (Hayba and Ingebritsen, 1994). This artificial phase is referred to as high-pressure fluid. With this definition, saturation, S_s, is equal to one above the critical pressure and zero otherwise and it always applies:

$$S_\mathrm{l} + S_\mathrm{v} + S_\mathrm{s} = 1 \tag{2.2}$$

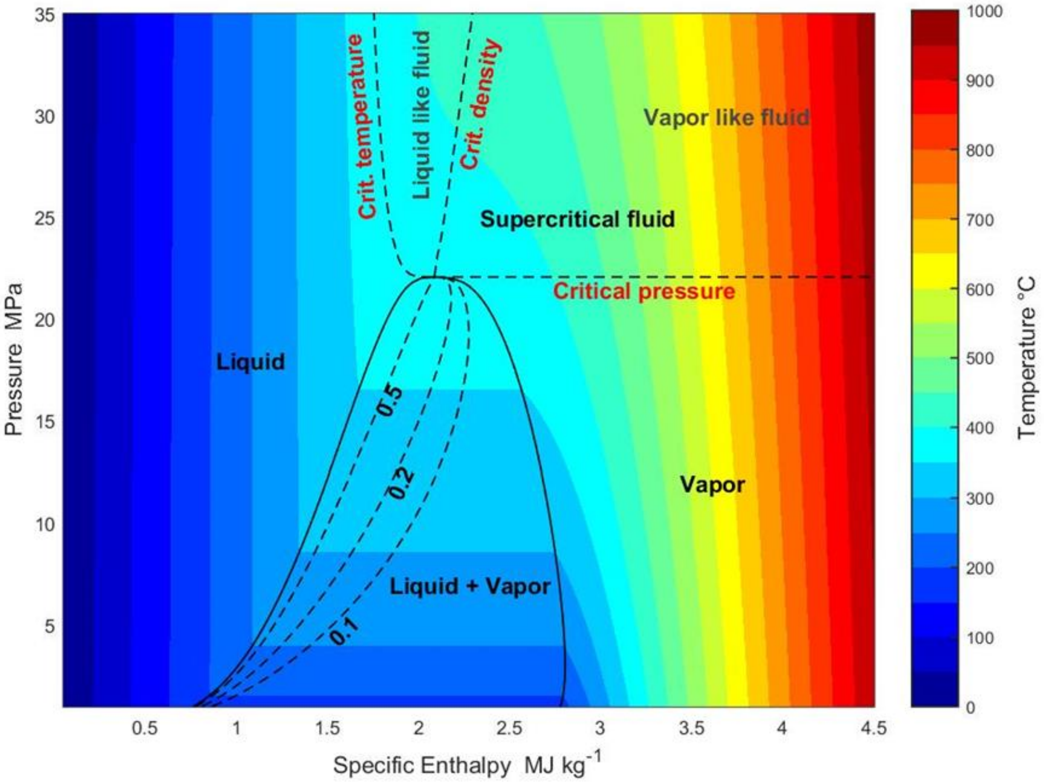

Figure 2.1: Phase diagram for pure water in pressure-specific enthalpy space relevant for magmatic hydrothermal systems. Phase boundaries are marked by solid black lines and liquid saturation by dashed lines within the two-phase region. The supercritical fluid state is outlined by dashed isolines of critical temperature and critical pressure. This region is devided by critical density isoline into liquid like and vapor like fluid. In the numerical scheme, we handle fluid above the critical pressure as a separate artificial phase and refer to it as high-pressure fluid

We follow the derivation of the conservation equations of mass and energy by Faust and Mercer (1977) and, in accordance, make the following model assumptions:

1. capillary pressure effects can be neglected
2. rock and fluid are in local thermodynamic equilibrium
3. rock enthalpy is related to temperature by a constant specific heat

We assume a stationary porosity and, in contrast to the derivation in Faust and Mercer (1979), we do not neglect parts of the pressure-volume work and the viscous dissipation term in the energy balance as they are, for example, not negligibly small in vapor-dominated systems (Garg and Pritchet, 1977).

The mass conservation equation is then given by

$$\Phi \frac{\partial \rho_{\mathrm{m}}}{\partial t} = \nabla \cdot \left(- \sum_{\mathrm{f} \in \{\mathrm{l,v,s}\}} \rho_{\mathrm{f}} \vec{\mathbf{v}}_{\mathrm{f}} \right) \tag{2.3}$$

where $\rho_{\mathrm{m}} = \sum_{\mathrm{f} \in \{\mathrm{l,v,s}\}} S_{\mathrm{f}} \rho_{\mathrm{f}}$ is the mean fluid density and the summation is done over the three phases. The energy conservation equation is given by

$$\begin{aligned} \frac{\partial E}{\partial t} &= \Phi \frac{\partial}{\partial t} (\rho_{\mathrm{m}} h_{\mathrm{m}}) + (1-\Phi) \rho_{\mathrm{r}} c_{p\mathrm{r}} \frac{\partial T}{\partial t} \\ &= \nabla \cdot K \nabla T - \nabla \cdot \left(\sum_{\mathrm{f} \in \{\mathrm{l,v,s}\}} h_{\mathrm{f}} \rho_{\mathrm{f}} \vec{\mathbf{v}}_{\mathrm{f}} \right) + \sum_{\mathrm{f} \in \{\mathrm{l,v,s}\}} \frac{\eta_{\mathrm{f}}}{k k_{r\mathrm{f}}} \vec{\mathbf{v}}_{\mathrm{f}}^2 + \Phi \frac{\partial p}{\partial t} + \sum_{\mathrm{f} \in \{\mathrm{l,v,s}\}} \vec{\mathbf{v}}_{\mathrm{f}} \nabla p \end{aligned} \tag{2.4}$$

Variables are given in Table 1 and the mean specific enthalpy is defined as:

$$h_{\mathrm{m}} = \frac{\sum_{\mathrm{f} \in \{\mathrm{l,v,s}\}} S_{\mathrm{f}} \rho_{\mathrm{f}} h_{\mathrm{f}}}{\sum_{\mathrm{f} \in \{\mathrm{l,v,s}\}} S_{\mathrm{f}} \rho_{\mathrm{f}}} \tag{2.5}$$

The third term on the RHS of Eq. (2.4) describes viscous dissipation and the forth term contains the part of the pressure-volume work that is not accounted for in the specific enthalpy. We summarize these two terms into the following expression, which is then back-substituted into Eq. (2.4):

$$\Phi \frac{\partial p}{\partial t} + \sum_{\mathrm{f} \in \{\mathrm{l,v,s}\}} \vec{\mathbf{v}}_{\mathrm{f}} \left(\rho_{\mathrm{f}} \vec{\mathbf{g}} \right) = - \sum_{\mathrm{f} \in \{\mathrm{l,v,s}\}} \vec{\mathbf{v}}_{\mathrm{f}} \left(\nabla p - \rho_{\mathrm{f}} \vec{\mathbf{g}} \right) + \left(\Phi \frac{\partial p}{\partial t} + \sum_{\mathrm{f} \in \{\mathrm{l,v,s}\}} \vec{\mathbf{v}}_{\mathrm{f}} \nabla p \right) \tag{2.6}$$

The resulting formulation describes the complete energy balance, in which potential energy is transformed into viscous heating and pressure-volume work by buoyancy driven flow; the kinetic energy terms are orders of magnitude smaller and hence can be neglected. These conservation equations provide a closed system of equations, when augmented with an equation of state. As primary variables we chose pressure and mean specific fluid enthalpy, which completely describe the fluid state under single and two-phase conditions (Fig. 2.1).

2.4 Numerical approach

2.4.1 Control volume method

The governing equations are discretized using a finite volume (FV) technique, in which a control volume is constructed around each node of an unstructured triangular finite element mesh (Fig. 2.2). The same discretization is used in CSMP++ and a similar approach in FEHM, where this approach is named control volume finite element (CVFE) method (Weis et al., 2014; Zyvoloski et al., 1997). This method guarantees a continuous mass and energy flux between two adjacent control volumes when using element-wise differentiation. Being locally mass and energy conserving, this method is better suited for nonlinear transport problems than standard FE methods (Huber and Helmig, 1999; Zyvoloski, 2007). Furthermore, it is more flexible than finite difference methods because unstructured meshes can be used.

In the FV method a control volume is constructed around each node of the finite element mesh by connecting the barycenters of the triangles with the midpoints of the associated triangle edges. Each triangle is thus divided into three equally large areas with the facets of each finite volume generally not being perpendicular to the triangle edges (Fig. 2.2). This kind of mesh construction can be found in earlier studies on modeling two-phase Darcy flow, for example in Lemonnier (1979) for a discontinuous FE approach and in Durlofsky (1994) for a CVFE approach.

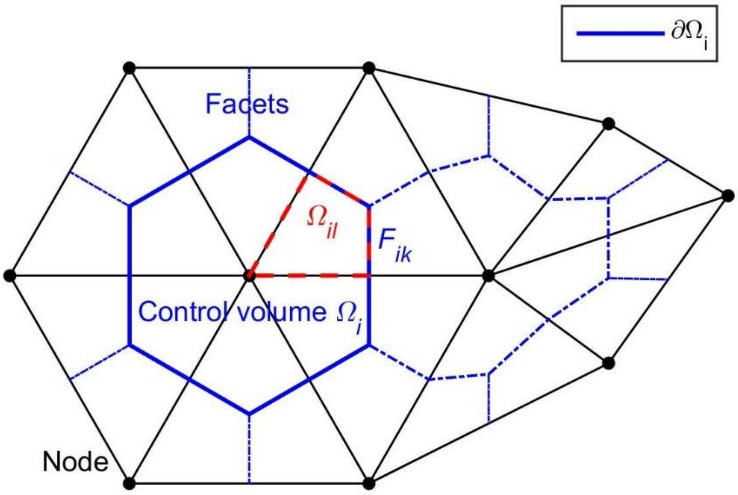

Figure 2.2: Construction of the control volumes Ω_i from an unstructured finite element triangle mesh (black lines)

The control volume method ensures that in each control volume Ω_i both conservation equations are satisfied. We obtain for each control volume Ω_i the integral formulations

$$\int_{\Omega_i} \Phi \frac{\partial \rho_\mathrm{m}}{\partial t} \mathrm{d}\Omega = -\int_{\Omega_i} \nabla \cdot \left(\sum_{\mathrm{f} \in \{\mathrm{l,v,s}\}} \rho_\mathrm{f} \vec{\mathbf{v}}_\mathrm{f} \right) \mathrm{d}\Omega \tag{2.7}$$

$$\int_{\Omega_i} \frac{\partial E}{\partial t} \mathrm{d}\Omega = \int_{\Omega_i} \nabla \cdot \left(K \nabla T - \sum_{\mathrm{f} \in \{\mathrm{l,v,s}\}} h_\mathrm{f} \rho_\mathrm{f} \vec{\mathbf{v}}_\mathrm{f} \right) + \Phi \frac{\partial p}{\partial t} + \sum_{\mathrm{f} \in \{\mathrm{l,v,s}\}} \vec{\mathbf{v}}_\mathrm{f} \left(\rho_\mathrm{f} \vec{\mathbf{g}} \right) \mathrm{d}\Omega \tag{2.8}$$

The divergence of the mass and energy fluxes within the control volume Ω_i is transformed into a contour integral on $\partial\Omega_i$ using the divergence theorem. We obtain

$$\int_{\Omega_i} \Phi \frac{\partial \rho_\mathrm{m}}{\partial t} \mathrm{d}\Omega = -\int_{\partial\Omega_i} \sum_{\mathrm{f} \in \{\mathrm{l,v,s}\}} \rho_\mathrm{f} \vec{\mathbf{v}}_\mathrm{f} \cdot \vec{\mathbf{n}}_i \mathrm{d}r \tag{2.9}$$

$$\int_{\Omega_i} \frac{\partial E}{\partial t} \mathrm{d}\Omega = \int_{\partial\Omega_i} \left(K \nabla T - \sum_{\mathrm{f} \in \{\mathrm{l,v,s}\}} -h_\mathrm{f} \rho_\mathrm{f} \vec{\mathbf{v}}_\mathrm{f} \right) \cdot \vec{\mathbf{n}}_i \mathrm{d}r + \int_{\Omega_i} \Phi \frac{\partial p}{\partial t} + \sum_{\mathrm{f} \in \{\mathrm{l,v,s}\}} \vec{\mathbf{v}}_\mathrm{f} \left(\rho_\mathrm{f} \vec{\mathbf{g}} \right) \mathrm{d}\Omega \tag{2.10}$$

where $\vec{\mathbf{n}}_i$ is the outward pointing unit normal vector field of the control volume boundary $\partial\Omega_i$.

The contour integral is calculated as a sum of integrals on facets, where F_{ik} are the facets of $\partial\Omega_i$ and N is the total number of facets. The control volume is divided into $N/2$ kite-shaped areas Ω_{il} that are each part of one adjacent triangular element.

$$\sum_{l=1}^{N/2}\int_{\Omega_{il}} \Phi \frac{\partial \rho_\mathrm{m}}{\partial t}\,\mathrm{d}\Omega = -\sum_{k=1}^{N}\int_{F_{ik}} \sum_{\mathrm{f}\in\{\mathrm{l,v,s}\}} \rho_\mathrm{f}\vec{\mathbf{v}}_\mathrm{f}\cdot\vec{\mathbf{n}}_{ik}\,\mathrm{d}r \tag{2.11}$$

$$\sum_{l=1}^{N/2}\int_{\Omega_{il}} \frac{\partial E}{\partial t}\,\mathrm{d}\Omega = \sum_{k=1}^{N}\int_{F_{ik}} \left(K\nabla T - \sum_{\mathrm{f}\in\{\mathrm{l,v,s}\}} h_\mathrm{f}\rho_\mathrm{f}\vec{\mathbf{v}}_\mathrm{f} \right)\cdot\vec{\mathbf{n}}_{ik}\,\mathrm{d}r + \sum_{l=1}^{N/2}\int_{\Omega_{il}} \Phi\frac{\partial p}{\partial t} + \sum_{\mathrm{f}\in\{\mathrm{l,v,s}\}} \vec{\mathbf{v}}_\mathrm{f}\left(\rho_\mathrm{f}\vec{\mathbf{g}}\right)\mathrm{d}\Omega \tag{2.12}$$

The primary variables pressure and mean specific fluid enthalpy h_m are discretized using standard linear finite element shape functions N so that the state variables can be interpolated to the CV facets:

$$p(x) = \sum_{j=1}^{n} N_j(x)\,p_j \tag{2.13}$$

$$h(x) = \sum_{j=1}^{n} N_j(x)\,h_j. \tag{2.14}$$

where x is an arbitrary point of Ω, j is the index of each node and its corresponding shape function, and n is the total number of nodes in the mesh. In the following we set mean specific enthalpy $h = h_\mathrm{m}$ to avoid multiple indices. To calculate gradients across the facets we use the spatial derivatives of standard linear finite element shape functions:

$$\nabla p(x) = \nabla\sum_{j=1}^{n} N_j(x)\,p_j = \sum_{j=1}^{n} \nabla N_j(x)\,p_j \tag{2.15}$$

$$\nabla T(x) = \nabla\sum_{j=1}^{n} N_j(x)\,T_j = \sum_{j=1}^{n} \nabla N_j(x)\,T_j \tag{2.16}$$

2.4.2 Numerical discretization in time

For numerical discretization in time we have implemented a variable combination of forward Euler method and backward Euler method, the so-called theta(θ)-method:

$$\frac{\partial u}{\partial t} = F(u,x,t) \tag{2.17}$$

$$\frac{u^{t+\Delta t} - u^{t}}{\Delta t} = \theta F(u,x,t)^{t+\Delta t} + (1-\theta)F(u,x,t)^{t} \tag{2.18}$$

Depending on the choice of θ this method is known under different names:

$\theta = 0$: Forward Euler Method,

θ = 1/2: Crank-Nicolson Method,

θ = 2/3: Galerkin Method,

θ = 1: Backward Euler Method

For the partial time derivatives we obtain:

$$\Phi \frac{\partial \rho_{\mathrm{m}}}{\partial t} = \Phi \frac{\rho_{\mathrm{m}}^{t+\Delta t} - \rho_{\mathrm{m}}^{t}}{\Delta t} \tag{2.19}$$

$$\frac{\partial E}{\partial t} = \frac{E^{t+\Delta t} - E^{t}}{\Delta t} = \Phi \frac{\left(\rho_{\mathrm{m}} h_{\mathrm{m}}\right)^{t+\Delta t} - \left(\rho_{\mathrm{m}} h_{\mathrm{m}}\right)^{t}}{\Delta t} + (1-\Phi)\rho_{\mathrm{r}} c_{pr} \frac{T^{t+\Delta t} - T^{t}}{\Delta t} \tag{2.20}$$

$$\Phi \frac{\partial p}{\partial t} = \Phi \frac{p^{t+\Delta t} - p^{t}}{\Delta t} \tag{2.21}$$

For the mass and energy transport term, respectively, we obtain for each fluid phase

$$\sum_{\mathrm{f} \in \{\mathrm{l,v,s}\}} \rho_{\mathrm{f}} \vec{\mathbf{v}}_{\mathrm{f}} = \theta \left(\sum_{\mathrm{f} \in \{\mathrm{l,v,s}\}} \rho_{\mathrm{f}} \vec{\mathbf{v}}_{\mathrm{f}} \right)^{t+\Delta t} + (1-\theta) \left(\sum_{\mathrm{f} \in \{\mathrm{l,v,s}\}} \rho_{\mathrm{f}} \vec{\mathbf{v}}_{\mathrm{f}} \right)^{t} \tag{2.22}$$

$$K \nabla T - \sum_{\mathrm{f} \in \{\mathrm{l,v,s}\}} h_{\mathrm{f}} \rho_{\mathrm{f}} \vec{\mathbf{v}}_{\mathrm{f}} = \theta \left(K \nabla T - \sum_{\mathrm{f} \in \{\mathrm{l,v,s}\}} h_{\mathrm{f}} \rho_{\mathrm{f}} \vec{\mathbf{v}}_{\mathrm{f}} \right)^{t+\Delta t} + (1-\theta) \left(K \nabla T - \sum_{\mathrm{f} \in \{\mathrm{l,v,s}\}} h_{\mathrm{f}} \rho_{\mathrm{f}} \vec{\mathbf{v}}_{\mathrm{f}} \right)^{t} \tag{2.23}$$

The terms describing the pressure-volume work and viscous dissipation are

$$\sum_{\mathrm{f} \in \{\mathrm{l,v,s}\}} \vec{\mathbf{v}}_{\mathrm{f}} \left(\rho_{\mathrm{f}} \vec{\mathbf{g}} \right) = \theta \left(\sum_{\mathrm{f} \in \{\mathrm{l,v,s}\}} \vec{\mathbf{v}}_{\mathrm{f}} \left(\rho_{\mathrm{f}} \vec{\mathbf{g}} \right) \right)^{t+\Delta t} + (1-\theta) \left(\sum_{\mathrm{f} \in \{\mathrm{l,v,s}\}} \vec{\mathbf{v}}_{\mathrm{f}} \left(\rho_{\mathrm{f}} \vec{\mathbf{g}} \right) \right)^{t} \tag{2.24}$$

2.4.3 Newton-Raphson-scheme

The main numerical difficulty in solving the above system of equations is the strong coupling between the mass and energy conservation equations and the strong non-linearity of the fluid properties. While the equation coupling is treated in our scheme by computing pressure and mean specific fluid enthalpy simultaneously during a single solve of the matrix equation, the non-linearity in fluid properties is resolved by NR-iterations. For this purpose we write the equations for each finite volume (or associated node) i in residual form:

$$R_i = -\sum_{k=1}^{N} \int_{F_{ik}} \sum_{\mathrm{f} \in \{\mathrm{l,v,s}\}} \rho_{\mathrm{f}} \vec{\mathbf{v}}_{\mathrm{f}} \cdot \vec{\mathbf{n}}_{ik} \mathrm{d}r - \sum_{l=1}^{N/2} \int_{\Omega_{il}} \Phi \frac{\partial \rho_{\mathrm{m}}}{\partial t} \mathrm{d}\Omega = 0 \tag{2.25}$$

$$G_i = \sum_{k=1}^{N} \int_{F_{ik}} \left(K\nabla T - \sum_{\mathrm{f}\in\{\mathrm{l,v,s}\}} h_\mathrm{f} \rho_\mathrm{f} \vec{\mathbf{v}}_\mathrm{f} \right) \cdot \vec{\mathbf{n}}_{ik} \mathrm{d}r + \sum_{l=1}^{N/2} \int_{\Omega_{il}} \Phi \frac{\partial p}{\partial t} + \sum_{\mathrm{f}\in\{\mathrm{l,v,s}\}} \vec{\mathbf{v}}_\mathrm{f} \left(\rho_\mathrm{f} \vec{\mathbf{g}} \right) - \frac{\partial E}{\partial t} \mathrm{d}\Omega \tag{2.26}$$

and obtain the following Newton-Raphson-procedure:

$$\frac{\partial R_i}{\partial p_j}\left(p_j^{l+1} - p_j^l\right) + \frac{\partial R_i}{\partial h_j}\left(h_j^{l+1} - h_j^l\right) = -R_i^l \tag{2.27}$$

$$\frac{\partial G_i}{\partial p_j}\left(p_j^{l+1} - p_j^l\right) + \frac{\partial G_i}{\partial h_j}\left(h_j^{l+1} - h_j^l\right) = -G_i^l \tag{2.28}$$

Here $l + 1$ refers to pressure and specific enthalpy after the next iteration step at time $t + \Delta t$. Since each nodal residuum value depends only on the adjacent mesh nodes that are connected by the elements, all other derivatives are zero and the resulting matrix is sparse. The linear system of equations shown in matrix notation is then:

$$\begin{pmatrix} \frac{\partial R_1}{\partial p_1} & \cdots & \frac{\partial R_1}{\partial p_n} & \frac{\partial R_1}{\partial h_1} & \cdots & \frac{\partial R_1}{\partial h_n} \\ \vdots & \ddots & \vdots & \vdots & \ddots & \vdots \\ \frac{\partial R_n}{\partial p_1} & \cdots & \frac{\partial R_n}{\partial p_n} & \frac{\partial R_n}{\partial h_1} & \cdots & \frac{\partial R_n}{\partial h_n} \\ \frac{\partial G_1}{\partial p_1} & \cdots & \frac{\partial G_1}{\partial p_n} & \frac{\partial G_1}{\partial h_1} & \cdots & \frac{\partial G_1}{\partial h_n} \\ \vdots & \ddots & \vdots & \vdots & \ddots & \vdots \\ \frac{\partial G_n}{\partial p_1} & \cdots & \frac{\partial G_n}{\partial p_n} & \frac{\partial G_n}{\partial h_1} & \cdots & \frac{\partial G_n}{\partial h_n} \end{pmatrix} \begin{pmatrix} p_1^{l+1} - p_1^l \\ \vdots \\ p_n^{l+1} - p_n^l \\ h_1^{l+1} - h_1^l \\ \vdots \\ h_n^{l+1} - h_n^l \end{pmatrix} = \begin{pmatrix} -R_1^l \\ \vdots \\ -R_n^l \\ -G_1^l \\ \vdots \\ -G_n^l \end{pmatrix}. \tag{2.29}$$

The calculation of R_i and G_i and their derivatives can be found in the Appendix (section 2.9.3). Since we use an implicit numerical method, R_i and G_i as well as their derivatives have to be calculated every time before solving the linear system of equations.

2.4.4 Upstream weighting method

For evaluating relative permeability and specific enthalpy at the finite volume facets we implemented an upwind scheme to overcome numerical oscillations. The variable values are averaged between values at the facet midpoint (cf) and the upstream nodes (up). The upstream weighting factor w_f for each phase depends on the magnitude of the forces driving flow across a finite volume facet. This can be expressed by the scalar product f_f of the unit normal vector of the facet and the hydrostatic pressure gradient at the facet midpoint:

$$f_\mathrm{f} = \left(\nabla p - \vec{\mathbf{g}} \rho_{\mathrm{f,cf}}\right) \cdot \vec{\mathbf{n}} \tag{2.30}$$

Using the fluid driving force has the benefit that no extra calculations are necessarry and that it is directly related to the Darcy velocity and thereby energy advection, the primary source of numerical oscilations. Similar to HYDROTHERM, we further introduce an adjustable threshold f_w that, when exceeded, leads to full upstream weighting. We use a linear upstream weighting below f_{w} and also define an empirically found minimum value of f_{w} below which no upstream weighting is used:

$$w_{\mathrm{f}} = 1 \text{ if } \left|f_{\mathrm{f}}\right| \geq f_{\mathrm{w}} \tag{2.31}$$

$$w_{\mathrm{f}} = \frac{\left(f_{\mathrm{f}} - {f_{\mathrm{w}}}/{10}\right)}{\left(f_{\mathrm{w}} - {f_{\mathrm{w}}}/{10}\right)} \text{ if } f_{\mathrm{w}} > \left|f_{\mathrm{f}}\right| > {f_{\mathrm{w}}}/{10} \tag{2.32}$$

$$w_{\mathrm{f}} = 0 \text{ if } \left|f_{\mathrm{f}}\right| \leq {f_{\mathrm{w}}}/{10} \tag{2.33}$$

We define the following linear weighting of the specific enthalpy and relative permeability:

$$h_{\mathrm{f}} = w_{\mathrm{f}} h_{\mathrm{f,up}} + (1 - w_{\mathrm{f}}) h_{\mathrm{f,cf}} \tag{2.34}$$

$$k_{r\mathrm{f}} = w_{\mathrm{f}} k_{r\mathrm{f,up}} + (1 - w_{\mathrm{f}}) k_{r\mathrm{f,cf}} \tag{2.35}$$

Care must be taken when different phases are stable at the upwind nodes and at the facet midpoints. The handling of these special cases is described in detail in the Appendix (section 2.9.2). We find that there is no need for upwind weighting of fluid viscosity and density; it is sufficient to use upwind weighting on the specific enthalpy h_{f} and on the relative permeability $k_{r\mathrm{f}}$.

2.4.5 Fluid properties

Hydrothermal flow solutions are known to strongly depend on the used EOS. For example, a series of studies have shown that for a given setup, the dominant temperatures of the re- and discharge limbs of a free hydrothermal convection cell are primarily controlled by the thermodynamic propterties of water (Bauer, 1998; Coumou et al., 2008; Hasenclever et al., 2014; Jupp and Schultz, 2000). We have implemented the full IAPS-84 EOS of pure water into a newly developed Matlab function. The code structure of this function is largely based on the C-library PROST (Bauer, 1998) but has been optimized for the use in coupled solution schemes. It takes specific enthalpy and pressure as input and computes all fluid properties, saturation, and fluid state as output. Liquid saturations below the critical pressure are defined as follows:

$$S_{\mathrm{l}} = \frac{\rho_{\mathrm{v}}\left(h_{\mathrm{v}} - h\right)}{h\left(\rho_{\mathrm{l}} - \rho_{\mathrm{v}}\right) - \left(h_{\mathrm{l}}\rho_{\mathrm{l}} - h_{\mathrm{v}}\rho_{\mathrm{v}}\right)} \tag{2.36}$$

$$S_{\mathrm{v}} = 1 - S_{\mathrm{l}} \tag{2.37}$$

We define the relative permeability identical to that in HYDROTHERM:

$$k_{r\mathrm{l}}\left(S_{\mathrm{l}}\right) = \frac{S_{\mathrm{l}} - S_{\mathrm{lr}}}{1 - S_{\mathrm{lr}}} \quad \forall S_{\mathrm{l}} > S_{\mathrm{lr}} \tag{2.38}$$

$$k_{r\mathrm{l}}\left(S_{\mathrm{l}}\right) = 0 \qquad \forall S_{\mathrm{l}} \leq S_{\mathrm{lr}} \tag{2.39}$$

where S_{lr} is the residual saturation of liquid water, below which the liquid phase is assumed immobile. This definition avoids steps within the permebility function and is therefore suitable for the Newton-Raphson-scheme. Relative permeability of vapor is defined as:

$$k_{rv} = 1 - k_{rl} \tag{2.40}$$

2.4.6 Code structure

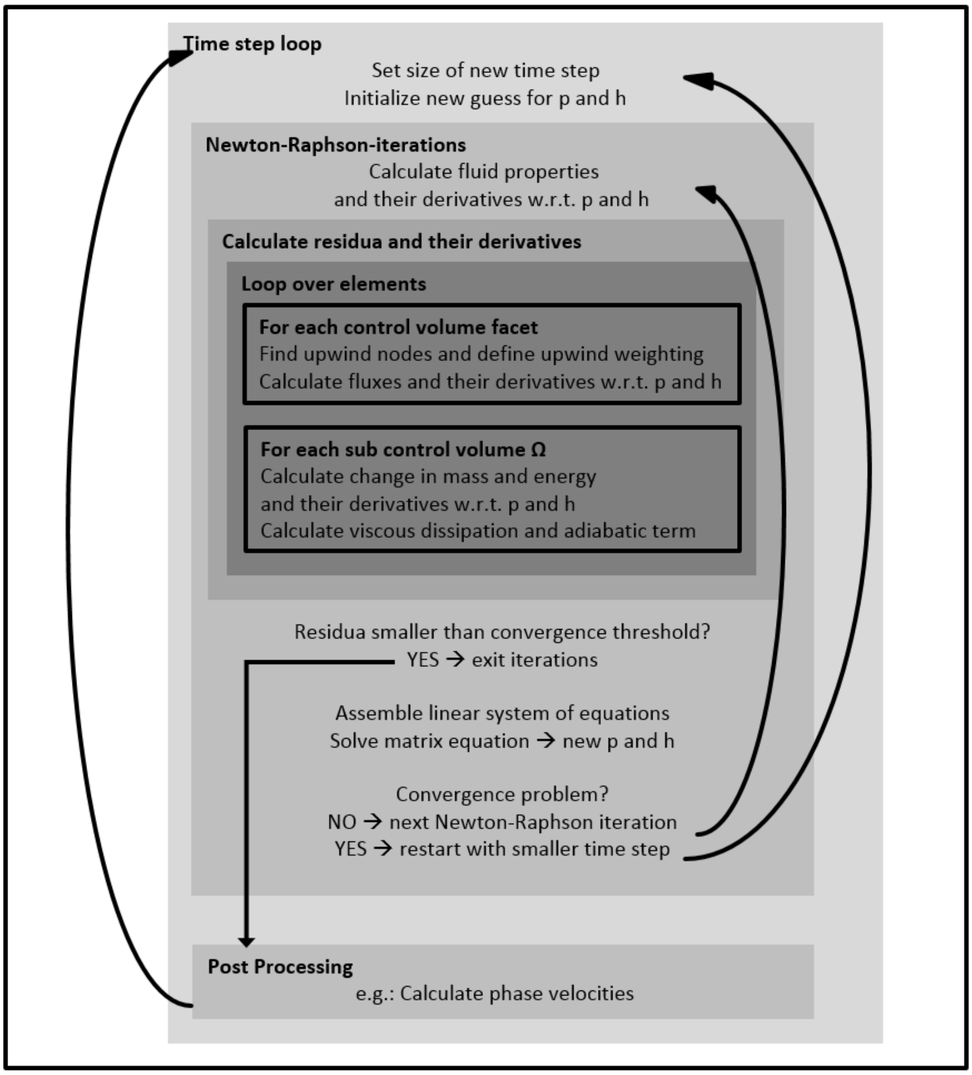

Figure 2.3: Code structure. Further details are given in the main text.

The numerical implementation has been done according to the structure shown in Figure 2.3 for a single computational time step. At the beginning of each time step a new step size Δt^{new} is calculated from the mass and energy changes during the previous time step to keep the maximum relative changes in density and/or specific enthalpy below a specified threshold.

The quality of the initial guesses for specific enthalpy and pressure strongly affects the convergence behavior of the NR-scheme. These are calculated using information on the changes that occurred over the last time step:

$$h^{t+\Delta t,\mathrm{new}} = h^t + f_t \Delta t^{\mathrm{new}} \frac{\left(h^t - h^{t-\Delta t,\mathrm{old}}\right)}{\Delta t^{\mathrm{old}}} \tag{2.41}$$

For pressure we use an equivalent formula. This equation leads to a good initial guess if the new changes in specific enthalpy and pressure are similar to the changes of the last time step. Thus for small time steps, f_t should be 1 while for larger time steps the factor should be reduced to 0.5.

Next, NR-iterations are performed. The inner computational sequence is based on a loop over all triangular finite elements, in which for each element the fluxes across its three CV facets are evaluated (Fig. 2.3). An assembly loop over finite elements instead of over finite volumes (i.e. nodes) results in a cleaner and more efficient code structure. The final coefficient matrix is then assembled after the three fluxes and three volume integrations have been evaluated for each element. Further details on the calculation of residua and their derivatives with respect to nodal specific enthalpy and pressure are given in the Appendix (2.9.2 & 2.9.3). To evaluate the convergence criterion, we choose the following norms for each control volume:

$$\|R_i\| = \frac{1}{\Omega_i \Phi_i \rho_{\mathrm{m},i}} R_i \tag{2.42}$$

$$\|G_i\| = \frac{1}{\Omega_i \Phi_i \rho_i h_i} G_i \tag{2.43}$$

We find a convergence threshold in the range of 0.01 to 0.001 per m² and per year of simulation time for $\|R_i\|$ and $\|G_i\|$ as favorable for a wide range of pressure-temperature-conditions. In the case of no convergence within a predefined maximum number of NR-iterations, the current time step is restarted with a smaller time step size Δt^{new}.

2.5 Code verification

We have performed a number of one-dimensional (1-D) and two-dimensional (2-D) benchmark tests with our newly developed model, called HT2_NR in the following, against the version 3.1 of HYDROTHERM in order to test the newly developed solution scheme and to demonstrate some of its advantages. In these tests, the rock properties have been kept constant. We use a porosity of $\Phi = 0.1$, an isotropic permeability of $k = 10^{-15}$ m², a rock heat capacity of $c_{pr} = 880$ J/(kg·K), a rock thermal conductivity of $K = 2$ W/(m·K) and a rock density of $\rho_{\mathrm{r}} = 2700$ kg/m³. The residual saturation of the liquid phase S_{lr} is set to 0.3.

2.5.1 One-dimensional simulations

The 1-D test cases are taken from Weis et al. (2014) (see Table 2.2), which were designed to test the code behavior along key p-T paths in the phase diagram of pure water. We have only changed the setup to a finer grid spacing of 5 m instead of 10 m and ran the tests in a 2-D-modeling domain with 2 km length and 5 m width. This leads to 400 rectangular boxes that are each split into two triangles. In these tests we have neglected the viscous dissipation and the adiabatic correction terms as those are not considered in HYDROTHERM. For the HYDROTHERM simulations we use the same size of the modeling domain and grid point spacing. Since HYDROTHERM applies boundary conditions in the center of the first and last grid cell, we add an extra grid point at 0.1 m distance to both ends of the 1-D domain. Hence the first and last boxes are smaller so that the boundary conditions are moved closer to the physical domain boundary. The boundary conditions of the 1-D tests cover all phase regions of pure water, and a 90º rotation of the modeling domain allows investigating gravity-free horizontal as well as vertical problems in which gravity-driven counter flow becomes important under two-phase conditions. Table 2.3 summarizes all 1-D setups that are presented in this paper.

Figure 2.4 shows the results of six test cases in comparison to HYDROTHERM. In all tests, hot fluid flows into the initially cold domain from the left side in the horizontal and from the bottom in the vertical setup. As HYDROTHERM uses a backward-in-time differencing method (Kipp Jr et al., 2008), we conduct the benchmark tests with HT2_NR also with this method and set θ to one (see Eqs. 2.22 – 2.24). For these tests no upwind weighting is necessary, because a sufficient number of grid points resolves the thermal front. Both codes show nearly identical solutions.

Table 2.2: Boundary conditions of 1-D tests

Setup	Boundary condition left/bottom	Boundary condition right/top
a	350 °C 50 MPa	150 °C 40 MPa
b	450 °C 40 MPa	300 °C 20 MPa
c	500 °C 15 MPa	350 °C 1 MPa
d	400 °C 20 MPa	150 °C 1 MPa

Table 2.3: Summary of 1-D-tests comparing HT2_NR and HYDROTHERM

Test	Setup	Orientation	Upwind weighting threshold
1	a	horizontal	no
2	a	vertical	no
3	b	horizontal	no
4	b	vertical	no
5	c	horizontal	no
6	c	vertical	no
7	d	horizontal	HT2_NR: f_w =1000 HY: 1e-4
8	d	vertical	HT2_NR: f_w =1000 HY: 1e-4

HY: HYDROTHERM

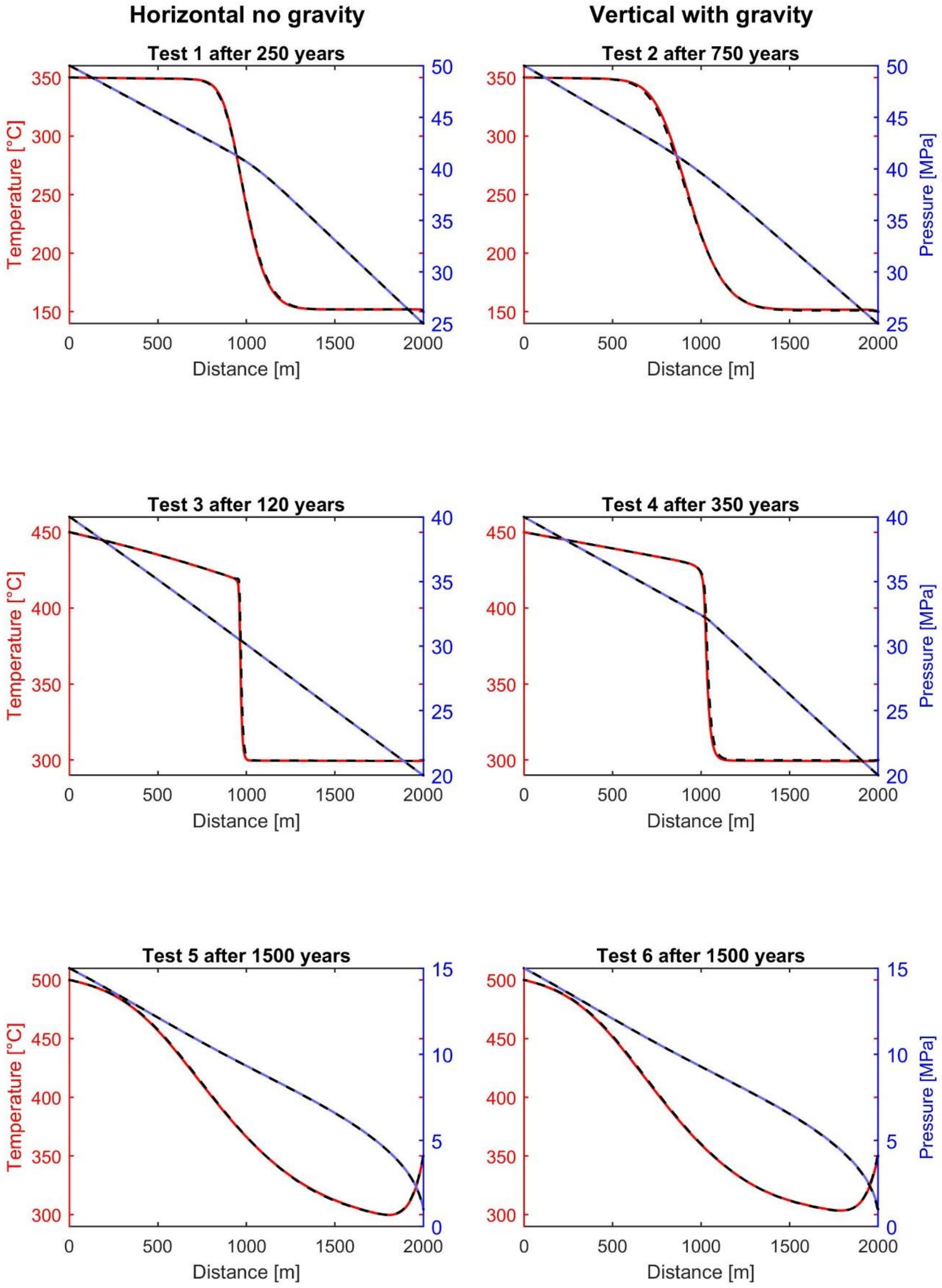

Figure 2.4: One-dimensional benchmark tests and comparison with HYDROTHERM. Simulations are in horizontal orientation without gravity (Test 1,3,5) and vertical orientation with gravity (Test 2,4,6) Solid lines show results of HT2_NR (temperature in red, pressure in blue) and dashed lines results from HYDROTHERM.

Another set of experiments addresses two-phase conditions. In setup (d) 400 °C hot vapor is injected into a rock saturated with liquid water at 150 °C. The pressure conditions are below the critical point of water leading to a boiling zone behind the thermal front. In contrast to the single-phase simulations, upwind weighting is now necessary to prevent oscillations that would form at the thermal front and propagate into the boiling zone. In HYDROTHERM, the upwind weighting threshold is the hydraulic pressure ratio between two cells, which leads to a full upwind weighting factor at values greater than 1 and to a logarithmic decrease of the weighting factor at lower ratios. We have found thresholds for HYDROTHERM (0.0001) and HT2_NR (f_w =1000 Pa/m) that give for both orientations, horizontal (Fig. 2.5 Test 7) and vertical (Fig. 2.5 Test 8), an almost perfect match between both codes. At horizontal orientation, the boiling zone shows a mobile liquid saturation slightly above 0.3. At vertical orientation the boiling zone is enlarged with a higher liquid saturation.

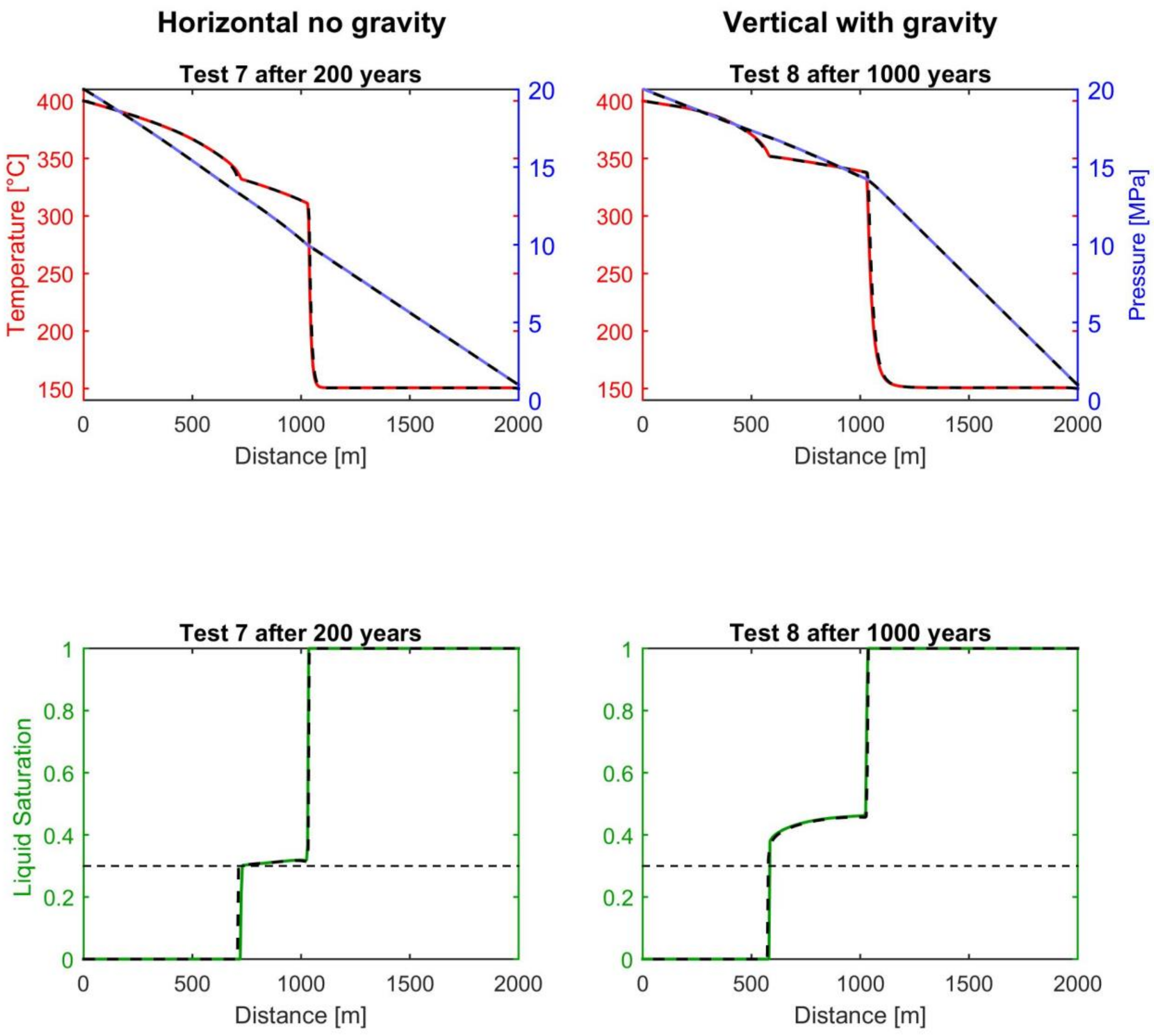

Figure 2.5: One-dimensional two-phase simulations in horizontal (Test 7) and vertical (Test 8) orientation. Solid lines are from HT2_NR (temperature in red, pressure in blue, liquid saturation in green at the lower part) and black dashed lines from HYDROTHERM. Upwind weighting threshold is set to f_w = 1000 Pa/m for HT2_NR and 0.0001 for HYDROTHERM

2.5.2 2-D two-phase tests

For the 2-D two-phase tests we model a 2 km x 2 km box of a cold rock at 10 °C with a basal heat source. We use a medium (8 W/m²) and high (15 W/m²) heat flux boundary condition along a 500 m long central section at the bottom and a low heat flux boundary condition of 0.05 W/m² elsewhere at the bottom. At the top is a fixed pressure boundary condition of 1 MPa and a temperature boundary condition of 10 °C, and we allow for free fluid in- and outflow. All other sides are no flow boundary condition and insulating. Full upwind weighting is used (i.e. $w_f = 1$).

In HYDROTHERM we use a uniform grid spacing of 25 m that leads to 80 boxes in each row and column and a total of 6561 grid points. With HT2_NR we use a regular grid of 60 x 60 boxes, which are each divided in four triangles with an extra grid point in the center of each box. This grid has 7321 points.

The first test case assumes a medium basal heat flux of 8 W/m² and results in boiling and the rise of a two-phase thermal plume (Fig. 2.6). The comparison with HYDROTHERM shows less agreement than in the 1-D simulations. HYDROTHERM predicts a slightly faster and more localized ascent of the boiling zone than HT2_NR. This tendency of HYDROTHERM was also noted by Weis et al. (2014). The high heat flux simulation (15 W/m²) initially shows two small upflow zones that later merge into one plume (Fig. 2.7). Compared to HT2_NR, HYDROTHERM shows a faster propagation of the thermal front after 1000 years.

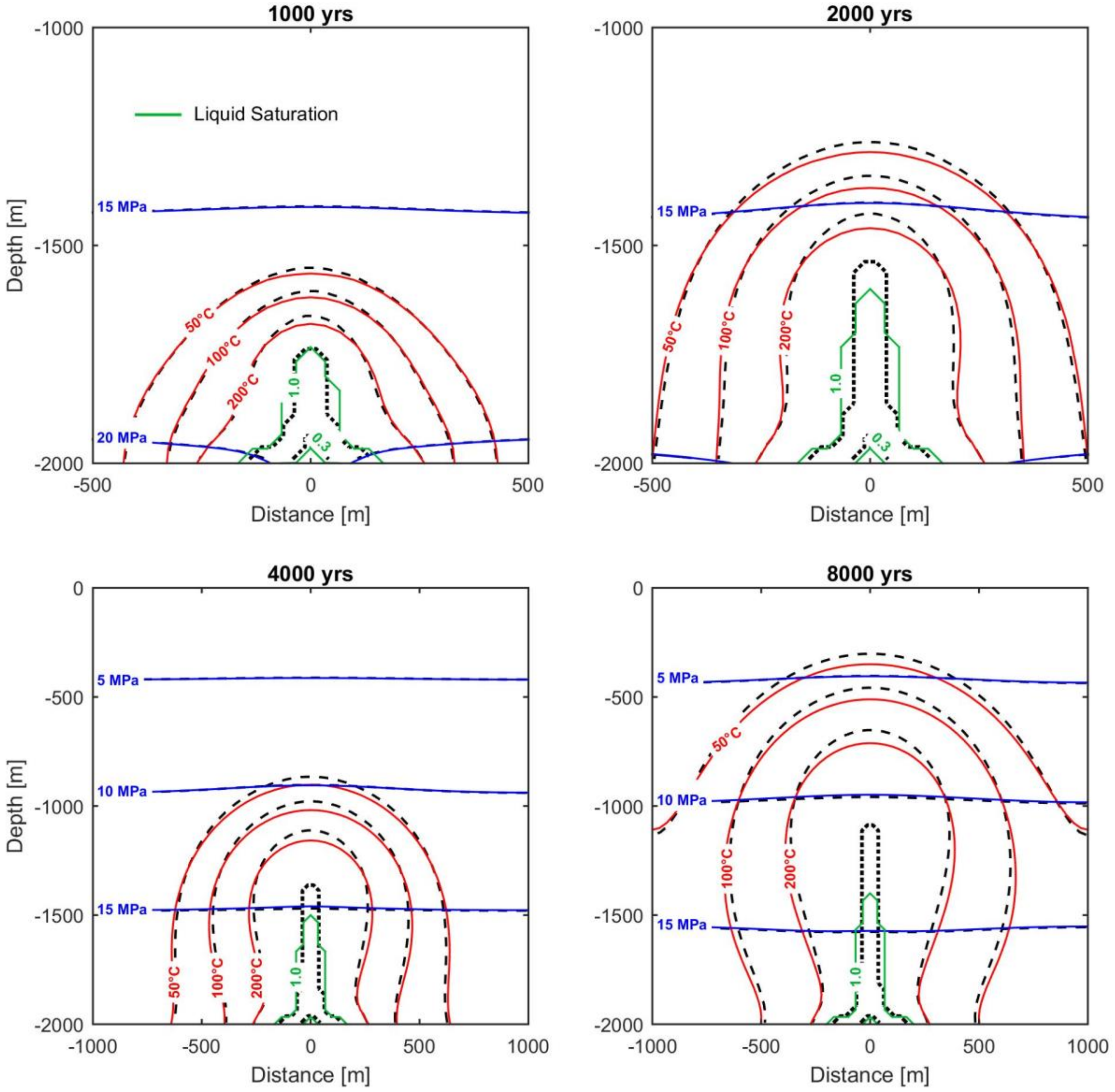

Figure 2.6: Contour plot of two-dimensional simulations with medium heat flux 8 W/m² and full upwind weighting. Comparison between HT2_NR (solid red, blue and green) and HYDROTHERM (dashed black)

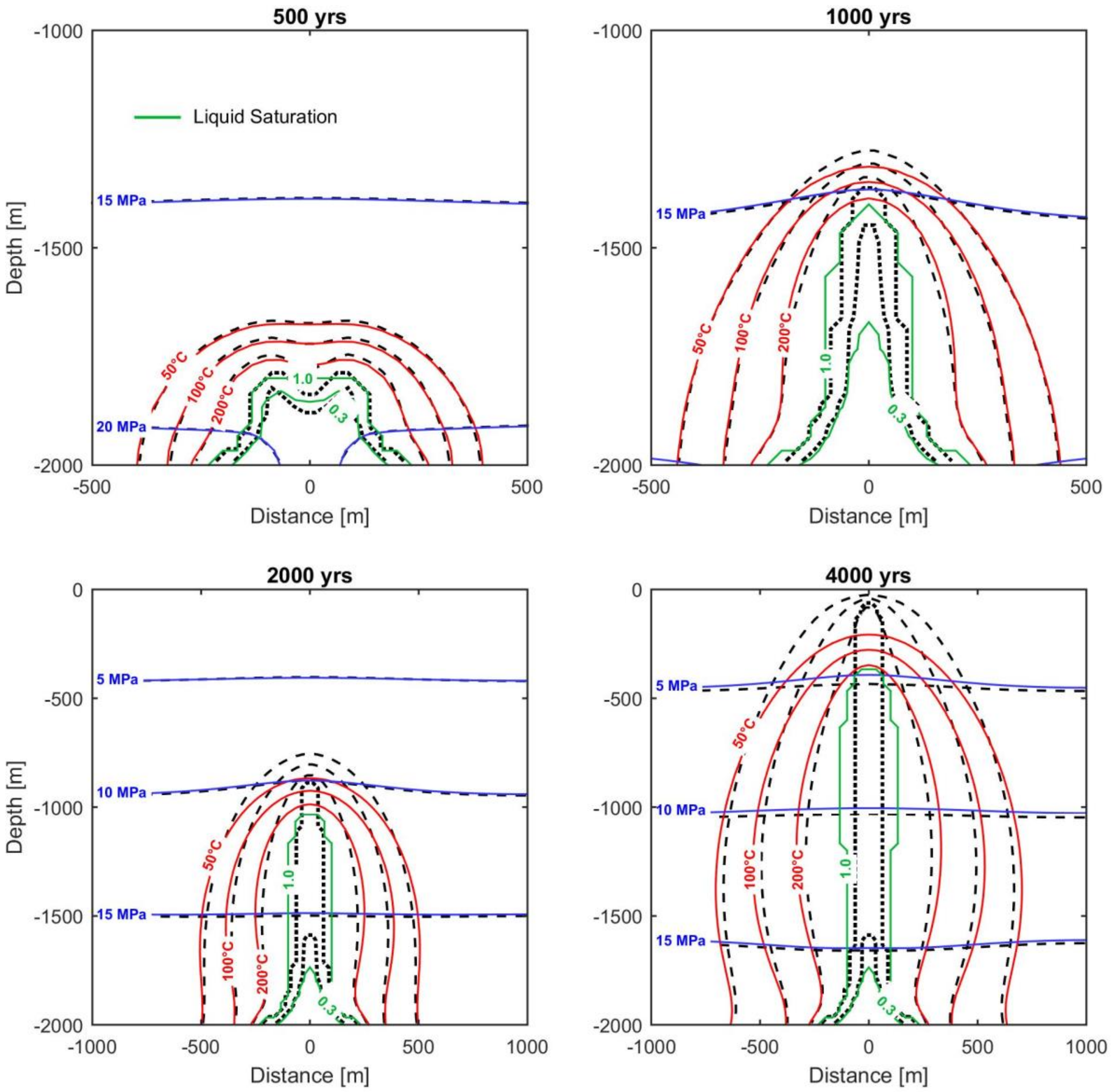

Figure 2.7: Contour plot of two-dimensional simulation with high heat flux 15 W/m² and full upwind weighting. Comparison between HT2_NR (solid red, blue and green) and HYDROTHERM (dashed black)

2.5.3 Subaerial simulations

Boiling and condensation phenomena are especially difficult to handle under low-pressure subaerial conditions, where the density contrast between the liquid and vapor phases are near their maximum. The robustness of the solution method in such a setting can be tested using the example of multiphase groundwater flow near a cooling pluton (Hayba and Ingebritsen, 1997). Here we have modeled a shallow magmatic intrusion driving a hydrothermal system, including fluid flow near the critical point and two-phase flow at pressure conditions from atmospheric to the critical point. The model setup comprises a homogeneous area of 4 km depth and 4 km width with a permeability of 10^{-15} m², which is intruded by a 900 °C hot pluton with a half width of 500 m (note that symmetry is imposed on the lateral boundaries) and 2000 m height. The permeability of the pluton is held constant at 10^{-18} m² to avoid fluid flow within the pluton. All other rock properties are as descripted in section 2.5.1. The sidewalls and the bottom are impermeable and insulating. At the top, we use a free venting boundary condition as described in the Appendix (section 2.9.1) and set atmospheric pressure conditions. The upwind weighting threshold is set to f_w = 500 Pa/m and θ = 2/3 for the time differencing scheme. The mesh is refined along the edges of the pluton. Fig. 2.8 shows results 500, 1500, and 4500 years after the magma has been emplaced. After 500 years, a fast-flowing upflow zone next to the pluton is established with temperatures of up to 400 °C. A pure vapor zone forms above the pluton. At 1500 years the two-phase up flow zone above the pluton has a liquid saturation between 0.8 and 1. After 4500 years venting of both vapor and liquid phases occurs.

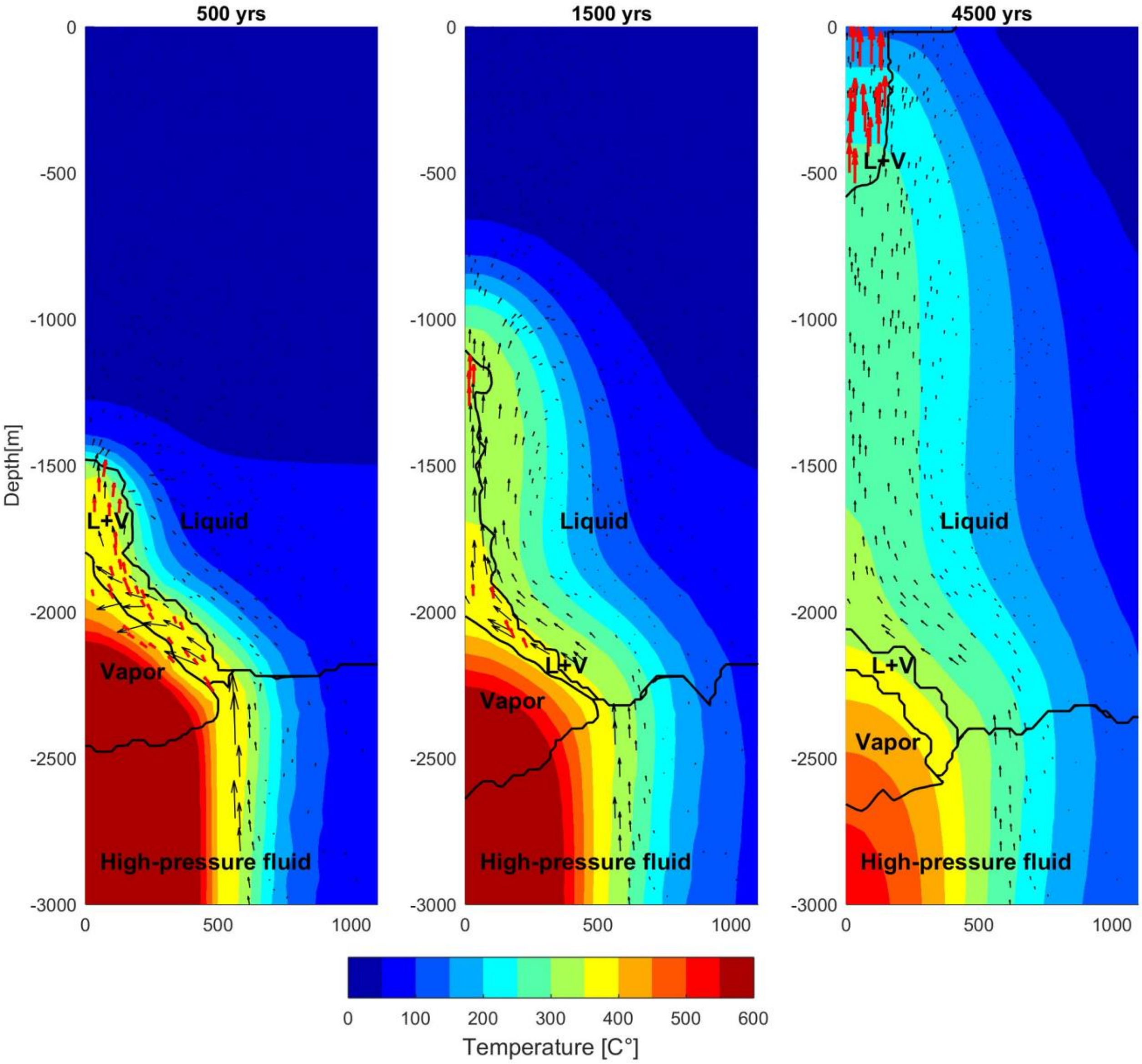

Figure 2.8: Color plot of fluid temperature and location of water phases. L+V denotes two-phase regions. Detailed view on upper left side of modeling area after 500, 1500 and 4500 years. Black arrows show liquid velocities and red arrows show vapor velocities. Vapor velocity arrows are scaled fifty times shorter than liquid arrows. Fluids higher than critical pressure are labeled with “High-pressure fluid”.

2.6 Accuracy, stability and efficiency analysis

2.6.1 Upwind weighting

Figure 2.9 & 2.10 show the impact of reducing the upwind weighting for the two-dimensional benchmarks presented in section 2.5.2. We chose a maximum upwind threshold of f_w =1500 Pa/m. This value ensures that numerical oscillations are very short lived and do not affect the NR-convergence. Lowering the upwind weighting results in a faster propagation of the thermal front towards the top, leading to temperature differences between 30 °C and -10 °C after 1000 years and a slightly different shape of the rising plume in the medium heat flux simulation (Fig. 2.9).

The high heat flux simulation, being more advection dominated, is more sensitive to the chosen upwind weighting. In Figure 2.10 the lowered upwind weighting leads to the formation of two adjacent plumes after 500 years and to higher temperatures at the bottom after 1000 year. When advection becomes stronger the low upwind weighting leads to more focused upward flow, which results in significant local temperature changes of ~80 °C at the top thermal front.

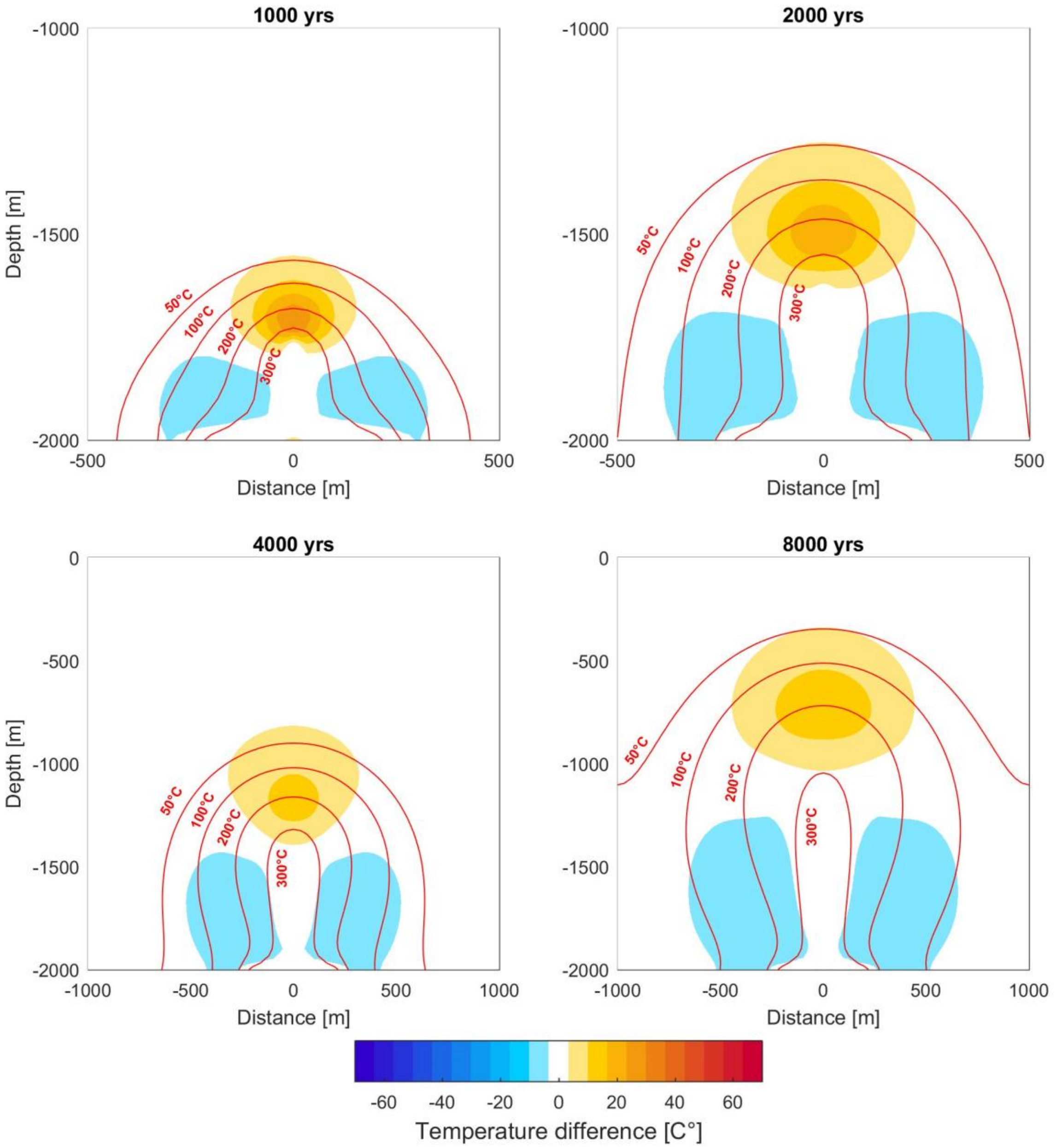

Figure 2.9: Temperature difference plot (less upwind (f_w = 1500 Pa/m) minus full upwind) for the 8 W/m² bottom heat flux test case (cf. Fig. 2.7). Temperature isotherms are plotted for full upwind case

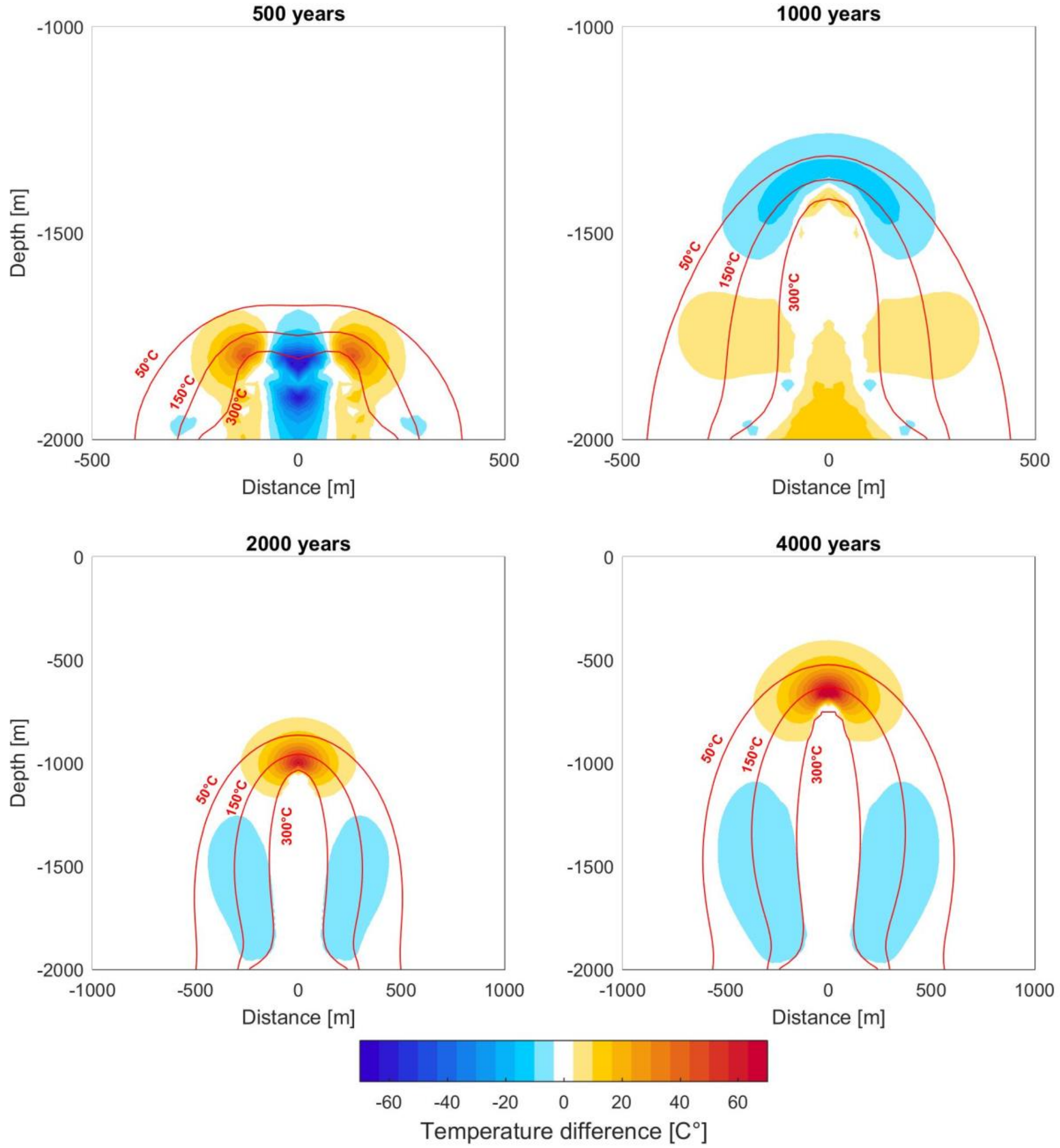

Figure 2.10: Temperature difference plot (less upwind (f_w = 1500 Pa/m) minus full upwind) for 15 W/m² basal heat flux. Temperature isotherms are plotted for full upwind case

2.6.2 Time-differencing and time step size limits

In our model we use two different time step criteria. These are the maximum allowed relative changes in specific enthalpy $\Delta h/h$ and density $\Delta\rho/\rho$ per time step. In Figure 2.11 we show the results of fluid advection for variable $\Delta h/h$ in combination with the backward in time differencing (θ = 1) and Crank-Nicholson method (θ = 0.5) using test case 1. For θ = 1 increasing time steps lead to higher numerical diffusion. For θ = 0.5 very little numerical diffusion is introduced when the time step size is increased. However, there is an upper physical limit ($\Delta h/h > 0.10$) above which nodes experience too high energy changes per time step leading to an overshooting near the thermal front.

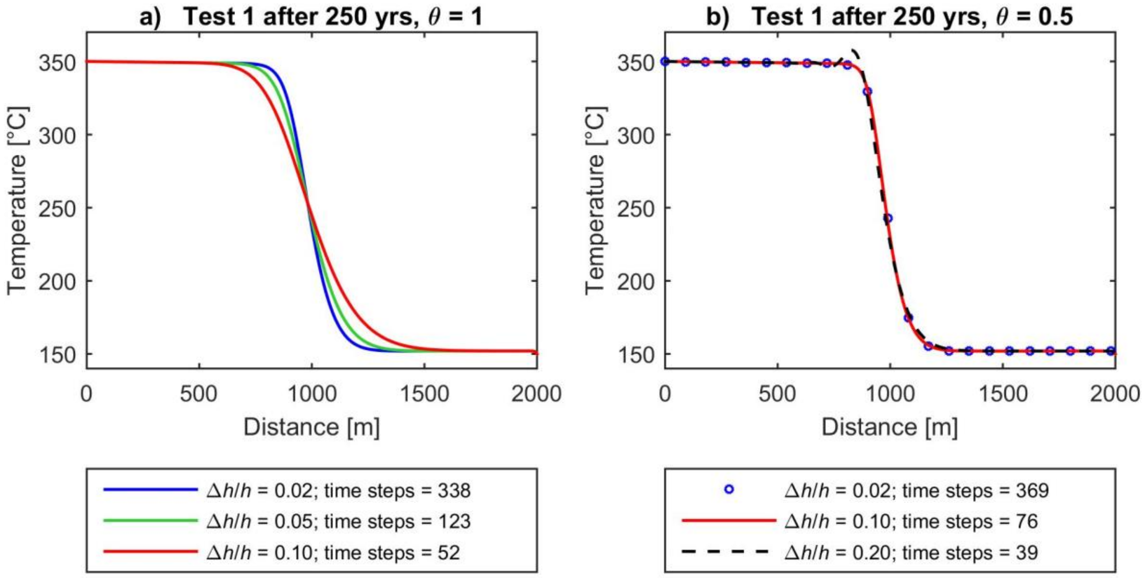

Figure 2.11: **a)** Results of test 1 (see section 2.5.1 and Table 2.3) for $\theta = 1$ and for different time step criteria $\Delta h/h$. **b)** Results of test 1 for $\theta = 0.5$ for different time step criteria $\Delta h/h$.

The behavior of the different time-differencing methods changes under two-phase conditions. Figure 2.12a shows that during boiling and condensation, fluid properties and not numerical diffusion control the shape of the thermal front. The time step size has only a minor impact on the results but an upper limit is reached when oscillations occur and the convergence behavior deteriorates. The time step size could be further increased by adding more upwind weighting to reduce such oscillations. It should be noted here that the usage of the density time-stepping criterion $\Delta\rho/\rho$ is preferable to the enthalpy criterion $\Delta h/h$ under two-phase conditions because it is more sensitive to the large density changes during boiling and condensation.

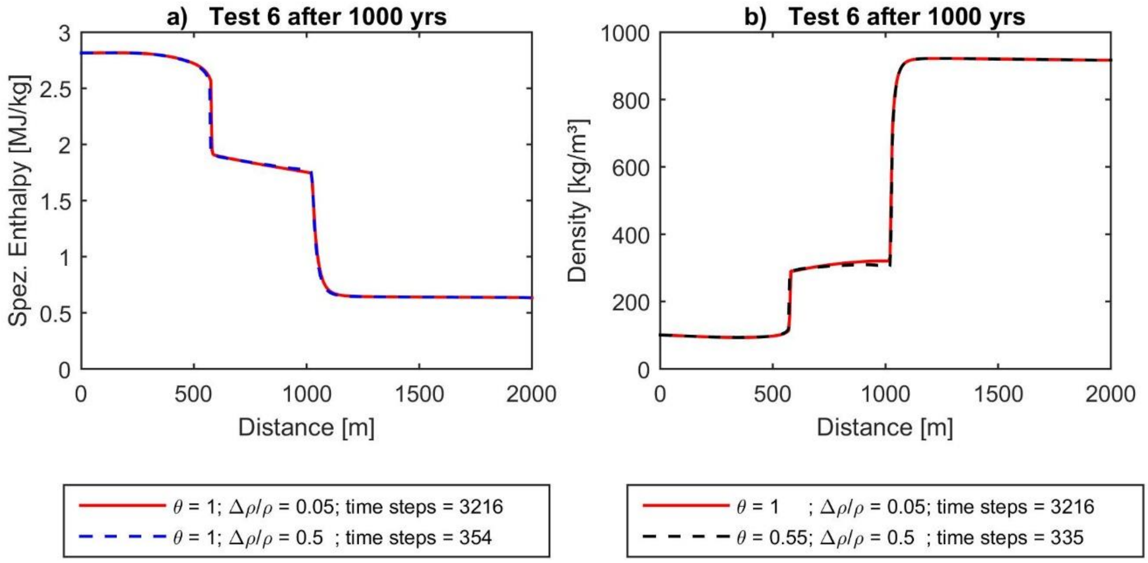

Figure 2.12: **a)** Results of test 6 (see section 2.5.1 and Table 2.3) for different time step criteria $\Delta\rho/\rho$. Shown is the mean specific enthalpy along the 1-D profile. **b)** Results of test 6 comparing $\theta = 1$ & $\Delta\rho/\rho = 0.05$ against $\theta = 0.55$ & $\Delta\rho/\rho = 0.5$. Shown is density along the 1-D profile.

2.6.3 2-D accuracy and efficiency tests of the θ time-differencing method

We have further investigated the benefits of using the θ-time-differencing scheme using the high heat flux 2-D convection simulations presented in section 2.5.2 as an example. A way to measure efficiency of the θ-method is the total number of NR-iterations until a certain simulation time has been reached. For the NR convergence criterion we have used a residual tolerance of 0.005 m^{-2} yr^{-1}, which leads to an error smaller than ±10 °C at the thermal front, and use a medium upwind threshold of f_w = 500 Pa/m. The time step size is controlled by the maximum allowed fluid density change $\Delta\rho/\rho$ per time step, and time steps are allowed to increase by no more than 10% from one time step to the next. Figure 2.13a shows the total number of NR-iterations for $\theta = 1$, $\theta = 4/5$ and $\theta = 2/3$ as a function of the mean time step size during the calculation, which in turn is controlled by the different constraints on the maximum density change over a time step. In panel b) the average number of NR-iterations per time step is plotted. For each value of θ, we find a certain range of $\Delta\rho/\rho$ values that result in both stable computations and good convergence of the NR-iterations (Fig. 2.13a). Below a certain threshold of $\Delta\rho/\rho$, time step sizes become very small and oscillations can occur at sharp fronts, which can only be damped by increasing the mesh resolution. Above a certain threshold of $\Delta\rho/\rho$, the number of NR-iterations per time step and the number of failed attempts increases sharply. For $\theta = 1$, the stable range starts at $\Delta\rho/\rho = 0.04$ and extends to 0.5, with the number of failed attempts steadily increasing with the maximum allowed density change per time step as shown be the offset between the solid and dashed lines. Lowering the value of θ results in a smaller zone of numerical stability but the total number of required NR-iterations has decreased and thereby the total computational effort. There is, however, a limit to how large the explicit component can be: no numerically stable range was found for $\theta \leq 0.55$. Overall, the Galerkin method showed the best performance by allowing for the largest time steps and lowest total number of NR-iterations to complete the simulation.

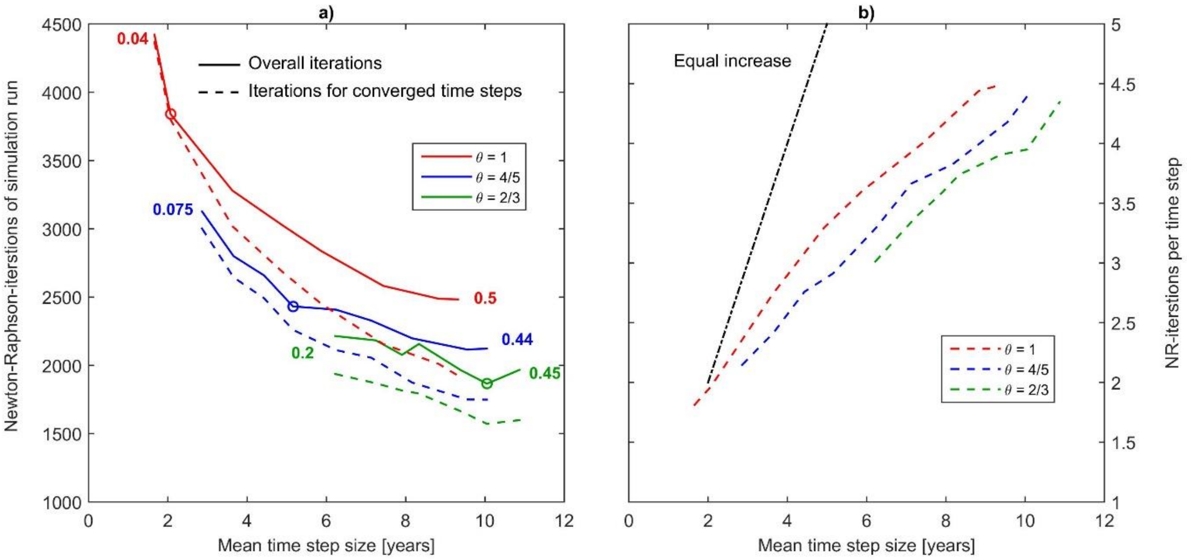

Figure 2.13: **a)** Plot of NR-iterations per simulation vs. mean time step size for $\theta = 1$, $\theta = 4/5$ and $\theta = 2/3$. Numbers show the time step limiting criterion Δρ/ρ and circles mark the simulation runs shown in Figure 2.14 and 2.15. **b)** Plot of NR-iterations per time step vs. mean time step size for $\theta = 1$, $\theta = 4/5$ and $\theta = 2/3$. The black dashed line shows for comparison an equal increase of NR-iterations per time step with time step size.

The average number of NR-iterations per time naturally also depends on the convergence criterion and thus on the allowed error in the coupled solution of pressure and mean specific enthalpy. We have tested this systematically for the Galerkin method and found that reducing the convergence criterion by a factor of five also reduces the temperature error by the same factor (±2 °C at the thermal front) but leads to approximately a doubling of the required NR-iterations.

In order to evaluate to which degree of accuracy is preserved in simulations using large time steps, we have compared the results of two end-member simulations ($\theta = 1$ & $\Delta\rho/\rho = 0.05$ vs. $\theta = 2/3$ & $\Delta\rho/\rho = 0.4$; see red and green circles in Fig. 2.13a). The $\theta = 2/3$ calculation uses an approximately 5-times larger time step than the $\theta = 1$ run (Fig. 2.13). Figure 14 shows that the differences in temperature are lower than ±7 °C. Hence, the loss in accuracy when using large time-steps with $\theta = 2/3$ is smaller than the error introduced by upwind weighting (cf. Fig. 2.10).

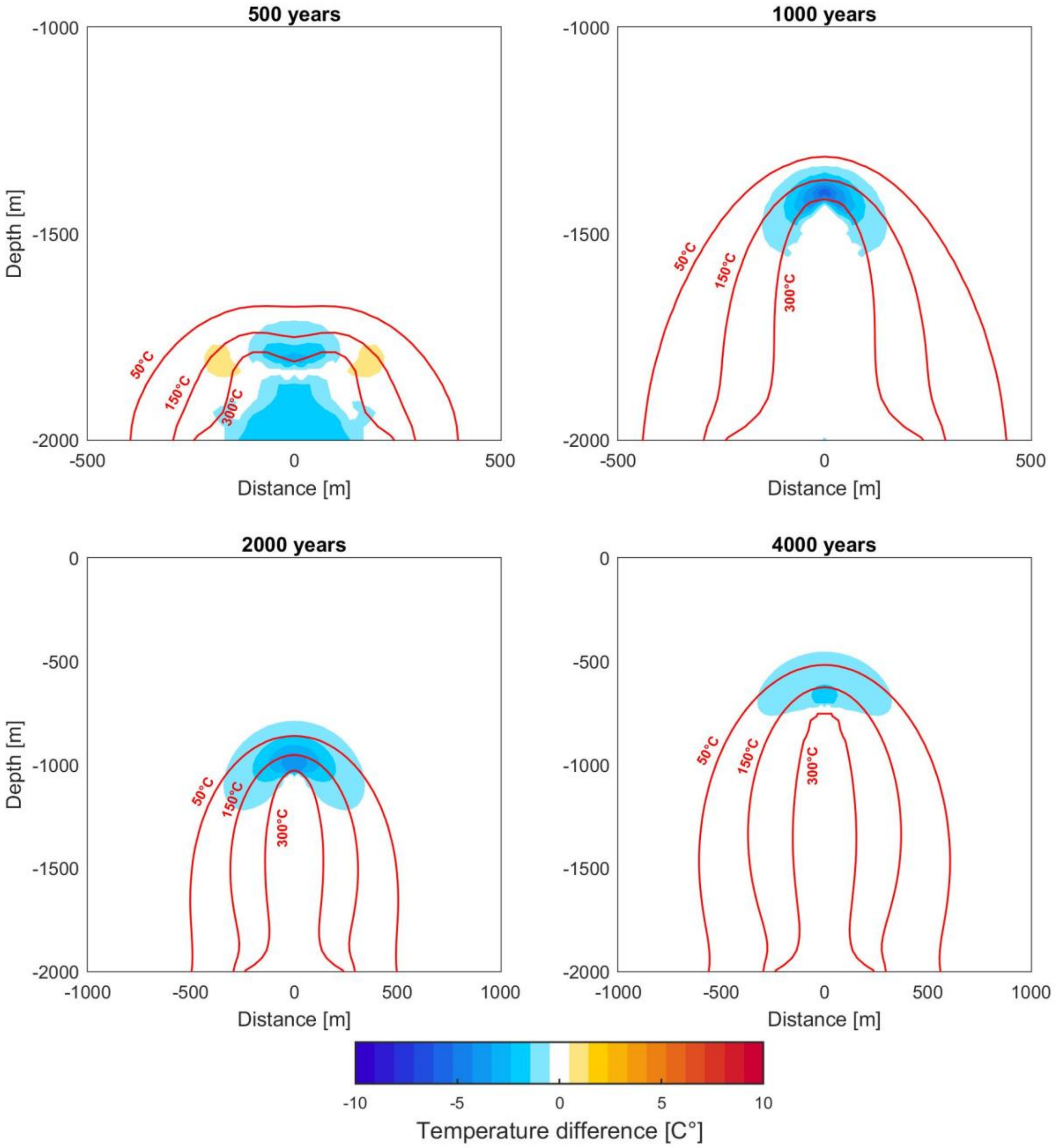

Figure 2.14: Temperature difference plot of a 'small time step'-setup ($\theta = 1$ & $\Delta\rho/\rho = 0.05$) minus a 'large time step'-setup ($\theta = 2/3$ & $\Delta\rho/\rho = 0.4$) for a convergence criterion of 0.001 $\mathrm{m}^{-2}\ \mathrm{yr}^{-1}$ and $f_\mathrm{w} = 500$ Pa/m

The possible increase in time step size in coupled simulations with respect to sequential schemes is visualized in Figure 2.15, which shows the distribution of time step sizes of simulation runs marked by circles in Figure 2.13a. For comparison we have calculated the Courant-Friedrichs-Lewy (CFL) criterion, which is used as an stability criterion in the decoupled numerical schemes in FISHES (Lewis and Lowell, 2009) and CSMP++ (Coumou et al., 2008; Weis et al., 2014). The CFL criterion is defined as

$$dt_{\mathrm{CFL}} \le \min\left|\frac{\Phi\ dx}{(\vec{\mathbf{v}}_\mathrm{l} + \vec{\mathbf{v}}_\mathrm{v} + \vec{\mathbf{v}}_\mathrm{s})\cdot\vec{\mathbf{n}}}\right| \tag{2.44}$$

where *dx* is the distance between the two nodes corresponding to the facet and $\vec{\mathbf{n}}$ is the normal vector of the facet. We have also calculated a second time step criterion ensuring that the mass flux of each phase out of a CV is less than the mass of that phase within the CV:

$$dt_{\text{out}} \le \min \frac{\Phi \; S_{\text{f}} \rho_{\text{f}} \Omega_i}{\left[\sum_{k=1}^{N} \int_{F_{ik}} \rho_{\text{f}} \vec{\mathbf{v}}_{\text{f}} \cdot \vec{\mathbf{n}}_{ik} \mathrm{d}r \right]_{\text{outflow}}} \tag{2.45}$$

This criterion was introduced by Weis et al. (2014) to avoid oscillations in the highly compressible two-phase region and is a physically meaningful extension of the CFL criterion to variable density flow.

During the first 1000 years the maximum allowed density change criterion in the coupled scheme leads to small time steps, because the high density gradients lead to rapid density changes at the bottom nodes. Afterwards, upon formation of a stable two-phase zone, the density gradients become smaller and the time step size increases to more than hundred times the CFL criterion for the most efficient parameter choice (green curve).

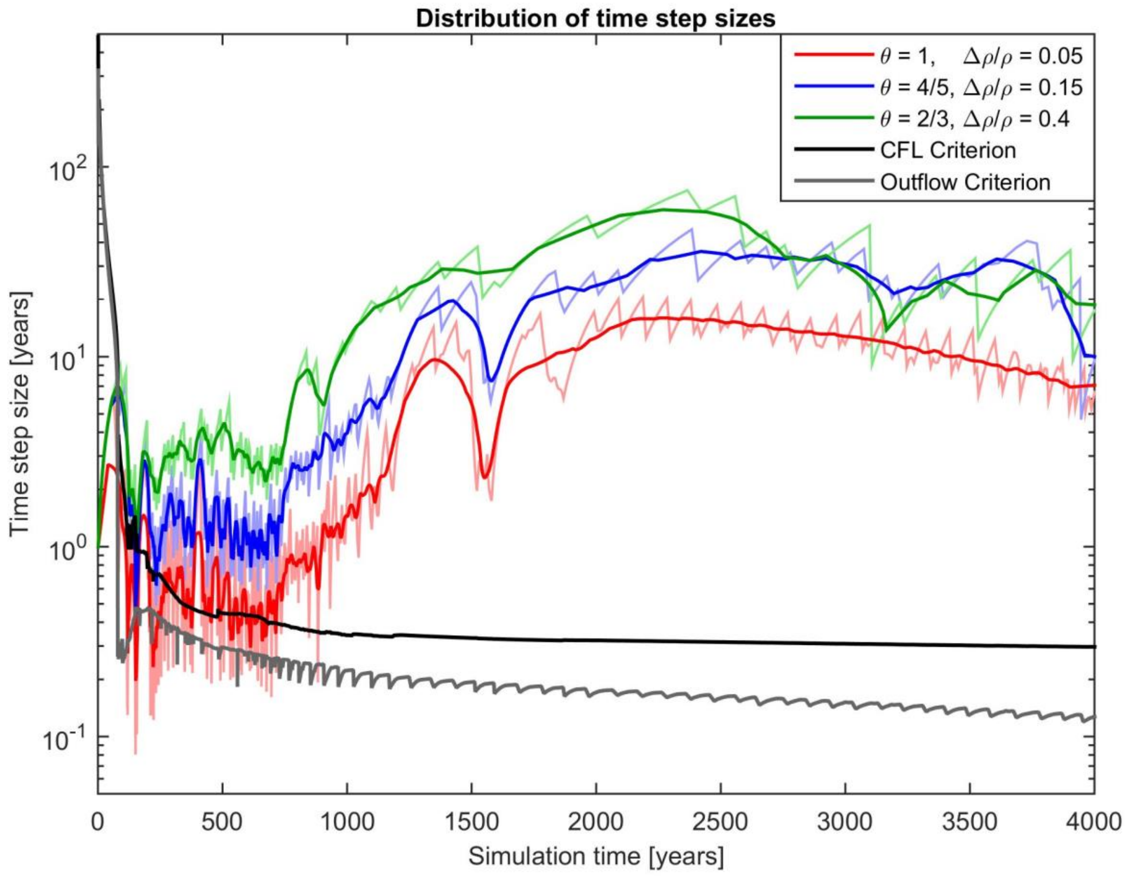

Figure 2.15: Plot of time step size vs. simulation time for three selected simulations marked by circles in Figure 2.13. Light colors show every single time step size, while bold colors show a moving-average time step size (30 steps average for red and 10 steps average for green and blue). CFL criterion and maximum mass change per control volume (Eq. 2.44) criterion are calculated during the simulation shown in red.

2.7 Discussion

We have investigated the behavior of a novel coupled CV-based scheme for simulating multi-phase pure water convection under sub- and supercritical conditions. The various 1-D tests show a perfect agreement with HYDROTHERM. In the 2-D free convection tests HYDROTHERM predicts a somewhat faster and more focused upward propagation of the hot thermal front. Here, grid orientation and resolution play an important role in the numerical solution of hydrothermal flow problems (Weis et al., 2014). In HYDROTHERM the grid points do not have a direct diagonal connectivity and mass and energy fluxes are evaluated by finite differences only between neighboring points in the horizontal and vertical directions. This may result in the more copped propagation of the thermal front (Fig. 2.7). The here used FV-technique on unstructured meshes does have a good diagonal connectivity between grid points and their corresponding control volumes. This leads to a somewhat flatter thermal front with a broader two-phase region. It thus seems that unstructured meshes are not only useful to resolve complex geometries but also to avoid mesh-introduced preferred directions of mass and energy transport in the numerical solution.

The details of the used upwind weighting are another important factor that can result in a certain model-dependence of a numerical solution. Upwinding is clearly required in both sequential and coupled schemes but the degree of upwinding affects the results. The results shown in Figure 2.9 & 2.10 illustrate the impact of a reduced upwind weighting on the self-organization of plume formation. Using full upwind weighting maximizes the stabilizing effect but results in severe numerical dispersion. A balance has therefore to be struck between stability and accuracy. We have implemented an algorithm that for each finite volume calculates an upwind weighting factor as a function of fluid driving forces on the volume’s facets. This method is similar to that implemented in HYDROTHERM and represents a practical way of minimizing the upwind weighting yet preserving stability. It takes advantage of the finding that upwind weighting is often only necessary in the two-phase flow regions.

In coupled schemes, like the one presented here, the numerical efficiency depends on the relationship between the number of NR-iterations per time step and the time step size. A good measure for this is the total number of iterations needed per simulation run (Fig. 2.13a). Tests with the implemented θ-time-differencing method show that the most efficient combination of time step size and required NR-iterations is obtained with the Galerkin method ($\theta = 2/3$). With this combination we obtained the highest speedup (the lowest number of total iterations), while the fully implicit time-differencing method ($\theta = 1$) gave the lowest speedup with respect to the CFL criterion. Accuracy in large time step simulations is also higher when using the Galerkin method.

Intrinsic to the NR-scheme is a linear approximation technique, yet the variations of the residua with the iteratively updated values of pressure and specific enthalpy at new time level $t+\Delta t$ are highly non-linear. For example, the derivatives of the mass and energy transport terms (see Eqs. 2.22 and 2.23) can change sign in-between iterations when boiling occurs (Huyakorn and Pinder, 1978) and these derivatives within the Jacobi matrix (Eq. 2.29) can then lead to poor convergence of NR-scheme. The Galerkin time-differencing method can help to mitigate this effect. By lowering θ from 1 to 2/3 the dependence of the transport terms and also of the residua R_i and G_i on pressure and specific enthalpy at time level $t+\Delta t$ is reduced (see Eqs. 2.22-2.23). The consequence is that the derivatives of the transport terms (see Appendix, section 2.9, Eqs. 2.63-2.66) have a smaller weighting and are less dominant in the Jacobi matrix leading to a reduced number of NR-iterations. However, a higher explicit part of the transport terms comes at the cost of reduced stability and even short-lived oscillations can cause massive computational efficiency losses. We found a value of θ = 2/3 to be best suited for most two-phase simulations and that a reduction below θ = 0.55 causes too severe stability problems to be useful.

Increasing the time step size generally leads to more NR-iterations per time step, especially under two-phase flow conditions. This mainly results from a reduced quality of the initial guess for the subsequent time step, which can be relatively poor when several nodes experience a phase change that did not occur in the previous time step. This raises the question whether coupled schemes really offer a better overall performance with respect to sequential schemes if larger time steps come at the cost of more NR-iterations (e.g. Geiger et al., 2006). Figure 2.13b shows that for the discussed types of problems the speedup resulting from larger time steps clearly dominates over the costs of more iterations. There is, however, an upper limit to this when the non-linearity in the basic equations too often results in a divergence rather than convergence of the residua. In this case, the time step has to be repeated with a smaller step size and/or modified initial guess. The terminations of the lines shown in Figure 2.13a at high time step sizes mark this limit. Increasing the time step beyond this limit leads to a rapid increase in the required number of iterations or even no convergence at all. Again an explicit component in the time-differencing scheme helps to stabilize large time steps, and the largest time steps are possible with the Galerkin time-differencing scheme. It remains nevertheless challenging to develop automated time stepping algorithms that find the parameters that allow for an optimal balance between time step size and good convergence behavior of the NR-iterations.

The above considerations need to be kept in mind when evaluating the efficiency of the two main solution techniques for modeling hydrothermal systems, the sequential (decoupled) and coupled approach. Although “objective” benchmarking of the different schemes is not feasible due to the many differences between different codes, some insights can be gained by comparing the numerical effort for each time step. In the here described 2-D coupled approach one single matrix equation of type **A**x=b, where **A** is a sparse, asymmetrical, square matrix of size [2•*n* x 2•*n*], with *n* being the number of mesh nodes, has to be solved during each NR-iteration. The decoupled/sequential approach has to solve two matrix equations for calculating the pressure and temperature fields, and has to perform two explicit advection steps for mass and energy. If a standard finite element method is used, the matrices in these two equations are sparse, symmetric, and only of size [*n* x *n*]. The advection steps are in comparison computationally cheap. In the best case, no iterations are required in sequential schemes but in practice some iterations are required to ensure the CFL criterion or additional constraints (e.g. Eq. 2.44) for stability reasons (Lewis and Lowell, 2009; Weis et al., 2014). If the time step size exceeds the CFL criterion, which is only known after solving for the new pressure field, the time step size needs to be adjusted and the computation of the respective time step must be repeated. In the best case, the minimum number of solving these two matrices is therefore the number of time steps. Doing a comparison for the high heat flux set up in section 2.5.2 we estimate from the CFL criterion (Fig. 2.15), which is on average 0.5 years, a minimum number of ~8000 time steps for the decoupled approach. For the same simulation time only about 2000 NR-iterations are required using our coupled method. The real time step size and error of the decoupled scheme are not accessible to us but the findings nevertheless provide a strong hint that the coupled method leads to significantly fewer NR-iterations than number of CFL-time steps. This, under the simplifying assumption that the computational cost of one time step in the decoupled scheme is approximately equal to one NR-iteration in the coupled scheme, implies a significant overall performance increase.

2.8 Conclusion

We have presented a numerical solution scheme for simulating magmatic hydrothermal systems that is based on a control-volume technique for solving simultaneously for mass and energy conservation using Newton-Raphson-iterations on unstructured meshes. A variable upwind weighting scheme for specific enthalpy and relative permeability is used to suppress oscillations along with the so-called theta-time-differencing scheme for higher accuracy and efficiency. It thereby integrates methods and ideas that proved to work well in sequential models into a fully coupled approach. This allows for stable and accurate hydrothermal flow solutions at large time steps, which results in a significant reduction of the computational effort with respect to previously proposed sequential schemes. The novel numerical scheme is presented for the simplified case of 2-D pure water convection but is, in principle, extendable to 3-D and to the system H_2O−NaCl. The obtained speedup in comparison to sequential/decoupled schemes is likely to make 3-D simulations more tractable, and the insights gained on how to handle the non-linearity of the basic equations will help dealing with the additional complexities of saltwater convection.

Further work needs to be invested into the analysis of how models can be made more realistic in terms of chemical reactions and the coupling to deformation (Ingebritsen et al., 2010). In coupled simulations of hydrothermal flow and tectonic deformation, the increase in model integration time to hundred-thousand years and more (Theissen-Krah et al., 2016) may render explicit advection steps intractable and may actually require a coupled approach. Likewise, the structured finite difference grids used in some hydrothermal flow models may be incompatible with the use of Lagrangian meshes that follow solid deformation (McCartin, 1998) thereby making the mechanical coupling more challenging. We have presented here a coupled modeling approach facilitating the use of large time steps on unstructured meshes that we hope will prove useful for the future development of realistic multiphase 3-D hydrothermal convection models.

2.9 Appendix

This appendix contains additional information on the numerical method presented in the main text. In section 2.9.1 we show how different boundary conditions can be implemented including a free venting boundary condition for submarine studies. Section 2.9.2 provides further details on some special cases for upwind weighting of mean specific enthalpy and relative permeability at phase boundaries. In section 2.9.3 we show in detail the calculation of the Jacobi matrix used in the Newton-Raphson-iteration scheme and in section 2.9.4 we derive local coordinates of triangular elements, which are used for the numerical evaluation of surface integrals.

2.9.1 Boundary conditions

Fixed pressure, specific enthalpy and temperature boundary condition:

Constant pressure boundary conditions are achieved by maintaining the selected pressure values during the calculation of the adjacent residuals R_i and G_i constant. The rows that comprise the residuum R_b, are removed from the linear system of equations. Also the columns of the matrix that comprise the derivatives of R_i and G_i with respect to p_b are removed. This establishes a mass flow through the boundary control volume and allows for free venting.

Constant enthalpy boundary conditions are implemented the same way. The selected boundary enthalpy values are integrated in the calculations of the adjacent residuals R_i and G_i. The rows that comprise the residuum G_b are removed from linear system of equations. Here also the columns of the matrix that comprise the derivatives of R_i and G_i with respect to h_b are removed. This establishes a conductive heat flow into the boundary control volume that is controlled by enthalpy gradient at the facets of boundary control volume.

Choosing pressure and enthalpy boundary condition for p_1, p_n, h_1, h_n, leads to following system:

$$\begin{pmatrix} \frac{\partial R_2}{\partial p_2} & \cdots & \frac{\partial R_2}{\partial p_{n-1}} & \frac{\partial R_2}{\partial h_2} & \cdots & \frac{\partial R_2}{\partial h_{n-1}} \\ \vdots & \ddots & \vdots & \vdots & \ddots & \vdots \\ \frac{\partial R_{n-1}}{\partial p_2} & \cdots & \frac{\partial R_{n-1}}{\partial p_{n-1}} & \frac{\partial R_{n-1}}{\partial h_2} & \cdots & \frac{\partial R_{n-1}}{\partial h_{n-1}} \\ \frac{\partial G_2}{\partial p_2} & \cdots & \frac{\partial G_2}{\partial p_{n-1}} & \frac{\partial G_2}{\partial h_{1-1}} & \cdots & \frac{\partial G_2}{\partial h_{n-1}} \\ \vdots & \ddots & \vdots & \vdots & \ddots & \vdots \\ \frac{\partial G_{n-1}}{\partial p_2} & \cdots & \frac{\partial G_{n-1}}{\partial p_{n-1}} & \frac{\partial G_{n-1}}{\partial h_2} & \cdots & \frac{\partial G_{n-1}}{\partial h_{n-1}} \end{pmatrix} \begin{pmatrix} p_2^{l+1} - p_2^l \\ \vdots \\ p_{n-1}^{l+1} - p_{n-1}^l \\ h_2^{l+1} - h_2^l \\ \vdots \\ h_{n-1}^{l+1} - h_{n-1}^l \end{pmatrix} = \begin{pmatrix} -R_2^l \\ \vdots \\ -R_{n-1}^l \\ -G_2^l \\ \vdots \\ -G_{n-1}^l \end{pmatrix}. \tag{2.46}$$

When choosing a temperature boundary condition for a boundary node, a corresponding specific enthalpy has to be computed before each time step. The specific enthalpy is calculated from the last pressure value and the chosen temperature using the equation-of-state. During the Newton-Raphson-iterations this specific enthalpy is held constant.

Flux boundary condition and fluid source:

Constant and variable heat and mass flux boundary conditions have also been implemented. Flux into a control volume i over a time step will be computed and is added as a source term to the respective residuum R_i or G_i.

A fluid source defined with mass source rate Q_m and with a specific enthalpy $h_\mathrm{m,source}$ can be treated. Energy source rate $Q_\mathrm{m,source}$ is than defined as:

$$Q_\mathrm{E,source} = Q_\mathrm{m} h_\mathrm{m,source} \tag{2.47}$$

A fluid source can be added to one control volume or divided over a greater area to more control volumes. As source terms are independent of pressure and specific enthalpy they drop out in the derivatives of R_i and G_i

Seafloor boundary condition:

Hydrothermal simulations should compute precisely the mass and energy flux through the seafloor. To achieve this objective a boundary condition has to be chosen that leads to an inflow into the crust with cold seawater and to an outflow into the ocean with ascending temperature of the upwelling fluid. For this purpose, a pressure boundary condition is set on all top boundary nodes. Bevor each time step, we calculate and sum the flow $q^{t}_{\mathrm{m},i}$ of a boundary control volume (Fig. 2.16) into the adjacent control volumes (the flow from the control volume out of the modeling domain is not calculated). If it is positive (the flow into adjacent control volumes is positive), the boundary node gets for the next time step a temperature boundary condition using water temperature of the sea floor. If it is negative, we calculate for this control volume an implicit heat flux boundary condition Q_i, which is updated during Newton-Raphson-iterations:

$$q_{\mathrm{m},i}^{t+\Delta t} = \int_{\partial\Omega_i} \left(\theta \left(\sum_{\mathrm{f}\in\{\mathrm{l,v,s}\}} \rho_{\mathrm{f}} \vec{\mathbf{v}}_{\mathrm{f}} \right)^{t+\Delta t} \right) \cdot \vec{\mathbf{n}}_i \mathrm{d}r \tag{2.48}$$

$$Q_i = -h_i^{t+\Delta t} q_{\mathrm{m},i}^{t+\Delta t} \tag{2.49}$$

$h_i^{t+\Delta t}$ is the mean specific enthalpy at node i. Q_i is added as source term to the respective residuum G_i. If there is a two-phase flow (vapor and liquid) into the boundary control volume, we calculate a specific enthalpy $h_{\mathrm{m},i}$, which we use as boundary condition:

$$h_{\mathrm{m},i} = \frac{\left(c\left(q_{\mathrm{m,l}}^{t+\Delta t} + q_{\mathrm{m,l}}^{t} \right) h_{l,i} + \left(q_{\mathrm{m,v}}^{t+\Delta t} + q_{\mathrm{m,v}}^{t} \right) h_{\mathrm{v},i} \right)}{\left(c\left(q_{\mathrm{m,l}}^{t+\Delta t} + q_{\mathrm{m,l}}^{t} \right) + \left(q_{\mathrm{m,v}}^{t+\Delta t} + q_{\mathrm{m,v}}^{t} \right) \right)} \tag{2.50}$$

where c is a factor that should be between 1 and 100 and depends on top pressure condition. $h_{\mathrm{l},i}$ is the specific enthalpy of the liquid phase and $h_{\mathrm{v},i}$ is the specific enthalpy of the vapor phase at the chosen boundary pressure condition in the two-phase region. This switch is necessary for a fast convergence of Newton-Raphson-iterations.

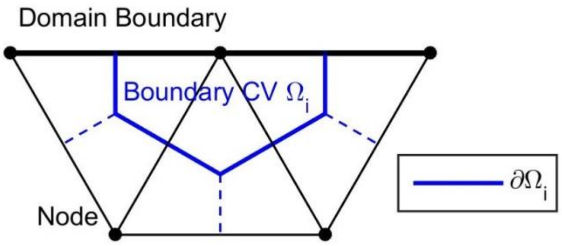

Figure 2.16: Boundary control volume

2.9.2 Special cases for upwind weighting of mean specific enthalpy and relative permeability

To calculate the weighted relative permeability and specific enthalpy of the liquid phase, we have to treat the following cases for each phase:

Liquid phase:

$$h_\mathrm{l} = h_\mathrm{l,up} \text{ and } k_{r\mathrm{l}} = k_{r\mathrm{l,up}} \quad \text{if} \quad h_\mathrm{l,up} > 0 \text{ and } h_\mathrm{l,cf} = 0 \text{ and } h_\mathrm{s,cf} = 0 \tag{2.51}$$

$$h_\mathrm{l} = h_\mathrm{l,cf} \text{ and } k_{r\mathrm{l}} = k_{r\mathrm{l,cf}} \quad \text{if} \quad h_\mathrm{l,cf} > 0 \text{ and } h_\mathrm{l,up} = 0 \text{ and } h_\mathrm{s,up} = 0 \tag{2.52}$$

$$h_\mathrm{l} = w_\mathrm{l} h_\mathrm{s,up} + \left(1 - w_\mathrm{l}\right) h_\mathrm{l,cf} \text{ and } k_{r\mathrm{l}} = k_{r\mathrm{l,cf}} \quad \text{if} \quad h_\mathrm{s,up} > 0 \text{ and } h_\mathrm{l,cf} > 0 \tag{2.53}$$

$$h_\mathrm{l} = w_\mathrm{l} h_\mathrm{l,up} + \left(1 - w_\mathrm{l}\right) h_\mathrm{s,cf} \text{ and } k_{r\mathrm{l}} = k_{r\mathrm{l,up}} \quad \text{if} \quad h_\mathrm{l,up} > 0 \text{ and } h_\mathrm{s,cf} > 0 \tag{2.54}$$

Vapor phase:

$$h_\mathrm{v} = h_\mathrm{v,up} \text{ and } k_{r\mathrm{v}} = k_{r\mathrm{v,up}} \quad \text{if} \quad h_\mathrm{v,up} > 0 \text{ and } h_\mathrm{v,cf} = 0 \text{ and } h_\mathrm{s,cf} = 0 \tag{2.55}$$

$$h_\mathrm{v} = h_\mathrm{v,cf} \text{ and } k_{r\mathrm{v}} = k_{r\mathrm{v,cf}} \quad \text{if} \quad h_\mathrm{v,cf} > 0 \text{ and } h_\mathrm{v,up} = 0 \text{ and } h_\mathrm{s,up} = 0 \tag{2.56}$$

$$h_\mathrm{v} = w_\mathrm{v} h_\mathrm{s,up} + \left(1 - w_\mathrm{v}\right) h_\mathrm{v,cf} \text{ and } k_{r\mathrm{v}} = k_{r\mathrm{v,cf}} \quad \text{if} \quad h_\mathrm{s,up} > 0 \text{ and } h_\mathrm{v,cf} > 0 \tag{2.57}$$

$$h_\mathrm{v} = w_\mathrm{v} h_\mathrm{v,up} + \left(1 - w_\mathrm{v}\right) h_\mathrm{s,cf} \text{ and } k_{r\mathrm{v}} = k_{r\mathrm{v,up}} \quad \text{if} \quad h_\mathrm{v,up} > 0 \text{ and } h_\mathrm{s,cf} > 0 \tag{2.58}$$

Artificial high-pressure fluid:

$$h_\mathrm{s} = 0 \text{ and } k_{r\mathrm{s}} = 0 \quad \text{if} \quad h_\mathrm{s,up} > 0 \text{ and } h_\mathrm{s,cf} = 0 \tag{2.59}$$

$$h_\mathrm{s} = 0 \text{ and } k_{r\mathrm{s}} = 0 \quad \text{if} \quad h_\mathrm{s,up} = 0 \text{ and } h_\mathrm{s,cf} > 0 \tag{2.60}$$

If the artificial high-pressure fluid s exists at a facet midpoint and a vapor or liquid phase exist at an upwind node, we calculate the f and w for each phases liquid or vapor with $f_\mathrm{s,cf}$ (see Eqs. 2.53 and 2.56), because the high-pressure fluid s can potentially convert into both phases at the critical point.

If the high-pressure fluid is not present and if liquid or vapor phase only exist at a potential upwind node, $f_\mathrm{l,v}$ is calculated with $\rho_\mathrm{l,up}$ and $\rho_\mathrm{v,up}$, respectively. After f is calculated, the potential upwind node is then either confirmed or not. If not, the phase will not be considered. Otherwise Eqs. (2.51) and (2.55) apply.

2.9.3 Calculation of residua and their derivatives

Numerical integration of the mass flux and the energy flux over facets are calculated with one sampling point at the facet center. We define local coordinates as:

$$cf_1 = \left(\frac{5}{12}, \frac{5}{12}, \frac{1}{6}\right),\ cf_2 = \left(\frac{1}{6}, \frac{5}{12}, \frac{5}{12}\right),\ cf_3 = \left(\frac{5}{12}, \frac{1}{6}, \frac{5}{12}\right) \tag{2.61}$$

Numerical integration of volume integrals are calculated with one sampling point at each kite barycenter *ce*. We define local coordinates as:

$$ce_1 = \left(\frac{22}{36}, \frac{7}{36}, \frac{7}{36}\right),\ ce_2 = \left(\frac{7}{36}, \frac{22}{36}, \frac{7}{36}\right),\ ce_3 = \left(\frac{7}{36}, \frac{7}{36}, \frac{22}{36}\right) \tag{2.62}$$

To calculate derivatives of residua to nodal pressure p_j and mean specific enthalpy h_j at time level $t+\Delta t$, we have to consider actual values at time level $t+\Delta t$ and obtain:

$$\frac{\partial R_i}{\partial p_j} = -\theta \sum_{k=1}^{N} \int_{F_{ik}} \sum_{\mathrm{f}\in\{\mathrm{l,v,s}\}} \left(\frac{\partial\left(\rho_f \vec{\mathbf{v}}_f\right)}{\partial p_j} \right)^{t+\Delta t} \cdot \vec{\mathbf{n}}_{ik} \mathrm{d}r - \sum_{l=1}^{N/2} \int_{\Omega_{il}} \left(\frac{\Phi}{\Delta t} \frac{\partial \rho_\mathrm{m}}{\partial p_j} \right)^{t+\Delta t} \mathrm{d}\Omega \tag{2.63}$$

$$\frac{\partial R_i}{\partial h_j} = -\theta \sum_{k=1}^{N} \int_{F_{ik}} \sum_{\mathrm{f}\in\{\mathrm{l,v,s}\}} \left(\frac{\partial\left(\rho_\mathrm{f} \vec{\mathbf{v}}_\mathrm{f}\right)}{\partial h_j} \right)^{t+\Delta t} \cdot \vec{\mathbf{n}}_{ik} \mathrm{d}r - \sum_{l=1}^{N/2} \int_{\Omega_{il}} \left(\frac{\Phi}{\Delta t} \frac{\partial \rho_\mathrm{m}}{\partial h_j} \right)^{t+\Delta t} \mathrm{d}\Omega \tag{2.64}$$

$$\frac{\partial G_i}{\partial p_j} = \theta \sum_{k=1}^{N} \int_{F_{ik}} \left(K \frac{\partial\left(\nabla T\right)}{\partial p_j} - \sum_{\mathrm{f}\in\{\mathrm{l,v,s}\}} \frac{\partial\left(h_\mathrm{f} \rho_\mathrm{f} \vec{\mathbf{v}}_\mathrm{f}\right)}{\partial p_j} \right)^{t+\Delta t} \cdot \vec{\mathbf{n}}_{ik} \mathrm{d}r - \sum_{l=1}^{N/2} \int_{\Omega_{il}} \frac{1}{\Delta t} \left(\frac{\partial E}{\partial p_j} \right)^{t+\Delta t} \mathrm{d}\Omega \tag{2.65}$$

$$\frac{\partial G_i}{\partial h_j} = \theta \sum_{k=1}^{N} \int_{F_{ik}} \left(K \frac{\partial\left(\nabla T\right)}{\partial h_j} - \sum_{\mathrm{f}\in\{\mathrm{l,v,s}\}} \frac{\partial\left(h_\mathrm{f} \rho_\mathrm{f} \vec{\mathbf{v}}_\mathrm{f}\right)}{\partial h_j} \right)^{t+\Delta t} \cdot \vec{\mathbf{n}}_{ik} \mathrm{d}r - \sum_{l=1}^{N/2} \int_{\Omega_{il}} \frac{1}{\Delta t} \left(\frac{\partial E}{\partial h_j} \right)^{t+\Delta t} \mathrm{d}\Omega \tag{2.66}$$

Note that we neglect in Eqs. (2.65) and (2.66) the derivatives of the viscous dissipation term and of the term that contains the part of the pressure-volume work that is not accounted for in the specific enthalpy (Eq. 2.6) as these are very small and do not influence the convergence behavior.

The values within volume integrals are calculated at kite barycenters via shape functions:

$$\rho_\mathrm{m}(ce) = \sum_{j=1}^{n} N_j(ce) \rho_{\mathrm{m},j} \tag{2.67}$$

$$E(ce) = \Phi \sum_{j=1}^{n} N_j(ce) \rho_{\mathrm{m},j} \sum_{j=1}^{n} N_j(ce) h_j + (1-\Phi) \rho_\mathrm{r} c_{p\mathrm{r}} \sum_{j=1}^{n} N_j(ce) T_j \tag{2.68}$$

We obtain these derivations of eqn. (2.68) and (2.69):

$$\frac{\partial \rho_\mathrm{m}}{\partial p_j}\left(ce\right) = N_j\left(ce\right) \frac{\partial \rho_{\mathrm{m},j}}{\partial p_j} \tag{2.69}$$

$$\frac{\partial \rho_\mathrm{m}}{\partial h_j}\left(ce\right) = N_j\left(ce\right) \frac{\partial \rho_{\mathrm{m},j}}{\partial h_j} \tag{2.70}$$

$$\frac{\partial E}{\partial p_j}\left(ce\right) = \Phi N_j(ce)\frac{\partial \rho_{\mathrm{m},j}}{\partial p_j}h(ce) + (1-\Phi)\rho_{\mathrm{r}}c_{p\mathrm{r}}N_j(ce)\frac{\partial T_j}{\partial p_j} \tag{2.71}$$

$$\frac{\partial E}{\partial h_j}(ce) = \Phi\left(N_j(ce)\frac{\partial \rho_{\mathrm{m},j}}{\partial h_j}h(ce) + \rho_{\mathrm{m}}N_j(ce)\right) + (1-\Phi)\rho_{\mathrm{r}}c_{p\mathrm{r}}N_j(ce)\frac{\partial T_j}{\partial h_j} \tag{2.72}$$

We obtain following derivatives of the mass and heat flux using product rule:

$$\frac{\partial\left(\rho_{\mathrm{f}}\vec{\mathbf{v}}_{\mathrm{f}}\right)}{\partial p_j} = +\frac{\partial \rho_{\mathrm{f}}}{\partial p_j}\vec{\mathbf{v}}_{\mathrm{f}} + \rho_{\mathrm{f}}\frac{\partial \vec{\mathbf{v}}_{\mathrm{f}}}{\partial p_j} \tag{2.73}$$

$$\frac{\partial\left(\rho_{\mathrm{f}}\vec{\mathbf{v}}_{\mathrm{f}}\right)}{\partial h_j} = +\frac{\partial \rho_{\mathrm{f}}}{\partial h_j}\vec{\mathbf{v}}_{\mathrm{f}} + \rho_{\mathrm{f}}\frac{\partial \vec{\mathbf{v}}_{\mathrm{f}}}{\partial h_j} \tag{2.74}$$

$$\frac{\partial\left(h_{\mathrm{f}}\rho_{\mathrm{f}}\vec{\mathbf{v}}_{\mathrm{f}}\right)}{\partial p_j} = \frac{\partial h_{\mathrm{f}}}{\partial p_j}\rho_{\mathrm{f}}\vec{\mathbf{v}}_{\mathrm{f}} + h_{\mathrm{f}}\frac{\partial \rho_{\mathrm{f}}}{\partial p_j}\vec{\mathbf{v}}_{\mathrm{f}} + h_{\mathrm{f}}\rho_{\mathrm{f}}\frac{\partial \vec{\mathbf{v}}_{\mathrm{f}}}{\partial p_j} \tag{2.75}$$

$$\frac{\partial\left(h_{\mathrm{f}}\rho_{\mathrm{f}}\vec{\mathbf{v}}_{\mathrm{f}}\right)}{\partial h_j} = \frac{\partial h_{\mathrm{f}}}{\partial h_j}\rho_{\mathrm{f}}\vec{\mathbf{v}}_{\mathrm{f}} + h_{\mathrm{f}}\frac{\partial \rho_{\mathrm{f}}}{\partial h_j}\vec{\mathbf{v}}_{\mathrm{f}} + h_{\mathrm{f}}\rho_{\mathrm{f}}\frac{\partial \vec{\mathbf{v}}_{\mathrm{f}}}{\partial h_j} \tag{2.76}$$

In Eq. (2.75) we set: $\partial h_{\mathrm{f}} / \partial p_j = 0$, because in the one-phase regions $\partial h_{\mathrm{f}} / \partial p_j$ is by definition zero and in the two-phase region $\partial h_{\mathrm{f}} / \partial p_j$ is usually negligible or becomes too high near the critical point (Fig. 2.1).

Deviating $\vec{\mathbf{v}}_{\mathrm{f}} = -k\frac{k_{r\mathrm{f}}}{\eta_{\mathrm{f}}}\left(\nabla p - \rho_{\mathrm{f}}\vec{\mathbf{g}}\right)$ product rule must be used. Setting $\partial k_{r\mathrm{f}} / \partial p_j = 0$, having the same reason as for $\partial h_{\mathrm{f}} / \partial p_j$ we obtain:

$$\frac{\partial \vec{\mathbf{v}}_{\mathrm{f}}}{\partial p_j} = -kk_{r\mathrm{f}}\left(-\frac{\partial \eta_{\mathrm{f}}}{\partial p_j}\frac{1}{\eta_{\mathrm{f}}^2}\left(\nabla p - \rho_{\mathrm{f}}\vec{\mathbf{g}}\right) + \frac{1}{\eta_{\mathrm{f}}}\left(\nabla N_j - \frac{\partial \rho_{\mathrm{f}}}{\partial p_j}\right)\right) \tag{2.77}$$

$$\frac{\partial \vec{\mathbf{v}}_{\mathrm{f}}}{\partial h_j} = -k\left(\frac{\partial k_{r\mathrm{f}}}{\partial h_j}\frac{1}{\eta_{\mathrm{f}}}\left(\nabla p - \rho_{\mathrm{f}}\vec{\mathbf{g}}\right) - \frac{\partial \eta_{\mathrm{f}}}{\partial h_j}\frac{1}{\eta_{\mathrm{f}}^2}\left(\nabla p - \rho_{\mathrm{f}}\vec{\mathbf{g}}\right) - \frac{1}{\eta_{\mathrm{f}}}\left(\frac{\partial \rho_{\mathrm{f}}}{\partial h_j}\vec{\mathbf{g}}\right)\right) \tag{2.78}$$

As fluid properties were calculated with p and h at facet, we obtain this rule for all properties a:

$$\frac{\partial a}{\partial p_j}\left(x_{\mathrm{F}}\right) = \frac{\partial p}{\partial p_j}\left(x_{\mathrm{F}}\right)\frac{\partial a}{\partial p}\left(x_{\mathrm{F}}\right) = \frac{\partial}{\partial p_j}\sum_{j=1}^{n}N_j\left(x_{\mathrm{F}}\right)p_j\frac{\partial a}{\partial p}\left(x_{\mathrm{F}}\right) = N_j\left(x_{\mathrm{F}}\right)\frac{\partial a}{\partial p}\left(x_{\mathrm{F}}\right) \tag{2.79}$$

where x_{F} is an arbitrary point on the facet. We obtain following derivatives of gradients, (Eqs. 2.15 and 2.16) at facets:

$$\frac{\partial}{\partial p_j}\nabla p\left(x_\mathrm{F}\right)=\frac{\partial}{\partial p_j}\nabla\sum_{j=1}^{n}\left(N_j\left(x_\mathrm{F}\right)p_j\right)=\nabla N_j\left(x_\mathrm{F}\right)\frac{\partial p_j}{\partial p_j}=\nabla N_j\left(x_\mathrm{F}\right) \tag{2.80}$$

$$\frac{\partial}{\partial p_j}\nabla T\left(x_\mathrm{F}\right)=\frac{\partial}{\partial p_j}\nabla\sum_{j=1}^{n}\left(N_j\left(x_\mathrm{F}\right)T_j\right)=\nabla N_j\left(x_\mathrm{F}\right)\frac{\partial T_j}{\partial p_j} \tag{2.81}$$

$$\frac{\partial}{\partial h_j}\nabla T\left(x_\mathrm{F}\right)=\frac{\partial}{\partial h_j}\nabla\sum_{j=1}^{n}\left(N_j\left(x_\mathrm{F}\right)T_j\right)=\nabla N_j\left(x_\mathrm{F}\right)\frac{\partial T_j}{\partial h_j} \tag{2.82}$$

The specific enthalpy and relative permeability are upwind weighted. This has to be considered for their derivative:

$$\frac{\partial k_{r\mathrm{f}}}{\partial h_j}\left(x_\mathrm{F}\right)=w_\mathrm{f}\,\frac{\partial k_{r\mathrm{f,up}}}{\partial h_j}+(1-w_\mathrm{f})N_j\left(x_\mathrm{F}\right)\frac{\partial k_{r\mathrm{f}}}{\partial h}\left(x_\mathrm{F}\right)\qquad\forall j=\mathrm{up} \tag{2.83}$$

$$\frac{\partial k_{r\mathrm{f}}}{\partial h_j}\left(x_\mathrm{F}\right)=(1-w_\mathrm{f})N_j\left(x_\mathrm{F}\right)\frac{\partial k_{r\mathrm{f}}}{\partial h}\left(x_\mathrm{F}\right)\qquad\forall j\neq\mathrm{up} \tag{2.84}$$

$$\frac{\partial h_\mathrm{f}}{\partial h_j}\left(x_\mathrm{F}\right)=w_\mathrm{f}\,\frac{\partial h_\mathrm{f,up}}{\partial h_j}+(1-w_\mathrm{f})N_j\left(x_\mathrm{F}\right)\frac{\partial h_\mathrm{f}}{\partial h}\left(x_\mathrm{F}\right)\qquad\forall j=\mathrm{up} \tag{2.85}$$

$$\frac{\partial k_{r\mathrm{f}}}{\partial h_j}\left(x_\mathrm{F}\right)=(1-w_\mathrm{f})N_j\left(x_\mathrm{F}\right)\frac{\partial k_{r\mathrm{f}}}{\partial h}\left(x_\mathrm{F}\right)\qquad\forall j\neq\mathrm{up} \tag{2.86}$$

For calculating relative permeability we obtain from Eqs. (2.36) to (2.38) of main text:

$$\frac{\partial S_\mathrm{l}}{\partial h}=\frac{-\rho_\mathrm{v}\left(h\left(\rho_\mathrm{l}-\rho_\mathrm{v}\right)-\left(h_\mathrm{l}\rho_\mathrm{l}-h_\mathrm{v}\rho_\mathrm{v}\right)\right)-\left(\rho_\mathrm{v}\left(h_\mathrm{v}-h\right)\left(\rho_\mathrm{l}-\rho_\mathrm{v}\right)\right)}{\left(h\left(\rho_\mathrm{l}-\rho_\mathrm{v}\right)-\left(h_\mathrm{l}\rho_\mathrm{l}-h_\mathrm{v}\rho_\mathrm{v}\right)\right)^2} \tag{2.87}$$

$$\frac{\partial k_{r\mathrm{l}}}{\partial h}\left(S_\mathrm{l}\right)=\frac{1}{1-S_\mathrm{lr}}\frac{\partial S_\mathrm{l}}{\partial h}\qquad\forall S_\mathrm{l}>S_\mathrm{lr} \tag{2.88}$$

$$\frac{\partial k_{r\mathrm{l}}}{\partial h}\left(S_\mathrm{l}\right)=0\qquad\forall S_\mathrm{l}\leq S_\mathrm{lr} \tag{2.89}$$

$$\frac{\partial k_{r\mathrm{v}}}{\partial h}=-\frac{\partial k_{r\mathrm{l}}}{\partial h} \tag{2.90}$$

In section 2.9.1 (seafloor boundary condition) we have derived an implicit heat flux boundary condition Q_i (Eq. 2.49). We obtain derivatives as follows:

$$\frac{\partial Q_i}{\partial p_j}=-h_i^{t+\Delta t}\,\frac{\partial q_{\mathrm{m},i}^{t+\Delta t}}{\partial p_j}\qquad\forall j\neq i \tag{2.91}$$

$$\frac{\partial Q_i}{\partial h_j} = -\frac{\partial q_{\mathrm{m},i}^{t+\Delta t}}{\partial h_j} h_i^{t+\Delta t} \qquad \forall j \neq i \tag{2.92}$$

$$\frac{\partial Q_i}{\partial h_j} = -\frac{\partial q_{\mathrm{m},i}^{t+\Delta t}}{\partial h_j} \cdot h_i^{t+\Delta t} \qquad \forall j \neq i \tag{2.93}$$

$$\frac{\partial Q_i}{\partial h_j} = -q_{\mathrm{m},i} - \frac{\partial q_{\mathrm{m},i}^{t+\Delta t}}{\partial h_j} \cdot h_i^{t+\Delta t} \qquad \forall j = i \tag{2.94}$$

Note that for this boundary condition a fixed pressure boundary is fixed and therefore for all boundary nodes *j* no new pressure p_j is searched for.

2.9.4 Deriving local coordinates of barycenter of kite shaped Ω_{il}

They are derived by splitting the kite shaped quadrangle Ω_{il} on the long edge and calculating the barycenter of both triangles (Fig. 2.2). The local coordinates of the triangular corners are:

$$a = (1,0,0) \quad b = \left(\frac{1}{3},\frac{1}{3},\frac{1}{3}\right) \quad c = \left(\frac{1}{2},0,\frac{1}{2}\right) \quad d = \left(\frac{1}{2},\frac{1}{2},0\right)$$

The barycenter of triangle are the midpoints in local triangular coordinates:

$$ce_1^1 = 1/3 \cdot (a+b+c) = \left(\frac{11}{18},\frac{2}{18},\frac{5}{18}\right) \tag{2.95}$$

$$ce_1^2 = 1/3 \cdot (a+b+d) = \left(\frac{11}{18},\frac{5}{18},\frac{2}{18}\right) \tag{2.96}$$

The kite barycenter is the intersection of the connecting line of ce_1^1 and ce_1^2 with the connecting line of *a* and *b*:

$$ce_1 = 1/2 \cdot \left(ce_1^1 + ce_1^2\right) = \left(\frac{22}{36},\frac{7}{36},\frac{7}{36}\right) \tag{2.97}$$

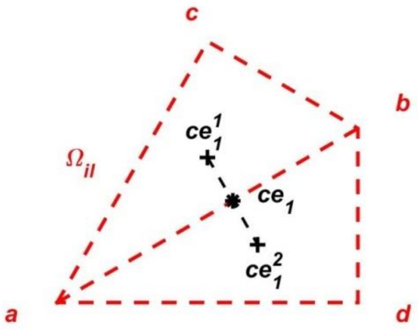

Figure 2.17: Draft of deriving local coordinates of barycenter of kite shaped Ω_{il}

2.10 Bibliography

Andersen, C., Rüpke, L., Hasenclever, J., Grevemeyer, I., Petersen, S., 2015. Fault geometry and permeability contrast control vent temperatures at the Logatchev 1 hydrothermal field, Mid-Atlantic Ridge. Geology, DOI:10.1130/G36113.1.

Bauer, O., 1998. PROST 4.1 PROperties of Water and STeam. at. Technische Universitat Hamburg-Harburg, Hamburg. <http://fluidos.etsii.upm.es/faculty/Jaime_Carpio/Fumatas_negas/PROST Properties of 550 Water and Steam.htm>.

Cathles, L.M., 2011. What processes at mid-ocean ridges tell us about volcanogenic massive sulfide deposits. Mineralium Deposita, 46(5-6): 639-657, DOI:10.1007/s00126-010-0292-9.

Coumou, D., Driesner, T., Heinrich, C.A., 2008. The structure and dynamics of mid-ocean ridge hydrothermal systems. Science, 321(5897): 1825-1828, DOI:10.1126/science.1159582.

Coumou, D., Driesner, T., Weis, P., Heinrich, C.A., 2009. Phase separation, brine formation, and salinity variation at Black Smoker hydrothermal systems. Journal of Geophysical Research, 114, DOI:10.1029/2008jb005764.

Driesner, T., Heinrich, C.A., 2007. The system H2O-NaCl. Part I: Correlation formulae for phase relations in temperature-pressure-composition space from 0 to 1000 degrees C, 0 to 5000 bar, and 0 to 1 X-NaCl. Geochimica Et Cosmochimica Acta, 71(20): 4880-4901, DOI:10.1016/i.gca.2006.01.033.

Durlofsky, L.J., 1994. Accuracy Of Mixed And Control-Volume Finite-Element Approximations To Darcy Velocity And Related Quantities. Water Resources Research, 30(4): 965-973, DOI:10.1029/94wr00061.

Faust, C.R., Mercer, J.W., 1977. A theoretical analysis of fluid flow and energy transport in hydrothermal systems. 77-60, Open-File Report.

Faust, C.R., Mercer, J.W., 1979. Geothermal Reservoir Simulation .1. Mathematical-Models For Liquid-Dominated And Vapor-Dominated Hydrothermal Systems. Water Resources Research, 15(1): 23-30, DOI:10.1029/WR015i001p00023.

Fontaine, F.J., Cannat, M., Escartin, J., Crawford, W.C., 2014. Along-axis hydrothermal flow at the axis of slow spreading Mid-Ocean Ridges: Insights from numerical models of the Lucky Strike vent field (MAR). Geochemistry, Geophysics, Geosystems, 15(7): 2918-2931, DOI:10.1002/2014GC005372.

Fontaine, F.J., Wilcock, W.S.D., Butterfield, D.A., 2007. Physical controls on the salinity of mid-ocean ridge hydrothermal vent fluids. Earth and Planetary Science Letters, 257(1-2): 132-145, DOI:10.1016/j.epsl.2007.02.027.

Garg, S.K., Pritchet, J.W., 1977. On Pressure-Work, Viscous Dissipation and the Energy Balance Relation for Geothermal Reservoirs. Advances in Water Recources, 1: 41-47.

Geiger, S., Driesner, T., Heinrich, C., Matthäi, S., 2006. Multiphase Thermohaline Convection in the Earth’s Crust: I. A New Finite Element – Finite Volume Solution Technique Combined With a New Equation of State for NaCl–H<sub>2</sub>O. Transport in Porous Media, 63(3): 399-434, DOI:10.1007/s11242-005-0108-z.

Gruen, G., Weis, P., Driesner, T., Heinrich, C.A., de Ronde, C.E.J., 2014. Hydrodynamic modeling of magmatic-hydrothermal activity at submarine arc volcanoes, with implications for ore formation. Earth and Planetary Science Letters, 404: 307-318, DOI:10.1016/j.epsl.2014.07.041.

Hasenclever, J. et al., 2014. Hybrid shallow on-axis and deep off-axis hydrothermal circulation at fast-spreading ridges. Nature, 508(7497): 508-512, DOI:10.1038/nature13174.

Hayba, D.O., Ingebritsen, S.E., 1994. The Computer Model Hydrotherm, A Three-Dimensional Finte Difference Model To Simulate Ground-Water Flow And Heat Transport In The Temperature Range Of 0 To 1,200°C. Report 94-4045, Water-Resources Investigations

Hayba, D.O., Ingebritsen, S.E., 1997. Multiphase groundwater flow near cooling plutons. Journal of Geophysical Research: Solid Earth, 102(B6): 12235-12252, DOI:10.1029/97JB00552.

Huber, R., Helmig, R., 1999. Multiphase Flow In Heterogeneous Porous Media: A Classical Finite Element Method Versus An Implicit Pressure–Explicit Saturation-Based Mixed Finite Element–Finite Volume Approach. Int. J. Numer. Meth. Fluids, 29: 899–920.

Huyakorn, P., Pinder, G.F., 1978. A pressure-enthalpy finite element model for simulating hydrothermal reservoir. Mathematics and Computers in Simulation, 20(3): 167-178.

Ingebritsen, S.E., Geiger, S., Hurwitz, S., Driesner, T., 2010. Numerical simulation of magmatic hydrothermal systems. Reviews of Geophysics, 47: 33, DOI:10.1029/2009rg000287.

Jupp, T., Schultz, A., 2000. A thermodynamic explanation for black smoker temperatures. Nature, 403(6772): 880-883.

Kipp Jr, K.L., Hsieh, P.A., Charlton, S.R., 2008. Guide to the Revised Ground-Water Flow and Heat Transport Simulator: HYDROTHERM-Version 3. U.S. Geol. Surv. Tech. Methods., 6(A25).

Kissling, W.M., 2005. Transport of three-phase hyper-saline brines in porous media: Theory and code implementation. Transport in Porous Media, 61(1): 25-44, DOI:10.1007/s11242-004-3306-1.

Lemonnier, A., 1979. Improvement of reservoir simulation by a triangular discontinuos finite element method. Society of Petroleum Engineers of AIME, 8249.

Lewis, K.C., Lowell, R.P., 2009. Numerical modeling of two-phase flow in the NaCl-H2O system: Introduction of a numerical method and benchmarking. Journal of Geophysical Research, 114, DOI:10.1029/2008jb006029.

Lowell, R.P., 1991. Modeling continental and submarine hydrothermal systems. Reviews of Geophysics, 29(3): 457-476, DOI:10.1029/91rg01080.

McCartin, B.J., 1998. Seven Deadly Sins of Numerical Computation. The American Mathematical Monthly, 105(10): 929-941, DOI:10.2307/2589285.

Pruess, K., Oldenburg, C., Moridis, G., 2012. TOUGH2 USER'S GUIDE, Version 2.1, Lawrence Berkeley National Laboratory, Berkeley, Calif., Report LBNL-43134.

Scott, S., Driesner, T., Weis, P., 2015. Geologic controls on supercritical geothermal resources above magmatic intrusions. Nature Communications, 6: 6, DOI:10.1038/ncomms8837.

Theissen-Krah, S., Rüpke, L.H., Hasenclever, J., 2016. Modes of crustal accretion and their implications for hydrothermal circulation. Geophysical Research Letters, 43(3): 1124-1131, DOI:10.1002/2015GL067335.

Travis, B.J., Janecky, D.R., Rosenberg, N.D., 1991. Three-dimensional simulations of hydrothermal circulation at mid-ocean ridges. Geophysical Research Letters, 18(8): 1441-1444.

Weis, P., Driesner, T., Coumou, D., Geiger, S., 2014. Hydrothermal, multiphase convection of H2O-NaCl fluids from ambient to magmatic temperatures: a new numerical scheme and benchmarks for code comparison. Geofluids, 14(3): 347-371, DOI:10.1111/gfl.12080.

Weis, P., Driesner, T., Heinrich, C.A., 2012. Porphyry-Copper Ore Shells Form at Stable Pressure-Temperature Fronts Within Dynamic Fluid Plumes. Science, 338(6114): 1613-1616.

Zyvoloski, G., 2007. FEHM: A control volume finite element code for simulating subsurface multi-phase multi-fluid heat and mass transfer, Los Alamos National Laboratory Document, LAUR-07-3359.

Zyvoloski, G.A., Robinson, B.A., Dash, Z.D., Trease, L.L., 1997. Summary of Models and Methods for the FEHM Application - A Finite-Element Heat- and Mass-Transfer Code, Los Alamos Natl. Lab., LA-13307-MS.

3 Brine formation and mobilization in submarine hydrothermal systems: insights from a novel multiphase hydrothermal flow model in the system H_2O–NaCl

3.1 Abstract

Numerical models have become indispensable tools for investigating submarine hydrothermal systems and for relating seafloor observations to physicochemical processes at depth. Particularly useful are multiphase models that account for phase separation phenomena, so that model predictions can be compared to observed variations in vent fluid salinity. Yet, the numerics of multiphase flow remain a challenge. Here we present a novel hydrothermal flow model for the system H_2O−NaCl able to resolve multiphase flow over the full range of pressure, temperature, and salinity variations that are relevant to submarine hydrothermal systems. The method is based on a 2-D finite volume scheme that uses a Newton-Rapson algorithm to couple the governing conservation equations and to treat the non-linearity of the fluid properties. The method uses pressure, specific fluid enthalpy and bulk fluid salt content as primary variables, is not bounded to the Courant time step size, and allows for a direct control of how accurately mass and energy conservation is ensured. In a first application of this new model, we investigate brine formation and mobilization in hydrothermal systems driven by a transient basal temperature boundary condition, analogue to seawater circulation systems found at mid-ocean ridges. We find that basal heating results in the rapid formation of a stable brine layer that thermally insulates the driving heat source. While this brine layer is stable under steady-state conditions, it can be mobilized as a consequence of variations in heat input leading to brine entrainment and the venting of highly saline fluids.

3.2 Introduction

Hydrothermal venting at the ocean floor is a key mechanism of biogeochemical exchange between the solid earth and the global ocean. Fluid circulation through the young ocean floor sustains unique ecosystems (Boetius, 2005), mobilizes metals from the crust to the ocean floor to form volcanogenic massive sulfide deposits (Hannington et al., 2011), and is a source of trace elements and isotopes that are now thought to play an important role in global scale biogeochemical ocean cycles (German et al., 2016). Much has been learned about these systems and their role in the Earth System from direct seafloor observations, water column measurements, ocean drilling, and geophysical imaging (Fornari et al., 2012; German and Seyfried, 2014; Humphris et al., 1995). Yet, the inner workings of submarine hydrothermal system remain inaccessible to direct observations. Instead, the sub-seafloor hydro-geochemical regime needs to be indirectly inferred. Investigating systematic pattern in vent fluid chemistry and their spatial as well as temporal variations is one powerful approach (e.g. Butterfield and Massoth, 1994; Mottl et al., 2011; Shanks, 2001; Von Damm, 2004). The chemistry of hundreds of vent fluid samples taken from hydrothermal systems located in diverse geological settings including fast-spreading and slow-spreading ridges as well as back-arc spreading centers have been published. The resulting dataset shows a spectacular diversity and complexity of vent fluid chemistry, yet some first-order features and trends are robust and clear. For example, vent fluid salinity often deviates from the seawater value pointing to phase separation and segregation phenomena at depth. When seawater is heated and intersects the two-phase boundary, it splits into a low-salinity vapor and a higher-salinity brine phase (Bischoff and Rosenbauer, 1984; Driesner and Heinrich, 2007). Segregation of these phases can result in the venting of fluids that have a higher or lower salinity than seawater. Observed vent fluid salinities vary between 5% and 200% of the seawater value (3.2 wt% NaCl). These salinity variations are particularly interesting in the context of metal mobilization and transport. Most metals, including Iron (Fe), are chloro-complexing and tend to travel with the more saline fluid phase, implying that phase separation has a first order effect on vent fluid chemistry (Butterfield et al., 1997; Jr. Seyfried et al., 1991; Von Damm, 2004). Figure 3.1 illustrates this for a selection of vent fluid samples from the East Pacific Rise (EPR) and some selected slow-spreading mid-ocean ridges.

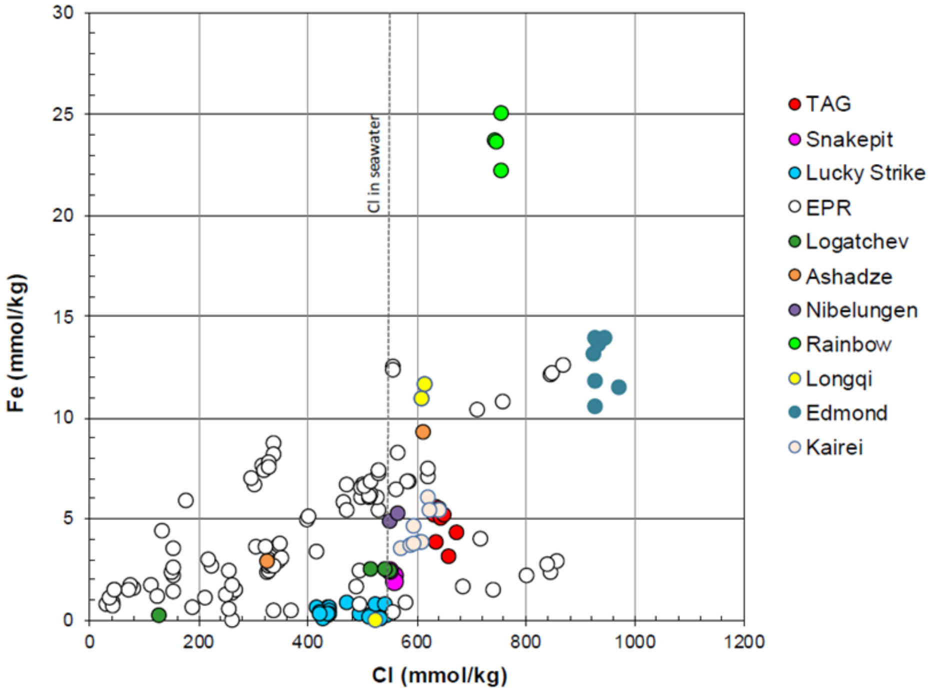

Figure 3.1: Plot of chloride versus total Iron for various vent fluids in mid-ocean ridge settings: East Pacific (Shanks, 2001; Von Damm, 2000; Von Damm, 2004), TAG (Edmonds et al., 1996), Snakepit (Von Damm, 1990), Lucky Strike (Charlou et al., 2000; Von Damm et al., 1998), Rainbow (Douville et al., 2002), Longqi (Ji et al., 2017), and Edmond/Kairei (Gallant and Von Damm, 2006; Kumagai et al., 2008).

Tracing salt within submarine hydrothermal systems is therefore a useful way of investigating metal transport within the oceanic crust and toward the seafloor. Yet, relating changes in vent fluid chemistry to hydrothermal processes at depth remains a challenge and requires numerical multi-phase transport models as well as a reliable equation-of-state (EOS) that can establish links between hydrothermal flow observations and physicochemical processes at depth.

Some insights into brine formation and salt re-distribution within hydrothermal convection cells can be gained from exploring the EOS of seawater (Driesner and Heinrich, 2007). Theoretical work on pure water (Jupp and Schultz, 2000), later extended to salt water (Geiger, 2005), have shown that the thermodynamic properties of (sea-)water result in an upper temperature limit of approximately 400 °C in the upflow limb of submarine hydrothermal circulations cells (the exact value is a function of pressure and salinity). The critical point of seawater with 3.2 wt% NaCl is at 29.8 MPa and 407 °C. Consequently, boiling can occur at vent fields located at water depths shallower than ~3000 m. Such shallow boiling (and condensation) processes in combination with brine entrainment into the upflow zone are thought to be the reason for the high spatial and temporal variability in vent fluid salinities, which are, for example, observed at the East Pacific Rise vent field at 9°N located in ~2600 m water depth (Pester et al., 2014; Von Damm, 2004; Von Damm et al., 1997). Boiling and entrainment processes are also likely to control vent fluid salinity at the ASHES vent field located in 1540 m water depth on the Juan de Fuca Ridge (JdFR), where chimneys just tens of meters apart show salinities below and above seawater (Butterfield et al., 1990). These ideas were tested and confirmed with numerical multiphase models by Coumou et al. (2009), who showed how the entrainment of brines formed in the upflow zone of relatively shallow hydrothermal systems can result in rapid and large fluctuations in vent fluid salinity.

If a fluid is intersecting the two-phase boundary at pressures higher than the critical pressure of seawater, small amounts of a highly saline brine phase are condensing from the fluid phase thereby depleting it in NaCl. Note that we do not use the terms “subcritical” and “supercritical” phase separation here, which are often found in mid-ocean ridge literature, because they refer to the miss-leading concept of a fixed salt content. We rather follow Coumou et al. (2009) and refer to the physical processes of boiling and condensation. Brine condensation is likely to happen above the driving heat source of a circulation system. In most mid-ocean ridge settings, magmatic heat sources like e.g. the axial melt lens at fast-spreading ridges or a gabbroic intrusion at slow-spreading ridges are located at hydrostatic pressures higher than the critical pressure of seawater and release their heat directly into the two-phase region. Within this region, the condensing dense brine phase will pool, while the less dense vapor phase will rise. This may result in a stable basal brine layer that insulates the heat source and through which heat transport is predominantly conductive.

Based on mass flux estimates and measured vent salinities at Main Endeavor Field, Fontaine and Wilcock (2006) estimated that a basal brine layer of ~100 m thickness should form within only 15 years. As this estimate was inconsistent with their calculated conductive heat balance, which required the brine layer to be thinner than 10 m to match the observed high heat flux, they argued that interfacial tension between fluid and solid phases will likely favor the segregation of vapor into the main fractures and brine into the smaller fissures. This would allow the vapor to flow efficiently through the system and to sustain large heat fluxes. Bischoff and Rosenbauer (1989) argued that double-diffusion will break the stable stratification of the brine layer leading to internal convection, which mines the required heat from below. So far, the viability of both explanations remains questionable as neither has been tested in fluid-dynamic simulations. A complementary explanation is lateral brine flow near the base of a circulation system. If brines move out of the two-phase region either by lateral migration or because heat supply is diminished, they would merge with the single-phase fluid flow above thus leading to the venting of highly saline fluids (Coumou et al., 2009). This process is likely to happen at the TAG hydrothermal mound on the Mid-Atlantic ridge, where stable brine venting (~125% of seawater salinity) has been documented to have occurred for more than a decade (Chiba et al., 2001). Long-term venting of brines is rare at intermediate to fast-spreading ridges. Venting on the Northern Cleft segment of the JdFR is such an exception. Here repeated fluid sampling in the early 1990s documented persistent venting of high salinity fluids, which has been interpreted as interaction with a previously formed brine layer (Butterfield and Massoth, 1994). At the Main Endeavor Field on the Juan de Fuca Ridge, vent fluid salinities have mostly been lower than seawater in the period 1984 to 2005 (Butterfield and Massoth, 1994; Foustoukos et al., 2009; Lilley et al., 2003). Also at the East Pacific Rise at 9°50’N, low salinity venting occurred for more than 13 years since 1991 (Von Damm, 2004). This predominance of lower-than-seawater salinity venting at intermediate to fast-spreading ridges raises again the question what the fate of the complementary brine phase is. It continues to be an unresolved question whether brines are pooling at the base of circulation systems or brine venting occurs diffusively or/and highly diluted.

It is in this context that we are here investigating brine formation and mobilization in submarine hydrothermal systems using a newly developed two-dimensional hydrothermal modeling code. First, we present our numerical approach and explain our motives for developing a new code and how our approach differs from other existing simulators like CSMP++, MUFITS, TOUGH-NaCl and FISHES. Second, we show results of a suite of model calculations investigating a geometrically simple setup designed to approximate the conditions of a hydrothermal system at a mid-ocean spreading center with a basal heat source. For different pressure conditions, we study brine layer formation, its stability and effect on heat transfer as well as the conditions that result in the mobilization of the brine phase into the upflow zone.

3.3 Numerical approach

3.3.1 Motivation for new code

Multi-phase simulations of thermohaline flow in submarine hydrothermal systems continue to be numerically challenging and are still not routinely done. It requires an EOS that fully describes the fluid’s state and thermodynamic properties over sufficiently wide pressure (P), temperature (T), salinity (X) ranges and a transport model able to handle multiphase flow and the strong non-linearity of the thermodynamic properties. Driesner and Heinrich (2007) and Driesner (2007) provide complete and realistic correlation formulae for phase stability relations and fluid properties at temperatures from 0 to 1000 °C, pressures from 0 to 5000 bar and compositions from 0 to 1 weight fraction NaCl. The provided EOS improves upon earlier works (Palliser and McKibbin, 1998a; Palliser and McKibbin, 1998b; Palliser and McKibbin, 1998c) in the correlation formulae and in that the complete fluid state can be calculated as a function of PTX including a comprehensive set of thermodynamic properties. The CSMP++ porous media simulator (Geiger et al., 2006a; Geiger et al., 2006b; Weis et al., 2014) uses this EOS and has been used for submarine hydrothermal systems (Coumou et al., 2009; Gruen et al., 2012; Gruen et al., 2014) and geothermal sites (Scott et al., 2016; Scott et al., 2017; Weis et al., 2012). Other existing simulators include NaCl-TOUGH2 (Kissling, 2005a; Kissling, 2005b), which uses different correlation formulae (Palliser and McKibbin, 1998a; Palliser and McKibbin, 1998b; Palliser and McKibbin, 1998c) and is an enhancement of TOUGH2 (Kipp Jr et al., 2008), which was originally developed for geothermal settings below 350°C. Yet this code was only used once for modelling in a case study for the Taupo Volcanic Zone in New Zealand (Kissling, 2005b). FISHES (for Fully Implicit Seafloor Hydrothermal Event Simulator) has been developed by Lewis and Lowell (2009), the thermodynamic properties are a synthesis of data and extrapolations from various studies (Anderko and Pitzer, 1993; Archer, 1992; Palliser and McKibbin, 1998a; Palliser and McKibbin, 1998b; Palliser and McKibbin, 1998c; Tanger and Pitzer, 1989), and it is appropriate/adequate for modeling two-phase problems at mid-ocean ridges (Choi and Lowell, 2015; Han et al., 2013; Singh et al., 2013). Most recently, the reservoir simulator MUFITS has been adapted to resolve multiphase hydrothermal flow using the EOS by Driesner and Heinrich (2007) and was used to simulate brine formation in a volcanic setting (Afanasyev et al., 2018).

According to publications, the well-documented CSMP++ simulator appears to be the most frequently used code. Interestingly, the employed sequential method of solving the governing equation is different to the typically used coupled approaches implemented in other hydrothermal and geothermal simulators. MUFITS, TOUGH2, HYDROTHERM and FEHM all use a coupled numerical approach, where mass and energy conservation equations are solved simultaneously using an iterative scheme, which is often the Newton-Raphson method. It remains a question of active research to assess to strengths and limitations of sequential versus coupled approaches in terms of efficiency, stability and accuracy. The reader can find further discussion on this in (Ingebritsen et al., 2010; Vehling et al., 2018).

Coupled approaches should be better equipped for handling the strong non-linearities in the governing conservation equations and their strong couplings – and should theoretically be more efficient by allowing for larger time-steps. In practice, the case is far from clear. For example, resolving the sharp phase boundaries and associated jumps in coefficients that occur over the relevant PTX ranges in the H_2O−NaCl system is a challenge in coupled approaches. Here the choice of the primary variables that define the thermodynamic state has to be done carefully. For the system H_2O−NaCl correlation formulae are a function of pressure, temperature and composition but the energetic state is not always resolved. For example, saturations in the three-phase region where vapor, liquid, and halite coexist and for the pure water two-phase region cannot be calculated in PTX-space (Fig. 3.2 & Fig. 3.3). One possible solution is primary variable switching (Class et al., 2002; Wu and Forsyth, 2001). However, if a phase boundary is crossed multiple times, and each crossing triggers a primary variable switch and associated variable initialization, convergence can be poor. In TOUGH-NaCl, this procedure leads to restrictions in the allowed phase state transitions (Kissling, 2005b). For example, from single phase it is not allowed to have a direct transition to the three-phase coexisting region.

Another option is to use a set of primary variables that always resolves the fluid state, like e.g. pressure, specific enthalpy (H), and salinity. The downside is that the existing EOSs for the system H_2O−NaCl use PTX so that the thermodynamic state has to be determined with a costlier iterative scheme or with interpolations on look-up tables. In HYDROTHERM (Hayba and Ingebritsen, 1994; Kipp Jr et al., 2008) this method has been shown to work well for the pure water two-phase region and also at difficult conditions around the critical point (22.06 MPa, 374.15 °C). Promising are also results obtained with MUFITS simulator which uses a PHX coupled scheme to resolve two-phase flow in the system H_2O−NaCl (Afanasyev et al., 2018).

In summary, the equation-of-state for the system H_2O−NaCl is reasonably well constrained but progress needs to be made in simulating multiphase transport. We see a large utility and potential for a hydrothermal simulator that uses the coupled approach with primary variables of pressure, spec. enthalpy, and composition. Recently, we have presented a coupled pressure/enthalpy scheme simulating pure-water multi-phase flow (Vehling et al., 2018). This method uses a higher order time differencing scheme (theta-time-differencing) that leads to higher accuracy, larger time step sizes, and a better convergence of the Newton-Raphson iteration scheme. We here extend this method to the system H_2O−NaCl by adding an additional conservation equation and by translating the EOS of (Driesner, 2007; Driesner and Heinrich, 2007) from PTX to PHX space.

3.3.2 Model assumptions and governing equations

We use an extension of the two-phase flow model and numerical approach presented in (Vehling et al., 2018), which is a pure water two-phase numerical code. We make again the following model assumptions:

1. capillary pressure effects are neglected
2. rock and fluid are in local thermodynamic equilibrium
3. rock enthalpy is related to temperature by a constant specific heat
4. the inertia energy terms are orders of magnitude smaller and hence can be neglected
5. we fully account for pressure-volume work and viscous dissipation

To describe the H_2O−NaCl-system, the conservation of mass of the combined H_2O−NaCl fluid (Eq. 3.1) and the conservation of energy (Eq. 3.2) is completed by salt mass conservation (Eq. 3.3):

$$\frac{\partial(\Phi \rho_{\mathrm{m}})}{\partial t} = -\nabla \cdot \left(\sum_{\mathrm{f} \in \{\mathrm{l},\mathrm{v}\}} \rho_{\mathrm{f}} \vec{\mathbf{v}}_{\mathrm{f}} \right) \tag{3.1}$$

$$\begin{aligned} \frac{\partial E}{\partial t} &= \frac{\partial}{\partial t}(\Phi \rho_{\mathrm{m}} h) + \rho_{\mathrm{r}} c_{p\mathrm{r}} \frac{\partial (T(1-\Phi))}{\partial t} \\ &= \nabla \cdot K \nabla T - \nabla \cdot \left(\sum_{\mathrm{f} \in \{\mathrm{l},\mathrm{v}\}} h_{\mathrm{f}} \rho_{\mathrm{f}} \vec{\mathbf{v}}_{\mathrm{f}} \right) + \sum_{\mathrm{f} \in \{\mathrm{l},\mathrm{v}\}} \frac{\eta_{\mathrm{f}}}{k k_{r\mathrm{f}}} \vec{\mathbf{v}}_{\mathrm{f}}^2 + \frac{\partial (p\Phi)}{\partial t} + \sum_{\mathrm{f} \in \{\mathrm{l},\mathrm{v}\}} \vec{\mathbf{v}}_{\mathrm{f}} \nabla p \end{aligned} \tag{3.2}$$

$$\frac{\partial(\Phi \rho_{\mathrm{m}} X)}{\partial t} = -\nabla \cdot \left(\sum_{\mathrm{f} \in \{\mathrm{l},\mathrm{v}\}} \rho_{\mathrm{f}} X_{\mathrm{f}} \vec{\mathbf{v}}_{\mathrm{f}} \right) + \nabla \cdot \left(\sum_{\mathrm{f} \in \{\mathrm{l},\mathrm{v}\}} D \rho_{\mathrm{f}} \nabla X_{\mathrm{f}} \right) \tag{3.3}$$

All variables are summarized in Table 3.1. Subscripts l, v, h stand for liquid, vapor and halite phase and f is either liquid or vapor. The third term on the RHS of Eq. (3.2) describes viscous dissipation, and the fourth and fifth term contains the part of the pressure-volume work that is not accounted for in the specific enthalpy. We summarize these terms into the following expression, which is then back-substituted into Eq. (3.2):

$$\frac{\partial(\Phi p)}{\partial t} + \sum_{\mathrm{f} \in \{\mathrm{l},\mathrm{v}\}} \vec{\mathbf{v}}_{\mathrm{f}} (\rho_{\mathrm{f}} \vec{\mathbf{g}}) = -\sum_{\mathrm{f} \in \{\mathrm{l},\mathrm{v}\}} \vec{\mathbf{v}}_{\mathrm{f}} (\nabla p - \rho_{\mathrm{f}} \vec{\mathbf{g}}) + \left(\frac{\partial(\Phi p)}{\partial t} + \sum_{\mathrm{f} \in \{\mathrm{l},\mathrm{v}\}} \vec{\mathbf{v}}_{\mathrm{f}} \nabla p \right) \tag{3.4}$$

The fluid velocity trough a porous medium is described by Darcy's law, where halite is treated as immobile phase, which is absent in advection terms.

$$\vec{\mathbf{v}}_{\mathrm{f}} = -k \frac{k_{r\mathrm{f}}}{\eta_{\mathrm{f}}} (\nabla p - \rho_{\mathrm{f}} \vec{\mathbf{g}}) \tag{3.5}$$

The mean density ρ_{m}, mean specific enthalpy h and mean salt mass fraction X are defined as follows, using $X_{\mathrm{h}} = 1$:

$$\rho_{\mathrm{m}} = S_{\mathrm{l}} \rho_{\mathrm{l}} + S_{\mathrm{v}} \rho_{\mathrm{v}} + S_{\mathrm{h}} \rho_{\mathrm{h}} \tag{3.6}$$

$$h = \frac{S_{\mathrm{l}} \rho_{\mathrm{l}} h_{\mathrm{l}} + S_{\mathrm{v}} \rho_{\mathrm{v}} h_{\mathrm{v}} + S_{\mathrm{h}} \rho_{\mathrm{h}} h_{\mathrm{h}}}{\rho_{\mathrm{m}}} \tag{3.7}$$

$$X = \frac{S_{\mathrm{l}} \rho_{\mathrm{l}} X_{\mathrm{l}} + S_{\mathrm{v}} \rho_{\mathrm{v}} X_{\mathrm{v}} + S_{\mathrm{h}} \rho_{\mathrm{h}} X_{\mathrm{h}}}{\rho_{\mathrm{m}}} \tag{3.8}$$

Whereby phase volumetric saturations adding themselves to one:

$$S_{\mathrm{l}} + S_{\mathrm{v}} + S_{\mathrm{h}} = 1 \tag{3.9}$$

Table 3.1: Variables

Variable	**Meaning**	**Unit**
$c_{p\mathrm{r}}$	specific rock heat	J/(kg·K)
D	salt diffusity	m/s²
do	subscript for downstream node	
E	total energy in fluid and matrix	J
$\vec{\mathbf{g}}$	gravitational acceleration	m/s²
h	mean specific enthalpy	J/kg
h_f	fluid specific enthalpy	J/kg
h_m	mean specific enthalpy	J/kg
K	mean conductivity of rock matrix and fluid	W/(m·K)
k	isotropic permeability of porous medium	m²
$k_{r\mathrm{f}}$	relative permeability	-
k_seg	computed permeability at segment	m²
n	Number of grid points	-
$\vec{\mathbf{n}}_i$	outward pointing unit normal vector of control volume *i*	-
N_i	finite element shape functions	-
p	pore pressure	Pa
S_l	liquid saturation	-
S_v	vapor saturation	-
S_h	halite saturation	-
S_lr	Residual liquid saturation	-
t	time	s
T	rock and fluid temperature	°C
up	subscript for upstream node	
$\vec{\mathbf{v}}_\mathrm{f}$	Darcy velocity	m/s
w_f	upstream weighting factor	-
X	mean salt composition	wt. fraction
X_f	fluid salt composition	wt. fraction
x	arbitrary point in domain Ω	m
η_f	fluid viscosity	Pa·s
ρ_f	fluid density	kg/m³
ρ_m	mean density of fluids	kg/m³
ρ_r	rock density	kg/m³
Ω	modeling domain	m²
Ω_i	control volume area	m²
$\partial\Omega_\mathrm{i}$	boundary of control volume *i*	m
θ	time differencing weighting	-
Φ	porosity	-

3.3.3 Equation of state in the system H_2O−NaCl

We implemented the equation of state in the system H_2O−NaCl published by (Driesner, 2007; Driesner and Heinrich, 2007), which is formulated for the pressure-temperature-composition space (Fig. 3.2). In total we find seven phase states. The black surface separates the single-phase region from the liquid + vapor (L+V) coexisting region. The red line (critical curve) following the crest of this surface indicates whether a single-phase fluid enters the two-phase region as vapor-like or liquid-like fluid. At pressures below the critical point of pure water (p_{crit} = 22.06 MPa, 374.15 °C) the critical curve is identical to the boiling curve of pure water. Here a single-phase fluid below the boiling temperature is always in a liquid state and would boil when heated to the two-phase boundary. At higher pressures, the critical curve moves to higher salt compositions, which implies that when a single-phase fluid with a salt content lower than the critical curve is heated until it hits the two-phase boundary, it would be a vapor-like fluid from which brine droplets are condensing.

Throughout this paper, we use the critical curve to distinguish between vapor- and liquid-like in the single-phase region at pressures higher than p_{crit} with vapor always having a lower density than a fluid on the critical curve for a given pressure. Therefore, a "vapor" is a fluid, which has a density below the density at the critical point of pure water (321.9 kg/m³), or a fluid having a higher temperature and a lower salt content than the critical curve at a given pressure.

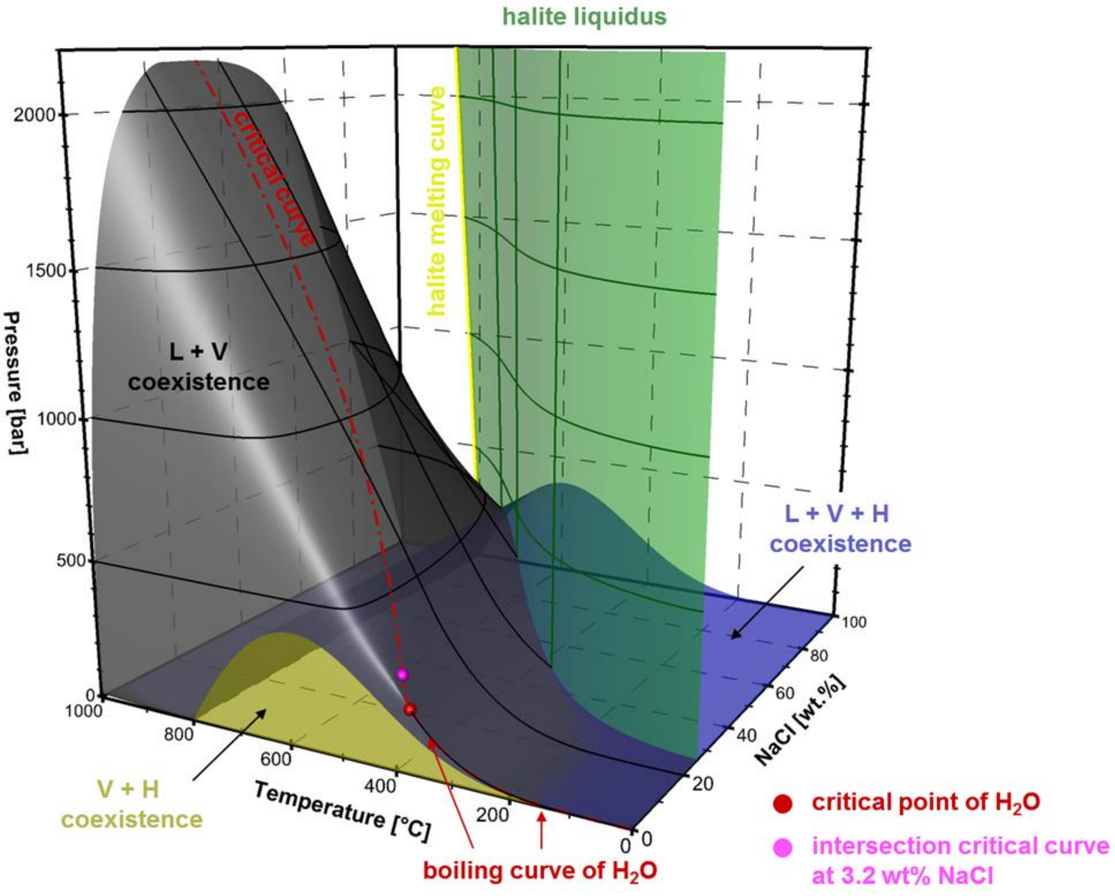

Figure 3.2: Phase diagram of the system H_2O−NaCl in temperature-pressure-composition coordinates with isolines for pressure and composition on surfaces.

The green surface marks the halite liquidus. In the liquid + halite (L+H) coexisting region, halite saturation increases linearly with increasing salt content, when temperature stays constant. The liquid, vapor and halite coexisting surface (blue) forms the lower pressure boundary of the L+V region and the upper boundary of the V+H coexisting region. The dark-yellow surface separates at low salinities the vapor region (single phase) from the V+H coexisting region.

We use a bisection method for the mapping between PTX and pressure, spec. enthalpy and composition space (PHX). Special care must be taken in regions where the fluid state is not uniquely described in PTX space, which are the three-phase, pure water boiling, and halite melting regions. Within those regions we make use of the constant temperature constraint for a given pressure, which allows solving directly for the unknown saturations. Figure 3.3 shows HX-slices for different pressures illustrating how the fluid state is uniquely described in PHX space. Pure water boiling below the critical pressure occurs at $X = 0$ between the specific enthalpies of vapor and liquid (Fig. 3.3a, b). If boiling occurs in the presence of salt (L+V region), the spec. enthalpies (and salt contents) of the vapor and liquid phases at a given temperature within the L+V-region can be read off at the intersection of the respective isotherm with the phase region boundaries (bold lines). Note how the vapor phase can carry several wt% NaCl within the lower temperature range of the L+V region at higher pressures (Fig. 3.3c, d). At pressures lower than 39.015 MPa, the isothermal L+V+H coexisting field appears twice and the spec. enthalpies of each phase can be read off at the triangle corners (Fig. 3.3a, b, c). Within each (isothermal) lower temperature L+V+H region, an increase in bulk specific enthalpy results in the separation of liquid into vapor and halite, i.e. the liquid saturation decreases with halite and vapor saturations increasing. In the higher temperature L+V+H regions, vapor and halite are progressively forming a very high salinity liquid (>85 wt% NaCl) with increasing bulk enthalpy. Finally, isothermal halite melting is resolved with saturations of solid and liquid halite varying between the yellow dots at $X = 100$ wt% NaCl.

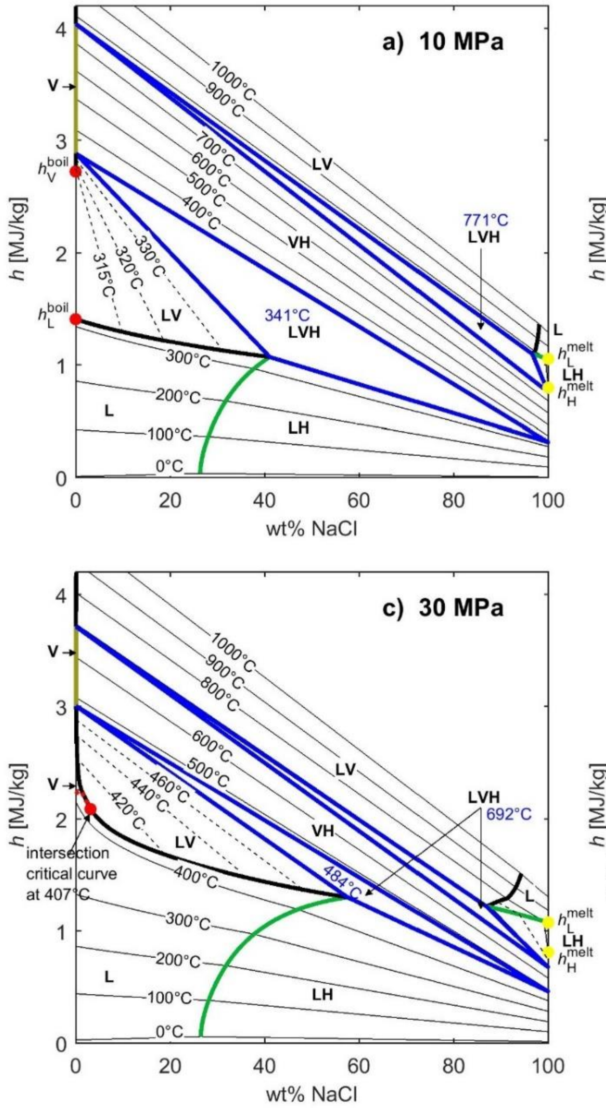

Figure 3.3: Isobaric cross sections of bulk spec. enthalpy versus fluid salt content within the PHX phase relation diagram. Colored bold lines show same phase region boundaries as in Figure 3.2. Thin black lines are isotherms, crossing phase region boundaries. Dashed thin black lines are isotherms restricted to phase regions. **a** and **b**: Red dots at the left border show spec enthalpy for boiling of pure water; boiling temperature is in a) 311 °C and in b) 366 °C. Temperatures of L+V+H regions are in blue. Yellow dots show spec. enthalpy of melting halite h_H and the corresponding melt h_L. Molten halite is part of phase region L. Figure design has been adapted from (Driesner, 2013)

We have implemented the EOS in MATLAB but for performance reasons use pre-computed 3-D look-up tables for the transport models. For this purpose, we mesh the different phase fields in 3-D PHX-space using an unstructured mesh of tetrahedral elements. In this way, we ensure that phase boundaries are well resolved and to not cross elements so that the interpolation scheme “knows” on which phase field it operates. Note that the EOS of Driesner and Heinrich (2007) does not include a parameterization of viscosity and we here use the one recently published by Klyukin et al. (2017).

3.3.4 Control volume method

As spatial discretization of the governing equations we use a finite volume technique, in which a control volume (CV) is constructed around each node of an unstructured triangular finite element mesh (Fig. 3.4). This approach is equal to that used in (Vehling et al., 2018) and has the advantage of being locally fluid mass, energy and salt mass conserving. Mass and energy fluxes between two adjacent CVs are continuous when using temperature and pressure gradients obtained from corner nodes of the triangle elements. The same discretization is used in CSMP++ (Weis et al., 2014).

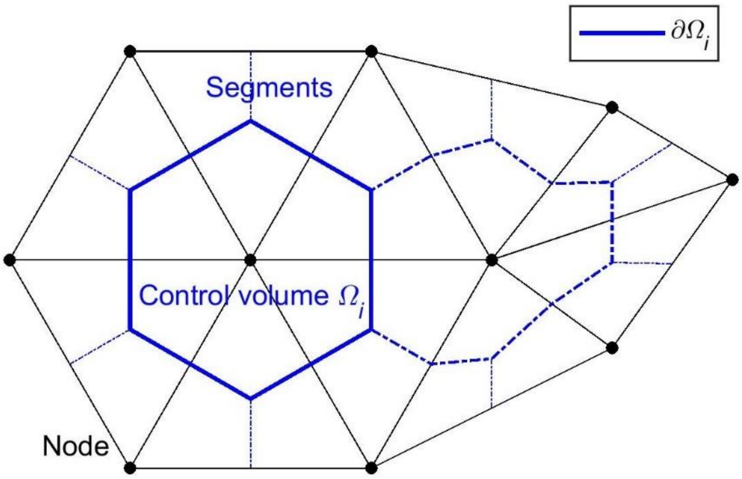

Figure 3.4: Construction of the control volumes Ω_i from an unstructured finite element triangle mesh (black lines). The control volume boundary is composed of straight segments, and each element contains three segments.

In the control finite volume method, fluxes are integrated over the boundary $\partial\Omega_i$ of each CV. For each control volume Ω_i, we obtain the integral formulations of Eqs. (3.1-3.3) by transforming the divergence of the flux terms into a line integral on $\partial\Omega_i$ using the divergence theorem.

$$\int_{\Omega_i} \frac{\partial(\Phi\rho_{\mathrm{m}})}{\partial t}\mathrm{d}\Omega = -\int_{\partial\Omega_i} \sum_{\mathrm{f}\in\{\mathrm{l,v}\}} \rho_{\mathrm{f}}\vec{\mathbf{v}}_{\mathrm{f}}\cdot\vec{\mathbf{n}}_i\mathrm{d}r \tag{3.10}$$

$$\int_{\Omega_i} \frac{\partial E}{\partial t}\mathrm{d}\Omega = \int_{\partial\Omega_i}\left(K\nabla T - \sum_{\mathrm{f}\in\{\mathrm{l,v}\}} -h_{\mathrm{f}}\rho_{\mathrm{f}}\vec{\mathbf{v}}_{\mathrm{f}}\right)\cdot\vec{\mathbf{n}}_i\mathrm{d}r + \int_{\Omega_i}\left(\frac{\partial(\Phi p)}{\partial t} + \sum_{\mathrm{f}\in\{\mathrm{l,v}\}}\vec{\mathbf{v}}_{\mathrm{f}}\left(\rho_{\mathrm{f}}\vec{\mathbf{g}}\right)\right)\mathrm{d}\Omega \tag{3.11}$$

$$\int_{\Omega_i} \frac{\partial(\Phi\rho_{\mathrm{m}}X)}{\partial t}\mathrm{d}\Omega = \int_{\partial\Omega_i}\left(\sum_{\mathrm{f}\in\{\mathrm{l,v}\}} D\rho_{\mathrm{f}}\nabla X_{\mathrm{f}} - \sum_{\mathrm{f}\in\{\mathrm{l,v}\}}\rho_{\mathrm{f}}X_{\mathrm{f}}\vec{\mathbf{v}}_{\mathrm{f}}\right)\cdot\vec{\mathbf{n}}_i\mathrm{d}r \tag{3.12}$$

Where $\vec{\mathbf{n}}_i$ is the outward pointing unit normal vector field of the control volume boundary $\partial\Omega_i$. To calculate gradients across the segments we use the spatial derivatives of standard linear finite element shape functions N.

$$\nabla p(x) = \nabla\sum_{j=1}^{n} N_j\left(x\right)p_j = \sum_{j=1}^{n}\nabla N_j(x)p_j \tag{3.13}$$

$$\nabla T\left(x\right)=\nabla\sum_{j=1}^{n}N_j\left(x\right)T_j=\sum_{j=1}^{n}\nabla N_j\left(x\right)T_j \tag{3.14}$$

$$\nabla X\left(x\right)=\nabla\sum_{j=1}^{n}N_j\left(x\right)X_j=\sum_{j=1}^{n}\nabla N_j\left(x\right)X_j \tag{3.15}$$

where x is an arbitrary point of Ω, j is the index of each node and its corresponding shape function, and n is the total number of nodes in the mesh.

3.3.5 Numerical discretization in time

For the numerical time discretization, we use a variable combination of forward Euler method and backward Euler method, the so-called theta(θ)-method:

$$\frac{\partial u}{\partial t}=F\left(u,x,t\right) \tag{3.16}$$

$$\frac{u^{t+\Delta t}-u^{t}}{\Delta t}=\theta F\left(u,x,t\right)^{t+\Delta t}+\left(1-\theta\right)F\left(u,x,t\right)^{t} \tag{3.17}$$

Based on our efficiency study in (Vehling et al., 2018) we favor the Galerkin Method with $\theta = 2/3$.

3.3.6 Newton-Raphson-scheme

The main numerical difficulty in solving the above system of equations is the strong coupling between the mass and energy conservation equations and the strong non-linearity of the fluid properties. While the equation coupling is treated in our scheme by computing pressure, mean specific fluid enthalpy, and bulk salt content simultaneously during a single solve of the matrix equation, the non-linearity in fluid properties (and states) is resolved by NR-iterations. For this purpose, we write the equations for each control volume (or associated node) i in residual form:

$$R_i=-\int_{\partial\Omega_i}\sum_{\mathrm{f}\in\{\mathrm{l,v,s}\}}\rho_{\mathrm{f}}\vec{\mathbf{v}}_{\mathrm{f}}\cdot\vec{\mathbf{n}}_i\mathrm{d}r-\int_{\Omega_i}\Phi\frac{\partial(\Phi\rho_{\mathrm{m}})}{\partial t}\mathrm{d}\Omega \tag{3.18}$$

$$G_i=\int_{\partial\Omega_i}\left(K\nabla T-\sum_{\mathrm{f}\in\{\mathrm{l,v}\}}h_{\mathrm{f}}\rho_{\mathrm{f}}\vec{\mathbf{v}}_{\mathrm{f}}\right)\cdot\vec{\mathbf{n}}_i\mathrm{d}r+\int_{\Omega_i}\left(\frac{\partial\left(\Phi p\right)}{\partial t}+\sum_{\mathrm{f}\in\{\mathrm{l,v}\}}\vec{\mathbf{v}}_{\mathrm{f}}\left(\rho_{\mathrm{f}}\vec{\mathbf{g}}\right)-\frac{\partial E}{\partial t}\right)\mathrm{d}\Omega \tag{3.19}$$

$$H_i=\int_{\partial\Omega_i}\left(\sum_{\mathrm{f}\in\{\mathrm{l,v}\}}D\rho_{\mathrm{f}}\nabla X_{\mathrm{f}}-\sum_{\mathrm{f}\in\{\mathrm{l,v}\}}\rho_{\mathrm{f}}X_{\mathrm{f}}\vec{\mathbf{v}}_{\mathrm{f}}\right)\cdot\vec{\mathbf{n}}_i\mathrm{d}r-\int_{\Omega_i}\frac{\partial(\Phi\rho_{\mathrm{m}}X)}{\partial t}\mathrm{d}\Omega \tag{3.20}$$

Then we create a linear system of equations by applying the Newton-Raphson-scheme for every residua R_i, G_i and H_i:

$$\sum_{j}^{n}\frac{\partial R_i}{\partial p_j}\left(p_j^{l+1}-p_j^{l}\right)+\sum_{j}^{n}\frac{\partial R_i}{\partial h_j}\left(h_j^{l+1}-h_j^{l}\right)+\sum_{j}^{n}\frac{\partial R_i}{\partial X_j}\left(X_j^{l+1}-X_j^{l}\right)=-R_i^{l} \tag{3.21}$$

$$\sum_j^n \frac{\partial G_i}{\partial p_j}\left(p_j^{l+1}-p_j^l\right)+\sum_j^n \frac{\partial G_i}{\partial h_j}\left(h_j^{l+1}-h_j^l\right)+\sum_j^n \frac{\partial G_i}{\partial X_j}\left(X_j^{l+1}-X_j^l\right)=-G_i^l \tag{3.22}$$

$$\sum_j^n \frac{\partial H_i}{\partial p_j}\left(p_j^{l+1}-p_j^l\right)+\sum_j^n \frac{\partial H_i}{\partial h_j}\left(h_j^{l+1}-h_j^l\right)+\sum_j^n \frac{\partial H_i}{\partial X_j}\left(X_j^{l+1}-X_j^l\right)=-H_i^l \tag{3.23}$$

Here $l + 1$ refers to pressure, specific enthalpy and salt composition after the next iteration step at time $t + \Delta t$. Since each nodal residuum value depends only on the adjacent mesh nodes that are connected by the elements, all other derivatives are zero and the resulting matrix is sparse. Since we use an implicit numerical method, these derivatives have to be calculated every time before solving the linear system of equations.

3.3.7 Calculation of Darcy velocity at segments

When modelling phase separation phenomena, fluid properties between two neighboring grid nodes can vary over orders of magnitudes, especially when different phases exist on nodes or when large gradients in salt content occur. Therefore, the density at the segment, which is used for calculating fluid flow directions $\left(\nabla p-\rho_{\mathrm{f}}\vec{\mathbf{g}}\right)$, should account for salt content at the upwind node and also for the temperature gradient. Therefore we calculate a density for each phase and for the nodes on both sides of the segment:

$$\rho_{\mathrm{f}1,\mathrm{seg}}=0.5\rho_{\mathrm{f}1}+0.5\rho_{\mathrm{f}}\left(p_2,T_2,X_1\right) \tag{3.24}$$

$$\rho_{\mathrm{f}2,\mathrm{seg}}=0.5\rho_{\mathrm{f}2}+0.5\rho_{\mathrm{f}}\left(p_1,T_1,X_2\right) \tag{3.25}$$

We use $\rho_{\mathrm{f1,seg}}$ for calculating fluid fluxes if node 1 is the upwind node and $\rho_{\mathrm{f2,seg}}$ if node 2 is the upwind node.

Often a vapor phase is flowing into a colder control volume without a vapor phase so that no vapor density can be calculated there. For avoiding extreme vapor velocities flowing into cold CV at pressure conditions below 22.7 MPa, we use the following equation for calculating the density of a vapor phase at a segment.

$$\begin{aligned}
&\rho_{\mathrm{v1,seg}}=0.5\rho_{\mathrm{v1}}+0.5\left(w\rho\left(p_2,T_2,X_{\mathrm{cc}}\right)+\left(1-w\right)\rho_{\mathrm{v,boil}}\right) \\
&w=1 && \forall T_2<T_{\mathrm{boil}}-15\ ^\circ\mathrm{C} \\
&w=0 && \forall T_2>T_{\mathrm{boil}}-5\ ^\circ\mathrm{C} \\
&w=\left(T_{\mathrm{boil}}-T_2-5\ ^\circ\mathrm{C}\right)/10\ ^\circ\mathrm{C} && \text{otherwise}
\end{aligned} \tag{3.26}$$

Note that boiling temperature T_{boil} and vapor density $\rho_{\mathrm{v,boil}}$ are a function of fluid pressure. X_{cc} is the salt content of a fluid at the critical curve (Fig. 3.2) for a given pressure p_2. This formulation takes into account the high difference between liquid and vapor densities and leads to a better convergence of the Newton-Raphson scheme. In Fig. 3.5 we show a result of expression (3.26) for a pressure p_2 of 15 MPa.

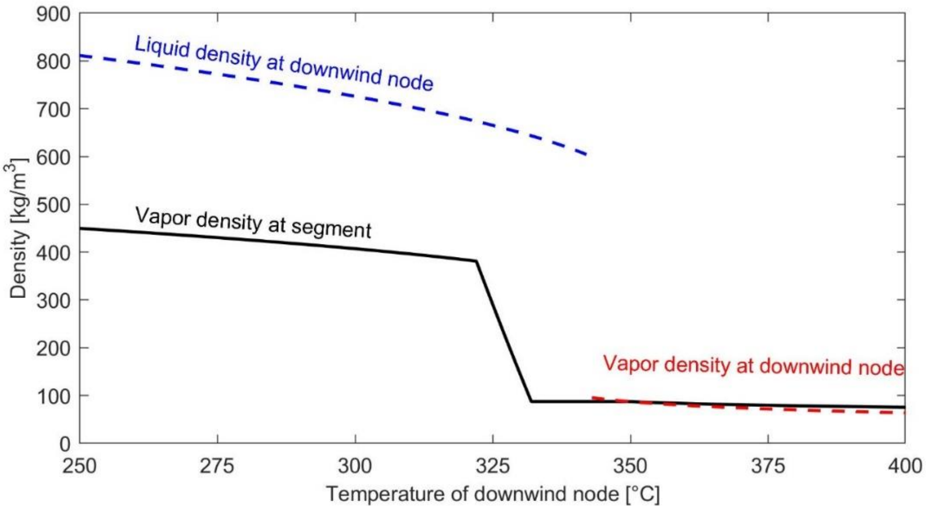

Figure 3.5: Vapor density at the segment as a function of downwind node temperature T_2 at a pressure p_2 of 15 MPa using expression (3.26). The upwind node has a temperature of T_1 = 350 °C, salt content of X_1 = 0 wt% NaCl and a vapor density of ρ_{v1} = 87.2 kg/m³.

When the phase exists at the upstream side, we calculate fluxes over the segment using the upstream weighting method for fluid enthalpy, viscosity, relative permeability and salt content. The density that is multiplied with the fluid velocity is also upwind weighted. We prefer full upwind weighting, because we want to avoid numerical oscillations in salt composition. Additionally, when a phase does not exist at the downstream node, we save computing time by not creating synthetically downstream fluid properties.

3.3.8 Permeability and relative phase permeability

When halite precipitates and fills up the pore space, rock permeability decreases. We have implemented the following function for the reduced permeability k_i, which is also used in TOUGH2 (Pruess et al., 2012):

$$k_i = k(1-S_\mathrm{h})^2 \tag{3.27}$$

We computed permeability at segments using a logarithmic average, as it can vary over orders of magnitudes:

$$k_\mathrm{seg} = \exp\left(\frac{\ln\left(k_{i,\mathrm{up}}\right)+\ln\left(k_{i,\mathrm{do}}\right)}{2}\right) \tag{3.28}$$

When permeability gets very low due to a high halite saturation, convergence of the Newton-Raphson scheme can become slow, especially for finding a good pressure solution for mass conservation. Therefore we define a halite saturation threshold $S_\mathrm{h,max}$, and if it is exceeded, we set the permeability k_seg to zero for all segments around this point. We then stop solving for mass and salt mass conservation at theses nodes, but still solve for energy conservation by heat conduction. In the presented examples $S_\mathrm{h,max}$ is set to 0.95. This value is lower than required for numerical stability but it is a reasonable assumption for submarine hydrothermal systems that permeability drops to very low values at such high halite saturations.

When calculating relative permeability for liquid and vapor phase ($k_{r\mathrm{l}}$ and $k_{r\mathrm{v}}$, resp.), we implemented a function in which the relative permeability is not additionally reduced by halite precipitation, because this is already accounted for in rock permeability (Eq. 3.28). Therefore, relative liquid permeability is a linear function from 0 to 1, when $S_\mathrm{l}/(1-S_\mathrm{h})$ exceeds the residual liquid saturation S_lr:

$$\begin{aligned} k_{r\mathrm{l}} &= \frac{S_\mathrm{l}/(1-S_\mathrm{h})-S_\mathrm{lr}}{1-S_\mathrm{lr}} && \forall\, S_\mathrm{l}/(1-S_\mathrm{h}) > S_\mathrm{lr} \\ k_{r\mathrm{l}} &= 0 && \forall\, S_\mathrm{l}/(1-S_\mathrm{h}) \le S_\mathrm{lr} \end{aligned} \tag{3.29}$$

$$k_{r\mathrm{v}} = S_\mathrm{v}/(1-S_\mathrm{h}) \tag{3.30}$$

3.3.9 Calculating fluid (salt) mass and energy in control volume

When modelling phase separation phenomena, salt composition varies over orders of magnitudes between adjacent nodes. For calculating the salt mass stored in a CV, we only use fluid properties of the node associated to the CV. Using the area of the CV we compute fluid (salt) mass and energy as follows:

$$\int_{\Omega_i} \Phi\rho_\mathrm{m}\,\mathrm{d}\Omega = \Phi_i\rho_{\mathrm{m},i}\Omega_i \tag{3.31}$$

$$\int_{\Omega_i} \left(\Phi\rho_\mathrm{m}h + (1-\Phi)\rho_\mathrm{r}c_{p\mathrm{r}}T\right)\mathrm{d}\Omega = \left(\Phi_i\rho_{\mathrm{m},i}h_i + (1-\Phi_i)\rho_\mathrm{r}c_{p\mathrm{r}}T_i\right)\Omega_i \tag{3.32}$$

$$\int_{\Omega_i} \Phi\rho_\mathrm{m}X\,\mathrm{d}\Omega = \Phi_i\rho_{\mathrm{m},i}X_i\Omega_i \tag{3.33}$$

3.3.10 Convergence criterion and error tracking

It is a challenging task to find good convergence criteria for the NR-approach, when fluid properties and time step size vary over order of magnitudes. For the mass and salt mass conservation we calculate an error of mass per square meter pore space over the time step Δt in a CV of size Ω_i:

$$\|R_i\|_\mathrm{a} := \frac{\Delta t}{\Omega_i\Phi_i}R_i \qquad \left[\frac{\mathrm{kg}}{\mathrm{m}^2}\right] \tag{3.34}$$

As density and salt content could become very small, we need a second criterion, where we normalize the error by density or respectively density and composition:

$$\|R_i\|_\mathrm{b} := \frac{\|R_i\|_\mathrm{a}}{\rho_{\mathrm{m},i}} \tag{3.35}$$

$$\|H_i\|_\mathrm{c} := \frac{\|H_i\|_\mathrm{a}}{\rho_{\mathrm{m},i}X_i} \tag{3.36}$$

For energy conservation we find that it is sufficient to work with an error displaying joule per square meter.

$$\left\|G_i\right\|_{\mathrm{d}} = \frac{\Delta t}{\Omega_i} G_i \qquad \left[\frac{\mathrm{J}}{\mathrm{m}^2}\right] \tag{3.37}$$

We use following magnitude of criteria:

$$\begin{aligned} &\left\|R_i\right\|_{\mathrm{a}} := 1\frac{kg}{m^2} \qquad \left\|H_i\right\|_{\mathrm{a}} := \frac{\left\|R_i\right\|_1}{3} \\ &\left\|R_i\right\|_{\mathrm{b}} := 0.01 \quad \left\|H_i\right\|_{\mathrm{c}} := 0.01 \qquad \left\|G_i\right\|_{\mathrm{d}} := 10^5 \frac{\mathrm{J}}{\mathrm{m}^2} \end{aligned} \tag{3.38}$$

To ensure strict mass, energy and salt mass conservation we save the residual errors R_i, G_i and H_i and add them as source term for the next time step. Here we have to consider old and new time step sizes:

$$R_{i,\mathrm{source}} = R_i^{\mathrm{old}} \frac{\Delta t^{\mathrm{old}}}{\Delta t} \qquad G_{i,\mathrm{source}} = G_i^{\mathrm{old}} \frac{\Delta t^{\mathrm{old}}}{\Delta t} \qquad H_{i,\mathrm{source}} = H_i^{\mathrm{old}} \frac{\Delta t^{\mathrm{old}}}{\Delta t} \tag{3.39}$$

3.3.11 Model implementation and limitations

The implemented Newton-Raphson method shows slower convergence, when the residual conserving functions R_i, G_i and H_i have discontinuities, which can arise from CVs experiencing phase transitions or from discontinuities in the relative permeability functions. Additionally, convergence is reduced when derivatives of the residual functions with respect to primary variables of the same CV become relatively small or change sign. A combination of both problems occurs, for example, at the phase transition into the isothermal L+V+H region for G_i (energy conservation). Here, performance losses have to be accepted for code stabilization and convergence is achieved by reducing time step size and updating primary variables by reduced increments of the NR corrections until convergence.

For performance reasons we use pre-computed look-up tables on unstructured tetrahedral meshes for all fluid properties and their derivatives. Over each tetrahedron, fluid properties vary linearly and derivatives have constant values. This simple discretization can potentially lead to convergence problems and in some cases it may well be better to use the original correlation functions to compute the derivatives. However, this is computationally costly as the correlation functions are in PTX formulations and iterative procedures are necessary to obtain them in PHX space.

Additionally the correlation functions for vapor density and vapor enthalpy in (Driesner, 2007) show an unexpected “loop” very close to the critical point of water at very low salt content. The vapor densities show a peak of too high values and the vapor enthalpies a peak of too low values. As a preliminary workaround we use a coarser mesh near this region in the PHX space, which effectively linearizes fluid properties over the width of a tetrahedron.

We have implemented the entire multiphase model in MATLAB building upon the highly efficient MILAMIN and MUTILS tools (Dabrowski et al., 2008). An alternative would have been to implement the scheme using one of the existing FV libraries and/or transport models such as PFLOTRAN (Hammond et al., 2014), OpenFOAM (Weller et al., 1998), or DUNE/pdelab (Bastian et al., 2010). We had opted for MATLAB because it provided us with the most flexibility and low-level control with regard to numerical implementation details. We hope that the presented details, especially on upwinding and phase weighting, will help with future 3D work on coupled multiphase hydrothermal flow models that may again be based on MATLAB or established FV libraries.

We tested our implementation against benchmarks and published results obtained by other codes. The respective benchmarks for pure water flow under single- and two-phase conditions have been presented in Vehling et al. (2018). Benchmarking of the saltwater case is less straight-forward as the results strongly dependent on the implemented EOS, which is unfortunately different among the various published numerical models. We nevertheless show results of test cases used in previously published studies in the Appendix (section 3.7).

3.4 Simulation result

3.4.1 Model setup

We explore brine formation and mobilization in a simplified setup that mimics the situation at intermediate to fast-spreading ridges, where hydrothermal circulation is mainly driven by heat released from a cooling axial melt lens (AML). The depth of the AML varies between 1-3 kilometers beneath the seafloor and depends on magma supply as well as spreading rate (Morgan and Chen, 1993; Theissen-Krah et al., 2011). The hydrostatic fluid pressure on top of the AML can therefore vary over tens of MPa between different ridge systems. We have performed numerical simulations for two different top pressure boundary conditions, 35 MPa and 20 MPa, in a domain of 3 km width and 1 km high. The grid has in total 6200 nodes and a refinement at the bottom center of 10 m node distance.

The sidewalls and the bottom domain boundaries are impermeable and a fixed pressure boundary condition is used on top, which allows for free venting. Top inflow seawater temperature is 5 °C and salt content is 3.2 wt%. The initial domain temperature is a linear function from top (5 °C) to the bottom (100 °C). At the bottom we set a Gaussian shaped temperature boundary condition with a maximum of 700 °C in the center and ~300 °C at the sides:

$$T_{\text{bot}}\left(x\right) = 300\ {}^{\circ}\text{C} + \Delta T \cdot \exp\left(-\frac{x^2}{2\sigma^2}\right) \tag{3.40}$$

Here σ is set to 450 m and x is the lateral coordinate in the interval from -1500 m to 1500 m. ΔT is 400 °C. In addition, we assume the bottom row of control volumes to be impermeable so that heat transfer here occurs by conduction only. After 900 years, ΔT is linearly reduced to 300 °C over a time span of 50 years to explore the response of a basal brine layer to long-term variations in heat supply (Fig. 3.5). Rock permeability is a function of depth z:

$$k\left(z\right) = k_{\text{top}} \cdot \exp(b \cdot z) \tag{3.41}$$

where $k_{\text{top}} = 1.5 \cdot 10^{-14}\ \text{m}^2$ and $b = 0.0012$. We use a porosity of $\Phi = 0.03$, a rock heat capacity of $c_{p\text{r}} = 880$ J/(kg K), a rock thermal conductivity of $K = 2$ W/(m K) and a rock density of $\rho_{\text{r}} = 2700\ \text{kg/m}^3$. The residual saturation of the liquid phase S_{lr} is set to 0.3.

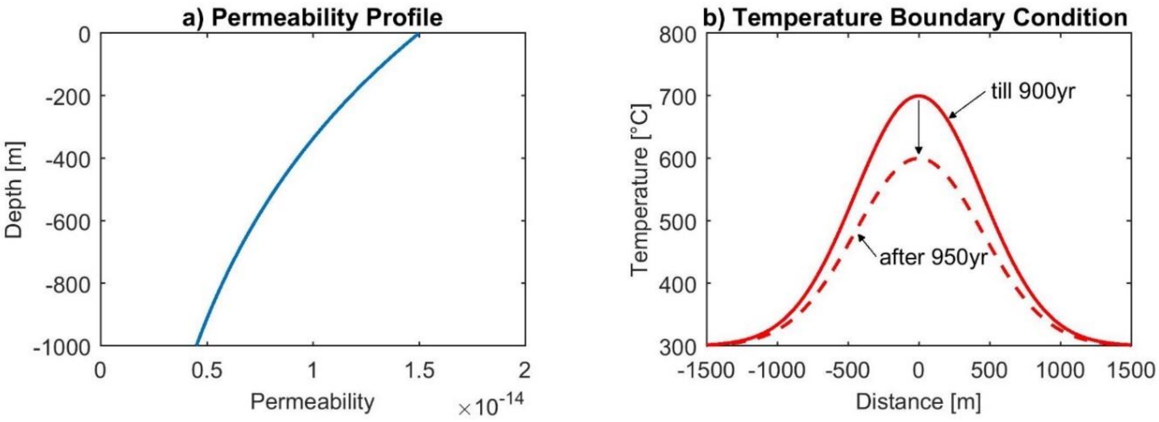

Figure 3.6: Rock permeability and temperature boundary conditions.

3.4.2 Simulation 1: High pressure conditions (35 MPa on top) lead to stable brine layer formation

The temperature boundary condition results in rapid heating within a central area of 1000 m width bringing the fluid into the two-phase regime. Figure 3.7a shows the situation after 300 years of heating: a basal brine phase containing up to 75 wt% NaCl has formed and the low-salinity vapor phase has merged with single-phase flow above, forming a large low-salinity region (1-1.5 wt% NaCl). As the salt signal travels at pore velocity and hence faster than the temperature signal, venting of low-salinity cold fluids occurs. Figure 3.7b and Figure 3.8a illustrate the stable quasi steady-state situation for this setup at t = 900 years. A stable basal brine layer has formed with little internal flow. Above it, and largely separated from it, single-phase high-temperature flow occurs at seawater salinity. In between, a thin two-phase region exists (Fig. 3.8a).

The central brine layer forms progressively from the bottom up. Brine saturations increase and two-phase flow occurs until the pore space is completely filled with brine. “Gaps” in the brine layer that can occur due to changes in the convective pattern are filled up by lateral spreading of brines. Once the pore space is completely filled with brine, active phase separation moves higher up, where brine saturations then start to increase. After 300 years the brine layer has its largest extension with a maximum height of 90 m. Due to this formation process, the brine salt content stays always very close to the liquid salt content side of the L+V coexisting surface (black surface in Fig. 3.2). No significant internal mixing of brines is observed and single-phase flow above is separated from the stably stratified brine layer.

The top of the brine layer is equal to the 462 °C isotherm (Fig. 3.8). At this temperature, vapor salinity at the L+V coexisting surface is equal to the seawater salt content of 3.2 wt% NaCl at 44 MPa. This implies that 462 °C is also the maximum temperature within the single-phase circulation system and that recharging fluids never experience phase separation once the system has reached this quasi-steady state. At this temperature the brine phase has a salt content of 19 wt% NaCl and a density of 686 kg/m^3, while the vapor phase has a density of 361 kg/m^3. This factor ~2 density contrast is shown in Fig. 3.9 and leads to an interface, where vapor-like fluids are divided and kept separate from the brines below.

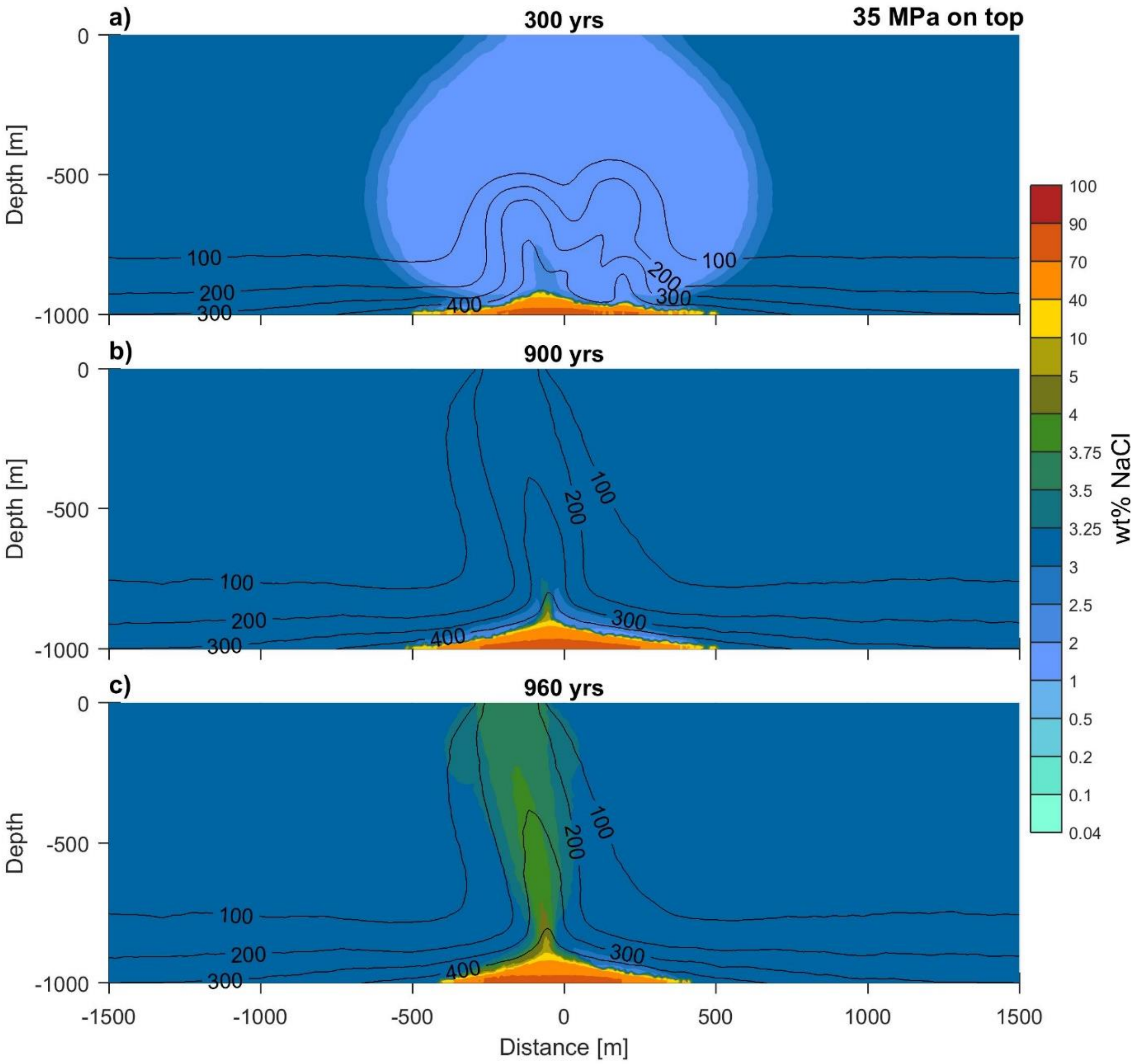

Figure 3.7: Simulation results for a top pressure of 35 MPa. Color plots of total salt content in the pore space in wt% NaCl and temperature contours in °C.

Figure 3.8 shows that the brine density increases with depth, which is a consequence of the increasing salt content with increasing pressure. Internal brine flow is therefore very low. At the top interface, brines are weakly affected by the overlying flow and are slowly flowing towards the central upflow zone (Fig. 3.8a). Lighter brines can flow upwards leaving the brine layer and heavier brines tend to flow very slowly downwards and then from the center toward the sides. The downward flowing brines become more saline and, as a result, very small amounts of vapor can form within the brine layer with saturation between 10^{-4} and 10^{-5}.

The brine layer itself acts as a thermal boundary layer. Over the first 40 years the total conductive heat flux into the domain decreases rapidly due to decreasing temperature gradients at the bottom. After 40 years, heat flux is further decreasing in concert with the increasing amount of salt accumulated in the basal brine layer (Fig. 3.10a). The formed low-salinity vapor phase mixes with single-phase flow above and after ~250 years low-salinity and low-temperature venting occurs. The temperature signal, being buffered by the host rock, travels slower and vent temperature only start to increase after 500 years. After the basal brine layer has reached its maximum extend, phase separation becomes limited as the single-phase circulation systems is effectively decoupled. Consequently, vent fluid salinities return to seawater values after approximately 600 years. When the temperature boundary condition is reduced after 900 years, the down flowing recharge fluids can merge with the brines at a lower temperature and therefore no formation of heavy brines and low salinity vapor occurs anymore (Fig. 3.8b). Instead, we find a higher mass flux of brines at the interface towards the center in between x-coordinate 60 m and 200 m. Also, deeper brines with high salinity are mobilized towards the center. These brines are further merging with recharge fluids and a single-phase high-salinity liquid of 5 to 10 wt% salt content forms that is sufficiently buoyant to rise. This merging process occurs over a very small temperature interval of 457−462 °C (T = 462 °C is temperature at critical curve at 44 MPa). At these temperatures, vapors have a relatively high salt content of 4 to 5 wt% (red arrows in Fig. 3.8b and Fig. 3.3c, d). Fluids of such high salinity, do not reach the surface but rather mix with ambient seawater resulting in vent fluid salinities of only 3.5 wt%. Such mixing of ascending fluids is further amplified by the increasing permeability towards the seafloor.

This mobilization of the brine phase in response to a decreasing bottom temperature results in a shrinking of the basal thermal boundary layer so that the 462 °C isotherm stabilizes at a deeper level. As a consequence, the bottom heat flow starts to increase again after 950 years and reaches nearly the old level after 1100 years (Fig. 3.10a) highlighting the importance of brine formation and mobilization in modulating heat input into the hydrothermal system. We have repeated the numerical experiment with a reduced permeability k_{top} of 10^{-14} m^2 and obtained the expected result of a 15 m thicker basal brine layer. This confirms the arguments stated above that brine layer thickness is controlled by the balance between conductive heat flux from below and heat carried by the hydrothermal circulation system, which in turn is controlled by permeability.

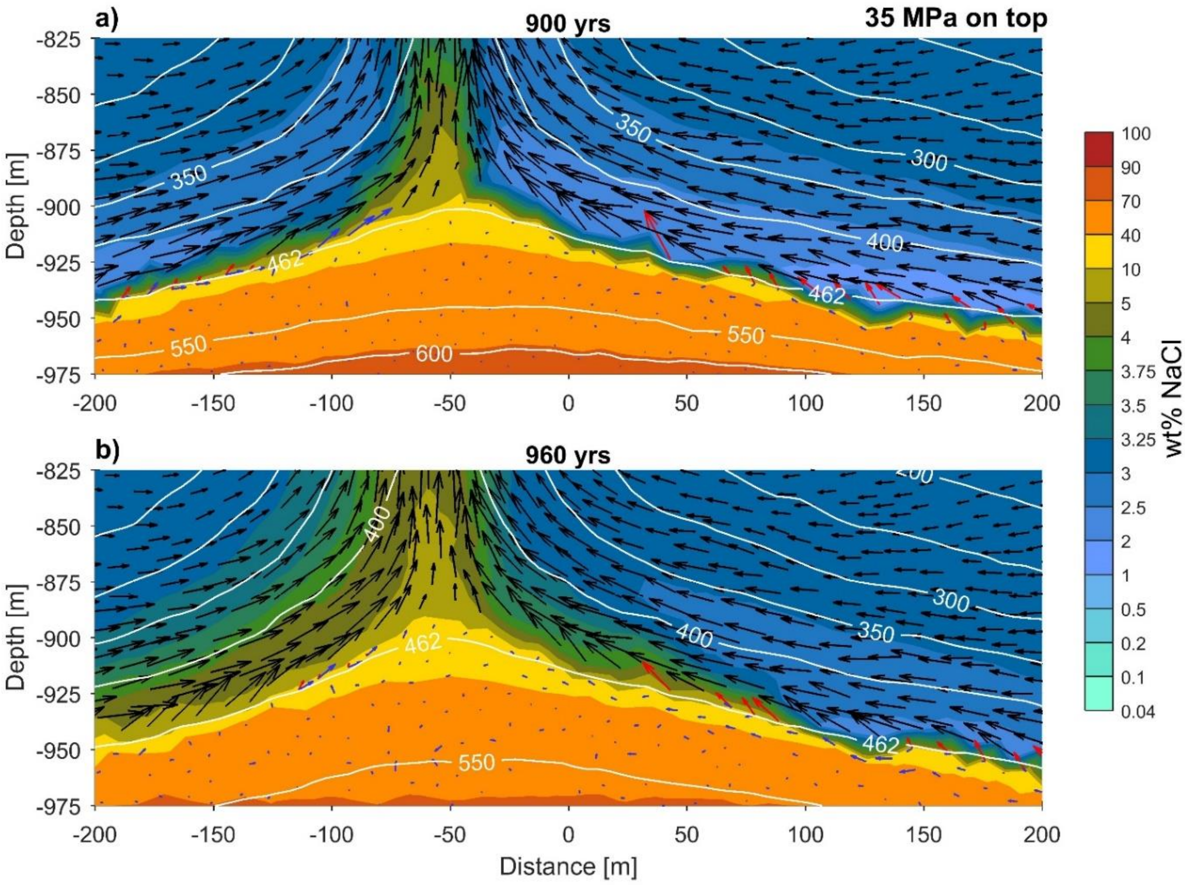

Figure 3.8: Scaled up color plot of salt content and mass fluxes for a top pressure of 35 MPa. Black arrows display liquids of $X < 10$ wt% NaCl. Blue arrows display liquids of $X > 10$ wt% NaCl. Red arrows display vapor (see definition for vapor in Section 3.4). Note that vapor can have up to 10 wt% NaCl at pressures of 45 MPa (see starting point of large red arrow in b) at 45 m with ~5 wt% NaCl). Arrow lengths have same scale factor for all colors. White contour lines show isotherms in °C.

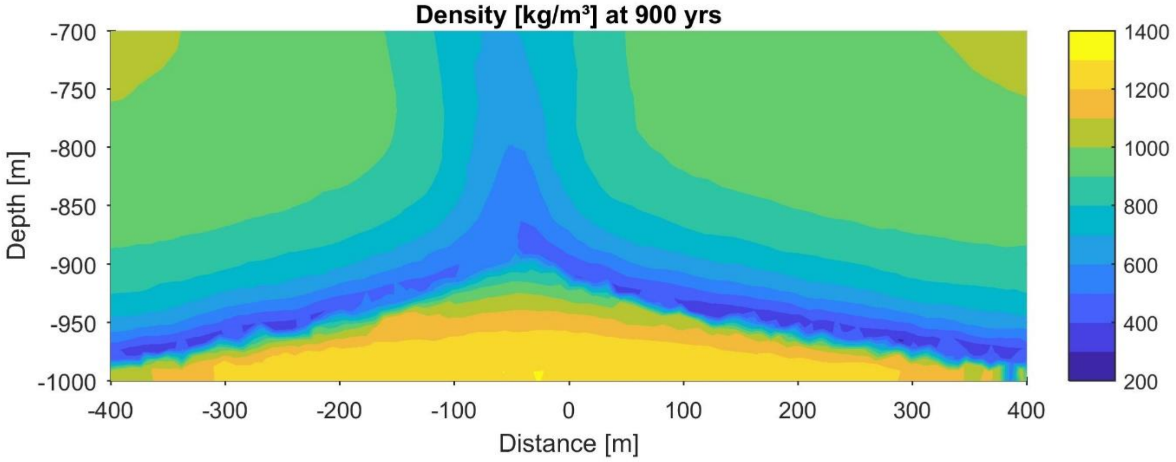

Figure 3.9: Fluid density and bulk density at L+V coexisting region

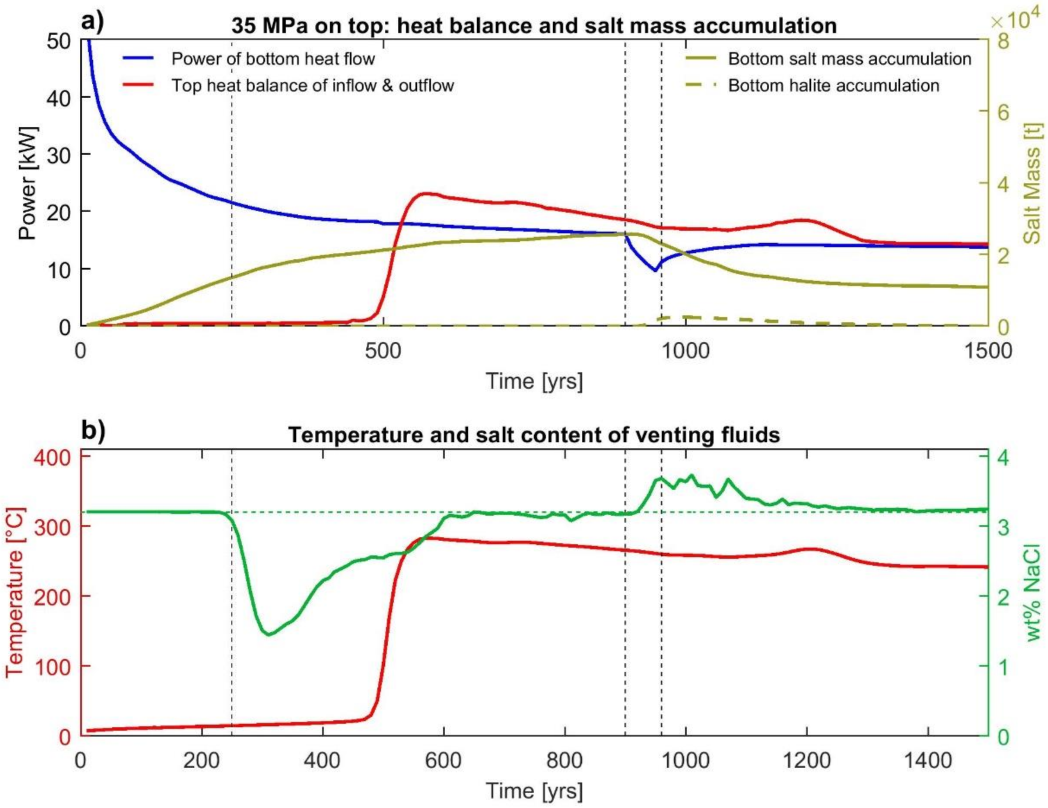

Figure 3.10: Simulation results for top pressure of 35 MPa. **a)** Blue line: total power of conductive heat flow from bottom nodes into domain. Red line: Top power balance of inflow and outflow. Dark yellow line: Bottom salt mass accumulation by considering halite and liquids with more than 10 wt% NaCl. Unit is tons of salt. Dashed black lines show the points in time pictured in Figure 3.7. **b)** Red line: Maximum outflow temperature. Green line: salt content of fluid with maximal outflow temperature. After 900 years, the green line shows maximal salt content of outflow. Green dashed line show seawater salt content.

3.4.3 Simulation 2: Mid pressure conditions (20 MPa on top) lead to a brine layer on top of a halite zone

A reduction in the top pressure boundary condition results in a change in the stable phase assemblages and the dynamics of basal brine formation. In the mid pressure set up, liquid-vapor separation is quickly followed by halite precipitation at the bottom. Here, at bottom pressures of 29 MPa, phase separation starts at temperatures of around 404 °C (Fig. 3.11 & Fig. 3.12). The rising vapor phase has a very low salt content of only 0.1 wt% (at a temperature of 435 °C). Therefore, salt is rapidly accumulating at the bottom within the forming brine phase, whereas the rising vapor phase mixes with seawater resulting in a central upflow zone with salt contents of 0.3 to 1 wt% after 250 years, which is lower than in the high pressure case presented above (Fig. 3.11a). The basal brine phase has a salt content of up to 55 wt% and, upon further heating to a temperature of 476.4 °C, enters three-phase conditions where liquid, vapor, and halite coexist (Fig. 3.3c). During further heating, the fluid leaves the three-phase region and the brine phase becomes separated into vapor and halite (upon entering the V+H field, Fig. 3.3c). Above the V+H region, brines that formed during phase separation within heated recharge fluids are slowly flowing (no visible blue arrows) into the V+H region where the salt of the brine is deposited as halite (Fig. 3.12a; dark red color at 100 m to 200 m). This process results in a clogging of the pore space, which progressively blocks the pathways for heat mining vapors.

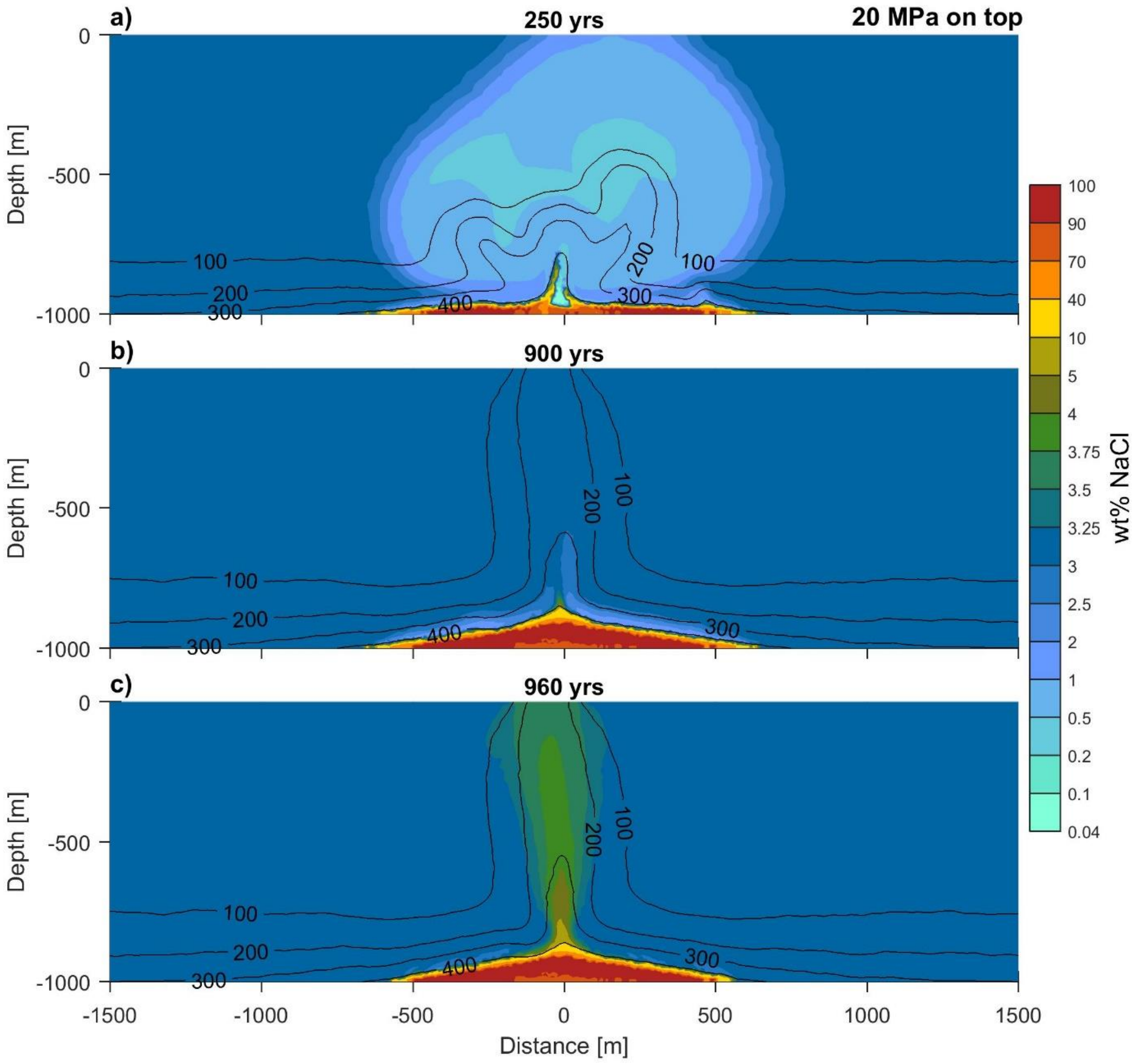

Figure 3.11: Simulation results for a top pressure of 20 MPa. Color plots of total salt content in pore space in wt% NaCl and temperature contours in °C.

Figure 3.13 shows that the V+H region is continuously growing and halite saturation reach values >90%. Also brine saturations in the overlying L+V region reach values of more than 95%. Compared to the high-pressure simulation the amount of salt accumulated in this basal boundary region is 3.5 times higher and consequently the salt content of venting fluids is substantially lower. After 900 years, a 20 m to 30 m thick brine layer has formed. This brine layer is less effectively separated from the overlying single-phase flow as it was in the high-pressure experiment (Fig. 3.12b). The reason is that the layer is thinner and that the density contrast to the above single-phase fluid is smaller. At 400°C, the low-salinity single-phase liquids (black arrows) and the vapor phase have similar flow directions and form a thin two-phase flow region that connects overlying convection with the brine layer. Yet, the hot brines (>400 °C) have a higher viscosity and a reduced buoyancy so that entrainment into the upflow zone is still very limited. Therefore, temperatures within the up flow zone never exceed 400 °C. Compared to the high pressure simulation, the total basal heat input is in steady-state state and 15% lower (Fig. 3.14a & Fig. 3.15).

When the temperature boundary condition is reduced after 900 yrs, brines are mobilized into the upflow zone at a rate that is similar to the high-pressure experiment. For the simulation time span between

950 yrs and 1100 yrs, a comparison of Figure 3.10 and Figure 3.14 reveals the same decline of bottom salt mass for both simulations. The reduced heat flow from below results in the merging of recharge fluids with brines at colder temperatures under single-phase conditions. Here, also brines with 5 to 10% salt are sufficiently buoyant for feeding the up flow zone, whereas brines with higher salt contents have to be diluted before they can rise. Figure 3.14a show that halite is constantly dissolved by diluted brines and that brine venting occurs for a longer period of time with respect to the high-pressure experiment.

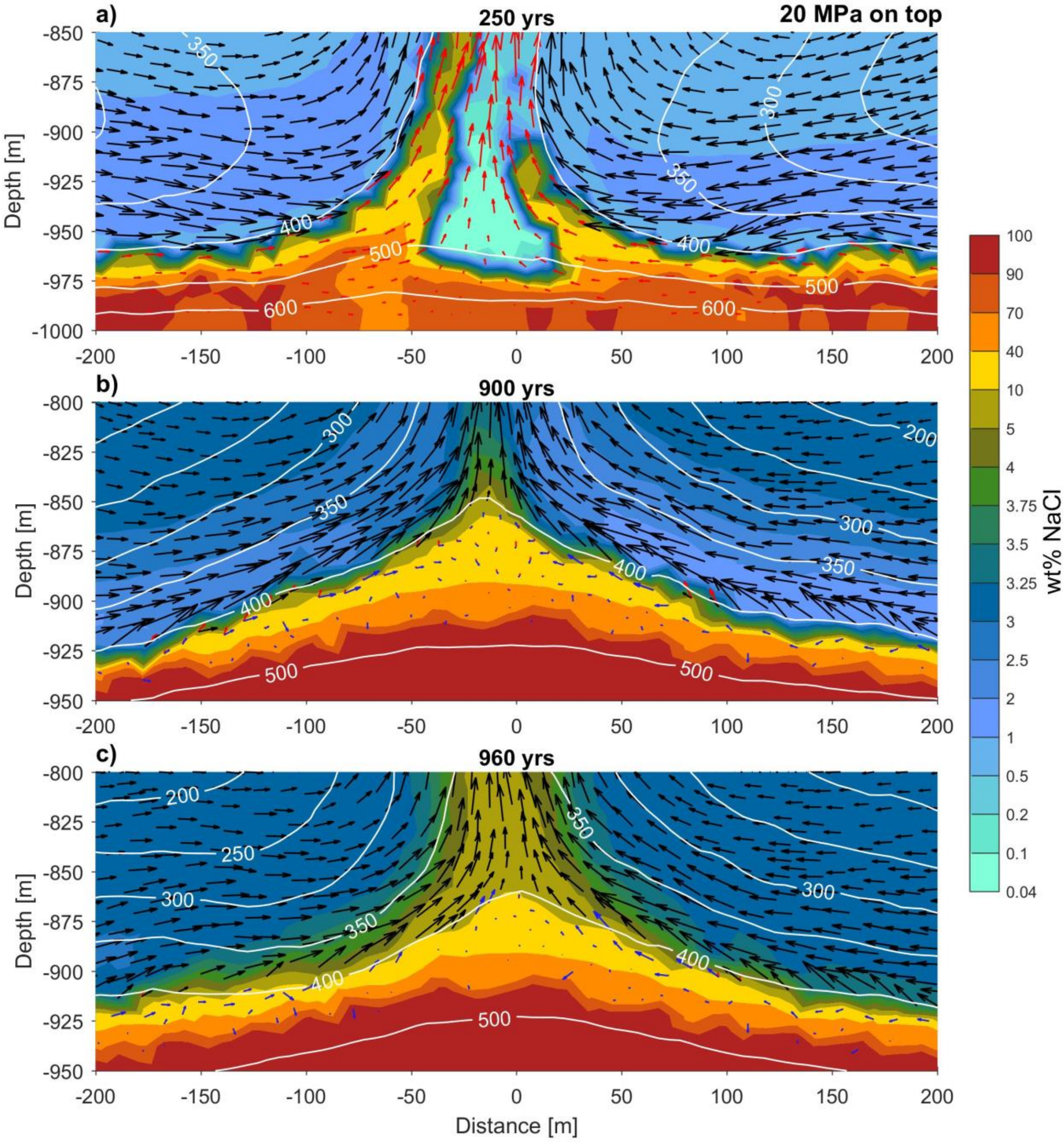

Figure 3.12: Scaled up color plot of total salt content and mass fluxes for a top pressure of 20 MPa. Black arrows display liquids of $X < 10$ wt% NaCl. Blue arrows display liquids of $X > 10$ wt% NaCl. Red arrows display vapor (see definition for vapor in Section 3.3.3). Arrow lengths have same scale factor for all colors. White contour lines show isotherms in °C.

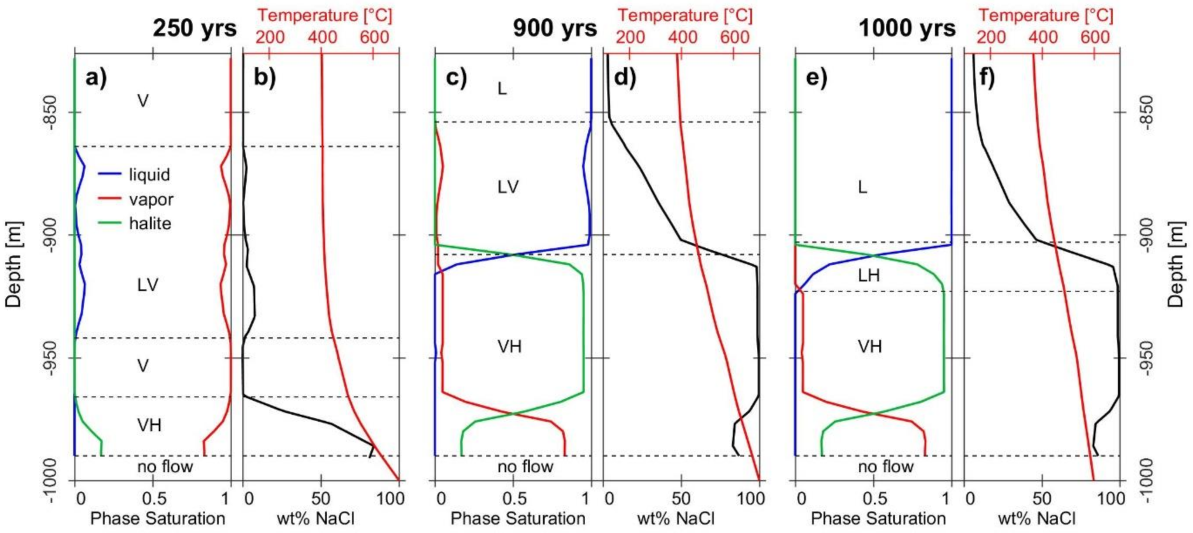

Figure 3.13: Simulation results for a top pressure of 20 MPa at central profiles from -825 m to -1000 m depth after 250 yrs, 900 yrs and 1000 yrs. **a), c), e)** Phase saturation with coexisting phase regions. **b), d), f)** fluid temperature and total salt content of pore space.

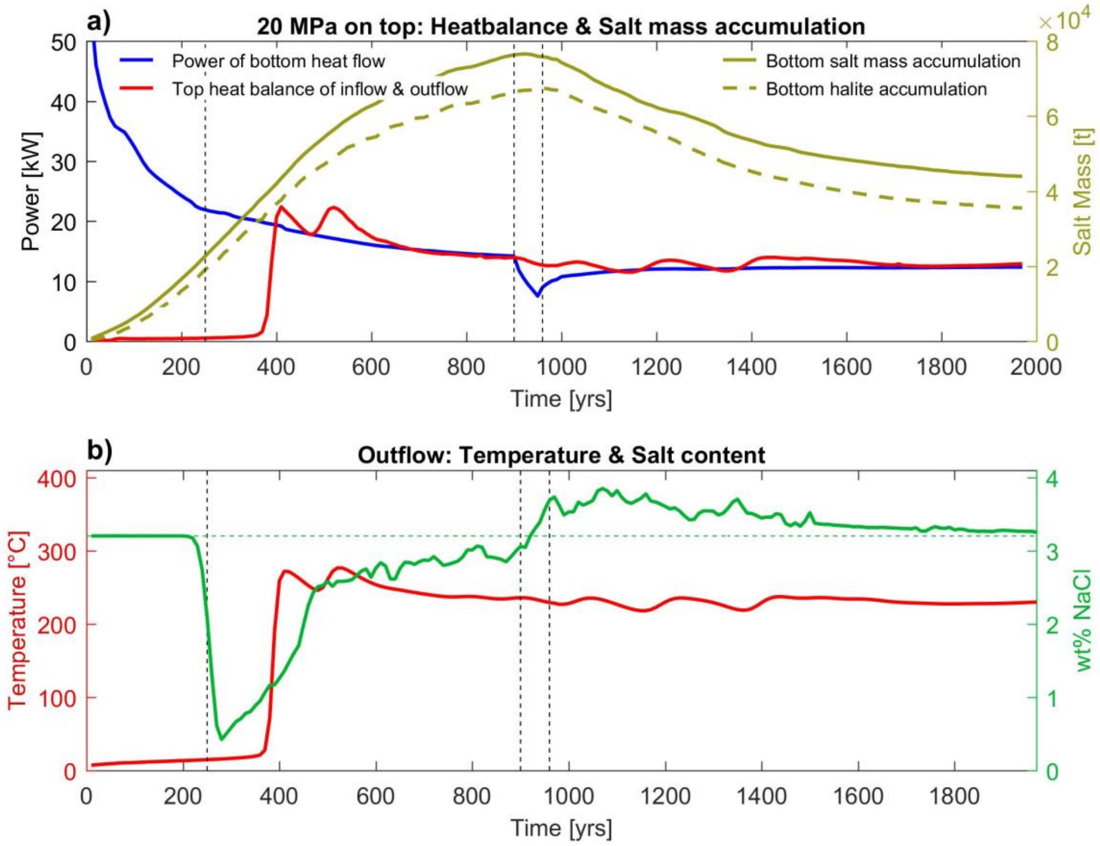

Figure 3.14: Simulation results for a top pressure of 20 MPa. **a)** Blue line: total power of conductive heat flow from bottom into the domain. Red line: Top power balance of inflow and outflow. Dark yellow line: Bottom salt mass accumulation by considering liquids with more than 10 wt% NaCl, and halite. Unit is tons of pure salt. Dashed black lines show points of time pictured in Figure 3.7. **b)** Red line: Maximum outflow temperature. Green line: salt content of fluid with maximal outflow temperature. After 900 years the green line shows maximal salt content of outflow. Green dashed line show seawater salt content.

3.5 Discussion

We have presented a novel coupled scheme of solving the governing conservation equations of hydrothermal transport in the system H_2O−NaCl. This methodology is an extension of the pure water model recently presented by Vehling et al. (2018). A key ingredient of this methodology is the mapping of the PTX equation-of-state presented by Driesner and Heinrich (2007) into PHX space, which allows resolving isothermal phase transitions like pure water boiling and liquid-vapor-halite coexistence. The governing conservation equations are solved simultaneously and implicitly, which allows for larger-than-explicit time-steps and for a direct control of the numerical error. However, quantifying the concrete strengths and limitations of this method requires an inter-code comparison with previous models that is beyond the scope of this paper.

Here we have presented a first application and investigate how brine formation and mobilization affect heat transport in a submarine hydrothermal system heated from below. We find that a basal internally stable stratified brine layer progressively forms with a maximum vertical extent that is controlled by a balance between basal heat input and hydrothermal heat transport. It is the vertical extent of this stable layer that controls heat transfer from a heat source below into the active circulation system above. The layer thickness is controlled by the stable phase assemblages (e.g. V+H versus V+L in the presented mid- and high-pressure simulations above), the bottom temperature boundary condition, and the permeability within the flow zone. How the different phase transitions affect heat input can be exemplified by comparing the mid- and high-pressure simulations. The temperature boundary condition and permeability structure is the same in both simulations, yet the heat input is different (Fig. 3.15). Up to simulation time 150 yrs, the mid pressure simulation has a 20% higher central heat flow because boiling occurs at lower temperatures and the formed vapor phase drives small-scale circulation, which results in a higher heat flux (Fig. 3.15b). This effect is reduced when brines and halite build up a conductive boundary layer. After 400 yrs, simulation 1 has a higher heat input because the recharge flow can be heated up to 462 °C (versus 400 °C in simulation 2) and hence has a higher enthalpy and can extract more heat from the conductive layer. Consequently, the layer is thinner and has a higher temperature gradient. When the simulations approach a steady-state at about 800 yrs and after 1400 yrs, the mid pressure simulation has an about 20% lower heat input.

Permeability directly controls the vigor of hydrothermal convection and thereby heat transport. The higher the permeability, the more effective heat transport becomes, and the thinner is the basal brine layer. This is exemplified by the predicted heat input of two models with different permeability shown (Fig. 3.16). Figure 3.16 further shows a comparison between a pure water model and simulation 1 for seawater. The predicted total basal heat input is about 25% higher in the pure water simulation. This shows the effectiveness of a basal brine layer in insulating the driving heat source. The progressive accumulation of a basal brine layer therefore reduces the conductive heat loss from the heat source.

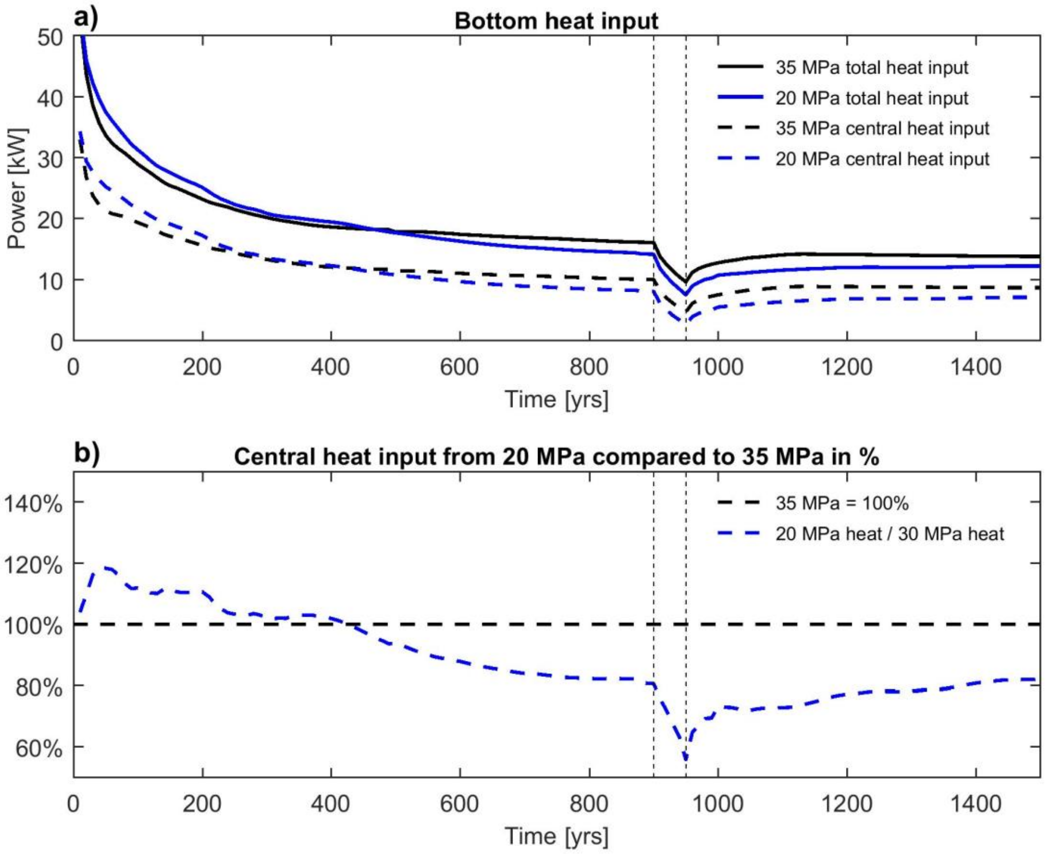

Figure 3.15: Total bottom heat input and **b)** central [-600 m, +600 m**]** heat input comparison. Vertical dashed lines mark the change in the temperature boundary condition between 900 yrs and 950 yrs.

The total steady heat flux of our simulations integrated over 1 kilometer along the ridge axis are 16 MW for the high-pressure and 14 MW for the mid-pressure simulation. Theoretical calculations of total heat flux released by crustal accretion and cooling for fast spreading ridges of 10 cm/yr are in the range of 44 MW to 71 MW per 1 km ridge axis (Fontaine et al., 2017) depending on whether lower crustal hydrothermal cooling is taking into account. Our predicted values are substantially lower, which may be due to relatively low values of permeability and/or transient as well as 2-D versus 3-D effects. Hydrothermal fields with the highest heat fluxes like Main Field Endeavour (450 MW) and EPR 9°50’N (160 MW) (Lowell et al., 2013) are related to recent magmatic eruptions and a high melt input to the AML. Coming back to the paradox of sustaining high heat fluxes despite the rapid formation of a basal brine layer (Fontaine and Wilcock, 2006), our results show that brines are not leaving the base by entrainment into the up flow zone, which again illustrates the problem of reconciling high heat fluxes with rapid brine formation. We find that brines with salt contents of more than ~10 wt% are significantly less buoyant than heated recharge flow so that they cannot be entrained and mobilized. Brines with a salt content of less than ~10 wt% can be partially mobilized but are rapidly diluted.

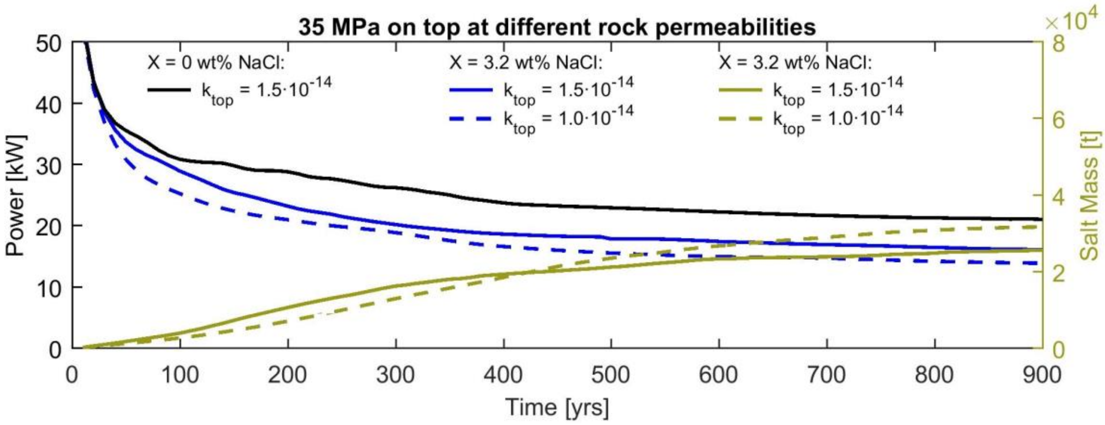

Figure 3.16: Blue lines: power of bottom heat flow. Dark yellow lines: Total salt mass accumulation by considering liquids with more than 10 wt% NaCl,

A possible solution to this conundrum is that brines are able to spread laterally. This requires a sufficient basal inclination and hot basal temperatures (within the two-phase region). A complementary possibility is that brines may be able to move to deeper crustal levels possibly along pathways newly formed by thermal cracking (Olive and Crone, 2018). At $T = 600$ °C (the approximate temperature at the brittle-ductile transition) and 45 MPa, brines have a density of ~1200 kg/m³, a salinity of ~70 wt% NaCl, and a viscosity of ~$2 \cdot 10^{-4}$ Pa·s (comparable to the viscosity of pure water at 150 °C and 45 MPa). They are therefore negatively buoyant and mobile providing good conditions for effective salt transport. This raises the interesting possibility of brine-redistribution to lower crustal levels. One possibility is along-axis brine flow driven by undulation in melt lens location and shape. Such variations in AML properties are shown in Xu et al. (2014) for EPR (9°30’N-10°00’N) and in (Canales et al., 2006) for the Juan de Fuca Ridge. Such along-axis brine flow may result in a “communication” between neighboring hydrothermal circulation cells. Another possibility is brine flow to deeper crustal levels perpendicular to the ridge-axis. For example, the inferred thermal structure at the EPR at 9°N (Dunn et al., 2000) may provide suitable conditions for the downward migration of the brine phase along the steep lateral margins of the central hot region – consistent with the proposed hybrid hydrothermal circulation model for fast spreading ridges (Hasenclever et al., 2014). Axis-perpendicular brine flow may also be related to off-axis melt lenses (OAML) close to the AML. Two mid-crustal OAMLs have been found within only 1.5 to 2.5 km lateral distance and at 200 m vertical distance from ridge axis at EPR 9°37.5’N to 9°57’N (Aghaei et al., 2017; Han et al., 2014). At the time of the seismic survey, these OAMLs had low melt fractions implicating that magma replenishment rates of the OAML are relatively low with respect to the AML. One of the discovered OAMLs has nevertheless appeared to have delivered the melts for extrusive eruptions. It is very likely that these OAML drive a hydrothermal circulation system with an independent up flow zone. Accumulation of an in-situ forming brine phase plus possibly down-flowing brines from the ridge axis may result in thermal insulation of OAMLs thereby helping to stabilize them despite a low melt supply. Testing these hypotheses require robust multiphase hydrothermal flow models and we hope that the presented methodology will help making multiphase flow models more accessible.

3.6 Conclusion

The presented modeling framework and its initial application to submarine hydrothermal systems illustrate the potential of coupled schemes in multiphase flow calculations. The benefits of this method are large time steps and an explicit error control in the mass and energy conservation over a time step. However, there are also some drawbacks that need to be addressed in future work. These include a review of the EOS and the corresponding derivatives in PHX space in order to improve the convergence behavior of coupled schemes and research into how iteration schemes can better handle isothermal phase boundaries, which are not buffered by the specific heat of the host rock.

The key findings of the application of the method to submarine hydrothermal systems heated from below are that 1) progressive brine formation limits conductive heat transfer from the driving heat source into the active circulation system, 2) the formation of a brine layer leads to the rapid decoupling of the basal two-phase flow region from an active single-phase convection cell above that feeds seafloor vent sites and 3) variations in basal heat supply can result in the mobilization of the brine phase and the venting of highly saline fluids. The implications of these findings are that pure water simulations may provide misleading results on heat transfer in submarine hydrothermal systems as they cannot resolve brine formation. The results further re-confirm the paradox of how very high heat fluxes as observed e.g. at the EPR at 9°N and at the JdF ridge can be sustained for a prolonged period of time given that a thick basal brine layer should rapidly insulate the driving heat source. These findings thereby illustrate the need for future integrated data-modeling work to better constrain the role of brines in modulating mass and energy transport in submarine hydrothermal systems.

3.7 Appendix

3.7.1 Thermohaline single phase convection

First we present two simple tests of a buoyancy-driven single phase flow. These thermohaline convection tests were also used by Geiger et al. (2006b) and had been originally published in (Oldenburg and Pruess, 1999). The comparison is particularly useful, as the Geiger et al. (2006b) model uses a very similar EOS. In these two tests, a fluid parcel of constant temperature and salinity is placed in the center of a 2D domain, first as a positively buoyant and secondly as a negatively buoyant anomaly (Fig. 3.17). The top of the domain is kept at a constant pressure and all other sides are closed (no flow). We use a regular mesh of 47x47 boxes, where each box is split into four triangles by adding an additional point in the box center. Compared to the mesh in Geiger et al. (2006b) with 4425 nodes, we get 4513 nodes for a similar spatial resolution. For test 1 (positive buoyancy) the initial parcel has a temperature of 300 °C and salinity of 10 wt% and for test 2 (negative buoyancy) a temperature of 250 °C and a salinity of 12 wt%.

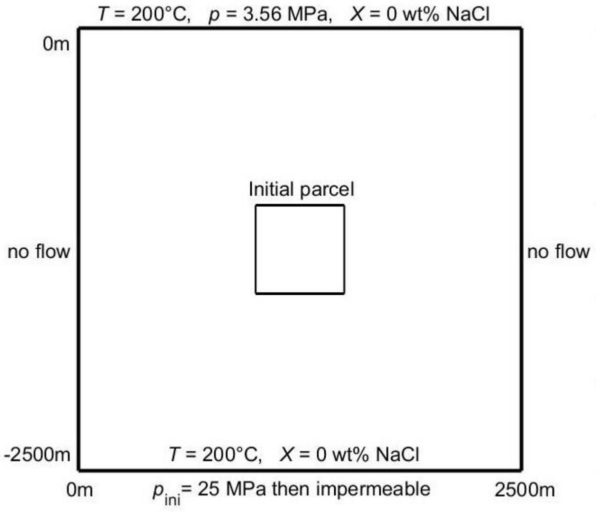

Figure 3.17: Model domain with initial and boundary condition after Oldenburg and Pruess (1999).

Table 3.2: Model parameter for thermohaline test

Properties	**Meaning**	**Value**	**Unit**
c_{pr}	specific rock heat capacity	1000	J/(kg·K)
D	salt diffusivity	10^{-8}	m/s^2
K	thermal conductivity	1.8	W/(m·K)
k	permeability	$5\cdot10^{-14}$	m^2
T	initial rock and fluid temperature	200	°C
X	initial mean salt composition	0.0	wt% NaCl
ρ_r	rock density	2650	kg/m^3
Φ	porosity	0.1	-

Our results show good overall agreement with those in (Geiger et al., 2006b). Differences are caused by different grids and mass transport schemes like upwind weighting of fluid properties. It should be noted that the numerical solutions of such compositional flows are known to suffer from a dependence on property weighting. Especially the second test of a negatively buoyant fluid is sensitive to this and the number of "falling drips" and their spacing is affected by grid resolution and segment density weighting, i.e. are model dependent (Figs. 3.18 & 3.19).

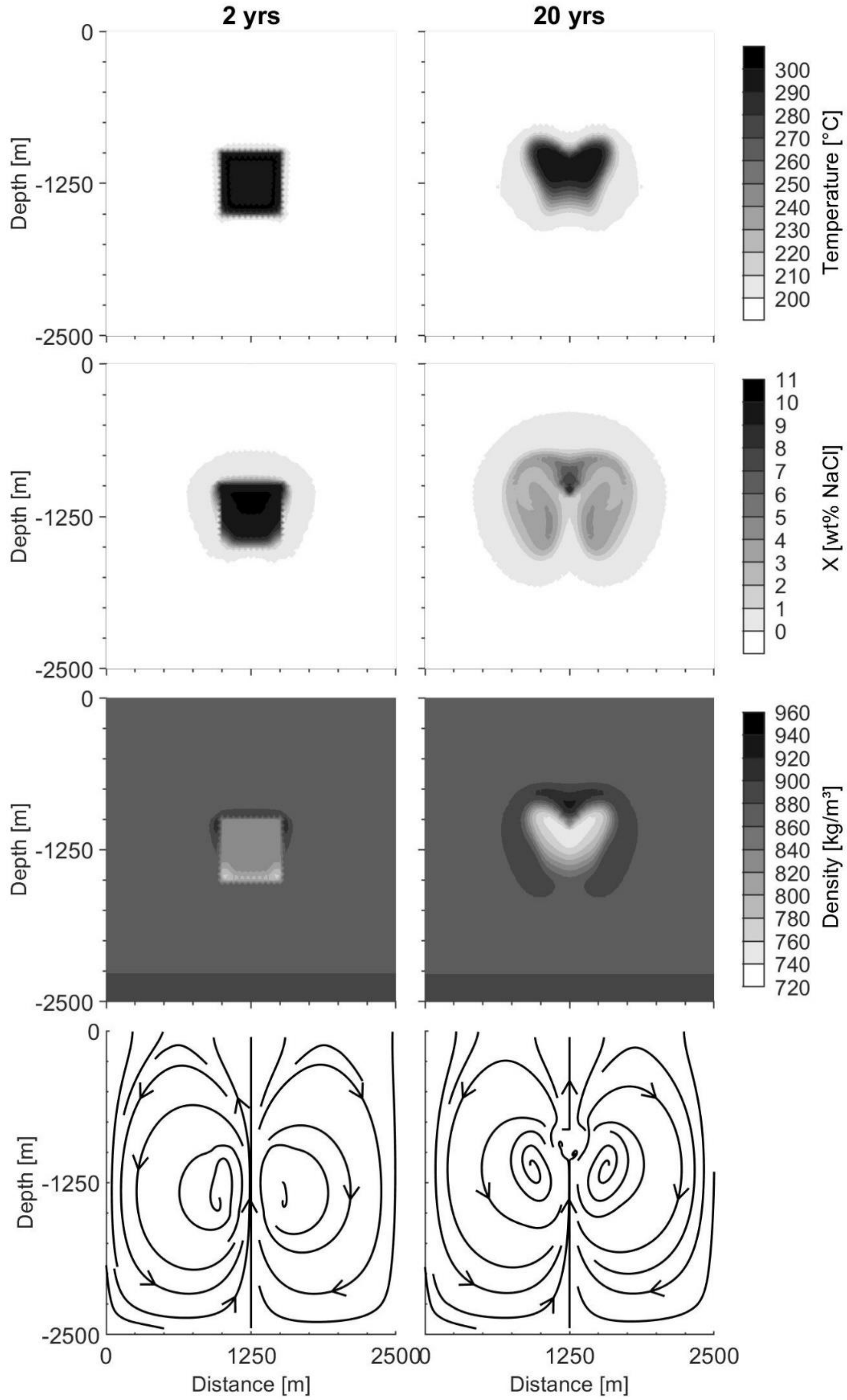

Figure 3.18: Test 1 after 2 yrs and 20 yrs simulation time. Lower panels show the velocity field.

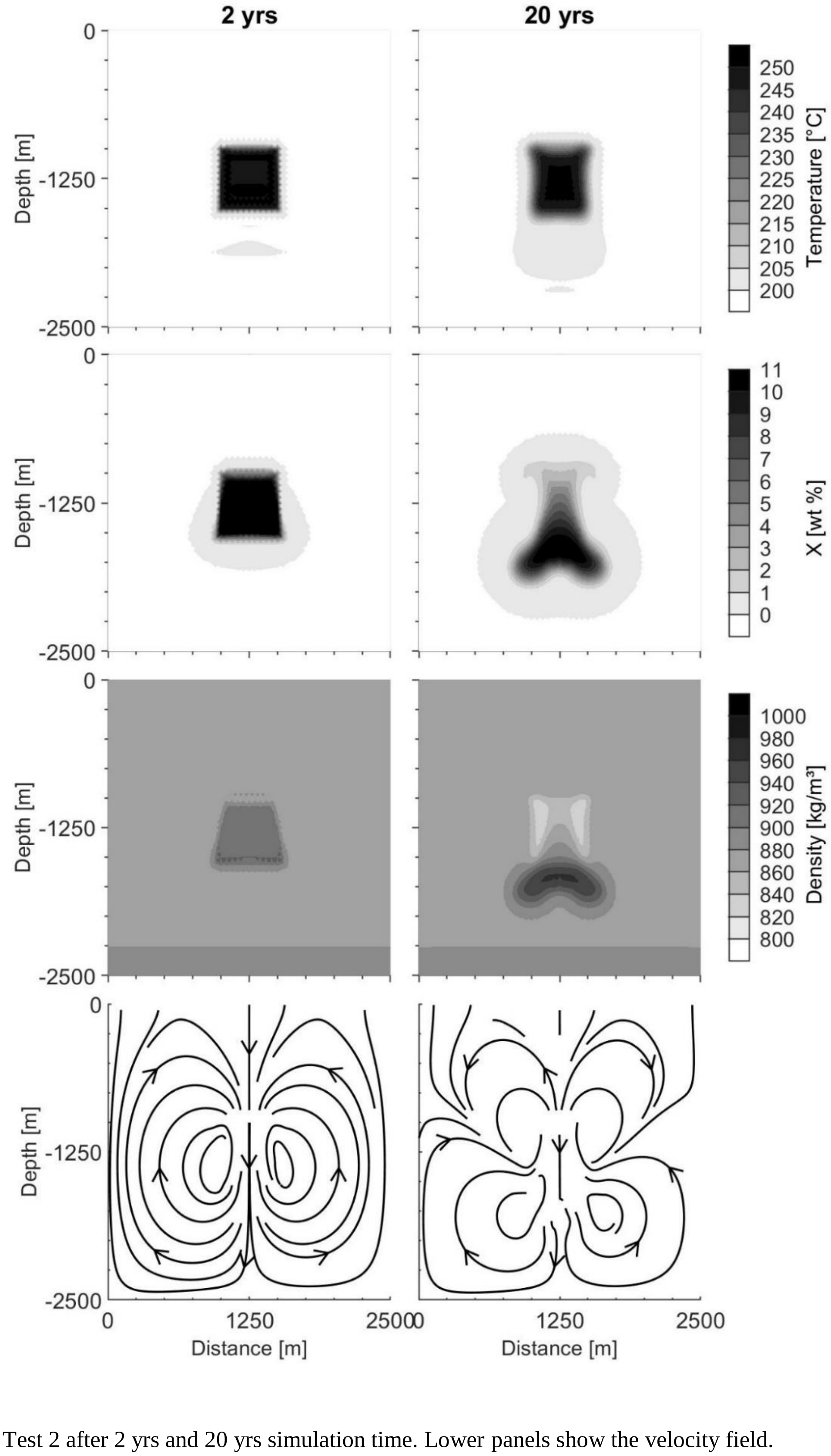

Figure 3.19: Test 2 after 2 yrs and 20 yrs simulation time. Lower panels show the velocity field.

3.7.2 One-dimensional multi-phase test with fluid extraction

The ability of the code to resolve two- and three-phase conditions is demonstrated in a 1-D test originally published by Kissling (2005a) and later also used by Lewis and Lowell (2009). A horizontal 1-D domain of 1000 m length is initially at constant pressure (p = 20 MPa), temperature (T = 350 °C) and salinity (X = 30 wt% NaCl). These conditions are kept constant at the left-hand boundary throughout the simulation. At the right-hand boundary, fluid is extracted at a rate of 0.0005 kg/(m²·s) until pressure is reaching almost zero after $4.8 \cdot 10^6$ s simulation time. During this drawdown experiment, a fluid flowing from left to right undergoes a series of phase transitions (L→ L+V → L+V+H → V+H). Relative permeability is set according to equations 3.29 and 3.30, while halite is assumed to not have an effect on flow in order to be consistent with Kissling (2005a). Because Kissling (2005a) used a different EOS, namely the one of Palliser and McKibbin (1998c), where brine viscosity is much higher, we reduce rock permeability to $3.05 \cdot 10^{-15}$ m^2 for a qualitative comparison of our results. This modification results in very similar pressure profiles but some differences remain due to differences in the phase densities and specific enthalpies (see also (Lewis and Lowell, 2009)).

Table 3.3: Model parameters for test in section 3.7.2

Properties	**Meaning**	**Value**	**Unit**
c_{pr}	specific rock heat capacity	1000	J/(kg·K)
K	conductivity	3	W/(m·K)
k	permeability Kissling	$5 \cdot 10^{-15}$	m²
k	permeability this study	$3.05 \cdot 10^{-15}$	m²
P	initial pressure	20	MPa
T	initial temperature	350	°C
X	initial salt composition	30	wt% NaCl
ρ_r	rock density	2650	kg/m³
Φ	porosity	0.01	-

Figure 3.20 shows our results when pressure at the right-hand boundary has reached 1 MPa after a simulation time of $4.793 \cdot 10^6$ s. The reduction in pressure induces phase transitions from single phase liquid to L+V, to L+V+H to V+H that cause a redistribution of salt and an accumulation of salt where halite is stable. The energy transport increases in the L+V+H region as a consequence of the increasing importance of vapor flow, which results in the strong temperature drop in the L+V+H region. While the pressure and the bulk salt concentration are relatively close to the solution presented Kissling (2005a), differences occur in the phase saturations. These differences result from different EOS for salt water and possibly due to the different numerical schemes. Note that TOUGH2 makes a switch in primary variables under two- and three-phase conditions. The test nevertheless shows the ability of our code to handle the continuous transitions between one-, two- and three-phase fluid states.

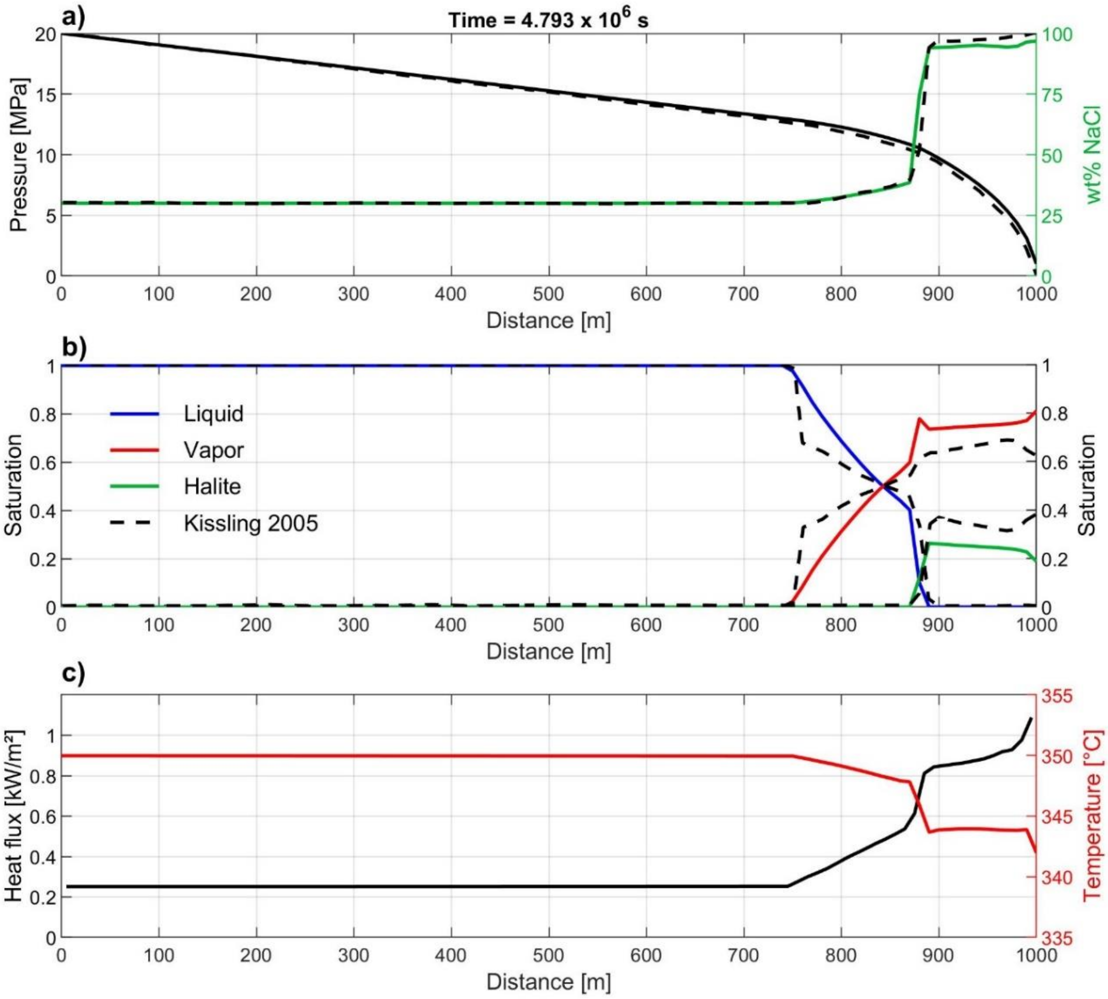

Figure 3.20: Results of a 1-D multi-phase experiment originally presented by Kissling (2005a). Fluid is extracted at the right-hand boundary triggering a sequence of phase transitions. While the pressure and salt solutions are similar to the ones presented by Kissling (2005a), differences occur in the phase saturations – mainly as a result of differences in the used equation-of-state. Lower panel plot shows in addition the temperature solution and how phase transitions affect horizontal energy transport.

3.7.3 One-dimensional vertical salt pipe

In this test case, originally performed in (Kissling, 2005a), we show that the code conserves mass for vertical counter flow of liquid and vapor. For the steady state of zero net mass flux one can analytically calculate the pressure gradient for given fluid properties by setting the sum of vapor mass flux and liquid mass flux to zero and solving for the pressure gradient:

$$0 = -k\frac{k_{\mathrm{rl}}\rho_{\mathrm{l}}}{\eta_{\mathrm{l}}}\left(\frac{\partial p}{\partial z}-\rho_{\mathrm{l}}\vec{\mathbf{g}}\right)-k\frac{k_{\mathrm{rv}}\rho_{\mathrm{v}}}{\eta_{\mathrm{v}}}\left(\frac{\partial p}{\partial z}-\rho_{\mathrm{v}}\vec{\mathbf{g}}\right) \tag{3.42}$$

$$\frac{\partial p}{\partial z}=\frac{\vec{\mathbf{g}}\left(k_{\mathrm{rl}}\rho_{\mathrm{l}}^{2}/\eta_{\mathrm{l}}+k_{\mathrm{rv}}\rho_{\mathrm{v}}^{2}/\eta_{\mathrm{v}}\right)}{k_{\mathrm{rl}}\rho_{\mathrm{l}}/\eta_{\mathrm{l}}+k_{\mathrm{rv}}\rho_{\mathrm{v}}/\eta_{\mathrm{v}}} \tag{3.43}$$

The model setup is adopted from Kissling (2005a), where the simulation is performed on a grid of 100 m with a node spacing of 1 m. The top boundary has a fixed pressure (p = 60 MPa) and temperature (T = 600 °C). Additionally liquid saturation is fixed to S_l = 0.5 here, which leads to a pressure gradient of -6978 Pa/m by using linear relative phase permeability ($k_{rl} = S_l$, $k_{rv} = S_v$) and calculated fluid properties in Table 5. The mean salt composition is computed to X = 47.78 wt% NaCl. According to the pressure gradient we fix pressure to 60.6987 MPa at the bottom, where also temperature is fixed to 600 °C. The initial domain conditions are T = 600 °C and p = 60 MPa. Rock properties are listed in Table 3.4. After a simulation time of approx. $8 \cdot 10^{12}$ s the system is in steady state and the simulated results are in agreement with the analytical results, derived at top conditions (see Tab. 3.6). Differences are caused by slightly changing fluid properties within the domain due to pressure increase. Further comparison with results of those in (Kissling, 2005a) or in (Lewis and Lowell, 2009), where this test also has been performed, are not reasonable as fluid properties differ to much due to EOS. Especially the lower liquid viscosity in this study leads to much higher pressure gradients and fluxes.

Table 3.4: Model parameters for test in 3.7.3 (One-dimensional vertical salt pipe)

Properties	Meaning	Value	Unit
c_{pr}	specific rock heat capacity	1000	J/(kg·K)
K	conductivity	3	W/(m·K)
k	permeability	10^{-16}	m²
ρ_r	rock density	2650	kg/m³
Φ	porosity	0.01	-

Table 3.5: Fluid Properties at T = 600°C and p = 60 MPa compared to those in Kissling (2005a)

Properties	Unit	Liquid	Liquid Kissling	Vapor	Vapor Kissling
Salinity	wt%	57.27	54.40	0.54	0.51
Density	kg/m³	1048	1156	211.4	236.6
Viscosity	Pa·s	$1.4 \cdot 10^{-4}$	$8.4 \cdot 10^{-4}$	$0.419 \cdot 10^{-4}$	$0.49 \cdot 10^{-4}$
Spec. enthalpy	MJ/kg	1.620	1.132	3.140	3.087

Table 3.6: Analytical versus simulated results of test 3.7.3 (One-dimensional vertical salt pipe)

Properties	Unit	Analytical	Simulated column average
Pressure gradient	Pa/m	-6978	-6978
Salt mass fraction	wt%	47.8	47.4
Liquid saturation	-	0.500	0.503
Liquid mass flux	kg/(m²·s)	$-1.234 \cdot 10^{-6}$	$-1.230 \cdot 10^{-6}$
Vapor mass flux	kg/(m²·s)	$1.235 \cdot 10^{-6}$	$1.226 \cdot 10^{-6}$
Pure water flux	kg/(m²·s)	$7.01 \cdot 10^{-7}$	$6.89 \cdot 10^{-7}$
Salt flux	kg/(m²·s)	$-7.00 \cdot 10^{-7}$	$-6.93 \cdot 10^{-7}$
Heat flux	W/m²	1.878	1.843

3.8 Bibliography

Afanasyev, A., Blundy, J., Melnik, O., Sparks, S., 2018. Formation of magmatic brine lenses via focussed fluid-flow beneath volcanoes. Earth and Planetary Science Letters, 486: 119-128, https://doi.org/10.1016/j.epsl.2018.01.013.

Aghaei, O. et al., 2017. Constraints on melt content of off-axis magma lenses at the East Pacific Rise from analysis of 3-D seismic amplitude variation with angle of incidence. Journal of Geophysical Research-Solid Earth, 122(6): 4123-4142, DOI:10.1002/2016jb013785.

Anderko, A., Pitzer, K.S., 1993. Equation-of-State Representation of Phase-Equilibria and Volumetric Properties of the System Nacl-H2o above 573-K. Geochimica Et Cosmochimica Acta, 57(8): 1657-1680.

Archer, D.G., 1992. Thermodynamic Properties of the Nacl+H2o System .2. Thermodynamic Properties of Nacl(Aq), Nacl.2h2o(Cr), and Phase-Equilibria. Journal of Physical and Chemical Reference Data, 21(4): 793-829, DOI:10.1063/1.555915.

Bastian, P., Heimann, F., Marnach, S., 2010. Generic Implementation of Finite Element Methods in the Distributed and Unified Numerics Environment (Dune). Kybernetika, 46(2): 294-315.

Bischoff, J.L., Rosenbauer, R.J., 1984. The critical point and two-phase boundary of seawater, 200-500°C. Earth and Planetary Science Letters, 68(1): 172-180.

Bischoff, J.L., Rosenbauer, R.J., 1989. Salinity Variations in Submarine Hydrothermal Systems by Layered Double-Diffusive Convection. Journal of Geology, 97(5): 613-623.

Boetius, A., 2005. Lost city life. Science, 307(5714): 1420-1422.

Butterfield, D.A. et al., 1997. Seafloor eruptions and evolution of hydrothermal fluid chemistry. Philosophical Transactions of the Royal Society of London. Series A: Mathematical, Physical and Engineering Sciences, 355(1723): 369-386, DOI:10.1098/rsta.1997.0013.

Butterfield, D.A., Massoth, G.J., 1994. Geochemistry of north Cleft segment vent fluids: Temporal changes in chlorinity and their possible relation to recent volcanism. Journal of Geophysical Research: Solid Earth, 99(B3): 4951-4968, DOI:10.1029/93JB02798.

Butterfield, D.A., Massoth, G.J., Mcduff, R.E., Lupton, J.E., Lilley, M.D., 1990. Geochemistry of Hydrothermal Fluids from Axial Seamount Hydrothermal Emissions Study Vent Field, Juan-De-Fuca Ridge - Subseafloor Boiling and Subsequent Fluid-Rock Interaction. Journal of Geophysical Research-Solid Earth and Planets, 95(B8): 12895-12921, DOI:10.1029/JB095iB08p12895.

Canales, J.P. et al., 2006. Seismic evidence for variations in axial magma chamber properties along the southern Juan de Fuco Ridge. Earth and Planetary Science Letters, 246(3-4): 353-366, DOI:10.1016/j.epsl.2006.04.032.

Charlou, J.L. et al., 2000. Compared geochemical signatures and the evolution of Menez Gwen (37 degrees 50 ' N) and Lucky Strike (37 degrees 17 ' N) hydrothermal fluids, south of the Azores Triple Junction on the Mid-Atlantic Ridge. Chemical Geology, 171(1-2): 49-75, DOI:10.1016/s0009-2541(00)00244-8.

Chiba, H., Masuda, H., Lee, S.Y., Fujioka, K., 2001. Chemistry of hydrothermal fluids at the TAG active mound, MAR 26 degrees N, in 1998. Geophysical Research Letters, 28(15): 2919-2922, DOI:10.1029/2000gl012645.

Choi, J., Lowell, R.P., 2015. The response of two-phase hydrothermal systems to changing magmatic heat input at mid-ocean ridges. Deep-Sea Research Part Ii-Topical Studies in Oceanography, 121: 17-30, DOI:10.1016/j.dsr2.2015.05.005.

Class, H., Helmig, R., Bastian, P., 2002. Numerical simulation of non-isothermal multiphase multicomponent processes in porous media.: 1. An efficient solution technique. Advances in Water Resources, 25(5): 533-550, https://doi.org/10.1016/S0309-1708(02)00014-3.

Coumou, D., Driesner, T., Weis, P., Heinrich, C.A., 2009. Phase separation, brine formation, and salinity variation at Black Smoker hydrothermal systems. Journal of Geophysical Research, 114, DOI:10.1029/2008jb005764.

Dabrowski, M., Krotkiewski, M., Schmid, D.W., 2008. MILAMIN: MATLAB-based finite element method solver for large problems. Geochemistry Geophysics Geosystems, 9, DOI:10.1029/2007gc001719.

Douville, E. et al., 2002. The rainbow vent fluids (36°14'N, MAR): the influence of ultramafic rocks and phase separation on trace metal content in Mid-Atlantic Ridge hydrothermal fluids. Chemical Geology, 184(1-2): 37-48.

Driesner, T., 2007. The system H2O-NaCl. Part II: Correlations for molar volume, enthalpy, and isobaric heat capacity from 0 to 1000 degrees C, 1 to 5000 bar, and 0 to 1 X-NaCl. Geochimica Et Cosmochimica Acta, 71(20): 4902-4919, DOI:10.1016/j.gca.2007.05.026.

Driesner, T., 2013. Enthalpy and phase relations in saline geothermal fluids to "supercritical" conditions, American Geophysical Union, 2013 Fall Meeting, San Francisco, California, 9-13 December, V33C-2761.

Driesner, T., Heinrich, C.A., 2007. The system H2O-NaCl. Part I: Correlation formulae for phase relations in temperature-pressure-composition space from 0 to 1000 degrees C, 0 to 5000 bar, and 0 to 1 X-NaCl. Geochimica Et Cosmochimica Acta, 71(20): 4880-4901, DOI:10.1016/i.gca.2006.01.033.

Dunn, R.A., Toomey, D.R., Solomon, S.C., 2000. Three-dimensional seismic structure and physical properties of the crust and shallow mantle beneath the East Pacific Rise at 9 degrees 30'N. Journal of Geophysical Research, 105(B10): 23537-23555.

Edmonds, H.N. et al., 1996. Continuation of the hydrothermal fluid chemistry time series at TAG, and the effects of ODP drilling. Geophysical Research Letters, 23(23): 3487-3489, DOI:10.1029/96gl01597.

Fontaine, F.J., Rabinowicz, M., Cannat, M., 2017. Can high-temperature, high-heat flux hydrothermal vent fields be explained by thermal convection in the lower crust along fast-spreading Mid-Ocean Ridges? Geochemistry Geophysics Geosystems, 18(5): 1907-1925, DOI:10.1002/2016gc006737.

Fontaine, F.J., Wilcock, W.S.D., 2006. Dynamics and storage of brine in mid-ocean ridge hydrothermal systems. Journal of Geophysical Research-Solid Earth, 111(B6), DOI:10.1029/2005jb003866.

Fornari, D.J. et al., 2012. The East Pacific Rise Between 9°N and 10°N: Twenty-Five Years of Integrated, Multidisciplinary Oceanic Spreading Center Studies. Oceanography, 25(1): 18-43.

Foustoukos, D.I., Pester, N.J., Ding, K., Seyfried, W.E., 2009. Dissolved carbon species in associated diffuse and focused flow hydrothermal vents at the Main Endeavour Field, Juan de Fuca Ridge: Phase equilibria and kinetic constraints. Geochemistry Geophysics Geosystems, 10, DOI:10.1029/2009gc002472.

Gallant, R.M., Von Damm, K.L., 2006. Geochemical controls on hydrothermal fluids from the Kairei and Edmond Vent Fields, 23°-25°S, Central Indian Ridge. Geochemistry, Geophysics, Geosystems, 7(6): n/a-n/a, DOI:10.1029/2005gc001067.

Geiger, S., 2005. On the dynamics of NaCl-H2O fluid convection in the Earth's crust. Journal of Geophysical Research, 110(B7), DOI:10.1029/2004jb003362.

Geiger, S., Driesner, T., Heinrich, C.A., Matthai, S.K., 2006a. Multiphase thermohaline convection in the earth's crust: I. A new finite element - Finite volume solution technique combined with a new equation of state for NaCl-H2O. Transport in Porous Media, 63(3): 399-434, DOI:10.1007/s11242-005-0108-z.

Geiger, S., Driesner, T., Heinrich, C.A., Matthai, S.L., 2006b. Multiphase thermohaline convection in the earth's crust: II. Benchmarking and application of a finite element - Finite volume solution technique with a NaCl-H2O equation of state. Transport in Porous Media, 63(3): 435-461, DOI:10.1007/s11242-005-0109-y.

German, C.R. et al., 2016. Hydrothermal impacts on trace element and isotope ocean biogeochemistry. Philosophical Transactions of the Royal Society a-Mathematical Physical and Engineering Sciences, 374(2081), DOI:10.1098/rsta.2016.0035.

German, C.R., Seyfried, W.E., 2014. Hydrothermal Processes. In: Holland, H.D., Turekian, K.K. (Eds.), Treatise on Geochemistry (Second Edition). Elsevier, Oxford, pp. 191-233.

Gruen, G., Weis, P., Driesner, T., de Ronde, C.E.J., Heinrich, C.A., 2012. Fluid-Flow Patterns at Brothers Volcano, Southern Kermadec Arc: Insights from Geologically Constrained Numerical Simulations. Economic Geology, 107(8): 1595-1611, DOI:10.2113/econgeo.107.8.1595.

Gruen, G., Weis, P., Driesner, T., Heinrich, C.A., de Ronde, C.E.J., 2014. Hydrodynamic modeling of magmatic-hydrothermal activity at submarine arc volcanoes, with implications for ore formation. Earth and Planetary Science Letters, 404: 307-318, DOI:10.1016/j.epsl.2014.07.041.

Hammond, G.E., Lichtner, P.C., Mills, R.T., 2014. Evaluating the performance of parallel subsurface simulators: An illustrative example with PFLOTRAN. Water Resources Research, 50(1): 208-228, DOI:10.1002/2012wr013483.

Han, L., Lowell, R.P., Lewis, K.C., 2013. The dynamics of two-phase hydrothermal systems at a seafloor pressure of 25 MPa. Journal of Geophysical Research-Solid Earth, 118(6): 2635-2647, DOI:10.1002/jgrb.50158.

Han, S.S. et al., 2014. Architecture of on- and off-axis magma bodies at EPR 9 degrees 37-40 ' N and implications for oceanic crustal accretion. Earth and Planetary Science Letters, 390: 31-44, DOI:10.1016/j.epsl.2013.12.040.

Hannington, M., Jamieson, J., Monecke, T., Petersen, S., Beaulieu, S., 2011. The abundance of seafloor massive sulfide deposits. Geology, 39(12): 1155-1158, 10.1130/g32468.1.

Hasenclever, J. et al., 2014. Hybrid shallow on-axis and deep off-axis hydrothermal circulation at fast-spreading ridges. Nature, 508(7497): 508-512, DOI:10.1038/nature13174.

Hayba, D.O., Ingebritsen, S.E., 1994. The Computer Model Hydrotherm, A Three-Dimensional Finte Difference Model To Simulate Ground-Water Flow And Heat Transport In The Temperature Range Of 0 To 1,200°C. Report 94-4045, Water-Resources Investigations

Humphris, S.E. et al., 1995. The Internal Structure of an Active Sea-Floor Massive Sulfide Deposit. Nature, 377(6551): 713-716, DOI:10.1038/377713a0.

Ingebritsen, S.E., Geiger, S., Hurwitz, S., Driesner, T., 2010. Numerical simulation of magmatic hydrothermal systems. Reviews of Geophysics, 47: 33, DOI:10.1029/2009rg000287.

Ji, F. et al., 2017. Geochemistry of hydrothermal vent fluids and its implications for subsurface processes at the active Longqi hydrothermal field, Southwest Indian Ridge. Deep Sea Research Part I: Oceanographic Research Papers, 122: 41-47, DOI:10.1016/j.dsr.2017.02.001.

Jr. Seyfried, W.E., Ding, K., Berndt, M.E., 1991. Phase equilibria constraints on the chemistry of hot spring fluids at mid-ocean ridges, 55, 3559-3580 pp.

Jupp, T., Schultz, A., 2000. A thermodynamic explanation for black smoker temperatures. Nature, 403(6772): 880-883.

Kipp Jr, K.L., Hsieh, P.A., Charlton, S.R., 2008. Guide to the Revised Ground-Water Flow and Heat Transport Simulator: HYDROTHERM-Version 3. U.S. Geol. Surv. Tech. Methods., 6(A25).

Kissling, W.M., 2005a. Transport of three-phase hyper-saline brines in porous media: Examples. Transport in Porous Media, 60(2): 141-157, DOI:10.1007/s11242-004-4795-7.

Kissling, W.M., 2005b. Transport of three-phase hyper-saline brines in porous media: Theory and code implementation. Transport in Porous Media, 61(1): 25-44, DOI:10.1007/s11242-004-3306-1.

Klyukin, Y.I., Lowell, R.P., Bodnar, R.J., 2017. A revised empirical model to calculate the dynamic viscosity of H2ONaCl fluids at elevated temperatures and pressures (≤1000 °C, ≤500 MPa, 0–100 wt % NaCl). Fluid Phase Equilibria, 433: 193-205, https://doi.org/10.1016/j.fluid.2016.11.002.

Kumagai, H. et al., 2008. Geological background of the Kairei and Edmond hydrothermal fields along the Central Indian Ridge: Implications of their vent fluids’ distinct chemistry. Geofluids, 8(4): 239-251, DOI:10.1111/j.1468-8123.2008.00223.x.

Lewis, K.C., Lowell, R.P., 2009. Numerical modeling of two-phase flow in the NaCl-H2O system: Introduction of a numerical method and benchmarking. Journal of Geophysical Research, 114, DOI:10.1029/2008jb006029.

Lilley, M.D., Butterfield, D.A., Lupton, J.E., Olson, E.J., 2003. Magmatic events can produce rapid changes in hydrothermal vent chemistry. Nature, 422(6934): 878-881, DOI:10.1038/nature01569.

Lowell, R.P., Farough, A., Hoover, J., Cummings, K., 2013. Characteristics of magma-driven hydrothermal systems at oceanic spreading centers. Geochemistry Geophysics Geosystems, 14(6): 1756-1770, DOI:10.1002/ggge.20109.

Morgan, J.P., Chen, Y.J., 1993. DEPENDENCE OF RIDGE-AXIS MORPHOLOGY ON MAGMA SUPPLY AND SPREADING RATE. Nature, 364(6439): 706-708.

Mottl, M.J. et al., 2011. Chemistry of hot springs along the Eastern Lau Spreading Center. Geochimica et Cosmochimica Acta, 75(4): 1013-1038, DOI:10.1016/j.gca.2010.12.008.

Oldenburg, C.M., Pruess, K., 1999. Plume separation by transient thermohaline convection in porous media. Geophysical Research Letters, 26(19): 2997-3000, DOI:10.1029/1999gl002360.

Olive, J.A., Crone, T.J., 2018. Smoke Without Fire: How Long Can Thermal Cracking Sustain Hydrothermal Circulation in the Absence of Magmatic Heat? Journal of Geophysical Research-Solid Earth, 123(6): 4561-4581, DOI:10.1029/2017jb014900.

Palliser, C., McKibbin, R., 1998a. A model for deep geothermal brines, I: T-p-X state-space description. Transport in Porous Media, 33(1-2): 65-80, DOI:10.1023/A:1006537425101.

Palliser, C., McKibbin, R., 1998b. A model for deep geothermal brines, II: Thermodynamic properties - Density. Transport in Porous Media, 33(1-2): 129-154, DOI:10.1023/A:1006597626918.

Palliser, C., McKibbin, R., 1998c. A model for deep geothermal brines, III: Thermodynamic properties - Enthalpy and viscosity. Transport in Porous Media, 33(1-2): 155-171, DOI:10.1023/A:1006549810989.

Pester, N.J., Ding, K., Seyfried, W.E., 2014. Magmatic eruptions and iron volatility in deep-sea hydrothermal fluids. Geology, 42(3): 255-258, DOI:10.1130/G35079.1.

Pruess, K., Oldenburg, C., Moridis, G., 2012. TOUGH2 USER'S GUIDE, Version 2.1, Lawrence Berkeley National Laboratory, Berkeley, Calif., Report LBNL-43134.

Scott, S., Driesner, T., Weis, P., 2016. The thermal structure and temporal evolution of high-enthalpy geothermal systems. Geothermics, 62: 33-47.

Scott, S., Driesner, T., Weis, P., 2017. Boiling and condensation of saline geothermal fluids above magmatic intrusions. Geophysical Research Letters, 44(4): 1696-1705, DOI:10.1002/2016gl071891.

Shanks, W.C., III, 2001. Stable Isotopes in Seafloor Hydrothermal Systems: Vent fluids, hydrothermal deposits, hydrothermal alteration, and microbial processes. Reviews in Mineralogy and Geochemistry, 43(1): 469-525, DOI:10.2138/gsrmg.43.1.469.

Singh, S., Lowell, R.P., Lewis, K.C., 2013. Numerical modeling of phase separation at Main Endeavour Field, Juan de Fuca Ridge. Geochemistry Geophysics Geosystems, 14(10): 4021-4034.

Tanger, J.C., Pitzer, K.S., 1989. Thermodynamics of Nacl-H2o - a New Equation of State for the near-Critical Region and Comparisons with Other Equations for Adjoining Regions. Geochimica Et Cosmochimica Acta, 53(5): 973-987, DOI:10.1016/0016-7037(89)90203-2.

Theissen-Krah, S., Iyer, K., Rüpke, L.H., Morgan, J.P., 2011. Coupled mechanical and hydrothermal modeling of crustal accretion at intermediate to fast spreading ridges. Earth and Planetary Science Letters, 311(3-4): 275-286, DOI:10.1016/j.epsl.2011.09.018.

Vehling, F., Hasenclever, J., Rüpke, L., 2018. Implementation Strategies for Accurate and Efficient Control Volume-Based Two-Phase Hydrothermal Flow Solutions. Transport in Porous Media, 121(2): 233-261, 10.1007/s11242-017-0957-2.

Von Damm, K.L., 1990. Seafloor Hydrothermal Activity - Black Smoker Chemistry and Chimneys. Annual Review of Earth and Planetary Sciences, 18: 173-204.

Von Damm, K.L., 2000. Chemistry of hydrothermal vent fluids from 9°–10°N, East Pacific Rise: "Time zero," the immediate posteruptive period. Journal of Geophysical Research: Solid Earth, 105(B5): 11203-11222, DOI:10.1029/1999JB900414.

Von Damm, K.L., 2004. Evolution of the Hydrothermal System at East Pacific Rise 9°50'N: Geochemical Evidence for Changes in the Upper Oceanic Crust. In: German, C.R., Lin, J., Parson, L. (Eds.), Mid-Ocean Ridges - Hydrothermal Interactions Between the Lithosphere and Oceans. American Geophysical Union, Washington, DC, pp. 285-304.

Von Damm, K.L., Bray, A.M., Buttermore, L.G., Oosting, S.E., 1998. The geochemical controls on vent fluids from the Lucky Strike vent field, Mid-Atlantic Ridge. Earth and Planetary Science Letters, 160(3-4): 521-536, DOI:10.1016/s0012-821x(98)00108-3.

Von Damm, K.L. et al., 1997. Direct observation of the evolution of a seafloor 'black smoker' from vapor to brine. Earth and Planetary Science Letters, 149(1-4): 101-111, DOI:10.1016/S0012-821x(97)00059-9.

Weis, P., Driesner, T., Coumou, D., Geiger, S., 2014. Hydrothermal, multiphase convection of H2O-NaCl fluids from ambient to magmatic temperatures: a new numerical scheme and benchmarks for code comparison. Geofluids, 14(3): 347-371, DOI:10.1111/gfl.12080.

Weis, P., Driesner, T., Heinrich, C.A., 2012. Porphyry-Copper Ore Shells Form at Stable Pressure-Temperature Fronts Within Dynamic Fluid Plumes. Science, 338(6114): 1613-1616.

Weller, H.G., Tabor, G., Jasak, H., Fureby, C., 1998. A tensorial approach to computational continuum mechanics using object-oriented techniques. Computers in Physics, 12(6): 620-631, DOI:10.1063/1.168744.

Wu, Y.-S., Forsyth, P.A., 2001. On the selection of primary variables in numerical formulation for modeling multiphase flow in porous media. Journal of Contaminant Hydrology, 48(3): 277-304, https://doi.org/10.1016/S0169-7722(00)00180-7.

Xu, M. et al., 2014. Variations in axial magma lens properties along the East Pacific Rise (9 degrees 30'N-10 degrees 00'N) from swath 3-D seismic imaging and 1-D waveform inversion. Journal of Geophysical Research-Solid Earth, 119(4): 2721-2744, DOI:10.1002/2013jb010730.

4 Thermohaline multiphase simulations explain variations in vent fluid salinity following diking events at fast-spreading ridges

4.1 Abstract

Hydrothermal fluids expelled at mid-ocean ridge vent sites show a large spatial and temporal variability in exit temperature and chlorinity. At the East Pacific Rise (EPR), 9°50.3'N, time series data for a 25+ year period reveal a correlation between these variations and magmatic diking events. Heat input from dikes appears to cause phase separation within the rising fluids splitting them into low-salinity vapor and a high-salinity liquid phases. The intrusion of a new dike is therefore likely to result in a characteristic salinity signal, with early post-eruptive fluids typically showing vapor-influenced low salinity and later brine-influenced fluids showing high salinity values.

We here use a multiphase hydrothermal flow model to relate these observations to processes and properties within the sub-seafloor such as permeability, porosity, background flow rates, and phase separation as well as segregation phenomena. The 2-D setup mimics hydrothermal convection on top of an axial magma lens, which is perturbed by a dike intrusion. In a comprehensive suite of model runs we have identified how multiphase flow phenomena in response to shallow magmatic intrusion affect the time evolution of vent fluid salinity and temperature. Based on these results, we are able to reproduce the characteristics of time-series data from the EPR at 9°50.3'N and infer the likely ranges of rock properties and the hydrothermal conditions within the oceanic crust beneath.

4.2 Introduction

Submarine hydrothermal systems sustain unique ecosystems, affect global-scale biogeochemical cycles, and mobilize metals from the oceanic crust to form volcanogenic massive sulfide deposits. Quantifying these processes requires linking seafloor observations to physico-chemical processes at depth. Hydrothermal flow observations at mid ocean spreading centers show a high spatial and temporal variability in vent fluid temperature, chlorinity and chemistry (Gallant and Von Damm, 2006; German and Von Damm, 2004; Seyfried et al., 2011; Von Damm, 2004). Especially at fast-spreading ridges, where magmatic events happen approximately every 10s of years, these variations occur on relatively short time scales and appear to correlate with diking events. At the fast-spreading East Pacific Rise at 9°N, a focus site of international hydrothermal research, variations in vent fluid salinity and temperature have been especially well documented (Detrick et al., 1987; Fornari et al., 1998; Fornari et al., 2012).

For two hydrothermal vents (P and Bio9) at EPR 9°50.3'N a complete record of fluid temperature and chemistry exists between 1991 and 2008 (Fig. 4.1). In late 1989, the high-temperature hydrothermal field was visually discovered in the axial summit trough (AST) including massive sulfide deposits and vent biota, but no exact temperature was measured (Haymon et al., 1991). The eruptive diking event of early 1991, which was visited during or a few days after the eruption, had buried some of the old vent chimneys and two new chimneys (P and Bio9) started to build up near to the eruptive fissure with a distance of 50 m between them (Haymon et al., 1993). The area was further characterized by widespread diffusive venting of gray to black smoke and cloudy water from holes, cracks and pits in very glassy, new-looking lava flows and rubble. After a second dike eruption in late 1991 to early 1992 (Rubin et al., 1994), which did not destroy the new vents, the chlorinity of Bio9 and P vent decreased to minimum and temperature increased to maximum values (Fornari et al., 1998). Samples from the next dives showed a reduced vent temperature and rising chlorinity, which goes along with cooling and thermal cracking of the dike at greater depth inferred from recorded micro seismicity (Sohn et al., 1998; Sohn et al., 1999). After a peak in 1995/1996 chlorinity dropped again and temperature slowly rose. With the 2005/06 extrusive eruption (Tolstoy et al., 2006; Xu et al., 2014), a new cycle began with very low chlorinity and temperatures reaching their highest values. Again, this was followed by an increase of chlorinity and decrease of temperatures very similar compared to the 1991/1992 diking event (Fornari et al., 2012).

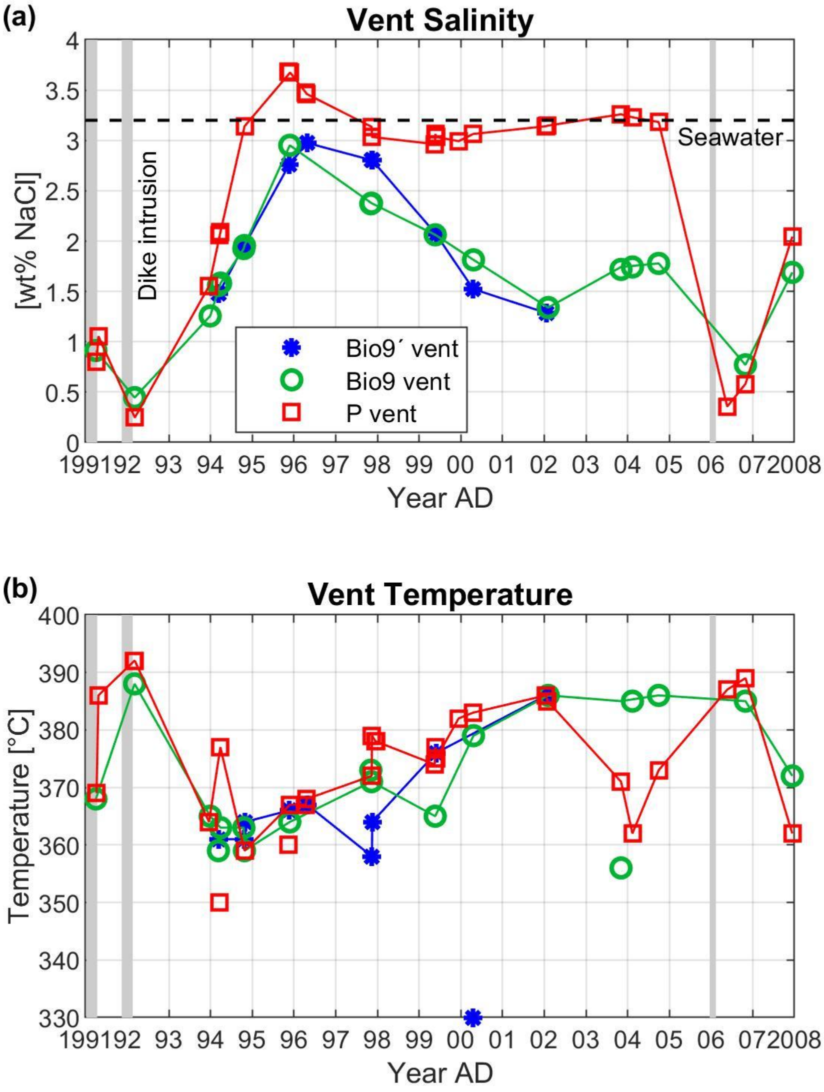

Figure 4.1: Salinity and temperature evolution for vents at 9°50.3’N: Bio9, Bio9’ and P. Vent data are from Von Damm (2004) and Fornari et al. (2012). Vertical lines mark time intervals of extrusive dike eruptions as dated by Rubin et al. (1994) and (Tolstoy et al., 2006).

These time series observations point to a characteristic evolution of vent fluid temperature and salinity during the first few years following a magmatic diking event. The salinity of vent fluids can change following a diking event, when the magmatic heat causes the rising hydrothermal fluids to separate into a high-salinity brine and a low-salinity vapor phase with differing mobilities, so that the formed phases segregate (Von Damm, 1990). The buoyant vapor phase rises, condenses, and vents as a low-salinity fluid. Later the denser brine phase is entrained and transported to the seafloor leading to higher salinity venting at decreasing temperatures before the vent returns to its background state, which is likely controlled by long-term phase separation phenomena on top of the axial magma lens (Vehling et al., 2021).

Such regular measurements without major gaps over several years make this data set ideal for being investigated by numerical models with the aim of linking seafloor observations to processes at depth. Previous models have focused on explaining time lags and magnitudes of temperature changes following tectono-magmatic events. These models mainly used single-pass flow loop approximations and successfully explained temperature evolution curves at the East Pacific Rise at 9°N and the Endeavor Field on the Juan de Fuca Ridge by perturbations to the shallow thermal and permeability structures (Germanovich et al., 2001; Germanovich et al., 2011; Ramondenc et al., 2008; Singh and Lowell, 2015). An alternative view was presented by Wilcock (2004) who explored how processes close to the melt lens could affect vent temperature on short time scales using dynamic pressure and thermal disequilibrium models.

These previous models did not consider variations in vent fluid salinity, although the salt signal may be the more sensitive proxy to sub-seafloor processes as it travels with the pore velocity and is not, unlike the temperature signal, buffered by the rock matrix. However, investigating the salinity signal requires multiphase transport models and an equation-of-state for the system H_2O-NaCl that covers the relevant p-T-X range. One early attempt was made by Lowell and Xu (2000) who modelled two-phase seawater convection near a dike intrusion at the EPR at 9°N. Yet, to our knowledge, no previous study has related the complete characteristic salinity signal following a dike event (Fig. 4.1) to multiphase phenomena in the sub-seafloor.

In our study we present results of several 2D multiphase simulations of a dike intrusion into a hydrothermal system at pressure conditions found at EPR 9°50.3'N (25 MPa). First, we analyze the fluid mechanics for a reference case. This includes early phase separation phenomena like brine accumulation and halite precipitation near the dike and subsequently brine mobilization, two-phase flow. An important model prediction is the time evolution of the salinity and temperature curves of venting fluids, which are compared against the measurements. In the second part we investigate the role of key parameters that control the vent salinity evolution like rock permeability and porosity as well as the background fluid temperature and salinity of the hydrothermal upflow zone. Afterwards, we compare the simulated salinity and temperature curve against P and Bio9 vent evolution at EPR 9°50.3'N after dike intrusions of 1991/1992 and discuss our model setup approach.

Table 4.1 Variables

Variable	**Meaning**	**Unit**
c_d	Specific heat (dike)	J/(kg·K)
c_r	Specific rock heat	J/(kg·K)
c_l	Specific latent heat (dike)	J/(kg·K)
do	Subscript for downstream node	-
D	Salt diffusivity	m^2/s^2
E	Total energy in fluid and matrix	J

E_d	Total energy of dike section	J
$\vec{\mathbf{g}}$	Gravitational acceleration	m/s^2
h	Mean specific enthalpy	J/kg
h_f	Fluid specific enthalpy	J/kg
h_h	Specific enthalpy of halite	J/kg
K	Mean conductivity of rock matrix and fluid	W/(m·K)
k	Isotropic permeability of rock	m^2
$k_{r\mathrm{f}}$	Relative permeability	-
k_seg	Computed permeability at segment	m^2
L	Latent heat	J
Q_d	Heat rate of dike section	J/s
Q_m	Mass rate	kg/s
Q_h	Heat rate	J/s
Q_X	Salt mass rate	kg/s
q_h	Heat flux	J/(m^2·s)
q_m	Mass flux	kg/(m^2·s)
q_X	Salt mass flux	kg/(m^2·s)
p	Pore pressure	Pa
p_crit	Pressure at critical point of H^2O	Pa
S_h	Halite saturation	-
S_l	Liquid saturation	-
S_v	Vapor saturation	-
S_lr	Residual liquid saturation	-
t	Time	s
T	Rock and fluid temperature	°C
T_b	Temperature at left boundary node	°C
T_d	Dike section temperature	°C
T_l	Liquidus temperature	°C
T_s	Solidus temperature	°C
up	Subscript for upstream node	-
$\vec{\mathbf{v}}_\mathrm{f}$	Darcy velocity	m/s
X	Mean salt composition	wt fract
X_f	Fluid salt composition	wt fract
$X_\mathrm{m,out}$	Calculated mean salt composition of venting fluids	wt fract
w	Half of dike thickness	m
η_f	Fluid viscosity	Pa·s
ρ_f	Fluid density	kg/m^3
ρ_m	Mean density of fluids	kg/m^3
ρ_r	Rock density	kg/m^3
Φ	Rock porosity	-

4.3 Numerical approach

4.3.1 Model assumptions and governing equations

We use the same numerical simulator as presented in (Vehling et al., 2021), where it has been proven to work for simulating hydrothermal systems. In brief we present the model assumptions and governing equations:

1. capillary pressure effects are neglected
2. rock and fluid are in local thermodynamic equilibrium
3. rock enthalpy is related to temperature by a constant specific heat
4. the kinetic energy terms are orders of magnitude smaller and hence can be neglected
5. we fully account for pressure-volume work and viscous dissipation

We solve for the conservation of fluid mass (Eq. 4.1) and energy (Eq. 4.2) and salt mass (Eq. 4.3):

$$\frac{\partial\left(\Phi\rho_{\mathrm{m}}\right)}{\partial t}=-\nabla\cdot\left(\sum_{\mathrm{f}\in\{\mathrm{l},\mathrm{v}\}}\rho_{\mathrm{f}}\vec{\mathbf{v}}_{\mathrm{f}}\right) \tag{4.1}$$

$$\begin{aligned}\frac{\partial E}{\partial t}&=\frac{\partial}{\partial t}(\Phi\rho_{\mathrm{m}}h)+\rho_{\mathrm{r}}c_{\mathrm{r}}\frac{\partial(T(1-\Phi))}{\partial t}\\&=\nabla\cdot K\nabla T-\nabla\cdot\left(\sum_{\mathrm{f}\in\{\mathrm{l},\mathrm{v}\}}h_{\mathrm{f}}\rho_{\mathrm{f}}\vec{\mathbf{v}}_{\mathrm{f}}\right)+\sum_{\mathrm{f}\in\{\mathrm{l},\mathrm{v}\}}\frac{\eta_{\mathrm{f}}}{kk_{r\mathrm{f}}}\vec{\mathbf{v}}_{\mathrm{f}}^{2}+\frac{\partial(p\Phi)}{\partial t}+\sum_{\mathrm{f}\in\{\mathrm{l},\mathrm{v}\}}\vec{\mathbf{v}}_{\mathrm{f}}\nabla p\end{aligned} \tag{4.2}$$

$$\frac{\partial(\Phi\rho_{\mathrm{m}}X)}{\partial t}=-\nabla\cdot\left(\sum_{\mathrm{f}\in\{\mathrm{l},\mathrm{v}\}}\rho_{\mathrm{f}}X_{\mathrm{f}}\vec{\mathbf{v}}_{\mathrm{f}}\right)+\nabla\cdot\left(\sum_{\mathrm{f}\in\{\mathrm{l},\mathrm{v}\}}D\rho_{\mathrm{f}}\nabla X_{\mathrm{f}}\right) \tag{4.3}$$

All variables are summarized in Table 4.1. Subscripts l, v, h stand for liquid, vapor and halite phase and f is either liquid or vapor. The fluid velocity trough a porous medium is described by Darcy's law, where halite is treated as immobile phase and is absent in advection terms. The third term on the right hand side of Eq. (4.2) describes viscous dissipation, and the fourth and fifth term contains the part of the pressure-volume work that is not accounted for in the specific enthalpy.

$$\vec{\mathbf{v}}_{\mathrm{f}}=-k\frac{k_{r\mathrm{f}}}{\eta_{\mathrm{f}}}\left(\nabla p-\rho_{\mathrm{f}}\vec{\mathbf{g}}\right) \tag{4.4}$$

For the calculation of the liquid and vapor relative permeability ($k_{r\mathrm{l}}$ and $k_{r\mathrm{v}}$, resp.), we implemented a function in which the relative permeability is not additionally reduced by halite precipitation, because this is already accounted for in rock permeability in Eq. (4.22). Therefore, relative liquid permeability is a linear function from 0 to 1, when $S_{\mathrm{l}}/\left(1-S_{\mathrm{h}}\right)$ exceeds the residual liquid saturation S_{lr}:

$$\begin{aligned}k_{r\mathrm{l}}&=\frac{S_{\mathrm{l}}/\left(1-S_{\mathrm{h}}\right)-S_{\mathrm{lr}}}{1-S_{\mathrm{lr}}}&&\forall S_{\mathrm{l}}/\left(1-S_{\mathrm{h}}\right)>S_{\mathrm{lr}}\\k_{r\mathrm{l}}&=0&&\forall S_{\mathrm{l}}/\left(1-S_{\mathrm{h}}\right)\leq S_{\mathrm{lr}}\end{aligned} \tag{4.5}$$

$$k_{r\mathrm{v}}=S_{\mathrm{v}}/\left(1-S_{\mathrm{h}}\right) \tag{4.6}$$

Whereas all volumetric phase saturations sum up to one:

$$S_\mathrm{l} + S_\mathrm{v} + S_\mathrm{h} = 1 \tag{4.7}$$

The mean fluid Density ρ_m, mean specific enthalpy h and mean salt mass fraction X are defined as follows, using X_h=1:

$$\rho_\mathrm{m} = S_\mathrm{l}\rho_\mathrm{l} + S_\mathrm{v}\rho_\mathrm{v} + S_\mathrm{h}\rho_\mathrm{h} \tag{4.8}$$

$$h = \frac{S_\mathrm{l}\rho_\mathrm{l}h_\mathrm{l} + S_\mathrm{v}\rho_\mathrm{v}h_\mathrm{v} + S_\mathrm{h}\rho_\mathrm{h}h_\mathrm{h}}{\rho_\mathrm{m}} \tag{4.9}$$

$$X = \frac{S_\mathrm{l}\rho_\mathrm{l}X_\mathrm{l} + S_\mathrm{v}\rho_\mathrm{v}X_\mathrm{v} + S_\mathrm{h}\rho_\mathrm{h}}{\rho_\mathrm{m}} \tag{4.10}$$

The simulator uses a Newton-Raphson approach, where a linear set of equations is solved simultaneously for the primary variables of pressure, mean specific enthalpy h and mean salt mass fraction X. These three variables uniquely describe the fluid state of the system H_2O−NaCl and are used to calculate fluid properties and phase saturations.

4.3.2 Equation of state in the system H_2O−NaCl

The simulator uses the equation of state in the system H_2O−NaCl published by Driesner and Heinrich (2007) and Driesner (2007). They have not published a parameterization of fluid viscosity and we therefore use those published by Klyukin et al. (2017). Figure 4.2 shows the phase diagram of the system H_2O−NaCl in temperature-pressure-composition coordinates. The green surface marks the halite liquidus. In the liquid + halite (L+H) coexisting region, halite saturation increases linearly with increasing salt content, when temperature stays constant. The liquid, vapor and halite coexisting surface (blue) forms the lower pressure boundary of the L+V region and the upper boundary of the V+H coexisting region. The dark-yellow surface separates at low salinities the vapor region (single-phase) from the V+H coexisting region.

Throughout this paper, we use the critical curve to distinguish between vapor- and liquid-like in the single-phase region at pressures higher than p_crit (22.06 MPa) with vapor always having a lower density than a fluid on the critical curve for a given pressure. Therefore, a “vapor” is a fluid, which has a density below the density at the critical point of pure water (321.9 kg/m^3), or a fluid having a higher temperature and a lower salt content than the critical curve at a given pressure.

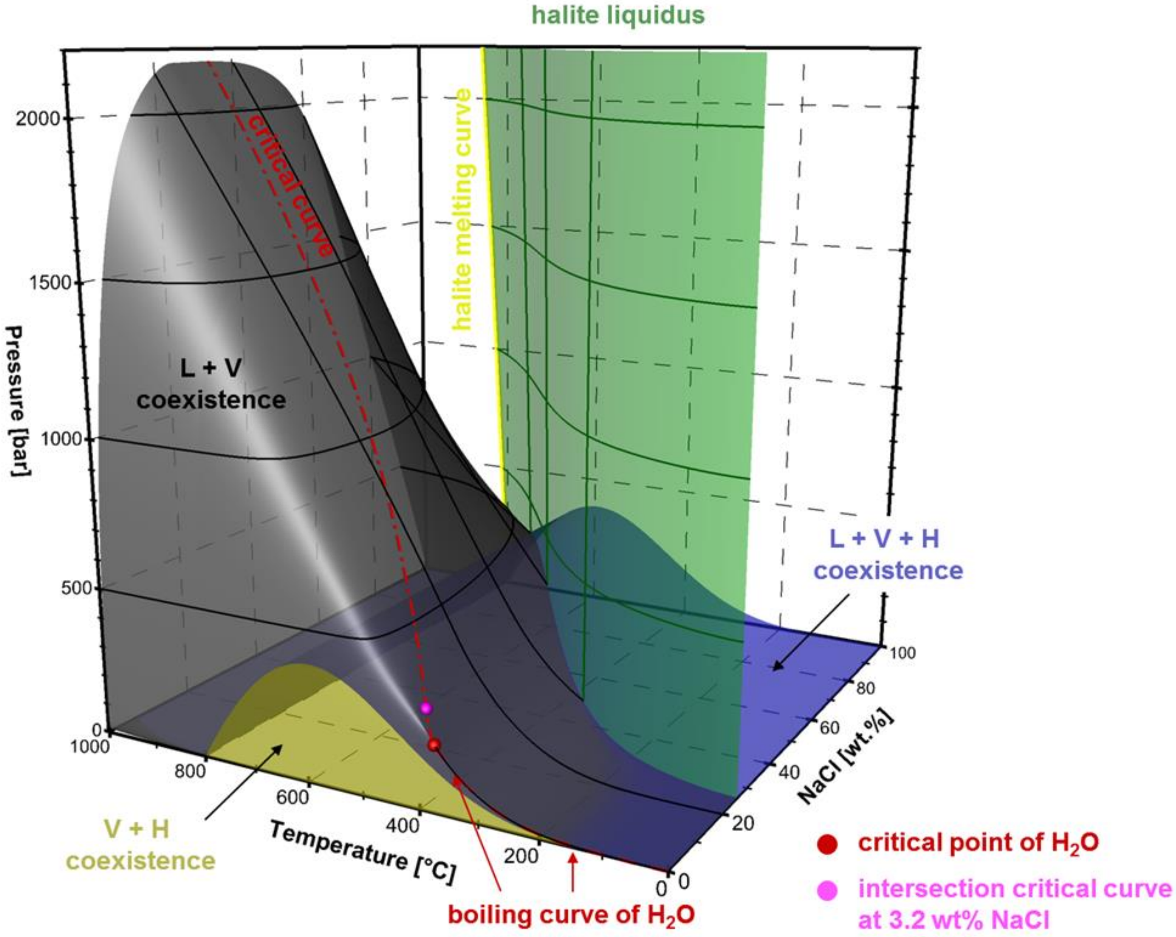

Figure 4.2: Phase diagram of the system H_2O-NaCl in temperature-pressure-composition coordinates with isolines for pressure and composition on surfaces.

4.3.3 Model setup

We explore dike events in a simplified setup that mimics the situation on the fast-spreading EPR. Our model domain covers one half of a two-dimensional cross section and the left boundary is the ridge axis, where dike events are simulated as boundary conditions (Fig. 4.3a, b). The model domain is 1 km high and 1.5 km long and we establish a hydrothermal circulation cell via Neumann boundary condition at the bottom. At the bottom left side from 0 m to 50 m, we set a mass flux condition into the domain and between 70 m and 1500 m, we set a negative mass flux boundary condition, so that the total bottom mass rate Q_m of inflow and outflow cancel each other out.

On top of the domain, we set a pressure boundary condition (25 MPa) allowing for free venting. The inflow temperature is T_top = 10 °C and the inflow salt content is equal to the bottom boundary condition X_bc. We further assume a uniform rock density of $\rho_\mathrm{r} = 2900$ kg/m³, rock heat capacity of $c_\mathrm{r} = 1100$ J/(kg·K) and a mean conductivity of $K = 2.5$ W/(m·K). The salt diffusivity is $D = 10^{-9}$.

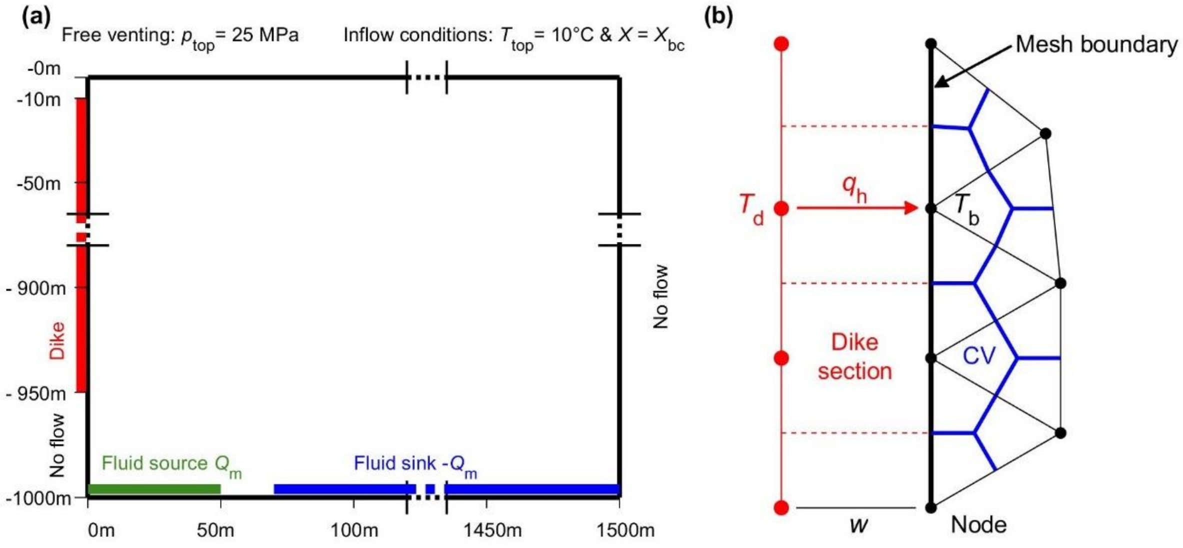

Figure 4.3: **a** Simulation domain boundary conditions. Borders of domain are disrupted for better visualization. **b** Close up of dike boundary condition with vertical discretization of the dike in red and grid nod in black.

We simulate the heat release of a cooling dike by a variable heat flux boundary condition at the left domain boundary. That means that the dike is not part of the modelling domain, but it is virtually attached via conductive heat exchange. The dike is vertically discretized so that every boundary CV (Node) has a corresponding section of the dike (Fig. 4.3b). The heat fluxes $q_h{}^i$ from the dike center to the domain boundary are calculated as follows for each CV:

$$q_\mathrm{h}^i = -K\frac{\left(T_\mathrm{b}^i - T_\mathrm{d}^i\right)}{w} \tag{4.11}$$

where T_b and T_d are the temperatures of boundary nodes and dike nodes, respectively. The distance w is 1 m and is half of the total dike thickness, so that $q_{\mathrm{h},i}$ represents the heat flow from the dike center to the dike wall. Converted to heat rate per CV we obtain:

$$Q_\mathrm{d}^i = q_\mathrm{h}^i \cdot y^i \tag{4.12}$$

where y^i is the dike section length.

In the Appendix (section 4.7.2) we present in detail the calculation of T_d for each time step considering latent heat of crystallizing magma. The initial dike temperature of 1200 °C is fixed for the first 4 simulation days, considering that extrusive events could last for several days, where fresh lava is flowing within the dike. In the Appendix (section 4.7.4) are descriptions of the implementation of the relative phase permeability and for thermal closure of rock porosity for temperatures higher than 600 °C. For discretization in time, we use the theta(θ)-method with θ = 0.66, which has shown good stability in Vehling et al. (2018). The specific phase enthalpy h_f and the phase salt content X_f are fully upwind weighted.

At a seafloor pressure of 25 MPa, a venting fluid could be in the L+V coexisting phase region when outflow temperature is higher than 387 °C. If this happens in the model, we calculate a mean fluid salinity $X_\mathrm{m,out}$ for each control volume using fluid phase (salt) mass fluxes $q_\mathrm{m,f}$ ($q_\mathrm{X,f}$) out of the modelling domain at the corresponding boundary CV. The outflow flux is calculated by adding mass flow rates, which flow into the boundary CV from inside the domain and then subtracted by the mass flow rate flowing out of this boundary CV into the domain. This net flow rate is divided by the length of the outer border of the CV. For $X_{\mathrm{m,out}}$ holds the following expression:

$$X_{\mathrm{m,out}} = \frac{\left(q_{\mathrm{X,l}} + q_{\mathrm{X,v}}\right)}{\left(q_{\mathrm{m,l}} + q_{\mathrm{m,v}}\right)} \tag{4.13}$$

4.4 Simulation results

4.4.1 Phase separation and NaCl accumulation at the dike

In this section we show detailed results of a reference simulation using the rock properties listed in Table 4.3 and bottom inflow temperature of T_{bc} = 375 °C and salinity of X_{bc} = 3.2 wt% NaCl. All time values given in figures and text are always time after the dike injection event.

Table 4.3. Model parameter in 4.4.1

Variable	**Meaning**	**Value**
k	Rock permeability	$1.5\cdot10^{-14}$ m^2
Q_{m}	Inflow mass rate	0.021 kg/s
S_{rl}	Residual liquid saturation	0.3
Φ	Rock Porosity	0.05

After a diking event, the salinity curve can be grouped into four stages: They are the (1) venting of low-salinity liquids or vapors, (2) the rise towards elevated salinities, (3) the stage, where salinities reach a plateau around the highest values, and (4) the decrease of venting salinities to background values. Regarding the salinity curve of the Bio9 and P vent after the 1991/92 diking event (Fig. 4.1), stage 1 lasts until 1993/94, stage 2 until 1995 and stage 3 until 1998. In stage 4 the Bio9 and P vent strongly differ in venting salinities and it is difficult to explain this because venting salinities seem not to be affected by previous phase separations at the dike.

In Figure 4.4 mass fluxes of the vapor and the liquid phase are shown in depths of -500 m for different points in time, which initiate the next stage of the venting salinity curve. When the heat of the dike is conducted through the left boundary, fluids rapidly heat up and enter the L+V region. Within 4 m distance to the dike, even the V+H coexisting region is reached, where halite precipitates from the liquid phase (Fig. 4.4a, b). This goes along with a large volume increase of the vapor phase, which consequently expands laterally and rises fast due to its high buoyancy. While the upflowing and venting low-salinity vapors mark stage 1 until 1.75 years, the liquid phase remains immobile as its saturation does not exceed the residual liquid saturation S_{lr} limit of 0.3. Close to the dike, the NaCl is temporarily fixed as halite. During stage 1, NaCl is constantly accumulated within the expanding L+V region when uprising vapors lose small amounts of NaCl. Additionally, NaCl is accumulated particularly at the lower part of the dike, where recharge flow of seawater salinity drops its NaCl at the dike.

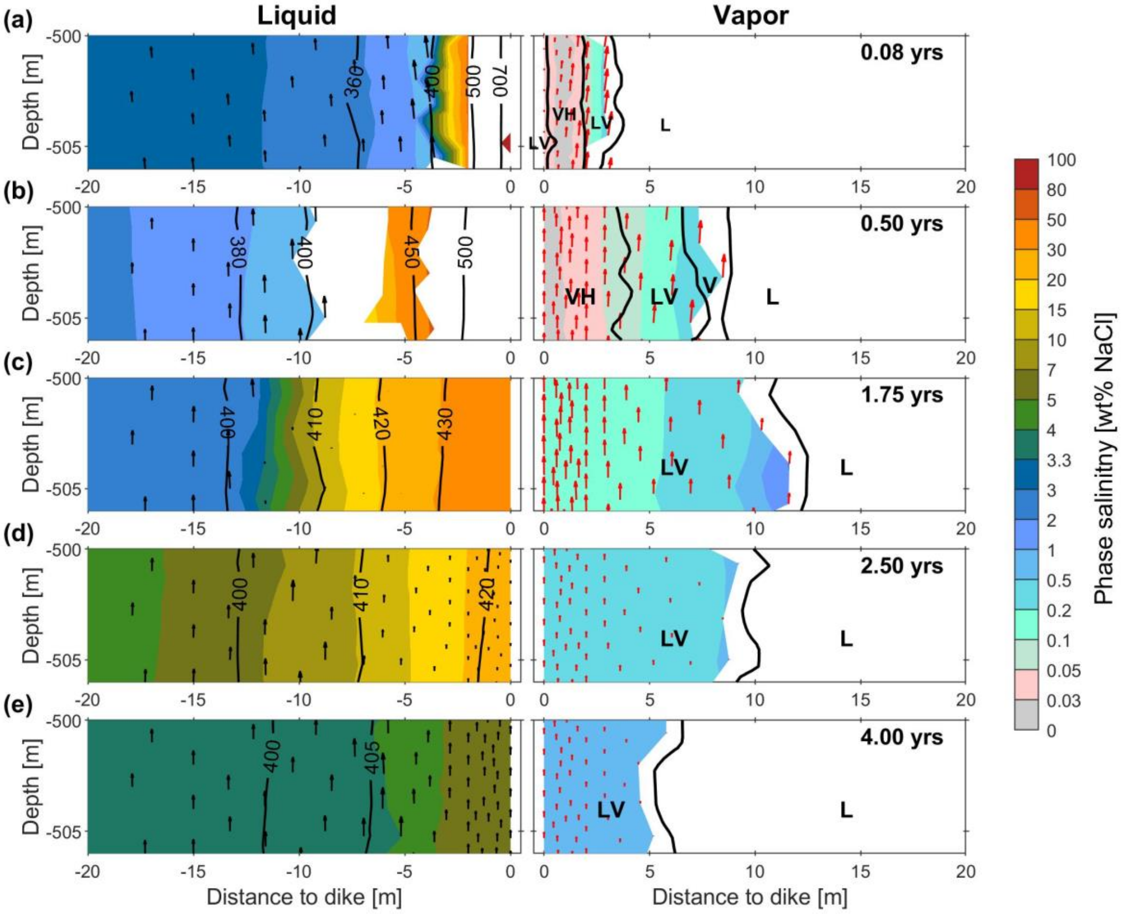

Figure 4.4: Color plot of liquid and vapor salinity with mass fluxes displayed as arrows at depth of -500 m. Contour lines show on left panels show isotherms in °C. Black lines on the right panels mark phase regions**.**

Stage 2 of rising venting salinities is initiated when the liquid phase starts to rise after 1.75 years at several depths. This starts first in in the colder region at 10m distance to the dike because the cooling leads to an H_2O uptake of the liquid phase (cf. Fig. 4.5b), which then exceeds the S_{lr} limit of 0.3. Additionally high-salinity liquids (> 20 wt% NaCl) from the lower part of the dike begin to move upwards.

Stage 3 with the highest venting salinities starts after 2.5 years when due to further cooling high-salinity liquids moves upwards at all distances to the dike (Fig. 4.4d). After 4 years most of the NaCl has been mined from the deeper parts, which is shown by liquid salinities below 4 wt% NaCl in the single phase region (Fig. 4.4e). This initiates stage 4 when after 5.5 years, default background salinities are venting at the seafloor.

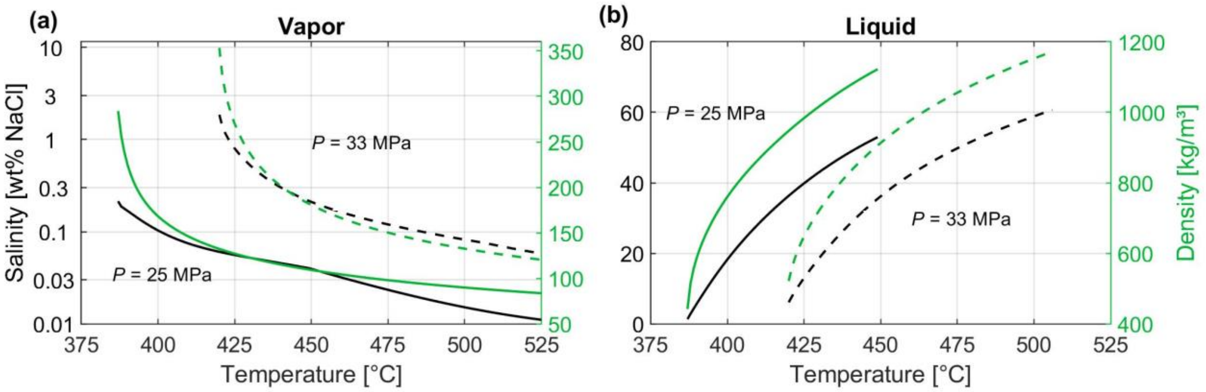

Figure 4.5: **a** Vapor and **b** liquid properties in the L+V coexisting region for pressures of p_{top} = 25 MPa (continous lines) and bottom pressure conditions of p = 33 MPa (dashed lines).

4.4.2 NaCl accumulation and mobilization at the dike

The fluids heated by the dike undergo a sequence of phase transitions. Within 4 m distance to the dike, the fluids enter the V+H region passing first the L+V region and then the L+V+H region (Fig. 4.6). Temperatures reach over 700 °C at the contact to the new dike, which brings the fluid into the L+V regime and leads to thermal closure of the pore space and thereby fluid expulsion (Fig. 4.4a). This also includes the expulsion of the formed ultra-high salinity liquid phase (> 70 wt% NaCl), which results in low total NaCl mass per cubic meter in combination with a high mean fluid salinity (Fig. 4.7a).

The expanding vapor phase takes the H_2O component away, whereas the liquid phase remains immobile as its saturation has not yet exceeded the residual liquid saturation S_{lr} limit of 0.3 resulting in an increase of mean fluid salinity (Fig. 4.6). Since the mean fluid salinity is strongly affected by varying densities of the vapor phase, we also use the unit salt mass per cubic meter to show how salt is accumulated and distributed at the dike (Fig. 4.7). Figure 4.6 shows a continuous increase of mean fluid salinity with temperature over time until 0.2 yrs, when temperature reaches here it maximum. After 0.5 years the mean salinity decreases to 20 wt% NaCl because the temperature decreases and consequently, the vapor contracts leading to an increase in H_2O mass. Despite the decrease in mean salinity, the salt mass per cubic meter is continuously increasing. The reason is that colder vapor with higher salinities from the side loses continuously small amounts of NaCl when it is heated at the dike or when it is depressurized during upflow until 1.75 yrs, the end of stage 1 (Fig. 4.5a and Fig. 4.7c, d). The salt mass increases from 10 kg/m³ at 0 yrs to ~23 kg/m³ at 1.75 yrs considering the mean value for the width of 10 m at the dike.

After 1.75 years stage 2 is initiated, when the temperature drops further within the 10 m thick L+V region, where NaCl has been accumulated. This causes a large density and salinity drop of the liquid phase (Fig. 4.5b) and simultaneously, the volumetric vapor saturation declines and liquid saturation rises to over 0.3, when they receive H_2O from the vapor phase (Fig. 4.6). After around 2.5 years stage 3 beginns and all liquids, even those at the dike wall, have started to move upwards. This leads to a two-phase up flow for 10 m around the dike (Fig. 4.7e, f) and for a distance larger than 10 m single phase liquid up flow, which has elevated salinities compared to seawater. After 2.5 years the liquid saturations at -500 m depth reach up to 0.7 and then they stay constant with small changes until 3.5 yrs, which puts it in the phase diagram Figure 4.6 slightly above the phase boundary between L region and L+V region.

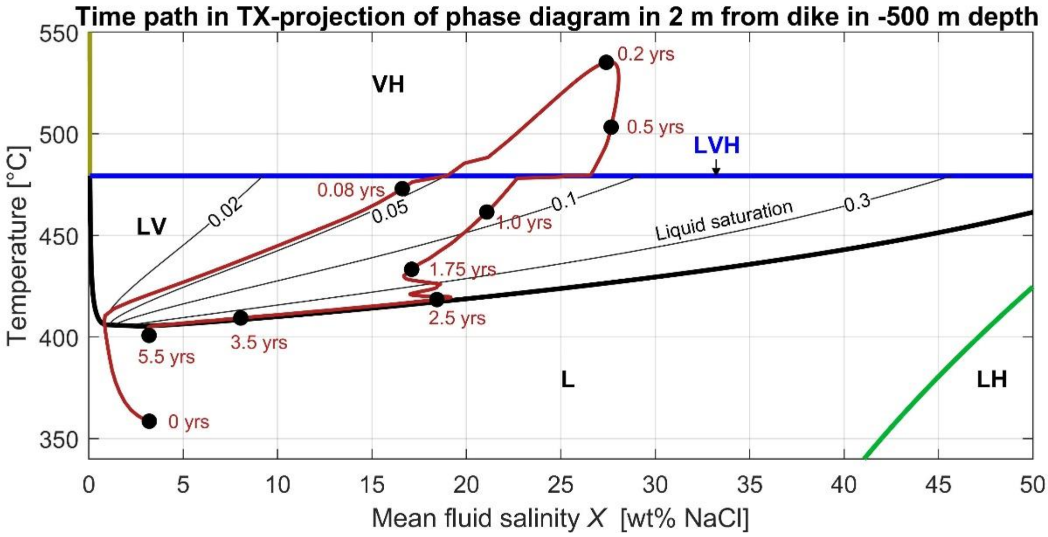

Figure 4.6: TX-projection of phase diagram for pressure of 29.4 MPa with time path for grid point at 2 m distance to dike in -500 m depth. Colors of phase boundaries are the same as in phase diagram in Fig. 4.2.

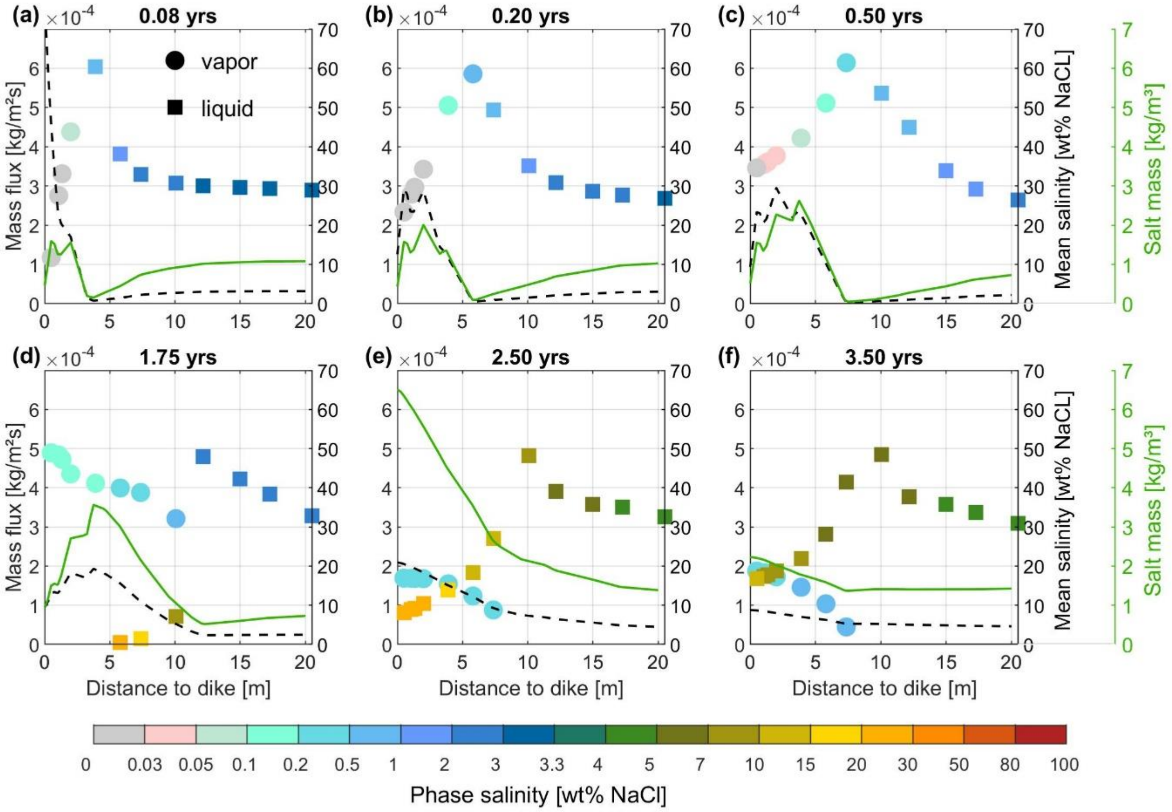

Figure 4.7: Plot of vertical mass fluxes of vapor and liquid with its salinity in color versus distance to dike at -500 m depth. Black dashed line show mean salinity *X* and green line show salt mass in pore space per cubic meter rock.

4.4.3 Vent salinity evolution

The vent salinity evolution is directly related to the thermodynamic processes stated above. Within the close area of 10 m from the dike, salinity is controlled by thermodynamic processes and for a larger distance, vent salinities become a product of mixing with phases generated at the dike and the recharge flow (Fig. 4.8). Due to fluid dispersion, elevated salinities are visible in distances up to 50 m from the dike. As the top of the simulated dike is only 10 m below the top of the simulation domain (Fig. 4.3a), rising vapors need only a few days to lower venting salinity to almost zero close to the dike (Fig. 4.8a). On the other hand, the temperature signal needs two weeks to arrive at the top because the rock matrix buffers the heat transport (Fig. 4.8b).

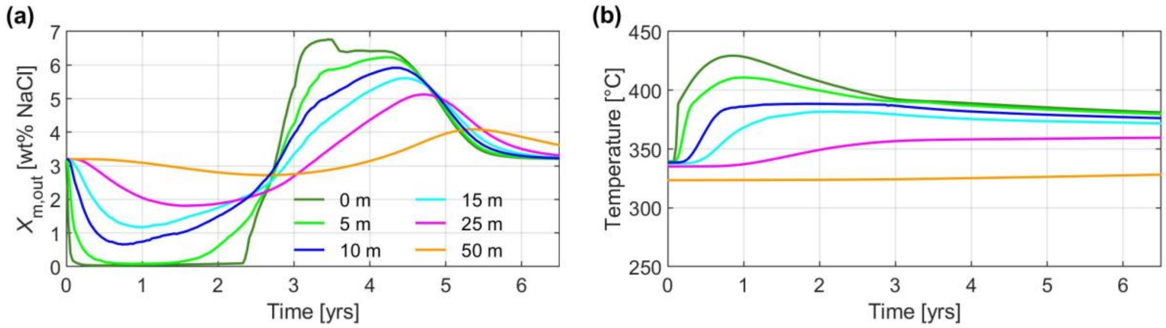

Figure 4.8: Mean vent salinity and vent temperature at different distances to the dike.

Figure 4.9 shows the salinity curve at 2 m distance to the dike, which is supplemented with panels for phase mass fluxes and vertical salt mass flux. During the first two years (stage 1), the vent salinity is dominated by the ascending flow of the vapor phase. At the dike the vapor phase loses almost all salt and salinity is below 0.1 wt% NaCl (Fig. 4.7). The vapor mass fluxes at a distance of two meters from the dike are relatively constant during this time (Fig. 4.9b). Furthermore, it shows that after 2 years (stage 2) salt mass fluxes start to rise when the liquid saturation exceeds 0.3. This indicates that the liquids are also buoyant at this time and move upwards. Now the curve of the liquid mass flux and the liquid salinity controls the salt mass flux (Fig. 4.9b) because the vapor phase has very low salinity in the L+V phase region at these pressure conditions. The mean salinity curve $X_{m,out}$ is then also closely related to the salt mass flux because the total mass flux is over one order of magnitude higher and has very small changes over time. The main reason that the liquid saturation becomes over 0.3 is the cooling and second the uptake of total salt mass, as explained above. The rise over 0.3 happens from 0 to -700 m depth over a short time period, leading first to a homogenization of the liquid saturation above 0.3. This is indicated by a small increase of the vent salinity until 2.5 years. The salinity increase after 2.5 yrs (stage 3) is also a result of the high salinity liquids mobilized from below -700 m depth (Fig. 4.7e and 4.9c). Here the NaCl has been accumulated at a faster rate during the first year because the recharge flow from below is a source of NaCl, which is deposited here within the liquid phase, whereas the resulting vapor flows upwards at the dike. Due to recharge flow from below and faster advective cooling at this place, the liquid phase can move upwards earlier.

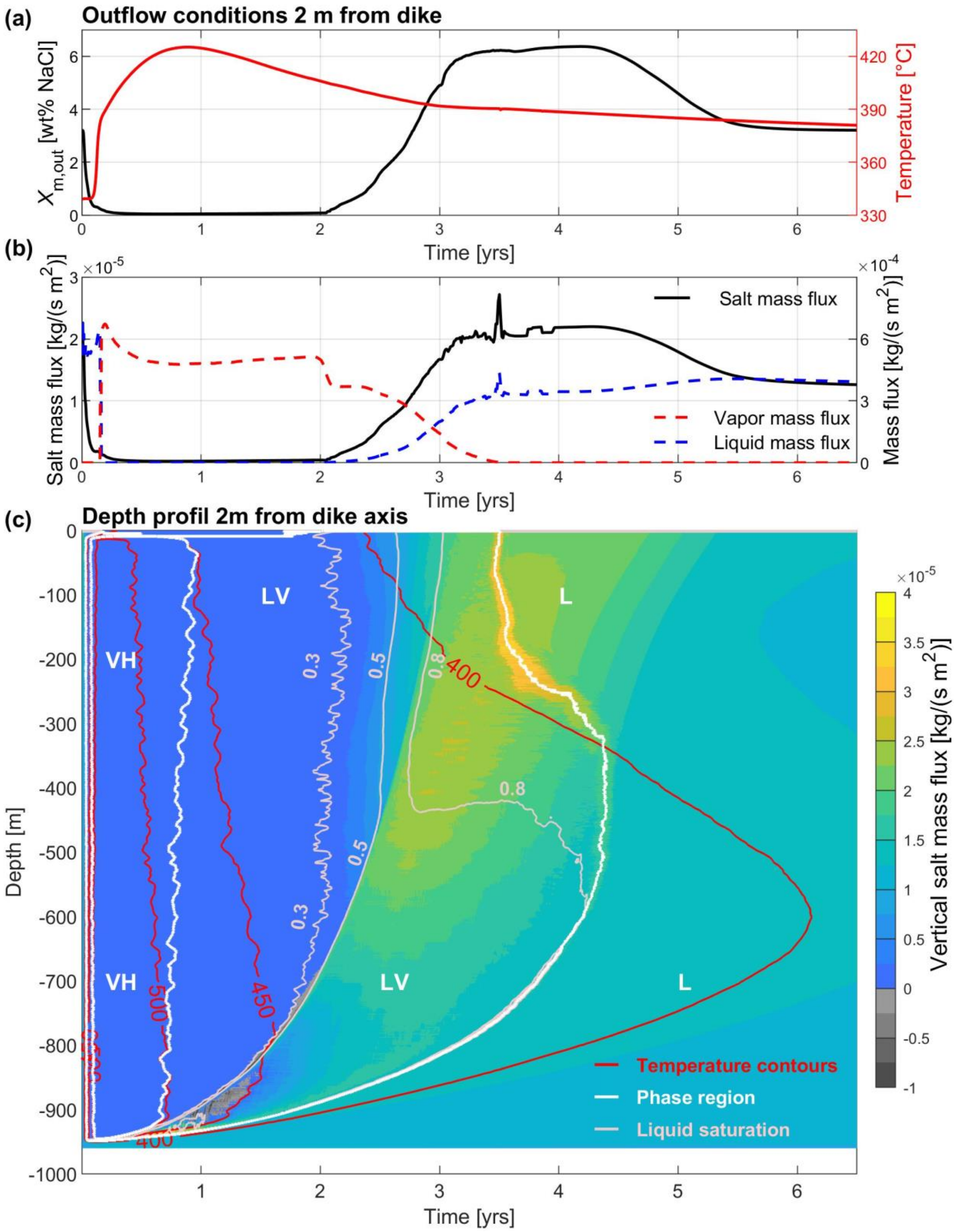

Figure 4.9: **a** Mean outflow salinity at 2 m distance to the dike versus time after the diking event. **b** Salt mass flux and mass flux for liquid and vapor. **c** Time profile of vertical salt mass fluxes of mesh nods at 2 m distance to dike, black lines are temperature contour lines in °C, white lines mark phase regions, grey thin line mark liquid saturations.

The transport of NaCl can be grouped in three parts (Fig. 4.7e, f). One part of NaCl moves slower upwards close to the dike as high salinity liquid (>15 wt% NaCl) within the L+V region. The second part mixes partly with the recharge flow and moves upwards as single-phase with approx. 8 wt% NaCl immediately close to the L+V region with the highest velocities because of the highest buoyancy.

Furthermore the liquids of the third part is more diluted with the recharge flow and flow upwards all along to the top at a distance of 15 m to 25 m having a salinity between 5 and 6 wt% NaCl. After three years at shallow depth lower than -400 m the liquids of the first two parts lead to an increase of the liquid saturation of up to 0.8 and a significantly higher liquid mass fluxes venting at the top. (Fig. 4.9c). In Figure 4.9c the short peak of the liquid mass flux is caused by the high sensitivity of temperature changes on the liquid density around the critical curve, which is shown in Figure 4.5b and leads to higher buoyancy of the liquid compared to the adjacent liquid in the hotter L+V region.

4.4.4 Parameter study of bottom inflow temperature (T_{bc}) and salinity (X_{bc}) on seafloor venting salinity curve

The vent salinity evolution found at the EPR 9°50.3'N after the 1991/92 diking event (Fig. 4.1) shows some differences and a higher complexity in the evolution of temperature and salinity than the reference simulation. The Bio9-vent shows an overall low salinity that stays below seawater salinity, with a slow decrease after the first local maximum. On the contrary, the P-vent salinity shows only a small decrease after the maximum and then it stays constant at seawater salinity. The temperature of both vents shows an increase of the temperature at 4 years after the eruption, which is not indicated by the reference simulation, where a continuous decrease of vent temperature is observed.

From previous studies we know that in hydrothermal systems of fast-spreading mid-ocean ridges, the uprising fluids change their temperature and salinity with changing heat supply released from the axial magma lens (AML). A replenishment of the AML and an onset of magma convecting therein leads to an increased heat supply into the overlying hydrothermal system. Higher basal temperatures lead to enhanced phase separation processes, which are followed by low salinity vapors entering the upflow zone and increasing temperatures. On the other hand, a freezing magma chamber leads to dilution of the prior condensed and pooled brines under colder single-phase conditions followed by brine venting at the seafloor (Vehling et al., 2021).

Therefore we have first applied a parameter study of bottom inflow temperature (T_{bc}) and salinity (X_{bc}) as these are the first-order control parameters of the vent salinity and temperature evolution. We have used the same rock parameter and inflow mass rate Q_m as in the previous section (Table 4.4).

Table 4.4. Model parameter in 4.4.4

Variable	**Meaning**	**Value**
k	Rock permeability	$1.5 \cdot 10^{-14}$ m^2
Q_m	Inflow mass rate	0.021 kg/s
S_{lr}	Residual liquid saturation	0.3
Φ	Rock porosity	0.05

The temperature has a high impact on the onset of increasing vent salinity and its salinity maximum (Fig. 4.10). For the high-temperature case (T_{bc} = 400 °C), the time period of phase separation (stage 1) takes much longer (+1.5 years), resulting in dominant vapor venting until 4 years and a rapid change, i.e. a shortened stage 2, to a high-salinity liquid dominated two-phase venting. The reason for the rapid onset of liquid dominated venting is a combination of exhausted initially produced vapors, which have been vented, and a following lower pressure gradient that could move the heavy high-salinity liquid. For the lower temperature cases (T_{bc} = 325 °C and T_{bc} = 350 °C) the time duration of vapor venting (stage 1) is shortened. Most of the produced vapor at the dike condensates and merge again with the high-salinity liquid producing little elevated venting liquid salinities (Fig. 4.15).

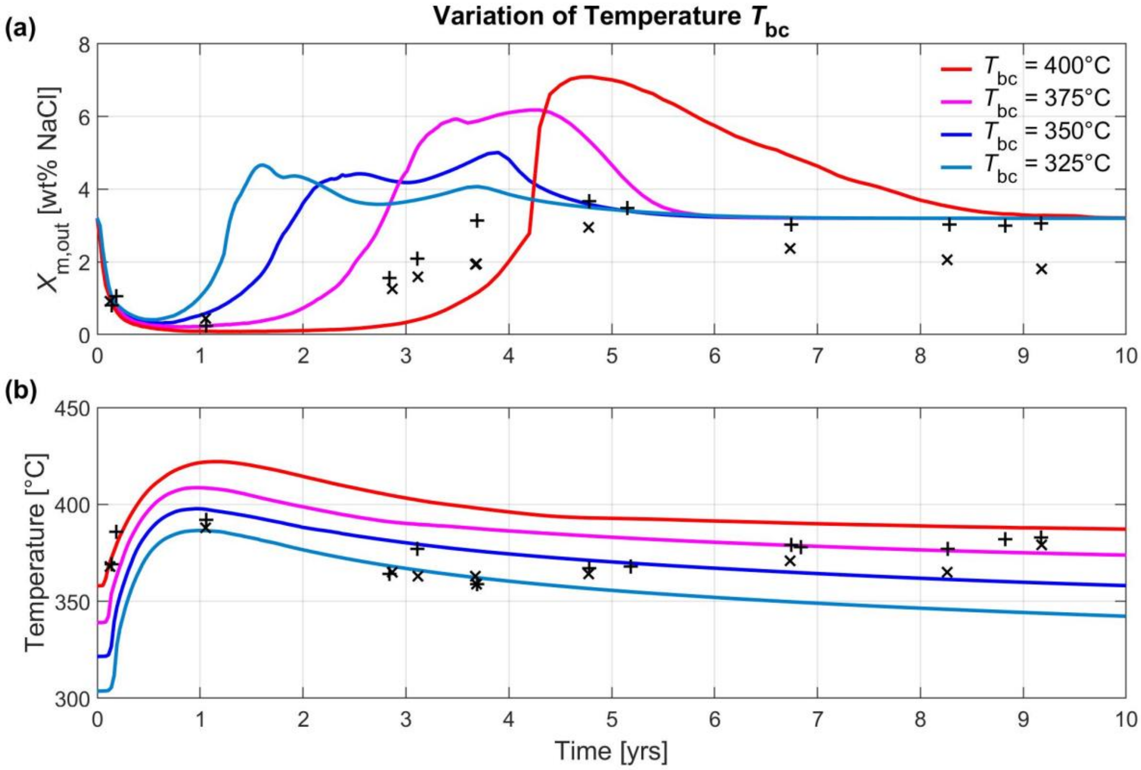

Figure 4.10: **a** Mean outflow salinity, **c** outflow temperature for different bottom inflow temperatures T_{bc} but for same bottom inflow salinity X_{bc} of 3.2 wt% NaCl. Properties are averaged over the distance of 10 m from dike. Observed vent salinities are marked by ‘x’ for vent Bio9 and ‘+’ for vent P (Von Damm, 2004).

The Variation of X_{bc} shows a linear shift of venting liquid salinity and a small extension of venting duration (stage 3) of increased salinities for higher X_{bc} (Fig. 4.11 & 4.15). The comparison of the simulated seafloor venting fluid salinity with measurements from EPR 9°50.3’N (P-vent and Bio9-vent) also show a vent salinity increase after 2 years, but the salinity does not surpass 4 wt% NaCl and the salinity curve is overall much smoother. The salinity drop of the second half of the Bio9 vent indicate that at least the bottom inflow salinity should be lower than 2 wt% NaCl because after 8 years the dike salinity signal should have vanished. The observation data fits better for a lower X_{bc} = 1.5 wt% NaCl, which we will take for further parameter studies.

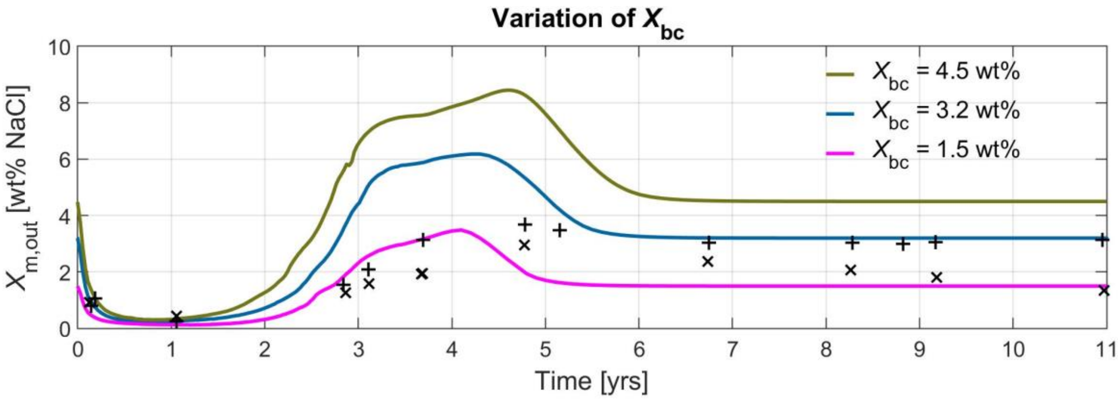

Figure 4.11: Mean outflow salinity for different bottom inflow salinity X_{bc} but for same inflow temperature T_{bc} of 375°C. Salinities are averaged over the distance of 10 m from dike. Observed vent salinities are marked by ‘x’ for vent Bio9 and ‘+’ for vent P (Von Damm, 2004).

4.4.5 Parameter study of rock properties on seafloor venting salinity curve

Rock permeability and porosity determine fluid particle velocity and therefore, they have a high impact on the venting salinity curve. Both rock properties are not well known, despite they obviously correlate positively. Nevertheless, the results of the previous section give bounds for rock properties, which will be further investigated. In the following studies, we use $X_{bc} = 1.5$ wt% NaCl and an inflow mass rate Q_m, which is linearly adjusted with rock permeability, to ensure the same pattern of flow field:

$$Q_m(k) = \frac{k}{1.5 \cdot 10^{-14}\,\mathrm{m}^2}\;0.021\ \mathrm{kg/s} \tag{4.14}$$

A higher permeability leads to an earlier start of increased venting salinity (stage 3) (Fig. 4.12). The main reason is a faster transport of the vapor phase and a minor reason is the cooling of the near dike region by enhanced recharge fluids from below. The cooling causes the early condensation of residual vapors and the start of single medium salinity liquid flow, which is more efficient and has a higher salt mass flux compared with two-phase flow.

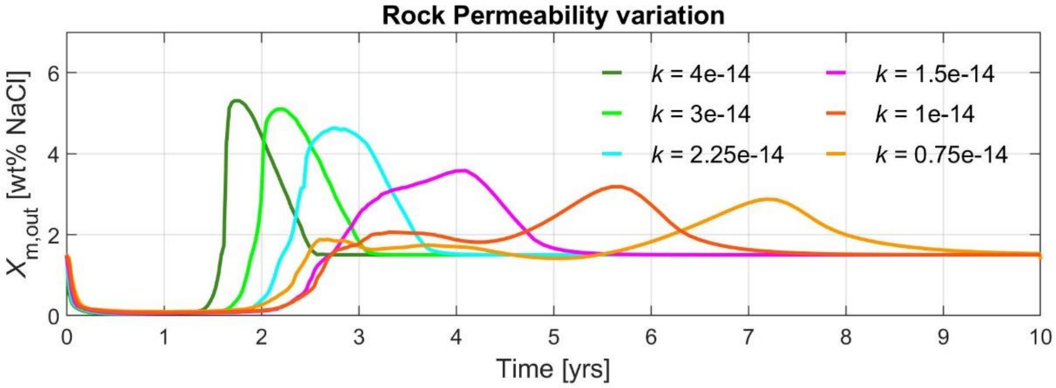

Figure 4.12: Variation of rock permeability: $T_{bc} = 375$ °C, $\Phi = 0.05$, $S_{lr} = 0.3$. Mean outflow salinity is averaged over the distance from 0 m to 10 m from dike.

A lower porosity has the same effect of earlier increased salinity like higher permeability because fluids also have higher travel velocities (Fig. 4.13). However, the same proportion of permeability and porosity has different results (Fig. 4.14). The temperature curve (Fig. 4.14b) shows that vent temperature rises earlier and this heat transport to the top is much higher for the high permeability and porosity case. This early heat loss and higher cooling rate of recharge flow from below lead to a higher drop in temperature, which is below the low permeability and porosity case. This faster temperature drop is the main reason for the faster switch to higher venting salinities. The phase separation process is also more effective when vapors are hotter and have less density and salinity. Maximum venting salinities are particularly high when the temperature drop coincides with the time when most of the produced vapors have been vented before they merge with the residual brines. For high-temperature simulation, the cooling from below is less efficient and the maximum brine peak of both cases (stage 3) has a higher time shift (see also Fig. 4.15). Setting the residual liquid saturation to zero has the simple effect of dampening the salinity curve (Fig. 4.13) because the liquid phase can move earlier.

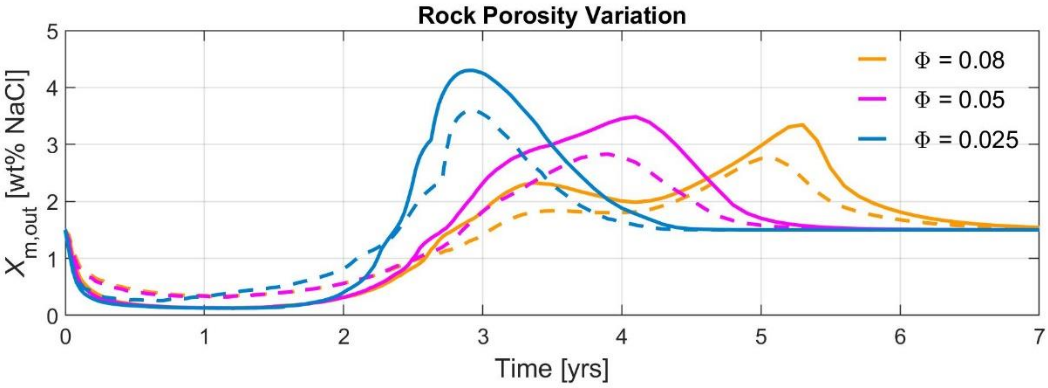

Figure 4.13: Mean outflow salinity for different rock porosity: T_{bc} = 375 °C, $k = 1.5 \cdot 10^{-14}$ m^2, Continuous lines show results for residual liquid saturation of S_{lr} = 0.3 and dashed lines show results for S_{lr} = 0. Vent salinity is averaged over the distance from 0 m to 10 m from dike.

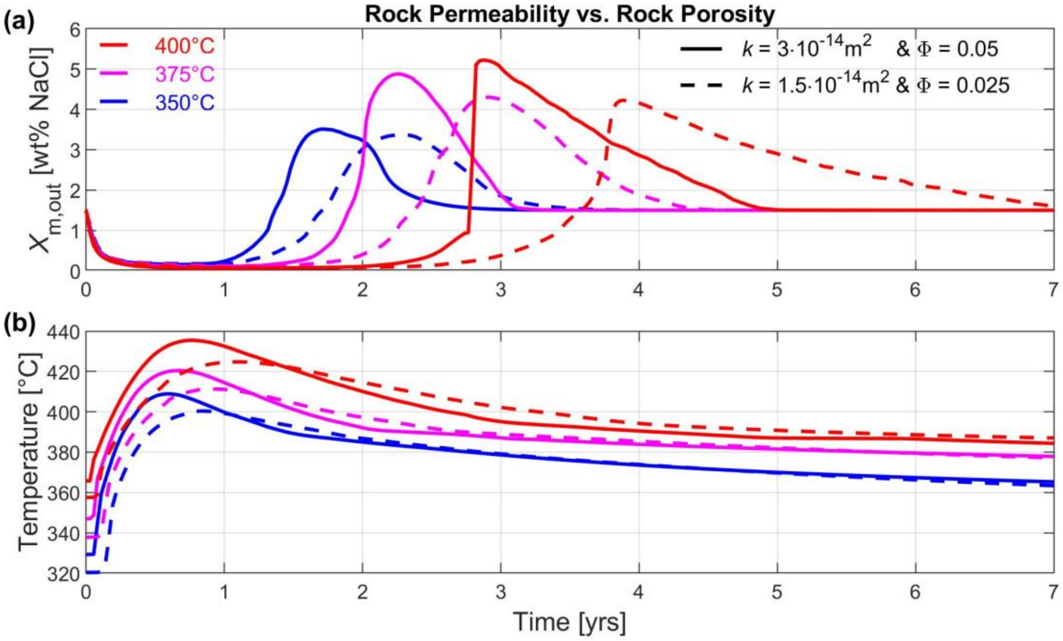

Figure 4.14: Rock permeability vs rock porosity: S_{lr} = 0.3. **a** vent salinity and **b** vent temperature. Properties are averaged over the distance from 0 m to 10 m from dike.

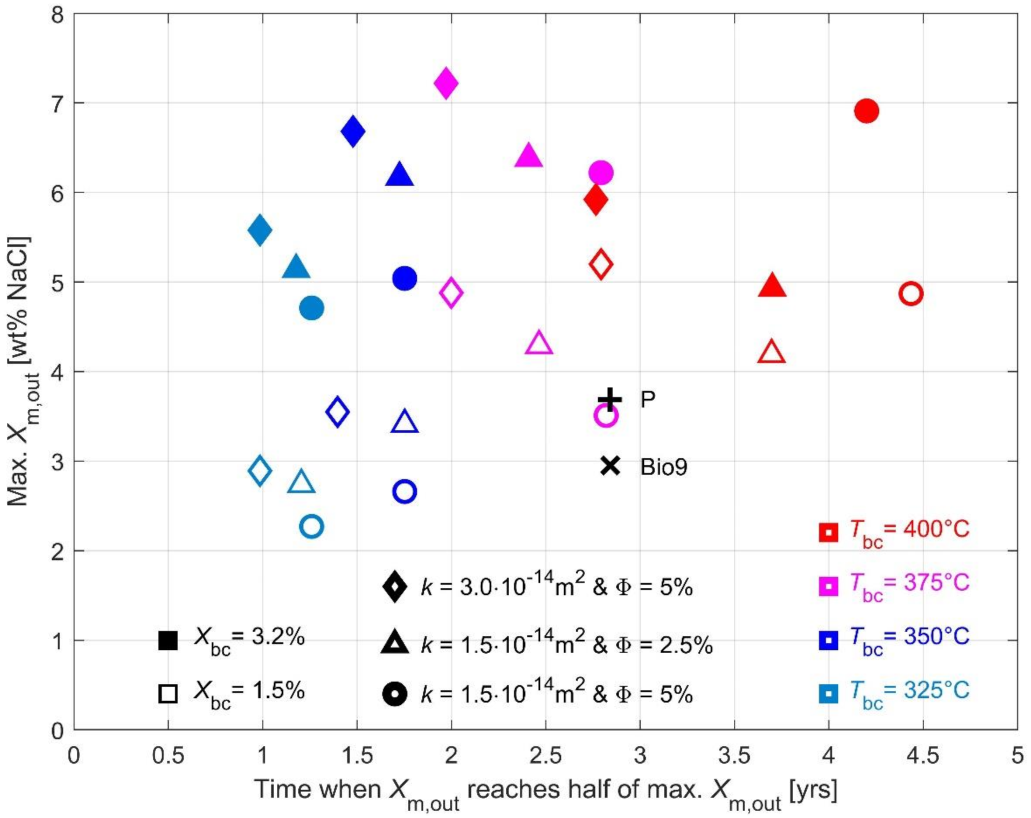

Figure 4.15: Scatter plot of maximum of salinity curve versus time, when salinity reaches half of its maximum of salinity curve. $S_{lr} = 0.3$. Observed vent salinities are marked by 'x' for vent Bio9 and '+' for vent P (Von Damm, 2004).

4.5 Discussion

The results have shown that we have found the key parameters which control the salinity curve evolution after a dike intrusion at a mid-ocean ridge system. We can approximate the salinity curve of the EPR 9°50.3'N Bio9 and P vents when we use inflow temperature and salinity of T_{bc} = 375 °C and X_{bc} = 1.5 wt% NaCl, a rock permeability of $k = 1.5 \cdot 10^{-14}$ m^2 and rock porosity of 0.05 (Fig. 4.10). A change in rock properties does only slightly change the results if the proportion of porosity and permeability are held constant.

On the other hand, the observed vent temperature curve of Bio9 and P vent may contradict our findings. The vent temperature falls below 370 °C, which implies a higher convective cooling rate and therefore a higher permeability. A somewhat higher permeability conforms with the 2006 diking event at EPR 9°50.3'N where temperature also drops from 385 °C to 371 °C (Bio9 vent) and 388 °C to 361 °C (P vent) within only two years (Fornari 2012). For a cooling below 380 °C of vent temperatures our simulations indicate a rapid mobilization of all produced high-salinity liquids leading to a prominent salinity peak and fast decrease to a constant background salinity afterwards, which is not observed for P vent and Bio9 vent, where after the salinity peak the salinity slowly changes.

In the following, we will describe two reasons for the model mismatch to the observed P vent and Bio9 vent salinities. First, in our model, the prominent salinity peak is mainly caused by a constant rock permeability, which leads to a uniform cooling of the near dike region and to a joint up rise start of all deep and shallow produced high-salinity liquids. In nature we have permeability decrease with depth and with distance to the ridge axis (Carlson, 2011). At the axis of the EPR 9°50 region, the thickness of the top pillow basalt layer 2A is seismically inferred between 150 m and 250 m (Harding et al., 1993; Xu et al., 2014). For altered layer 2A, borehole measurements show a permeability on the order of 10^{-14} m^2 to10^{-13} m^2 (Anderson et al., 1985; Carlson, 2011). Seismic wave velocities show a significant increase with crustal age at the ridge axis (Nedimović et al., 2008), caused by porosity decrease due to mineral precipitation. Therefore the permeability could be higher than 10^{-13} m^2 for newly created crust at the dike and the advective cooling of the dike is faster. Subsequently the initial increase of vent salinity consists of shallow produced and mobilized liquids and vapors separated at deeper parts of the dike. (Additionally, seawater recharge fluids could be mixed into the upflow zone at the dike-pillow basalt transition zone). For the deeper crustal layer 2B, sheeted dikes, where permeability linearly increases with depth, the high-salinity liquids at the dike stay hot within the two-phase region much longer and are fixed because they are too heavy to move upwards. The dike cools gradually with greater depth and the adjacent high-salinity liquids will be slowly mixed with up flowing fluids from the basal heat source that dampens the salinity of venting fluids at the top.

The second reason for dampening of the venting salinity curve could be an increasing intensity of phase separation caused by higher heat release of the basal AML. After the 1991/92 event, no seismic imaging of the AML has been done, but the 2008 survey has shown a melt poor AML after the 2005/06 extrusive eruption (Xu et al., 2014). As this eruption has covered a large amount of seafloor within the AST starting at the venting side of P vent and Bio9 vent (Soule et al., 2009; Soule et al., 2007; Tan et al., 2016; Xu et al., 2014), we follow the scenario of a melt rich AML, which was drained for melt supply for the 2005/2006 event. However, also melt supply from deeper sub crustal AMLs are likely to have contributed (Marjanović et al., 2018). In line with this scenario, we think that after the 1991/92 eruption, the AML was likely also drained. Afterwards, a constant replenishment starts, which restarts higher heat supply from the AML and subsequent phase separation and basal vapor uprise again some years later. From vent temperature increase after 1995, we can’t say if heat supply from the AML is the main reason for the increase, as this vent temperature could also be affected by mineral precipitation in the uppermost layer, which can focus uprising fluids and prevent them from diffusive cooling. So it is in principle possible that low-salinity vapors have mixed with high-salinity liquids at the dike and have dampened the observed salinity peak between 1995 and 1998. However, it is also likely that significant basal low salinity vapor uprise started later and caused the salinity drop for Bio9 vent after 1997.

As Bio9 vent and P vent are direct neighbors having only a distance of 50 m between each other, it is notable that the salinity of P vent is different and stays at seawater salinity until the 2005/06 eruption. Here we think that 3D effects of fluid circulations and redistribution of upflow and downflow zones play a role when the dike has cooled. The cooling is indicated by the vanishing of venting areas observed shortly after the dike eruption (Haymon et al., 1993; Rubin et al., 1994). The low average vent salinity of Bio9 vent below seawater salinity leads to a mass balance problem, which could be solved by constant NaCl accumulation on top of the AML. Numerical simulations from (Vehling et al., 2021) show that the stable basal brine layers are not convecting and strongly reduce conductive heat supply from the AML into the system and heat is needed for phase separation. Therefore, we think that magmatic activity has significantly increased from 1995 at this ridge segment. The counterpart of this magmatic active segment is the segment 10 km to the south between EPR 9°26.1’N and EPR 9°37.1’N, where vents still have a salinity between 4.7 - 5.1 wt% NaCl during the 1991/92 eruption until 1994, where magmatic events were not observed (Oosting and Von Damm, 1996; Von Damm, 2000).

4.6 Conclusion

At the EPR 9°50.3’N changes in vent fluid salinity and temperature at individual vents have been observed, which have been related to the 1991/92 eruptive diking event. In this study we have applied two-dimensional simulations of dike intrusions into the axial part of a mid-ocean hydrothermal convection cell. The model setup considers different axial upflow temperatures and salinities by variable axial bottom boundary conditions. For a representative case study we have analyzed how NaCl accumulated and mobilized close to the dike and how this correlates to the characteristic salinity signal of seafloor vents. Within a study of parameters we found that fluid salinity and temperature of the upflow zone and the rock permeability have the highest impact on the fluid salinity curve beneath rock porosity and residual liquid saturation.

Due to these results we were able to find the key parameters that fit the first order characteristics of the observed salinity curve at the EPR 9°50.3’N. The observed differences can be addressed to model simplifications such as homogeneous rock permeabilities and constant temperature and salinity of the upflow zone. Our results indicate that approx. 5 years after the 1991/92 diking event the salinity and temperature curve is strongly influenced by heat release and subsequent phase separation processes above the axial magma lens. Further simulations that combine dike intrusions with phase separation and transient brine accumulation on top of the AML should be applied to investigate how the brine layer is affected by the dike intrusion and how this is related to subsequent seafloor venting salinities.

4.7 Appendix

4.7.1 Mass and heat flux boundary condition

The total mass rate for the bottom boundary condition was found in a simulation run using a set up with a Gaussian-shaped temperature boundary condition (T_{max} = 700 °C, T_{min} = 300 °C) representing the heat source of a magma chamber. Then we took the total mass rate venting at the top of the domain of the pre-setup. We use this mass rate as inflow mass rate Q_{m}, but adjust it slightly in that way, that a buoyancy-driven up the flow of injected fluids (350 °C to 400 °C) is established. As we use a constant Q_{m} for all temperatures, the low-temperature case of 325 °C is slightly not buoyancy-driven. When we change rock permeability k, we change Q_{m} with the same factor.

We control bottom inflow temperature T_{bc} by calculating the corresponding specific enthalpy h_{bc}, which also depend on inflow fluid salinity X_{bc} and bottom pressures. Therefore h_{bc} has to be recalculated during simulation to hold T_{bc}. Total heat rate Q_{E} and salt mass rate Q_{X} are then defined by the following expressions:

$$Q_{\mathrm{E}} = Q_{\mathrm{m}} \cdot h_{\mathrm{bc}} \tag{4.15}$$

$$Q_{\mathrm{X}} = Q_{\mathrm{m}} \cdot X_{\mathrm{bc}} \tag{4.16}$$

4.7.2 Calculation of dike section temperatures

After each time step Δt the new dike temperatures T_d for each section are calculated by considering the one-dimensional (horizontal) energy conservation equation:

$$\frac{\partial E_\mathrm{d}}{\partial t} = c_\mathrm{d} w \rho_\mathrm{d} \frac{\partial T}{\partial t} = -q_\mathrm{h} \tag{4.17}$$

where w is one half of the dike thickness because we simulate only one-sided cooling and c_d is the specific heat capacity of the dike. The specific heat capacity c_d of a dike section depends on temperature because of the release of latent heat at liquid basalt crystallization. For the interval between liquidus temperature T_l (1200 °C) and solidus temperature T_s (1000 °C), we additionally calculate a constant specific heat c_l:

$$c_\mathrm{l} = \frac{L}{\left(T_\mathrm{l} - T_\mathrm{s}\right)} \tag{4.18}$$

where L is the latent heat for basalt, which has a value of $3.35 \cdot 10^{-5}$ J/kg (Rupke and Hort, 2004)

We then define specific heat capacity for two temperature intervals:

$$c_\mathrm{d} = \left(c_\mathrm{r} + c_\mathrm{l}\right) \qquad \text{if} \quad T > T_\mathrm{s} \ \wedge \ T < T_\mathrm{l} \tag{4.19}$$

$$c_\mathrm{d} = c_\mathrm{r} \qquad \text{if} \ \ T < T_\mathrm{s} \tag{4.20}$$

For calculating a new dike section temperature, we obtain following procedure from Eq. (4.15):

$$\begin{aligned}
T_\mathrm{d}^\mathrm{new} &= T_\mathrm{d}^\mathrm{old} - \frac{q_\mathrm{h}\Delta t}{\left(c_\mathrm{r} + c_\mathrm{l}\right)\rho_\mathrm{d} w} && \text{if} \ \ T_\mathrm{d}^\mathrm{new} < T_\mathrm{l} \ \wedge \ T_\mathrm{d}^\mathrm{old} >= T_\mathrm{s} \\
T_\mathrm{d}^\mathrm{new} &= T_\mathrm{s} - \frac{q_\mathrm{h}\Delta t - \left(c_\mathrm{r} + c_\mathrm{l}\right)\rho_\mathrm{d} w \left(T_\mathrm{d}^\mathrm{old} - T_\mathrm{s}\right)}{c_\mathrm{r}\rho_\mathrm{d} w} && \text{if} \ \ T_\mathrm{d}^\mathrm{new} > T_\mathrm{s} \ \wedge \ T_\mathrm{d}^\mathrm{old} < T_\mathrm{s} \\
T_\mathrm{d}^\mathrm{new} &= T_\mathrm{d}^\mathrm{old} - \frac{q_\mathrm{h}\Delta t}{c_\mathrm{r}\rho_\mathrm{d} w} && \text{if} \ \ T_\mathrm{d}^\mathrm{old} < T_\mathrm{s}
\end{aligned} \tag{4.21}$$

4.7.3 Permeability

When halite precipitates, due to heating of the dike intrusion, it fills up the pore space and rock permeability decreases. For this set up we use the following function for the reduced permeability k_i, which is also used in the TOUGH2 geothermal simulator (Pruess et al., 2012):

$$k_i = k(1 - S_\mathrm{h})^2 \tag{4.22}$$

We computed permeability at segments using a logarithmic average, as it can vary over orders of magnitudes:

$$k_\mathrm{seg} = \exp\left(\frac{\ln\left(k_{i,\mathrm{up}}\right) + \ln\left(k_{i,\mathrm{do}}\right)}{2}\right) \tag{4.23}$$

If halite saturation becomes larger than 0.95 at a grid point, then permeability k_{seg} is set to zero for all segments around this point. We then stop solving mass and salt mass conservation at these nodes, but still solve for energy conservation by heat conduction.

4.7.4 Thermal closure of rock porosity and reduced rock permeability

The basalts, which are in direct contact with the dike intrusion, are so far heated up that they become ductile. Then rock porosity and permeability decrease. We model a brittle-ductile transition zone for temperatures between 600 °C (T_{br}) and 800 °C (T_{du}):

$$\Phi(T) = \frac{(\Phi + \Phi_{\mathrm{du}})}{2} + \frac{(\Phi - \Phi_{\mathrm{du}})}{2} \cos\left(\frac{\pi (T - T_{\mathrm{br}})}{T_{\mathrm{du}} - T_{\mathrm{br}}} \right) \tag{4.24}$$

$$k(T) = \frac{(k + k_{\mathrm{du}})}{2} + \frac{(k - k_{\mathrm{du}})}{2} \cos\left(\frac{\pi (T - T_{\mathrm{br}})}{T_{\mathrm{du}} - T_{\mathrm{br}}} \right) \tag{4.25}$$

When the temperature exceeds 800 °C, we stop solving for mass and salt mass conservation at these nodes, but still solve for energy conservation by heat conduction. In Table 4.2 we list setup parameters fixed for all simulation runs.

4.7.5 Fixed model setup parameter

Table 4.2

Variable	**Meaning**	**Value**	**Unit**
c_{r}	Specific heat rock	1100	J/(kg·K)
c_{l}	Additional specific heat between solidus and liquidus temperature	1675	J/(kg·K)
K	Mean conductivity of rock matrix and fluid	2.5	W/(m·K)
k_{du}	Permeability at T_{du}	10^{-17}	m^2
p_{top}	Top pressure boundary condition	25	MPa
T_{br}	Temperature (brittle boundary)	600	°C
T_{du}	Temperature (ductile boundary)	800	°C
T_{d}	Initial dike temperature (hold for first 4 days after dike injection)	1200	°C
T_{l}	Liquidus Temperature of dike	1200	°C
T_{s}	Solidus Temperature of dike	1000	°C
T_{top}	Top inflow temperature boundary condition	10	°C
w	Half of dike thickness	1	m
ρ_{r}	Rock density	2900	$\mathrm{kg/m}^3$
ρ_{d}	Dike density	2900	$\mathrm{kg/m}^3$
Φ_{du}	Porosity at T_{du}	0.001	-
X_{top}	Top inflow fluid salinity $X_{\mathrm{top}} = X_{\mathrm{bc}}$		wt fract

4.7.6 Mesh sensitivity at the dike

We performed three simulations to figure out how the mesh resolution changes the salinity curve. For the regular mesh, which is used for all simulations, the CV close the dike have a size of 0.5 m², whereas the boundary CV at the dike have a size of 0.25 m². A coarser mesh leads to minor changes of the salinity curve demonstrating that the chosen mesh resolution is sufficient (Fig. 4.16).

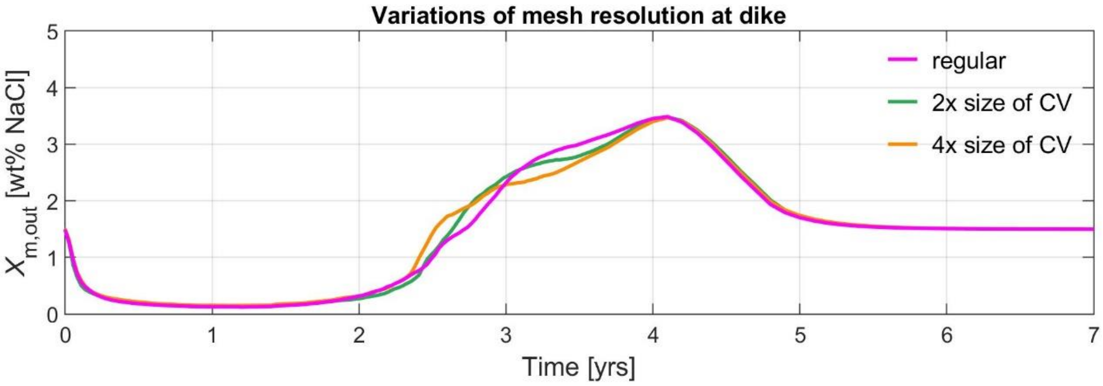

Figure 4.16: Mesh sensitivity on mean salinity outflow at the dike for different sizes of CV's at the dike. Salinities are averaged over a distance of 10 m from dike.

4.7.7 Early salt accumulation at the lower part of the dike

After 0.75 years at the bottom of the simulated dike at depth of -950 m high-salinity liquids have been accumulated (Fig. 4.17a). Here our model does not represent reality in detail, because we do not simulate the brine layer on top of the magma chamber, where the dike would also intrude into. In a scenario with a brine layer, some parts of the high-salinity liquids would stay longer at the dike. In our model the high-salinity liquids could probably cool faster as we have more fluid flow from below than recharge flow from the side how it would be in reality. When the liquids exceed the residual liquid saturation a small convection cell evolves (Fig. 4.17a). Hot liquids (480 °C > T > 460 °C and > 55% NaCl) flow downwards at the dike wall (negative vertical salt mass flux in Fig. 4.9c) and merge with seawater like fluid from below. One part of the mixed liquids flow outside of the L+V region to the seafloor and have a salinity of up to 8 wt% NaCl. The accumulated heavy high-salinity liquids lead to an increase of the absolute value of the pressure gradient to 10000 Pa/m because they block pathway of the upflow zone. This enables liquids with up to 35 wt% NaCl to flow upwards inside the L+V region, where they are reheated at the dike and undergo again phase separation. Here, vapors disappear straight to the top and heavy high-salinity liquid accumulate at the dike and refill the space the vapors have left. Figure 4.17b shows the high-salinity liquid upflow front at the dike, where the liquid saturation rises above 0.5. This front causes the sudden rise of vertical salt mass fluxes in Fig. 4.9c.

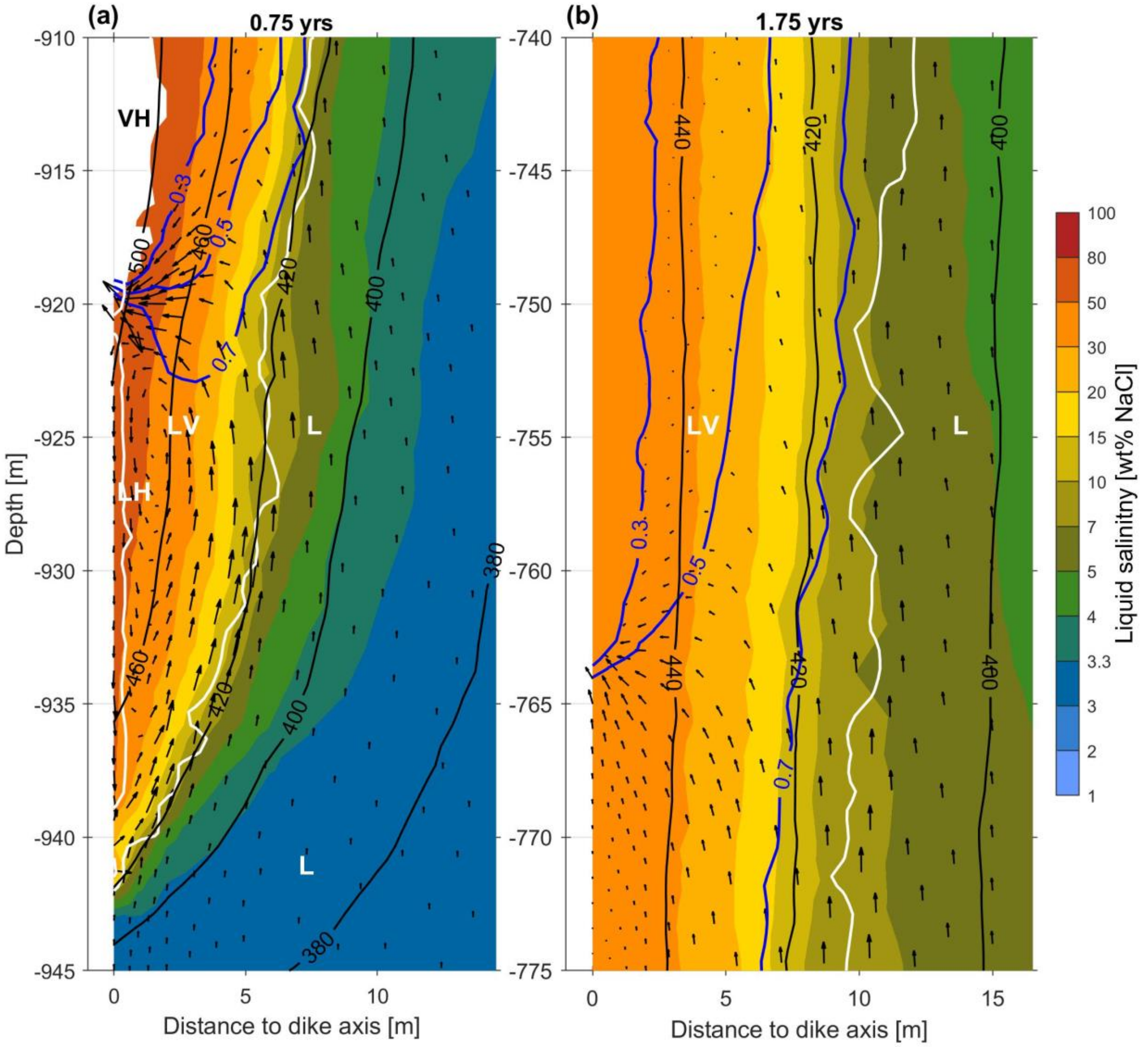

Figure 4.17: Color plot of liquid salinity at the dike after **a** 0.75 yrs and **b** 1.75 yrs after dike intrusion. Black arrows show salt mas flux. Black contour lines show isotherms in °C. White lines mark different phase regions and blue contour lines mark liquid saturations.

4.8 Bibliography

Anderson, R.N., Zoback, M.D., Hickman, S.H., Newmark, R.L., 1985. Permeability versus depth in the upper oceanic crust: In situ measurements in DSDP hole 504B, eastern equatorial Pacific. Journal of Geophysical Research: Solid Earth, 90(B5): 3659-3669, https://doi.org/10.1029/JB090iB05p03659.

Carlson, R.L., 2011. The effect of hydrothermal alteration on the seismic structure of the upper oceanic crust: Evidence from Holes 504B and 1256D. Geochemistry Geophysics Geosystems, 12, DOI:10.1029/2011gc003624.

Detrick, B. et al., 1987. Class-Ii Antigen Expression on Retinoblastoma Cells. Medical and Pediatric Oncology, 15(6): 321-321.

Driesner, T., 2007. The system H2O-NaCl. Part II: Correlations for molar volume, enthalpy, and isobaric heat capacity from 0 to 1000 degrees C, 1 to 5000 bar, and 0 to 1 X-NaCl. Geochimica Et Cosmochimica Acta, 71(20): 4902-4919, DOI:10.1016/j.gca.2007.05.026.

Driesner, T., Heinrich, C.A., 2007. The system H2O-NaCl. Part I: Correlation formulae for phase relations in temperature-pressure-composition space from 0 to 1000 degrees C, 0 to 5000 bar, and 0 to 1 X-NaCl. Geochimica Et Cosmochimica Acta, 71(20): 4880-4901, DOI:10.1016/i.gca.2006.01.033.

Fornari, D.J. et al., 1998. Time-series temperature measurements at high-temperature hydrothermal vents, East Pacific Rise 9 degrees 49 '-51 ' N: evidence for monitoring a crustal cracking event. Earth and Planetary Science Letters, 160(3-4): 419-431, DOI:10.1016/S0012-821x(98)00101-0.

Fornari, D.J. et al., 2012. The East Pacific Rise Between 9°N and 10°N: Twenty-Five Years of Integrated, Multidisciplinary Oceanic Spreading Center Studies. Oceanography, 25(1): 18-43.

Gallant, R.M., Von Damm, K.L., 2006. Geochemical controls on hydrothermal fluids from the Kairei and Edmond Vent Fields, 23°-25°S, Central Indian Ridge. Geochemistry, Geophysics, Geosystems, 7(6): n/a-n/a, DOI:10.1029/2005gc001067.

German, C.R., Von Damm, K.L., 2004. Hydrothermal processes. In: Holland, H.D., Turekian, K.K., Elderfield, H. (Eds.), Treatise on geochemistry, Vol. 6. The oceans and marine geochemistry. Elsevier-Pergamon, pp. 181-222.

Germanovich, L.N., Lowell, R.P., Astakhov, D.K., 2001. Temperature-dependent permeability and bifurcations in hydrothermal flow. Journal of Geophysical Research: Solid Earth, 106(B1): 473-495, DOI:10.1029/2000jb900293.

Germanovich, L.N., Lowell, R.P., Ramondenc, P., 2011. Magmatic origin of hydrothermal response to earthquake swarms: Constraints from heat flow and geochemical data. Journal of Geophysical Research, 116(B5), DOI:10.1029/2009jb006588.

Harding, A.J., Kent, G.M., Orcutt, J.A., 1993. A Multichannel Seismic Investigation of Upper Crustal Structure at 9-Degrees-N on the East Pacific Rise - Implications for Crustal Accretion. Journal of Geophysical Research-Solid Earth, 98(B8): 13925-13944, DOI:10.1029/93jb00886.

Haymon, R.M. et al., 1991. Hydrothermal Vent Distribution Along the East Pacific Rise Crest (9-Degrees-09'-54'n) and Its Relationship to Magmatic and Tectonic Processes on Fast-Spreading Midocean Ridges. Earth and Planetary Science Letters, 104(2-4): 513-534, DOI:10.1016/0012-821x(91)90226-8.

Haymon, R.M. et al., 1993. Volcanic-Eruption of the Midocean Ridge Along the East Pacific Rise Crest at 9-Degrees-45-52'n - Direct Submersible Observations of Sea-Floor Phenomena Associated with an Eruption Event in April, 1991. Earth and Planetary Science Letters, 119(1-2): 85-101, DOI:10.1016/0012-821x(93)90008-W.

Klyukin, Y.I., Lowell, R.P., Bodnar, R.J., 2017. A revised empirical model to calculate the dynamic viscosity of H2ONaCl fluids at elevated temperatures and pressures (≤1000 °C, ≤500 MPa, 0–100 wt % NaCl). Fluid Phase Equilibria, 433: 193-205, https://doi.org/10.1016/j.fluid.2016.11.002.

Lowell, R.P., Xu, W.Y., 2000. Sub-critical two-phase seawater convection near a dike. Earth and Planetary Science Letters, 174(3-4): 385-396, DOI:10.1016/S0012-821x(99)00275-7.

Marjanović, M. et al., 2018. Crustal Magmatic System Beneath the East Pacific Rise (8°20′ to 10°10′N): Implications for Tectonomagmatic Segmentation and Crustal Melt Transport at Fast-Spreading Ridges. Geochemistry, Geophysics, Geosystems, 19(11): 4584-4611, https://doi.org/10.1029/2018GC007590.

Nedimović, M.R. et al., 2008. Upper crustal evolution across the Juan de Fuca ridge flanks. Geochemistry, Geophysics, Geosystems, 9(9), https://doi.org/10.1029/2008GC002085.

Oosting, S.E., Von Damm, K.L., 1996. Bromide/chloride fractionation in seafloor hydrothermal fluids from 9-10 degrees N east Pacific rise. Earth and Planetary Science Letters, 144(1-2): 133-145, Doi 10.1016/0012-821x(96)00149-5.

Pruess, K., Oldenburg, C., Moridis, G., 2012. TOUGH2 USER'S GUIDE, Version 2.1, Lawrence Berkeley National Laboratory, Berkeley, Calif., Report LBNL-43134.

Ramondenc, P., Germanovich, L.N., Lowell, R.P., 2008. Modeling Hydrothermal Response to Earthquakes at Oceanic Spreading Centers. Magma to Microbe: 97-121, DOI:10.1029/178GM06.

Rubin, K.H., Macdougall, J.D., Perfit, M.R., 1994. Po-210-Pb-210 Dating of Recent Volcanic-Eruptions on the Sea-Floor. Nature, 368(6474): 841-844, DOI:10.1038/368841a0.

Rupke, L.H., Hort, M., 2004. The impact of side wall cooling on the thermal history of lava lakes. Journal of Volcanology and Geothermal Research, 131(1-2): 165-178, DOI:10.1016/S0377-0273(03)00361-5.

Seyfried, W.E., Pester, N.J., Ding, K., Rough, M., 2011. Vent fluid chemistry of the Rainbow hydrothermal system (36 degrees N, MAR): Phase equilibria and in situ pH controls on subseafloor alteration processes. Geochimica Et Cosmochimica Acta, 75(6): 1574-1593, DOI:10.1016/j.gca.2011.01.001.

Singh, S., Lowell, R.P., 2015. Thermal response of mid-ocean ridge hydrothermal systems to perturbations. Deep Sea Research Part II: Topical Studies in Oceanography, 121: 41-52, DOI:10.1016/j.dsr2.2015.05.008.

Sohn, R.A., Fornari, D.J., Von Damm, K.L., Hildebrand, J.A., Webb, S.C., 1998. Seismic and hydrothermal evidence for a cracking event on the East Pacific Rise crest at 9 degrees 50 ' N. Nature, 396(6707): 159-161, DOI:10.1038/24146.

Sohn, R.A., Hildebrand, J.A., Webb, S.C., 1999. A microearthquake survey of the high-temperature vent fields on the volcanically active East Pacific Rise (9°50′N). Journal of Geophysical Research: Solid Earth, 104(B11): 25367-25377, https://doi.org/10.1029/1999JB900263.

Soule, S.A., Escartín, J., Fornari, D.J., 2009. A record of eruption and intrusion at a fast spreading ridge axis: Axial summit trough of the East Pacific Rise at 9–10°N. Geochemistry, Geophysics, Geosystems, 10(10), https://doi.org/10.1029/2008GC002354.

Soule, S.A., Fornari, D.J., Perfit, M.R., Rubin, K.H., 2007. New insights into mid-ocean ridge volcanic processes from the 2005-2006 eruption of the East Pacific Rise, 9 degrees 46 ' N-9 degrees 56 ' N. Geology, 35(12): 1079-1082, DOI:10.1130/G23924a.1.

Tan, Y.J., Tolstoy, M., Waldhauser, F., Wilcock, W.S.D., 2016. Dynamics of a seafloor-spreading episode at the East Pacific Rise. Nature, 540(7632): 261-+, DOI:10.1038/nature20116.

Tolstoy, M. et al., 2006. A sea-floor spreading event captured by seismometers. Science, 314(5807): 1920-1922, DOI:10.1126/science.1133950.

Vehling, F., Hasenclever, J., Rupke, L., 2018. Implementation Strategies for Accurate and Efficient Control Volume-Based Two-Phase Hydrothermal Flow Solutions. Transport in Porous Media, 121(2): 233-261, DOI:10.1007/s11242-017-0957-2.

Vehling, F., Hasenclever, J., Rupke, L., 2021. Brine Formation and Mobilization in Submarine Hydrothermal Systems: Insights from a Novel Multiphase Hydrothermal Flow Model in the System H2O-NaCl. Transport in Porous Media, 136(1): 65-102, DOI:10.1007/s11242-020-01499-6.

Von Damm, K.L., 1990. Seafloor Hydrothermal Activity - Black Smoker Chemistry and Chimneys. Annual Review of Earth and Planetary Sciences, 18: 173-204.

Von Damm, K.L., 2000. Chemistry of hydrothermal vent fluids from 9°–10°N, East Pacific Rise: “Time zero,” the immediate posteruptive period. Journal of Geophysical Research: Solid Earth, 105(B5): 11203-11222, DOI:10.1029/1999JB900414.

Von Damm, K.L., 2004. Evolution of the Hydrothermal System at East Pacific Rise 9°50'N: Geochemical Evidence for Changes in the Upper Oceanic Crust. In: German, C.R., Lin, J., Parson, L. (Eds.), Mid-Ocean Ridges - Hydrothermal Interactions Between the Lithosphere and Oceans. American Geophysical Union, Washington, DC, pp. 285-304.

Wilcock, W.S.D., 2004. Physical response of mid-ocean ridge hydrothermal systems to local earthquakes. Geochemistry, Geophysics, Geosystems, 5(11): n/a-n/a, DOI:10.1029/2004gc000701.

Xu, M. et al., 2014. Variations in axial magma lens properties along the East Pacific Rise (9°30′N–10°00′N) from swath 3-D seismic imaging and 1-D waveform inversion. Journal of Geophysical Research: Solid Earth, 119(4): 2721-2744, https://doi.org/10.1002/2013JB010730.

5 Outlook

In this thesis, two critical processes at mid-ocean fast-spreading ridges have been investigated, which have an impact on the heat transport pattern of the hydrothermal convection and the temporal changes of hydrothermal venting temperature and salinity. In this outlook, I propose further applications for the developed two-dimensional thermohaline numerical simulator and in the second part I point out the direction of upcoming research in the context of submarine hydrothermal systems.

5.1 Further applications for the developed two-dimensional thermohaline numerical simulator

At fast-spreading mid-ocean ridges, the crustal permeability structure is still debated. Different geological layers such as pillow basalts, gabbroic dikes, and the lower crust have different permeabilities varying with age and depth. For the accretion of the lower crust, two formation models have been suggested. In the gabbro glacier model crystallization occurs in the axial melt lens (AML). Solidified material subsides from the AML and also forms the lower part of the crust as it viscously flows downward and then sideward away from the spreading axis. In the other end-member model the lower crust is accreted by many sill intrusions along the axis building in situ gabbroic crust. Both end-member hypotheses as well as combined models are still highly debated as a petrological study by VanTongeren et al. (2015) and a geochemical study by Wanless and Shaw (2012) prefer different model combinations.

Quantitative energetic considerations for the accretion of the oceanic crust are widespread (Cathles, 2011; Morgan and Chen, 1993; Wolery and Sleep, 1976) because the spreading rate of the ridge axis governs the rate of mantle melts with a known temperature that has to be emplaced to fill the spreading gap. This boundary condition could be used for numerical simulations that couple the crustal accretion with cooling through hydrothermal flow. These simulations were fitted by adjusting the permeability structure of the upper and lower crust to the thermal structure of the EPR inferred by seismic tomography from Dunn et al. (2000). They have shown that a wide range of model combinations could be realized (Maclennan et al., 2004; Theissen-Krah et al., 2016). Theissen-Krah et al. (2016) predict that less than 50% of the lower crust crystallizes in situ as sills because a higher percentage would lead to too high melt fraction in this lower crustal melt zone, which is inconsistent with the maximal melt fractions based on studies of the Oman ophiolite (Nicolas and Boudier, 2015).

The above-mentioned coupled simulations could be significantly improved if simulations consider hydrothermal cooling with phase separation of seawater because Theissen-Krah et al. (2016) have applied pure water simulations. First, the coupled thermohaline simulations could find more realistic bulk permeabilities of the upper crust that fit the observed melt fraction and depth of the AML because the formation of a brine layer on top of the AML (cf. Chapter 3) has an insulation effect, which provides a higher permeability and flow rates to cool the AML. For the gabbro glacier model, where most of the mantle melts are injected into the AML, the highest permeabilities of the upper crust (sheeted dikes) are required to fit the observed melt fraction and depth of the AML. Therefore upper bounds of the permeabilities in the upper crust could be derived from this model. These upper bounds could be compared to permeabilities inferred from numerical simulations such as dike intrusions (cf. Chapter 4).

Second, coupled thermohaline simulations could answer the question how brines are distribute in the hot crustal region close to the steep lateral margins of the lower central hot region. At greater depth, the stability field of coexistent liquid + vapor moves to higher temperatures and brines become a single phase. Mixing these brines with single-phase recharge flow could potentially lead to off-axis (> 1 km distance) venting of fluids with increased salinity compared to seawater salinity. This scenario can fix the NaCl mass imbalance problem within the crust, which is predicted based upon observations that on-axis vents at the EPR show salinities below that of seawater over long periods.

As discussed in Chapter 4, the vent salinity and temperature evolutions after a diking event at the EPR are controlled during the first two to three years by the heat release of the dike, subsequent phase separation and low-salinity vapor venting. The second part of increased vent salinities is more challenging to explain. The numerical simulations predict an overshooting of salinities and a direct decline to starting value. In contrast, the observations show a dampening of the curve, and salinities are limited close above seawater salinity. One of the proposed dampening processes is the additional production of low-salinity vapors at the basal AML, which mix on their way up with brines at the dike. Addressing the second hypothesis, future numerical simulations have to explore dike intrusions in a setup where hydrothermal convection and phase separation on top of the AML is done by using a variable basal boundary condition. This basal boundary condition should represent the variable heat flux through the conductive boundary layer between the AML and the hydrothermal convection above when magma flow drains or replenishes the AML. In this scenario, the dike will intrude through the basal brine layer, which will affect the cooling of the lower dike and local brine accumulation. This scenario has not been investigated yet and could also affect the salinity evolution curve.

The second proposed reason for the dampening of the observed salinity curve is the inhomogeneous permeability and porosity of the crust. The uppermost layer 2A is approx. 200 m to 300 m deep at the axis and has noticeably higher permeability and porosity. Additionally, the permeability decreases with depth in layer 2A and 2B. This is thought to be the reason for faster cracking and cooling of the dike because the saline liquids are mobilized earlier and mix with low-salinity vapor from the deeper layer 2B (sheeted dikes). For proving this assumption, a more realistic permeability structure of layer 2A and 2B should be implemented for the numerical simulation setup in Chapter 4. Nevertheless, the interpretation of the results has to consider that this numerical simulation will not account for the permeability decrease caused by mineral precipitation such as anhydrite around the hot upflow zone, preventing entrainment of colder ambient seawater into the upflow zone.

5.2 Upcoming research in context of submarine hydrothermal systems

One of two open research questions is how the total mass flux of seafloor hydrothermal vents is distributed between focused flow, having high black smoker temperatures of around ~350 °C, and colder diffusive venting (10 °C to ~150 °C). This is crucial to better quantify the total metal mass flux into the ocean, as predominantly black smokers release metals. At fast-spreading ridges, black smoker vents are found at the axis, but the spatial distribution off-axis is not known. The distribution of diffusive venting is also not known, as they are difficult to find. It has been estimated that less than 10% of the heat is discharged from black smokers at the ridge axis (Baker et al., 1987; Hannington et al., 2005). The second question is which mechanism is responsible for the fact that some fluids stay hot prior to venting and others are highly diluted with shallow entrained seawater.

For the high-temperature vents, it is suggested that anhydrite and minor silica and pyrite precipitation is mounts a chimney-like structure around the upflow zone. This enables hot fluids, which rise principally with temperatures around 400 °C (Jupp and Schultz, 2000) from the basal reaction zone, to reach the seafloor, build black smoker chimneys and carry dissolved metals into the ocean. This mechanism is needed as numerical simulations of hydrothermal flow through the permeability discontinuity between layer 2A and layer 2B show entrainment of cold ambient seawater into the upflow zone, leading to considerable lower venting temperatures compared to observed temperatures (Hasenclever et al., 2014; Lowell et al., 2007). Also, a steady decrease of permeability with depth shows too low venting temperatures in simulations (see Chapter 3). Until today no boreholes at the axis of fast-spreading mid-ocean ridges have been drilled to infer how this mechanism works in detail, but numerical simulations of anhydrite precipitation have demonstrated how chimney-like structures could be formed (Guo et al., 2020; Kawada and Yoshida, 2010; Lowell et al., 2003). The recent work of Guo et al. (2020) has studied the accumulation rate and distribution of anhydrite and pyrite precipitates in a setup where hot black-smoker-like fluids are injected from below into 300 m thick high-permeable layer representing the layer 2A. In addition, the increase of venting total mass flux and temperature due to shell-like sealing of the upflow zone over time has been analyzed. Due to the model limitations in Guo et al. (2020), the mineral precipitation process is simplified as only fluid cooling and mixing has been considered. However, these novel results demonstrate how valuable a coupled approach of fluid flow and geochemical fluid-rock reactions that can track dissolved aqueous ions and complexes in two-phase flow would be in the future. This approach would allow simulations to explore rock alteration and mineral precipitation and gives insights into the temporal and spatial variability of black smoker vents.

For magmatic hydrothermal systems, the development of a so-called reaction-transport simulator, which is defined as a time step-wise coupled approach of fluid flow and geochemical reactions, is challenging. One challenge is the calculation of the thermodynamic properties of the aqueous ions and complexes for the entire needed PT-space. This is realized with the numerical formalism of the Helgeson-Kirkham-Flowers (HKF) equation of state, which was originally developed for 1000°C and 5 kbar but is restricted to H_2O density below 350 kg/m³ and therefore not suitable around the critical point of pure water and super-hot conditions (<375 °C) (Helgeson and Kirkham, 1974; Miron et al., 2019). For these conditions, where properties have non-linear changes, integration over accurate and dense experimental thermodynamic data are needed, which are difficult to derive, or a new EOS for the aqueous ions and complexes, similar to the HKF-EOS has to be developed for the problematic PT-space.

The second challenge is to efficiently combine fluid flow calculations with the calculations of geochemical reactions. Due to the high computational cost of both calculation of multicomponent flow and geochemical reactions of many components, a parallelized numerical scheme is reasonable. The recently published reactive transport simulator CSMP++GEM exemplary shows the progress in this field (Yapparova et al., 2017; Yapparova et al., 2019). Here the hydrothermal simulator CSMP++ (Weis et al., 2014) is combined with the GEMS3K software library (Kulik et al., 2013), which calculates the geochemical reactions.

5.3 Bibliography

Baker, E.T., Massoth, G.J., Feely, R.A., 1987. Cataclysmic Hydrothermal Venting on the Juan-De-Fuca Ridge. Nature, 329(6135): 149-151, DOI:10.1038/329149a0.

Cathles, L.M., 2011. What processes at mid-ocean ridges tell us about volcanogenic massive sulfide deposits. Mineralium Deposita, 46(5-6): 639-657, DOI:10.1007/s00126-010-0292-9.

Dunn, R.A., Toomey, D.R., Solomon, S.C., 2000. Three-dimensional seismic structure and physical properties of the crust and shallow mantle beneath the East Pacific Rise at 9 degrees 30'N. Journal of Geophysical Research, 105(B10): 23537-23555.

Guo, Z. et al., 2020. Anhydrite-Assisted Hydrothermal Metal Transport to the Ocean Floor—Insights From Thermo-Hydro-Chemical Modeling. Journal of Geophysical Research: Solid Earth, 125(7): e2019JB019035, https://doi.org/10.1029/2019JB019035.

Hannington, M.D. et al., 2005. Sea-Floor Tectonics and Submarine Hydrothermal Systems, One Hundredth Anniversary Volume. Society of Economic Geologists, pp. 0.

Hasenclever, J. et al., 2014. Hybrid shallow on-axis and deep off-axis hydrothermal circulation at fast-spreading ridges. Nature, 508(7497): 508-512, DOI:10.1038/nature13174.

Jupp, T., Schultz, A., 2000. A thermodynamic explanation for black smoker temperatures. Nature, 403(6772): 880-883.

Kawada, Y., Yoshida, S., 2010. Formation of a hydrothermal reservoir due to anhydrite precipitation in an arc volcano hydrothermal system. Journal of Geophysical Research: Solid Earth, 115(B11), https://doi.org/10.1029/2010JB007708.

Kulik, D.A. et al., 2013. GEM-Selektor geochemical modeling package: revised algorithm and GEMS3K numerical kernel for coupled simulation codes. Computational Geosciences, 17(1): 1-24, DOI:10.1007/s10596-012-9310-6.

Lowell, R.P., Gosnell, S., Yang, Y., 2007. Numerical simulations of single-pass hydrothermal convection at mid-ocean ridges: Effects of the extrusive layer and temperature-dependent permeability. Geochemistry, Geophysics, Geosystems, 8(10), https://doi.org/10.1029/2007GC001653.

Lowell, R.P., Yao, Y., Germanovich, L.N., 2003. Anhydrite precipitation and the relationship between focused and diffuse flow in seafloor hydrothermal systems. Journal of Geophysical Research: Solid Earth, 108(B9), https://doi.org/10.1029/2002JB002371.

Maclennan, J., Hulme, T., Singh, S.C., 2004. Thermal models of oceanic crustal accretion: Linking geophysical, geological and petrological observations. Geochemistry, Geophysics, Geosystems, 5(2), https://doi.org/10.1029/2003GC000605.

Morgan, J.P., Chen, Y.J., 1993. The genesis of oceanic crust: Magma injection, hydrothermal circulation, and crustal flow. Journal of Geophysical Research: Solid Earth, 98(B4): 6283-6297, https://doi.org/10.1029/92JB02650.

Nicolas, A., Boudier, F., 2015. Structural contribution from the Oman ophiolite to processes of crustal accretion at the East Pacific Rise. Terra Nova, 27(2): 77-96, https://doi.org/10.1111/ter.12137.

Theissen-Krah, S., Rüpke, L.H., Hasenclever, J., 2016. Modes of crustal accretion and their implications for hydrothermal circulation. Geophysical Research Letters, 43(3): 1124-1131, DOI:10.1002/2015GL067335.

VanTongeren, J.A., Hirth, G., Kelemen, P.B., 2015. Constraints on the accretion of the gabbroic lower oceanic crust from plagioclase lattice preferred orientation in the Samail ophiolite. Earth and Planetary Science Letters, 427: 249-261, https://doi.org/10.1016/j.epsl.2015.07.001.

Wanless, V.D., Shaw, A.M., 2012. Lower crustal crystallization and melt evolution at mid-ocean ridges. Nature Geoscience, 5(9): 651-655, DOI:10.1038/ngeo1552.

Weis, P., Driesner, T., Coumou, D., Geiger, S., 2014. Hydrothermal, multiphase convection of H2O-NaCl fluids from ambient to magmatic temperatures: a new numerical scheme and benchmarks for code comparison. Geofluids, 14(3): 347-371, DOI:10.1111/gfl.12080.

Wolery, T.J., Sleep, N.H., 1976. Hydrothermal Circulation and Geochemical Flux at Mid-Ocean Ridges. Journal of Geology, 84(3): 249-275, DOI:10.1086/628195.

Yapparova, A., Gabellone, T., Whitaker, F., Kulik, D.A., Matthäi, S.K., 2017. Reactive Transport Modelling of Dolomitisation Using the New CSMP++GEM Coupled Code: Governing Equations, Solution Method and Benchmarking Results. Transport in Porous Media, 117(3): 385-413, DOI:10.1007/s11242-017-0839-7.

Yapparova, A., Miron, G.D., Kulik, D.A., Kosakowski, G., Driesner, T., 2019. An advanced reactive transport simulation scheme for hydrothermal systems modelling. Geothermics, 78: 138-153, https://doi.org/10.1016/j.geothermics.2018.12.003.

6 Danksagung

An dieser Stelle möchte ich mich ganz besonders bei meinem Betreuer Lars Rüpke bedanken. Ich habe Ihn als stets gut gelaunten Menschen schätzen gelernt, der so für eine gute Arbeitsatmosphäre gesorgt hat. Das in mich gesetzte Vertrauen hat die Entwicklung des Hydrothermal-Simulators ermöglicht, auch wenn manches länger gebraucht hat, als es geplant war. Die kompetente Betreuung hat mich zu einem selbständigen Wissenschaftler werden lassen.

Vielen Dank an Jörg Hasenclever, der mich immer hilfsbereit untersützt hat und als Mitautor meiner Publikationen viel für die hohe Qualität beigetragen hat. Ich habe viel von ihm gelernt, besonders durch seine Erfahrungen in der Programmierung von numerischen Simulatoren.

Ich bin sehr dankbar, dass ich als Stipendiat in die transatlantische Graduiertenschule HOSST der Helmholtz-Gemeinschaft aufgenommen wurde. Die gut organisierten Exkursionen sowie der Gastaufenthalt an der Dalhousie Universität waren sehr interessant und lehrreich. Dabei möchte ich mich insbesondere bei Mladen Nedimović für die gastfreundschaftliche Betreung bedanken.

Bei meinen Eltern möchte ich mich für die stetige Unterstüzung besonders während des Studiums bedanken.

Großer Dank gebührt Gerald Rohde, Nellia Bleyer und Zhikui Guo für die wertvollen Korrekturvorschläge.

7 Erklärung

Hiermit erkläre ich, Falko Vehling, dass ich diese Doktroarbeit selbständig und ohne Zuhilfenahme unerlaubter Hilfsmittel erstellt habe. Weder diese noch eine ähnliche Arbeit wurde an einer anderen Abteilung oder Hochschule im Rahmen eines Prüfungsverfahrens veröffentlicht oder zur Veröffentlichung vorgelegt. Ferner versichere ich, dass die Arbeit unter Einhaltung der Regeln guter wissenschaftlicher Praxis der Deutschen Forschungsgemeinschaft entstanden ist. Ich versichere, dass mir noch kein akademischer Titel entzogen wurde.

Ort/Datum Unterschrift